

Ge-Sb-Se chalcogenide glass for near- and mid-infrared nonlinear photonics

by

Molly Rebecca Krogstad

B.S., University of Minnesota, 2011

M.S., University of Colorado, 2014

A thesis submitted to the

Faculty of the Graduate School of the

University of Colorado in partial fulfillment

of the requirements for the degree of

Doctor of Philosophy

Department of Physics

2017

This thesis entitled:
Ge-Sb-Se chalcogenide glass for near- and mid-infrared nonlinear photonics
written by Molly Rebecca Krogstad
has been approved for the Department of Physics

Professor Juliet T. Gopinath

Professor Scott Diddams

Date _____

The final copy of this thesis has been examined by the signatories, and we find that both the content and the form meet acceptable presentation standards of scholarly work in the above mentioned discipline.

Krogstad, Molly Rebecca (Ph.D., Physics)

Ge-Sb-Se chalcogenide glass for near- and mid-infrared nonlinear photonics

Thesis directed by Professor Juliet T. Gopinath

The chalcogenide glass, $\text{Ge}_{28}\text{Sb}_{12}\text{Se}_{60}$, is a promising material platform for compact, low-threshold nonlinear optical devices operating in the near- to mid-infrared. It is particularly attractive given its wide range of transparency, large Kerr coefficient, and relatively weak multi-photon absorption. The nonlinear optical properties of $\text{Ge}_{28}\text{Sb}_{12}\text{Se}_{60}$ were investigated in bulk and waveguide forms, over a range of wavelengths from 1.0 to 3.5 μm . From z-scan measurements at 1.03 μm , using circularly polarized, 200 fs pulses at 374 kHz, bulk $\text{Ge}_{28}\text{Sb}_{12}\text{Se}_{60}$ glass was found to have a nonlinear refractive index ~ 130 times that of fused silica and a two-photon absorption coefficient of 3.5 cm/GW. Ge-Sb-Se waveguides and microresonators were designed and characterized, laying groundwork for the development of efficient, compact nonlinear devices such as frequency combs and optical switches. In particular, single-mode Ge-Sb-Se strip waveguides, fabricated by photo- or e-beam lithography, followed by thermal evaporation and lift-off, were demonstrated with average propagation losses of 11.8 dB/cm at 1.03 μm and 4.0-6.1 dB/cm at 1.55 μm . Nonlinear optical waveguides were characterized with measurements of spectral broadening and intensity-dependent transmission, revealing a large measured nonlinear figure of merit of 5.2 ± 1.6 at 1.55 μm . Hybrid chalcogenide-silica wedge microresonators were characterized from 1500-1630 nm, with loaded quality factors up to 1.5×10^5 and thermal resonant shifts ~ 60.5 pm/ $^\circ\text{C}$. Finally, planar chalcogenide-based ring resonators were designed for operation at 1.55 and 3.5 μm , simulating dispersion and optimizing waveguide dimensions for maximum four-wave mixing conversion efficiency. Ring resonators with 6- and 20- μm radii were demonstrated with intrinsic quality factors of $1-2 \times 10^4$ and 8.3×10^4 , respectively.

Dedication

To my teachers, for encouraging my love of learning.

Acknowledgements

This work would not have been possible without the help and support of my advisor, collaborators, colleagues, family, and friends. I am grateful for the mentorship provided by my advisor, Professor Juliet Gopinath. Her guidance has been crucial, and her ability to encourage and motivate has been inspiring. I would also like to thank my committee members, including Dr. Scott Diddams, Dr. Thomas Schibli, Dr. Wounghang Park, and Dr. Bob McLeod. They provided useful feedback and insightful comments on my research.

I am grateful for the help of the chalcogenide project team, including Dr. Juliet Gopinath, Dr. Wounghang Park, Dr. Sungmo Ahn, Dr. Gumin Kang, Suehyun Cho, Michael Grayson, Xi Chen, Lisa Rengnath, and Martin Kronberg. In particular, Sungmo, Gumin, and Michael have been instrumental in fabricating chalcogenide devices. I would also like to thank Rick Bojko at the University of Washington, and Kevin Roberts at the University of Minnesota, for e-beam fabrication and fruitful discussions.

I would like to acknowledge help and advice from members of the Optics and Photonics Lab, past and present, including Rob Niederriter, Kenneth Underwood, Xi Chen, Brendan Heffernan, Andrew Jones, Mo Zohrabi, Caroline Hughes, Alex Anderson, and Megan Kelleher. Their curiosity, support, and willingness to help have made the lab a great place to work!

I would also like to thank my teachers and mentors. Fred Orsted and Professor Paul Crowell made me fall in love with the physics approach to problem solving. Chad Geppert pushed and inspired me as an experimentalist. My REU mentors Noah Fitch, Colin O'Sullivan, Professor Heather Lewandowski, and Professor Bob Boyd showed incredible patience as I learned practical

lab skills. Professor Jim Leger encouraged my exploration of experimental optics—his thoughtful lectures and hands-on labs motivated me to learn more, and his advice has been invaluable.

Finally, I would like to thank my family and friends for their support throughout this process. My friend Suehyun helped me stay on track through thesis club and made me realize that temporarily becoming a morning person is not so bad. My friends from my folk music group and quintet provided a fun diversion when I needed a break, and my friends from Mount Cal offered a listening ear throughout the ups and downs of grad school. My family provided support, encouragement, and perspective during this journey, reminding me who I am, where I come from, and what really matters most.

Contents

Chapter

1. Introduction

1.1 Motivation for nonlinear integrated photonics.....	1
1.2 Introduction to nonlinear photonics.....	4
1.3 Mid-infrared applications and sources.....	7
1.4 Why chalcogenide glasses?.....	15
1.5 Thesis outline.....	20

2. Optical characterization of bulk $\text{Ge}_{28}\text{Sb}_{12}\text{Se}_{60}$

2.1 Overview.....	21
2.2 Introduction to z-scan.....	21
2.3 Z-scan measurements of third-order nonlinearity in $\text{Ge}_{28}\text{Sb}_{12}\text{Se}_{60}$	27
2.4 Discussion of z-scan results.....	33
2.5 Linear absorption measurements of $\text{Ge}_{28}\text{Sb}_{12}\text{Se}_{60}$	35
2.6 Conclusion.....	37

3. Optical waveguide design and characterization

3.1 Overview.....	39
3.2 Waveguides for nonlinear optics.....	40
3.2.1 Waveguide loss.....	42
3.2.2 Chromatic dispersion.....	47
3.2.3 Waveguide nonlinearity.....	51

3.2.4	Waveguide design geometries.....	52
3.2.5	Linear loss characterization techniques.....	53
3.2.6	Nonlinear loss characterization techniques.....	55
3.2.7	Nonlinear refractive index characterization techniques.....	58
3.3	Waveguides at 1.0 μm	59
3.3.1	Waveguide design and fabrication at 1.0 μm	59
3.3.2	Linear waveguide characterization at 1.0 μm	61
3.3.3	Nonlinear waveguide characterization at 1.0 μm	65
3.4	Waveguides at 1.55 μm	68
3.4.1	Motivation.....	68
3.4.2	Waveguide design at 1.55 μm	68
3.4.3	Waveguide fabrication at 1.55 μm	70
3.4.4	Linear waveguide characterization at 1.55 μm	71
3.4.5	Nonlinear waveguide characterization at 1.55 μm	74
3.5	Waveguides at 3.5 μm	81
3.6	Conclusion.....	82
4	Ge-Sb-Se Ring Resonators	
4.1	Overview.....	84
4.2	Ring resonators for nonlinear optics.....	85
4.2.1	Ring resonator motivation and applications.....	85
4.2.2	Ring resonator properties.....	86
4.2.3	Four-wave mixing and resonant enhancement.....	90
4.2.4	Ring coupling design.....	97

4.3 Ge-Sb-Se ring resonators for four-wave mixing.....	101
4.3.1 Near-infrared ring resonator design.....	101
4.3.2 Mid-infrared ring resonator design.....	106
4.3.3 Ring resonator fabrication.....	110
4.3.4 Ring resonator characterization.....	111
4.4 Conclusion.....	117
5. Ge-Sb-Se wedge resonators	
5.1 Overview.....	119
5.2 Wedge resonators motivation.....	120
5.3 Wedge resonator design and fabrication.....	121
5.4 Q measurements in wedge resonators.....	124
5.5 Thermal characterization of wedge resonators.....	131
5.6 Conclusion.....	136
6. Conclusions	
6.1 Summary.....	138
6.2 Future directions.....	140
References.....	144
 Appendices	
A. Circuit schematic for pulse-picking.....	164
B. Z-scan fitting procedure.....	166
C. Waveguide design code.....	170

C.1	Number of modes.....	170
C.2	Second-order dispersion.....	172
C.3	Effective area and nonlinear parameter.....	175
C.4	Bend loss for curved waveguides.....	178
C.5	Higher-order dispersion.....	179
D.	Split-step code.....	184
D.1	Split-step base code with two-photon absorption.....	184
D.2	Example using split-step code to calculate spectral broadening.....	193
E.	Ring resonator design code.....	197
E.1	Ring code for four-wave mixing.....	197
E.2	Phase matching code for concentric (pulley) couplers.....	205
F.	Derivation of thermal resonant wavelength shift in wedge resonator.....	208
G.	Microscope components.....	212

List of Tables

1.1 Comparison of n_2 at 1.55 μm in nonlinear optics material platforms	15
2.1 Typical magnitude and response time of nonlinear refractive index.....	25
3.1 Average loss for Ge-Sb-Se waveguides at 1.53 μm	74
4.1 Summary of ring design for 800 nm (w) x 330 nm (h) Ge-Sb-Se rings at $\lambda=1.55\mu\text{m}$	105
4.2 Summary of coupling gap designs to for 1220 (w) x 520 (h) Ge-Sb-Se rings at $\lambda=3.5\mu\text{m}$	110
F.1 Thermo-optic and thermal expansion coefficients.....	210
F.2 Summary of measured thermal resonant shift and thermo-optic coefficient.....	211
G.1 Parts list for microscope.....	212

List of Figures

1.1. Free-space photonics and integrated photonics.....	2
1.2. Four-wave mixing schematic.....	6
1.3 Mid-infrared chemical fingerprint region.....	8
1.4 Illustration of various microresonator geometries.....	11
1.5 Optical frequency comb.....	13
1.6 Material platforms used in frequency comb generation.....	14
1.7 Transmission for common optical materials.....	16
1.8 Continuous random network structure.....	17
1.9 Example of coordination defect in chalcogenide $\text{Ge}_2\text{S}_6\text{H}_4$	18
2.1 General schematic of z-scan setup.....	22
2.2 Experimental setup for z-scan.....	28
2.3 Schematic of Yb-doped fiber laser.....	29
2.4 Experimental z-scan traces for $\text{Ge}_{28}\text{Sb}_{12}\text{Se}_{60}$	31
2.5 Two-photon absorption and nonlinear refractive index for Ge-Sb-Se.....	32
2.6 Experimental setup for Brewster angle absorption measurement.....	36
3.1 Side-view schematic of planar waveguide.....	42
3.2 Comparison of fundamental waveguide mode profile for various bend radius.....	45

3.3 Frequency dependence of refractive index (top) and absorption (bottom).....	49
3.4 Wavelength dependence of refractive index of bulk Ge ₂₈ Sb ₁₂ Se ₆₀	50
3.5 Wavelength dependence of material group velocity dispersion (β_2) for bulk Ge ₂₈ Sb ₁₂ Se ₆₀	50
3.6 Typical waveguide geometries.....	53
3.7 Illustration of scattered light waveguide loss method.....	54
3.8 Fabrication process flow for strip waveguides.....	60
3.9 Atomic composition, SEM image, and mode profile of thin-film Ge-Sb-Se devices.....	61
3.10 Waveguide characterization setup.....	62
3.11 Ge-Sb-Se waveguide propagation loss at 1.03 μm	63
3.12 Nonlinear loss in Ge-Sb-Se waveguide at 1.03 μm	66
3.13 Spectral broadening in Ge-Sb-Se waveguide at 1.03 μm	67
3.14 Mode profiles of Ge-Sb-Se waveguide at 1550 nm.....	68
3.15 Dispersion and SEM of Ge-Sb-Se waveguide at 1550 nm.....	70
3.16 Schematic illustrating sub-micron waveguide fabrication flow.....	70
3.17 Band edge measurements of bulk and thin-film Ge-Sb-Se.....	72
3.18 Er-doped fiber laser schematic.....	75
3.19 Er-doped fiber laser optical spectrum and intensity autocorrelation.....	75
3.20 Nonlinear absorption in Ge-Sb-Se waveguides at 1550 nm.....	76
3.21 Spectral broadening experiment and simulation for Ge-Sb-Se waveguides.....	78
3.22 Strip waveguide schematic and simulated dispersion at 3.5 μm	82
4.1 Schematic of all-pass ring resonator and add-drop ring resonator.....	87
4.2 Example transmission spectra for an all-pass ring resonator.....	88

4.3 Illustration of degenerate four-wave mixing.....	91
4.4 Field enhancement factor as a function of wavelength.....	94
4.5 Phase mismatch for air-clad, Ge-Sb-Se ring resonators on SiO ₂ at 1550 nm.....	95
4.6 Theoretical four-wave mixing efficiency.....	96
4.7 Schematic of bus-to-ring coupling and coupling strength.....	97
4.8 Schematic of alternative coupling schemes.....	99
4.9 Propagation constant vs. bus width for concentric (pulley) coupler.....	100
4.10 Phase-matched width vs. gap distance for concentric (pulley) coupler.....	100
4.11 Design process for ring resonators optimized for four-wave mixing.....	101
4.12 Four-wave mixing for various chalcogenide waveguide dimensions.....	102
4.13 Simulated bend loss vs. radius and corresponding fit for Ge-Sb-Se waveguide.....	103
4.14 Example Lumerical varFDTD simulation of pulley coupler.....	104
4.15 Coupling strength vs. gap for straight coupler with various ring radii.....	105
4.16 Chip layout for ring resonators at 1550 nm.....	106
4.17 Four-wave mixing efficiency vs. radius for chalcogenide (ChG) ring at 3500 nm.....	107
4.18 Four-wave mixing efficiency vs. radius for ChG rings, for optimized dimensions.....	108
4.19 Simulated bend loss vs. radius and corresponding fit for ChG-on-MgF ₂ at 3500 nm.....	109
4.20 Example straight coupler simulated using Lumerical varFDTD.....	109
4.21 Plot of extracted coupling strength as a function of bus-ring gap distance at $\lambda=3.5\mu\text{m}$	110
4.22 Ring resonator coupling schematic.....	112
4.23 Average TE propagation loss vs. waveguide width for various samples.....	112
4.24 Near-infrared transmission vs. wavelength for Ge-Sb-Se ring with 6 μm radius.....	113
4.25 Lorentzian fit to resonance for an all-pass ChG ring with 6 μm radius.....	114

4.26 Schematic of pattern discretization in a ring resonator.....	115
4.27 Scanning electron micrographs (SEMs) of ring resonator sample.....	116
4.28 Transmission spectra from drop port of 20 μm add-drop ring resonator.....	117
5.1 Fabrication process flow for hybrid chalcogenide-silica wedge resonators.....	121
5.2 Simulated fundamental mode profiles of hybrid wedge resonators.....	122
5.3 Scanning electron micrographs (SEMs) of hybrid wedge resonators.....	123
5.4 Wedge resonator coupling schematic.....	124
5.5 Coupling setup and wedge resonator.....	125
5.6 Transmission vs. wavelength for 46.5 μm diameter hybrid wedge resonator.....	126
5.7 Fit for one resonant mode from the 46.5 μm diameter hybrid wedge resonator.....	126
5.8 Transmission vs. wavelength for 13.5 μm diameter hybrid wedge resonator.....	127
5.9 Fit for critically-coupled mode from the 13.5 μm diameter hybrid wedge resonator.....	128
5.10 Inverted-plate ChG resonator for mid-infrared operation.....	129
5.11 Simulated fundamental mode properties of As_2S_3 chalcogenide fiber.....	130
5.12 Thermal characterization setup for wedge resonators.....	131
5.13 Wedge resonator transmission spectra, taken at various temperatures.....	132
5.14 Shift in resonant wavelength as a function of temperature.....	133
5.15 Athermal three-layer hybrid wedge simulation.....	136
A.1 Circuit schematic for driving pulse picker.....	165
F.1 Schematic of hybrid wedge resonator cross section.....	209

1. INTRODUCTION

1.1 Motivation for nonlinear integrated photonics

Photonics, a field which focuses on the generation, manipulation, and detection of light, has become ubiquitous in everyday life. For example, photonics plays a crucial role in global data communications and telecommunications. Roughly 99 percent of all intercontinental data traffic, including internet usage, phone calls, and texts, goes through undersea fiber-optic cables [1]. Photonics is also used in a number of consumer electronics, including smart phone cameras and displays, DVD players, and barcode scanners. In addition, medical applications have benefited from photonics. For example, lasers are routinely used for LASIK eye surgery, and both microscopy and endoscopy exploit optical components for imaging. Finally, photonics finds use in travel. Optical gyroscopes aid in-flight navigation, and a light-based version of radar known as LiDAR (Light Detection And Ranging) is being explored to guide self-driving cars.

Integrated photonics may open new frontiers in computing, communications, and sensing. The term “integrated photonics” refers to fabricating several photonic components, such as optical sources, beam splitters, couplers, and detectors, on a single planar substrate. This integration can enable the control of light on a much smaller scale, with sub-micron waveguides and $< \text{cm}^2$ footprints, at sub-mW operating powers. An illustration comparing free space photonics and integrated photonics is shown in Figure 1.1 [2,3]. In addition to reduced size, fully integrated systems could also offer improved stability and reliability by eliminating the need for alignment.

The idea of integrated photonics was first proposed by S. E. Miller in 1969 [4], with the goal of miniaturizing optical systems. Miller envisioned the development of integrated optical circuits, in which both active and passive components were all incorporated on a single substrate [4]. Analogous to electronic circuits, photonic integrated circuits could use photons, instead of electrons, to perform an array of functions, including splitting, combining, switching, amplifying, and modulating signals.

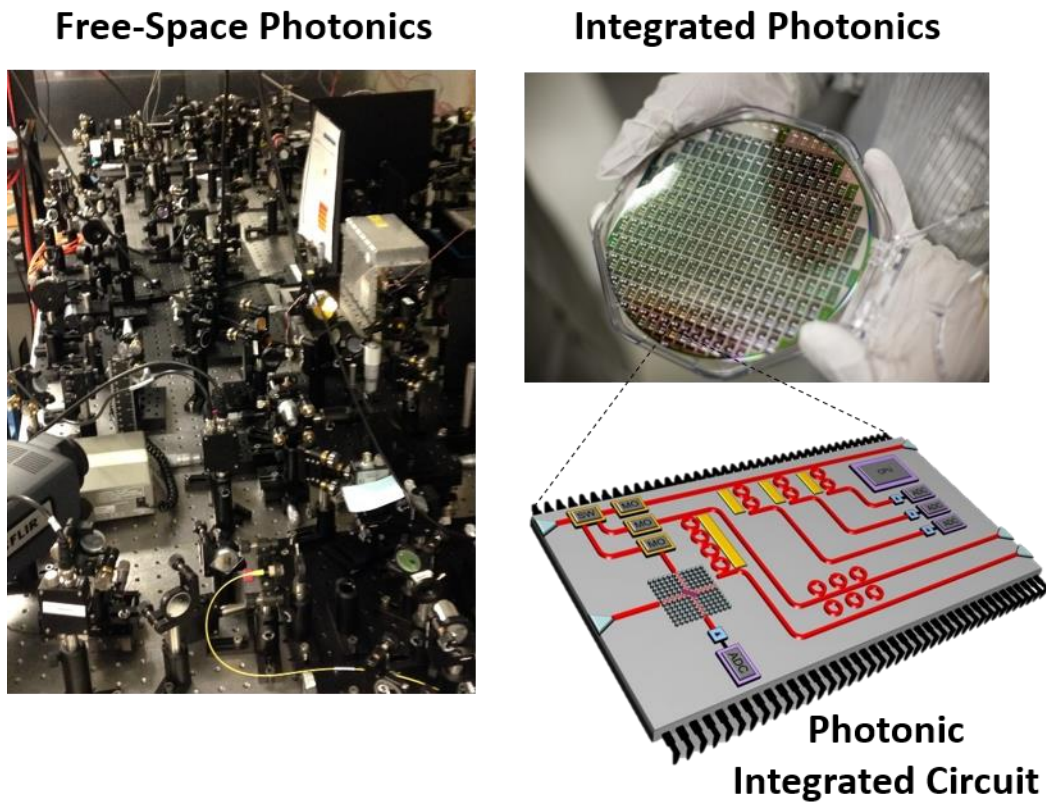


Figure 1.1. Free-space photonics and integrated photonics. Left: A picture of free-space photonic components on ~5-foot by 10-foot optical table. Upper right: A ~6-inch diameter wafer containing many photonic integrated circuits. Lower right: A schematic of a ~1 cm² photonic integrated circuit, consisting of several different components. Integrated photonics images reproduced from [2,3].

Many of the functions desired for signal processing are nonlinear. The nonlinear refractive index, or optical Kerr nonlinearity, provides a mechanism to perform these functions, such as

switching and amplifying, in integrated photonics. The refractive index of a material, n , describes how light propagates through a material, and the index determines how much light is bent, or refracted, when it enters a material. The nonlinear refractive index, n_2 , describes how the refractive index of a material changes with intensity I , such that

$$n(I) = n_0 + n_2 I, \quad (1.1)$$

where n_0 is the linear refractive index. The Kerr nonlinearity produces several nonlinear effects, including self-phase modulation and four-wave mixing. Self-phase modulation refers to changes in the phase and resulting frequency of a pulse, which can lead to spectral broadening. Four-wave mixing is a type of nonlinear frequency conversion caused by the Kerr nonlinearity. Both of these effects will be described in more detail in Section 1.2.

The Kerr nonlinearity opens doors to many sought-after applications in integrated photonics, including high-speed communications, frequency conversion, sensing, and quantum photonics. The Kerr effect's ultrafast response time, on the order of femtoseconds [5], provides broad bandwidths, with the potential to push current GHz electronic computing towards petahertz (10^{15}) rates using all-optical signal processing and switching [6,7]. Additionally, Kerr-based nonlinear effects can be used for generating a wide range of optical sources. For example, spectral broadening, produced by changes in phase from the nonlinear refractive index, can help enable the generation of short pulsed sources [8]. Four-wave mixing can be used to produce optical frequency combs [9,10], which can span mid-infrared spectral regimes useful for sensing and spectroscopy. Nonlinear frequency conversion may also be exploited to develop quantum sources for quantum information [6,11-12,233], which may offer solutions out of reach for classical computing [233].

While these applications hold great interest, the Kerr effect is often small, with $n_2 \sim 10^{-20}$ to 10^{-19} m²/W for common optical materials [5], leading to high thresholds for nonlinear effects and requiring specialized sources. Additionally, lack of suitable materials, particularly in the mid-infrared, can limit the wavelength range of operation. To overcome these challenges, this research explores the use of a highly nonlinear, broadly transparent chalcogenide material, combined with strong light-matter interaction provided by sub-micron waveguide and microresonator structures. The ultimate goal of this research is to develop compact, low threshold, nonlinear integrated optical devices in the near-to mid-infrared spectral regime.

1.2 Introduction to nonlinear photonics

A material's response to an applied electric field can be described by its polarization, or net dipole moment per unit volume,

$$\mathbf{P} = \varepsilon_0[\chi^{(1)}\mathbf{E} + \chi^{(2)}\mathbf{E}^2 + \chi^{(3)}\mathbf{E}^3 + \dots], \quad (1.2)$$

where \mathbf{E} is the field, ε_0 is the permittivity of free space, and $\chi^{(n)}$ is the n^{th} order susceptibility [5]. Here, the polarization has been written as a power series expansion in terms of the field. In general, the susceptibility $\chi^{(n)}$ is a $(n+1)^{\text{th}}$ rank tensor, and the field and polarization are vectors, but they are written as scalars here for simplicity. Centrosymmetric materials are those which display inversion symmetry, meaning that the materials remain the same when the position of each atom in the material, \vec{r} , is moved to its inverse, $-\vec{r}$. Common examples of centrosymmetric materials include liquids, gases, and amorphous solids. For centrosymmetric materials, including amorphous chalcogenide glasses, even-ordered susceptibility including $\chi^{(2)}$ is zero, and the third-order susceptibility, $\chi^{(3)}$, is the lowest-order nonlinear response.

As noted in Equation 1.1, it is also useful to define a nonlinear refractive index, n_2 , which describes the change in refractive index n with intensity I . The nonlinear refractive index is directly related to the real part of $\chi^{(3)}$ as

$$n_2 = \frac{3\chi^3}{4n_0^2\epsilon_0c}, \quad (1.3)$$

where ϵ_0 is the permittivity of free space and c is the speed of light [5]. While various physical mechanisms can produce a change in the refractive index, the $\chi^{(3)}$ -based nonlinear refractive index is caused by electronic polarization, or distortion of the electronic cloud, and is of particular interest due to its ultrafast response time.

The $\chi^{(3)}$ -based nonlinear refractive index drives several different physical processes, including self-phase modulation and four-wave mixing [5]. For example, the nonlinear refractive index is responsible for self-phase modulation, a nonlinear effect in which the phase of an optical pulse changes as it propagates through the nonlinear medium. For a pulse with intensity $I(t)$, the nonlinear refractive index will cause an intensity-dependent change in index. The corresponding phase change $\phi(t)$ experienced by a pulse can be written as

$$\phi(t) = \frac{n_2 I(t) \omega_0 L}{c}, \quad (1.4)$$

where t is the time, L is the length of the medium, c is the speed of light, and ω_0 is the frequency. This assumes an instantaneous response and negligible dispersion relative to the material length and pulse duration [5]. Due to this time-varying phase, the spectrum will also be modified. In particular, the instantaneous frequency of the pulse, $\omega(t)$, is given by

$$\omega(t) = \omega_0 + \delta\omega(t), \quad (1.5)$$

where

$$\delta\omega(t) = -\frac{d\phi(t)}{dt}. \quad (1.6)$$

Differentiating Equation 1.4 with respect to time, the nonlinear phase will change the instantaneous frequency of the pulse, such that

$$\delta\omega(t) = -\frac{n_2\omega_0 L}{c} \frac{dI(t)}{dt}. \quad (1.7)$$

Self-phase modulation can cause spectral broadening [13], which is useful for applications such as supercontinuum generation [14,15] and pulse compression [16]. Additionally, the interplay of self-phase modulation and dispersion, the wavelength dependence of refractive index, affects pulse formation in nonlinear media such as fibers and waveguides [17].

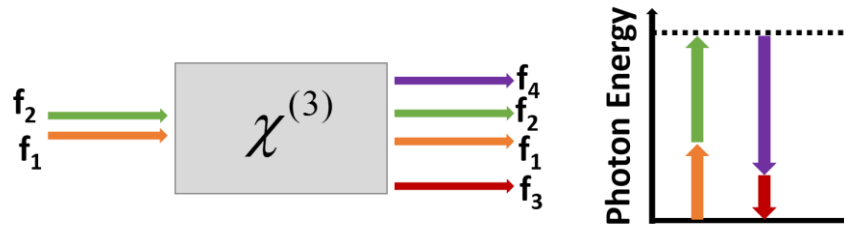


Figure 1.2. Four-wave mixing schematic. Left: In four-wave mixing, two frequencies f_1 and f_2 combine in a $\chi^{(3)}$ nonlinear crystal to produce two additional optical frequencies, f_3 and f_4 , obeying energy and momentum conservation. Right: Corresponding energy level diagram for four-wave mixing.

The nonlinear refractive index also drives four-wave mixing, a nonlinear effect which provides an attractive approach to frequency conversion. In the four-wave mixing process, two optical frequencies combine in a nonlinear crystal and produce two additional optical frequencies, obeying energy and momentum conservation (See Figure 1.2). In contrast to narrowband atomic and molecular energy level transitions used for lasing, four-wave mixing has broadband gain, limited only by material transparency and dispersion [9]. This feature enables the generation of

light at previously hard-to-reach frequencies. For example, four-wave mixing has been used for mid-infrared optical parametric amplification [18], optical parametric oscillation [19], and frequency comb generation [10,20].

Through frequency conversion and spectral broadening effects, the nonlinear refractive index enables the creation of a broader range of optical sources, with uses in diverse fields ranging from communications and sensing, to defense and medicine. Nonlinear optics pairs particularly well with photonic integration, since micron-scale waveguide dimensions tightly confine light to a small area, increasing the intensity and enhancing efficiency of nonlinear optical processes. Furthermore, the Kerr nonlinearity's fast response on the order of fs pushes new frontiers in high speed optical processing, and nonlinear frequency conversion enables development of broadband optical sources in the mid-infrared, ideal for sensing. While telecom applications have been well-developed, applications in the mid-infrared are still in their infancy. In Section 1.3, potential mid-infrared applications and sources are explored.

1.3 Mid-infrared applications and sources

Analogous to harmonic oscillators, many molecules exhibit vibrational resonances, corresponding to the bending or stretching of molecular bonds. Since the resonant frequencies will depend on the masses of the constituent atoms and bond strengths, these frequencies can be used to help identify the given molecule. The mid-infrared spectral region, covering wavelengths from $\sim 2\text{-}20\ \mu\text{m}$, is often dubbed the chemical fingerprint region [21], given the abundance of characteristic absorption signatures of many molecules (See Figure 1.3 [20]). Furthermore, absorption strengths in the mid-infrared are typically 10 to 1000 times greater than those in the visible or near-infrared [21]. Mid-infrared spectroscopy is useful for a wide range of environmental, defense, scientific, and health applications [23]. For example, absorption

measurements can be used to detect trace gases in the atmosphere [24], analyze samples for explosive residues [25], or non-invasively monitor levels of glucose in patients [26].

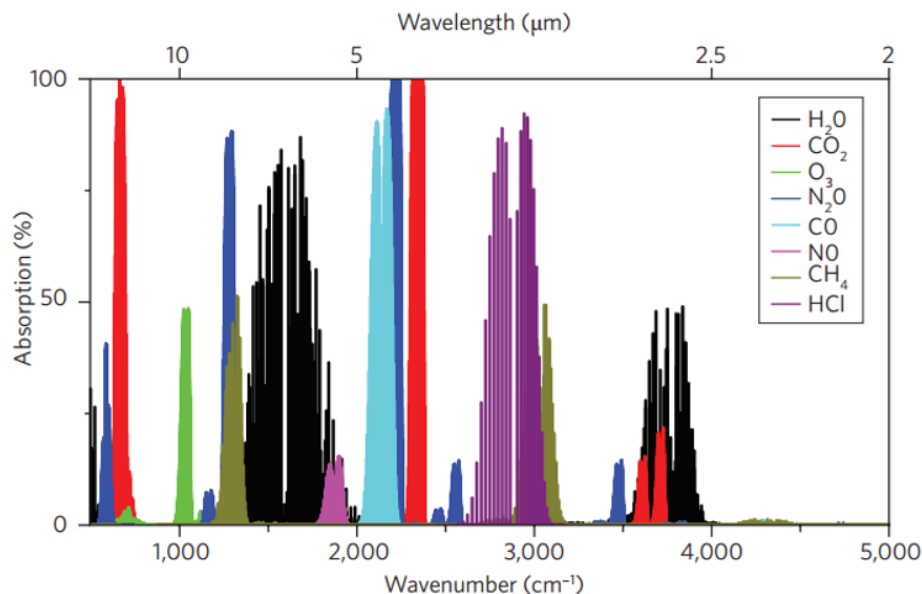


Figure 1.3. Mid-infrared chemical fingerprint region. Absorption vs. wavelength (top axis) and wavenumber (bottom axis) is plotted for a variety of gaseous molecules from 2-20 μm over a path length of 1 cm [20]. Note that various molecules have unique absorption spectra, or ‘chemical fingerprints’. Figure reprinted by permission from Macmillan Publishers Ltd: Nature Photonics [20], copyright 2012.

Although the mid-infrared region provides many strong, characteristic absorption lines useful for distinguishing many chemicals [20,27], this spectral region presents challenges for photonics-based technology. Sources in this spectral regime are limited and often lack the broadband coverage desired for spectroscopy [28]. Current mid-infrared sources include direct sources based on energy level transitions, such as semiconductor diode lasers [29], quantum cascade lasers [30], and fiber lasers [31], as well as sources based on nonlinear wavelength conversion [32,33].

Direct bandgap semiconductor diode lasers generate light based on radiative recombination of electrons and holes. Direct bandgap III-V semiconductor diode lasers can operate at room

temperature from wavelengths of 2.3-2.7 μm [29], but performance at longer wavelengths is severely restricted by Auger recombination, a nonradiative process in which the energy and momentum of an electron-hole pair is transferred to another electron or hole. Auger recombination limits the carrier lifetime, reducing the efficiency [34].

An alternative to diode lasers is a quantum cascade laser (QCL), a semiconductor laser based on intersubband transitions [30]. QCLs have advanced significantly over the past 20 years, offering high cw output power up to several watts and commercial availability [30,35]. However, QCLs can suffer from undesirable noise on their free-running linewidth [22], with frequency noise power spectral density at 1 Hz \sim 12 orders of magnitude higher than an optical frequency comb [227], making stabilization a challenge.

Finally, fiber lasers provide another means to generate mid-infrared light, by utilizing transitions of rare-earth dopants [31]. However, mid-infrared fiber lasers are still in the early stages of development. Although a variety of host fiber glasses and rare earth cation dopants have been studied, output power decreases drastically with increased wavelength, and fiber laser emission beyond 3 or 4 μm is a significant challenge [31, 36]. This is in part due to an increased quantum defect at longer wavelengths [31]. Additional problems include the lack of efficient longer-wavelength pump sources and limited rare earth transitions in the mid-infrared, along with difficulties developing suitably doped mid-infrared fiber with good performance [31].

The challenges with mid-infrared optical sources are in part due to undesirable properties of many materials in the mid-infrared. For instance, the long-wavelength transparency of many materials is limited by multi-phonon absorption [234], in which a single photon is absorbed, and multiple phonons, or quantized vibrations, are created. Additionally, multi-phonon non-radiative decay can also significantly reduce the lifetime of lasing transitions, decreasing the upper-state

population and thereby limiting the achievable laser gain [37]. Finally, materials which are transparent in the mid-infrared, such as fluorides, can often suffer from poor mechanical strength and low thermal conductivities [38].

Frequency conversion through nonlinear optical processes, such as difference frequency generation, parametric amplification, or four-wave mixing, offers an alternative approach to generating mid-infrared light. For example, mid-infrared sources have been developed based on difference frequency generation (DFG), by mixing two frequencies in a crystal with $\chi^{(2)}$ nonlinearity to generate light at the frequency difference of the inputs. DFG-based sources offer a simple single-pass geometry requiring no cavity alignment [20]. Phase matching schemes such as periodic poling have been used to help reduce phase mismatch and allow DFG effects to add coherently over longer lengths [32]. However, even with these techniques, imperfect phase-matching and material transparency often limit achievable bandwidths [32]. For example, C. Erny et al. demonstrated DFG with mid-infrared output from 3 μm up to 5 μm , limited by absorption in the $\text{MgO}:\text{LiNbO}_3$ crystal [32]. Alternatively, an optical parametric oscillator (OPO) is another source based on nonlinear frequency conversion. An OPO consists of a nonlinear optical crystal in an optical cavity. By utilizing parametric amplification and feedback from a cavity, an OPO converts light at a pump frequency into light at signal and idler frequencies obeying energy and momentum conservation. While table-top OPOs provide wide wavelength tunability over several μm [33] and reasonable photon conversion slope efficiency $\sim 54\%$ [228], they can have a large footprint of several to 10 ft^2 and complex cavity geometry.

Nonlinear integrated photonics can provide a solution for an efficient, compact mid-infrared light source. In particular, microresonator-based frequency combs, generated through four-wave mixing, hold promise as potential chip-scale mid-infrared sources, offering the

advantage of a robust, portable platform. Optical microresonators are dielectric resonators, ranging in radius from a few microns to mm, which guide and confine light through total internal reflection.

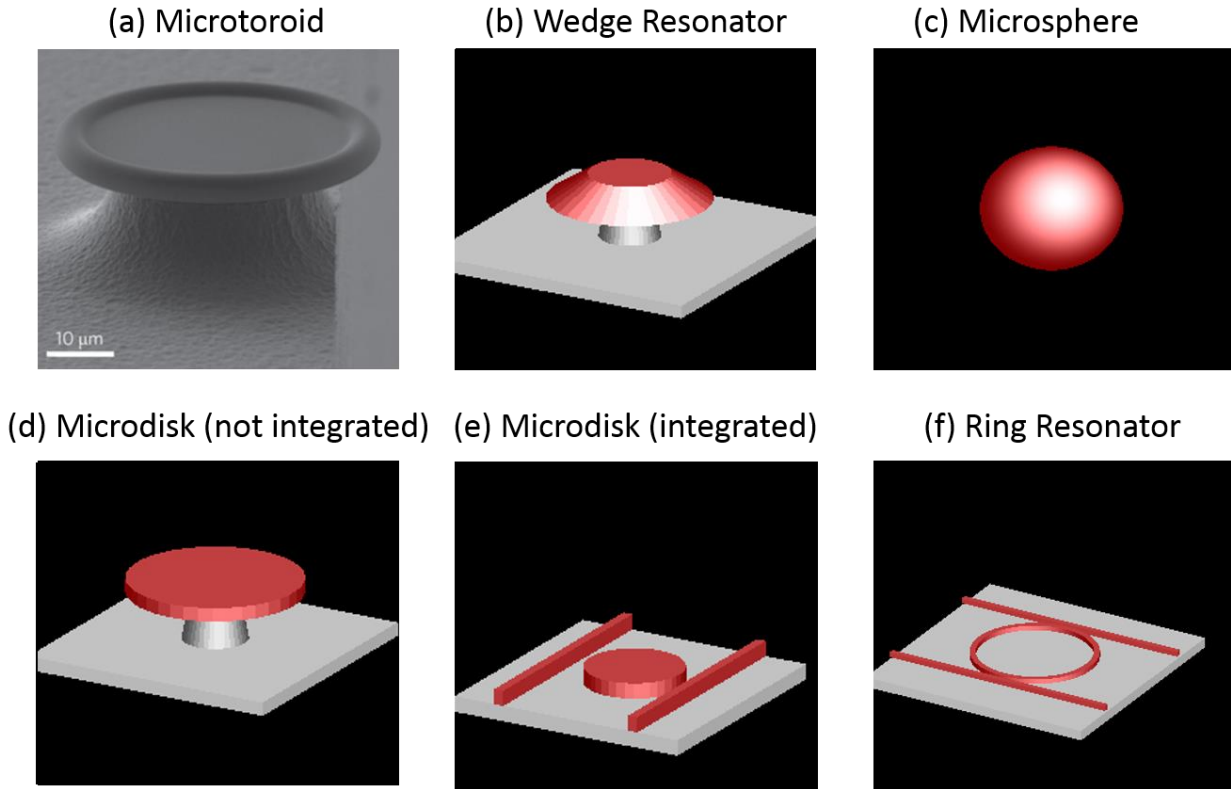


Figure 1.4 Illustration of various microresonator geometries. Six microresonator geometries are illustrated, including the (a) donut-shaped microtoroid (reproduced from [40]), (b) mushroom-shaped wedge resonator, (c) spherical microsphere, (d,e) cylindrical microdisks (non-integrated and integrated), and (f) ring-shaped ring resonator with integrated waveguides. Adapted by permission from Macmillan Publishers Ltd: Nature Photonics [40], copyright 2014.

A number of different microresonator geometries exist, including microtoroids [40,41], wedge resonators [42], microspheres [43], microdisks (integrated and non-integrated) [44,45], and ring resonators [46], as illustrated schematically in Figure 1.4. Microresonators can confine light to small mode volumes while allowing light to build up as it circulates many round trips before

decaying, significantly reducing thresholds for nonlinear effects. A microresonator's capacity to circulate and store light can be quantified by a quality factor, Q , which represents the number of oscillations of the electric field before the energy is reduced to $1/e$ of its initial value. Extremely high Q s have been achieved in mm-scale devices, including Q s $\sim 10^{10}$ to 10^{11} in crystalline fluoride microresonators [47,48], Q s of 8.75×10^8 in silica wedge resonators [42], and Q s $\sim 8.1 \times 10^7$ silicon nitride ring resonators [49]. In micron-scale devices with radii on the order of 10s μm , state-of-the-art integrated waveguide-coupled resonators have Q s $\sim 10^6$ [49-51].

Optical microresonators are essential building blocks for a wide variety of applications [52], including label-free biosensors [53], integrated photonic devices [54] and nonlinear optics [55,56]. One application of significant interest is a microresonator-based optical frequency comb, which is a source consisting of evenly spaced lines in frequency, as illustrated in Figure 1.5 [9]. If the frequency modes have a fixed phase relationship, then in the time domain, the evenly spaced spectral lines correspond to a pulse train with a periodic envelope function (See Fig. 1.5b) [9,20]. While the envelope of the pulse train travels at the group velocity, the carrier wave of the pulse travels at the phase velocity. Dispersion in the resonator causes the phase velocity to differ from the group velocity, so that the electric field of the pulse slips by some constant phase amount from pulse to pulse [20]. This phase slip leads to an overall frequency offset of the comb, f_0 , called the carrier-envelope offset frequency [20]. Optical modes are found at frequencies $f_n = f_0 + n f_r$, where n is an integer and f_r is the repetition rate [9,20].

One way to produce a frequency comb is to couple continuous wave (cw) light into a microresonator and utilize the nonlinear optical process of four-wave mixing [9]. For a microresonator made from a $\chi^{(3)}$ -based nonlinear material, degenerate four-wave mixing will

convert two pump photons into a pair of frequency up- and down-shifted photons (at signal and idler frequencies), which conserve both energy and momentum [9]. If the resonator is designed such that the signal and idler frequencies align with the resonator cavity modes, the nonlinear process will be enhanced [9]. When the generated signal and idler frequencies seed additional (non-degenerate) four-wave mixing, based on interactions of four different frequency photons, a frequency comb can be generated, consisting of many equidistant frequency sidebands, as illustrated in Figure 1.5 [9].

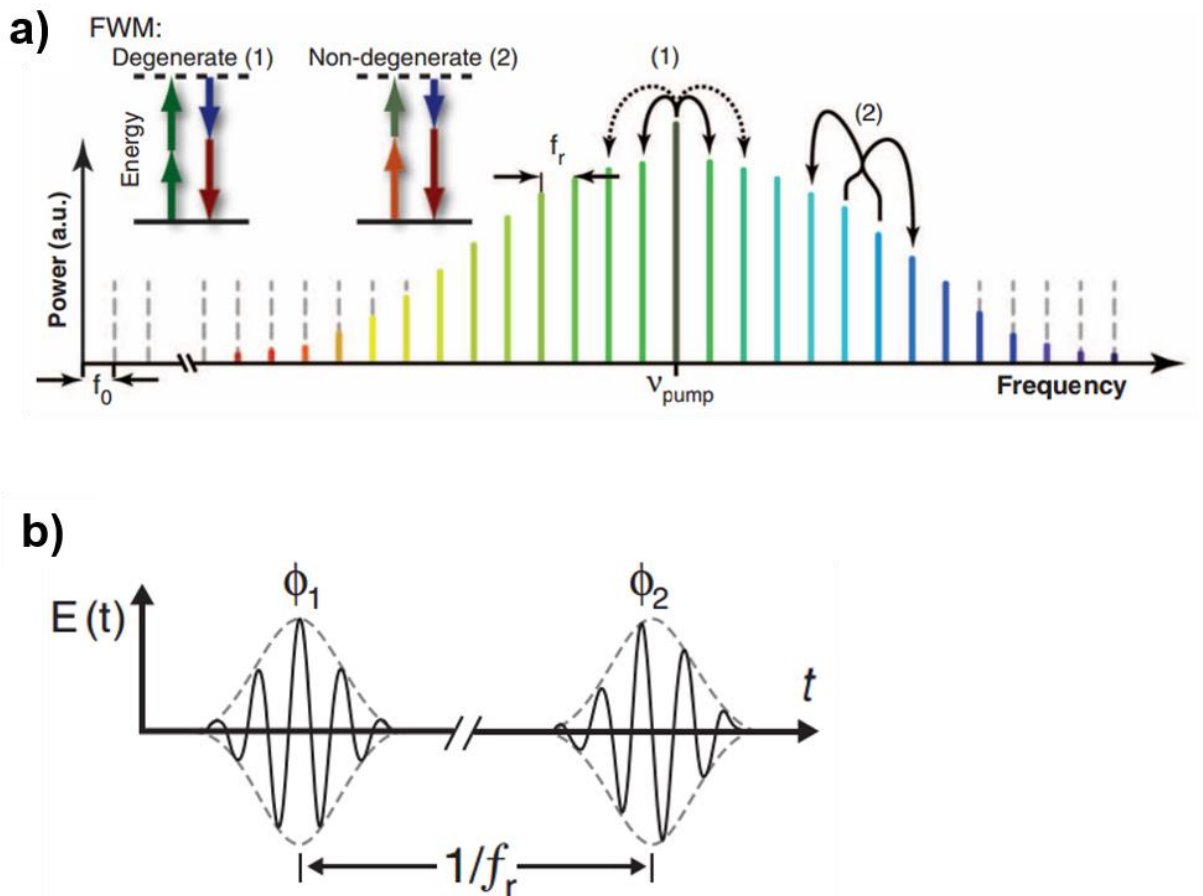


Figure 1.5. Optical frequency comb. (a) An optical frequency comb, consisting of evenly spaced lines in frequency, is generated through the processes of (1) degenerate four-wave mixing (FWM) and (2) cascaded four-wave mixing. Optical modes are found at frequencies $f_n = f_0 + n f_r$, where n is an integer, f_r is the repetition rate, and f_0 is the carrier-envelope offset frequency. (b) Time

domain representation of optical frequency comb. Adapted from [9]. Reprinted with permission from AAAS.

Microresonator-based optical frequency combs have been demonstrated in a number of different material systems, including silica [55,57], silicon nitride [39,58], crystalline CaF_2 [59], crystalline MgF_2 [60], and silicon [10] (See Figure 1.6). A new chalcogenide glass-based microresonator platform offers several unique advantages. Selenide-based chalcogenides provide extremely large nonlinearities, with $n_2 \sim 9 \times 10^{-18}$ to $1 \times 10^{-17} \text{ m}^2/\text{W}$ [61], which are orders of magnitude larger than nonlinearity in other commonly used materials, as shown in Table 1.1. While the semiconductors AlGaAs and GaAs also feature high nonlinearity at 1550 nm, they contain toxic arsenic and suffer from two-photon absorption $\sim 0.4 \text{ cm/GW}$ and 10 cm/GW , respectively, at 1550 nm [240,241].

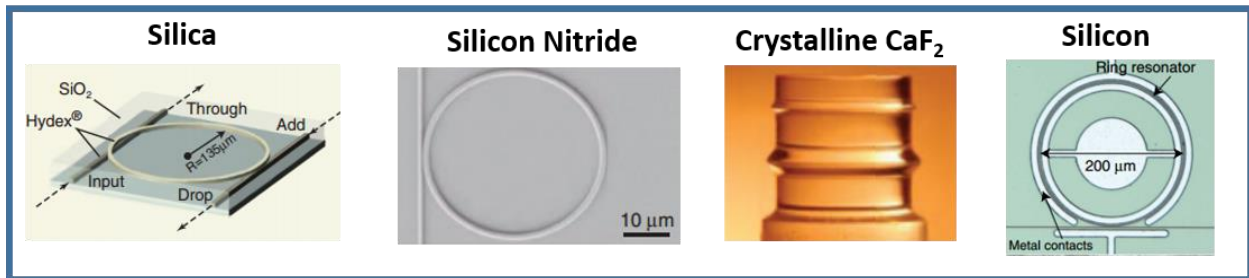


Figure 1.6 Material platforms used in frequency comb generation. Microresonator-based frequency combs have been demonstrated in a variety of materials. These include silica microrings and microresonators [55,57], silicon nitride ring resonators and finger-shaped resonators [58,39], crystalline fluoride whispering gallery mode resonators [59,60], and silicon ring resonators [10]. Figure adapted from [9] and reprinted with permission from AAAS. Silicon ring figure adapted from [10] and reprinted by permission from Macmillan Publishers Ltd: Nature Communications, copyright 2015.

Additionally, chalcogenides offer broad transparency, from near-infrared wavelengths out to the long-wave infrared around $14 \mu\text{m}$. Finally, unlike crystalline semiconductors or crystalline

fluorides, chalcogenides are amorphous, allowing them to be easily deposited onto a variety of substrates for integrated, on-chip devices. By harnessing the chalcogenide material's large nonlinearity, broader transparency, and flexible options for integration, optical frequency comb operation may be extended to longer wavelengths in the mid-infrared using lower pump powers, to produce compact, efficient devices.

Table 1.1 Comparison of n_2 at 1.55 μm in nonlinear optics material platforms

<i>Material</i>	<i>n_2 ($\times 10^{-20} \text{ m}^2/\text{W}$)</i>	<i>Reference</i>
Fused silica	2.6	[62]
Si_3N_4	24	[63]
SiN_x	140	[63]
CaF_2	1.9	[64]
MgF_2	0.9	[64]
Si	400	[63]
$\text{Ge}_{28}\text{Sb}_{12}\text{Se}_{60}$	936	[65]
AlGaAs	1800	[240]
GaAs	2000	[241]

1.4 Why chalcogenide glasses?

Chalcogenide glasses are composed of a chalcogen element such as S, Se, or Te covalently bonded to at least one other element. They have relatively high glass densities compared to oxides and consist of atoms with strong polarizability, giving rise to high linear and nonlinear refractive indices [61,72]. Since chalcogenides consist of heavy atoms, their resonant vibrational frequencies are lower than oxides', providing excellent long wavelength transparency out to ~ 12 , 14 and 20 μm for sulfides, selenides, and tellurides, respectively [61]. For comparison, the transparency range of a few chalcogenide glasses, fluorides, crystalline semiconductors, and other common optical materials is shown in Figure 1.7. Finally, due to relatively large bandgaps compared to common semiconductors such as Si or Ge, chalcogenides can exhibit large figures of merit (ratio

of nonlinearity to two-photon absorption) [73]. Since two-photon absorption often limits nonlinear device performance, the relatively low two-photon absorption can make these glasses good candidates for efficient optical switching.

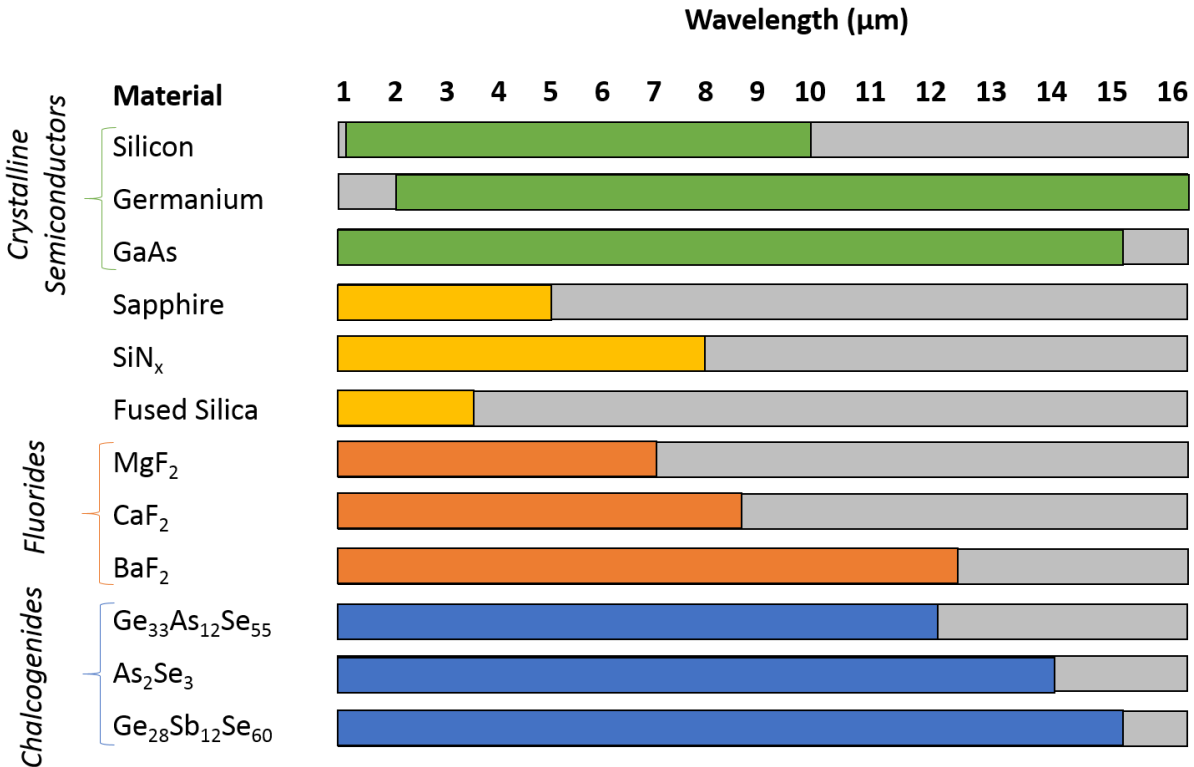


Figure 1.7. Transparency ranges for various materials. Note the materials are transparent over the colored range, and absorbing over the gray range. Transmission from the near- to long-wave infrared is compared for a variety of materials, including crystalline semiconductors, fluorides, and chalcogenide glasses [66-71]. The chalcogenide glass Ge₂₈Sb₁₂Se₆₀ exhibits excellent transparency from ~1-15 μm, is arsenic-free, and its amorphous nature offers flexible substrate choice.

Chalcogenide glasses behave as amorphous semiconductors, with bandgap energies ranging from 1 to 3 eV [74]. Since chalcogenide glasses have localized states extending into the bandgap, they can still absorb some radiation at energies less than the bandgap energy. The existence of these energy states causes the chalcogenide glass absorption spectra to exhibit a long, decaying exponential Urbach absorption tail, rather than a sharp absorption edge [75]. On an

atomic scale, chalcogenide glasses such as Ge-Sb-Se consist of covalently bonded atoms and are ordered in a ‘continuous random network’ structure [61,76]. This means that the glass structure, similar to amorphous SiO₂, lacks periodicity throughout the material [77], as illustrated in Figure 1.8 [78].

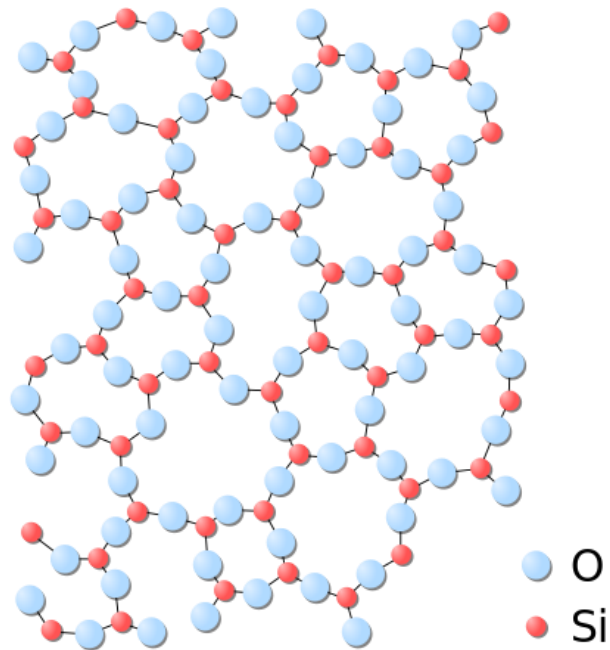


Figure 1.8 Continuous random network structure. Two-dimensional illustration of continuous random network structure for amorphous SiO₂ [78]. Blue circles represent oxygen atoms, and red circles represent Si atoms. Note that while each Si atom is covalently bonded to three neighboring O atoms, the glass structure lacks periodicity or long-range order. Reproduced from [78].

The network structure can be further characterized by the mean coordination number (MCN), or the average valence number of the constituent atoms [61]. For example, for Ge₂₈Sb₁₂Se₆₀, consisting of Ge, Sb, and Se with valence of 4, 3, and 2 respectively, the MCN would be $4(0.28)+3(0.12)+2(0.60)=2.68$. Thorpe et al. [79] and Tanaka [80] have predicted phase transitions, where the material transitions from a flexible to a more rigid phase, at MCN of 2.4 and 2.67, respectively. W. –H. Wei et al. have shown that, in addition to MCN, chemical composition

also plays a role in determining both the physical and structural properties of chalcogenide glasses [81]. If an atom has more or fewer bonds than expected for its valence, the network will contain “coordination defects,” which lead to tail states in the bandgap that can further influence both optical and electronic properties [61]. An illustration of an example coordination defect is shown in Figure 1.9 [82].

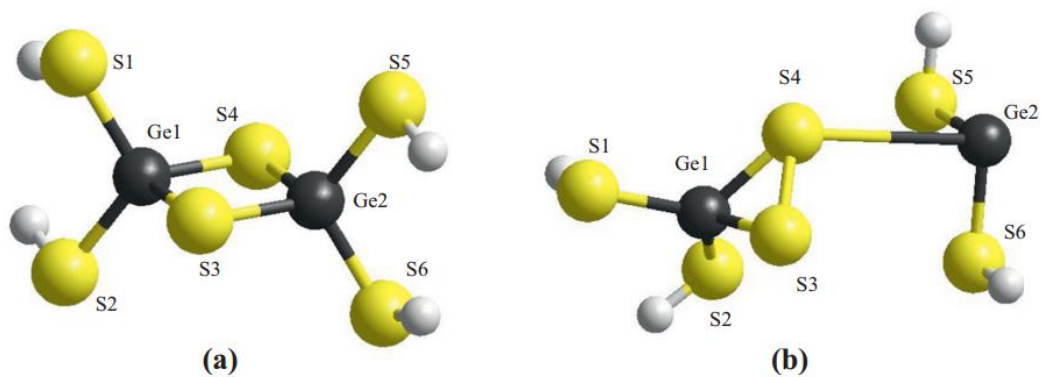


Figure 1.9 Example of coordination defect in chalcogenide $\text{Ge}_2\text{S}_6\text{H}_4$. a) Non-defective $\text{Ge}_2\text{S}_6\text{H}_4$ configuration. b) Defective $\text{Ge}_2\text{S}_6\text{H}_4$ configuration. While each Ge atom is usually bonded to 4 neighboring S atoms, in the defective configuration, one of the Ge atoms only has 3 neighboring S atoms. Reproduced from [82], with permission from Elsevier.

Chalcogenides also exhibit photosensitivity, meaning that when exposed to light near their band edge, their chemical bonds can change [83]. The photosensitivity of chalcogenides has raised some concern about potential device stability, particularly when operating near the band edge. However, photosensitivity has been successfully exploited for certain applications, such as laser-writing of waveguides [84,85] or post-fabrication device trimming [86], and photosensitivity remains an active area of research [83]. In particular, the magnitude and stability of photosensitive changes have been shown to vary greatly with illumination conditions [83]. While a number of

different mechanisms have been proposed [87], more work is needed to clearly identify the exact origins of photosensitivity and accurately model the dependence on key parameters such as exposure time, intensity, wavelength, and absorption.

Although chalcogenides are susceptible to photosensitivity and additional absorption from defect-induced energy states, their amorphous structure offers a significant advantage of flexible photonic integration. In contrast with crystalline fluorides or crystalline semiconductors, glassy materials can be easily deposited onto a wide array of substrates to make thin film devices [88]. For example, chalcogenide waveguides have been demonstrated with substrates such as sapphire [89], MgF_2 [90], and oxide-coated Si [88].

Bulk chalcogenide glasses and devices have been researched extensively. The optical nonlinearity of a range of bulk chalcogenide glasses, including Ge-As-Se, Ge-Se, As_2Se_3 , As_2S_3 , and Ge-Sb-Se has been studied [65,91-95]. While most of this work has focused on telecom wavelengths near 1550 nm, recent studies have examined properties at mid-infrared wavelengths at 2.5-4.0 μm [95-97]. Many simple chalcogenide-based devices have also been demonstrated, such as fibers [98], tapers [99], and waveguides [61,100-102]. Additionally, more complex devices have been developed, including microfluidic sensors [103], flexible photonic circuits [104], microresonators [105-106], components for high speed processing [107], and photonic crystal resonators [237-239]. To date, chalcogenide microresonator research has focused primarily on linear characterization, and more work remains to harness the excellent nonlinear properties of chalcogenide glasses in microresonator geometries.

This thesis focuses specifically on the chalcogenide glass $\text{Ge}_{28}\text{Sb}_{12}\text{Se}_{60}$ due to its As-free composition, large bandgap [108], broad transparency to $\sim 15 \mu\text{m}$ [109], and high glass transition temperature of 300°C [108]. The properties of bulk $\text{Ge}_{28}\text{Sb}_{12}\text{Se}_{60}$ are investigated in the near-

infrared. Optical waveguides and microresonators based on this material are designed, fabricated, and characterized, laying groundwork for the development of chip-scale nonlinear optical devices for the near- and mid-infrared.

1.5 Thesis outline

This thesis is organized into six chapters. Chapter 1 describes the motivation for the work, introducing integrated optics, discussing potential applications of nonlinear photonics, and explaining why chalcogenide materials were chosen. Chapter 2 covers nonlinear optical characterization of bulk $\text{Ge}_{28}\text{Sb}_{12}\text{Se}_{60}$ using the z-scan method. Chapters 3-5 focus on thin-film chalcogenide-based devices. More specifically, Chapter 3 describes optical waveguide design and characterization. Basic principles of optical waveguide design and characterization techniques are introduced, and the design and characterization of waveguides at near- and mid-infrared wavelengths are discussed. Chapter 4 introduces ring resonators, describing how devices can be designed for optimal four-wave mixing efficiency, providing designs completed at both 1.55 and 3.5 μm , and summarizing optical characterization of such resonators. Chapter 5 describes the development and optical characterization of a first generation of hybrid chalcogenide-silica wedge resonators. Chapter 6 summarizes the main results from this thesis and suggests future extensions.

2. OPTICAL CHARACTERIZATION OF BULK $\text{Ge}_{28}\text{Sb}_{12}\text{Se}_{60}$

2.1 Overview

The linear and nonlinear optical properties of $\text{Ge}_{28}\text{Sb}_{12}\text{Se}_{60}$ bulk glass are characterized at a wavelength of 1.03 μm . In addition to large nonlinear refractive index, the bulk material has significant two-photon absorption, making it a potential candidate for optical limiting in this spectral region. The new understanding of the basic optical properties of $\text{Ge}_{28}\text{Sb}_{12}\text{Se}_{60}$ at 1.03 μm will be useful for photonic device design over broader bandwidths. In Section 2.2, the z-scan method is introduced. In Section 2.3, z-scan experiments measuring the nonlinear refractive index and nonlinear absorption are described, and z-scan results are further discussed in Section 2.4. In Section 2.5, measurements of the linear absorption on bulk $\text{Ge}_{28}\text{Sb}_{12}\text{Se}_{60}$ are summarized.

During this work, we benefited from technical discussions with the Gopinath lab group, Professor Wounjhang Park, and Lisa Rengnath. Bulk linear absorption at 1.55 μm was measured by Caroline Hughes (University of Colorado Boulder). Funding for this work was provided by the University of Colorado Boulder Innovative Seed Grant Program, NSF grant EECS-1232077, the Colorado Measurement Science and Engineering Fellowship, and the National Defense Science and Engineering Graduate (NDSEG) Fellowship. This chapter is adapted from [56].

2.2 Introduction to z-scan

Although the nonlinear refractive index is useful for a wide range of applications, the nonlinear refractive index is very small, typically on the order of 10^{-20} m^2/W for silica [5] and

$\sim 10^{-18}$ - 10^{-17} m²/W for chalcogenide glasses [61]. At incident intensities of 1 GW/cm², these values correspond to small changes in refractive index on the order of 10^{-7} to 10^{-4} . Detecting such small changes requires sensitive techniques. Two methods most widely used to measure the nonlinear refractive index in bulk materials are z-scan and degenerate four-wave mixing [110].

In the degenerate four-wave mixing technique, an intense, short-pulse pump is focused onto a sample, and the output beam is reflected back through the sample to produce a counterpropagating pump [111]; a third, weak probe beam is incident at some angle on the material, and a fourth beam, propagating counter to the probe, is generated through four-wave mixing [111, 112]. By varying the time delay between the pump and probe, the temporal behavior can be studied. The main disadvantage of this technique is the complex experimental setup [110], requiring careful spatial and temporal alignment of the pump and probe.

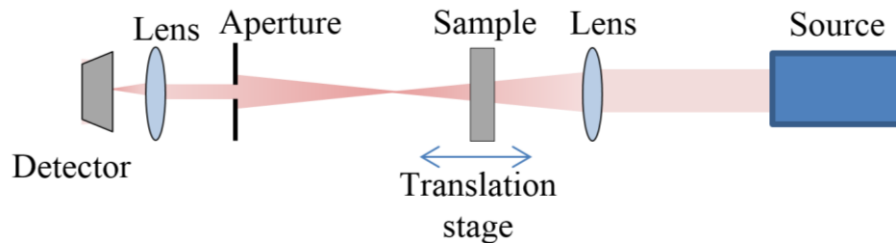


Figure 2.1 General schematic of z-scan setup. A Gaussian beam is focused onto a sample using a lens. The sample is translated through the focus of the beam, and the resulting transmission through an aperture is recorded as a function of position, producing a “closed aperture” z-scan trace sensitive to both nonlinear refraction and nonlinear absorption. Additional transmission measurements without the aperture produce an “open aperture” z-scan trace, and these can be used to separately determine nonlinear absorption.

The z-scan technique is a simple, single-beam technique. To characterize the nonlinear refractive index n_2 and two-photon absorption coefficient β using the z-scan technique [113], a sample is translated through the focus of a Gaussian beam, and the transmission through a circular

aperture, placed in the far field, is recorded. A schematic of a z-scan experimental setup is shown in Figure 2.1. The nonlinear sample acts like a lens, with largest phase shift near the center of the beam, and weak phase shift near the edges of the Gaussian beam. This lensing effect, which is strongest near the focus where the intensity is the highest, changes the fraction of light that passes through the aperture, producing a characteristic z-scan transmission trace. If the aperture is removed and all the light is collected, the scan is no longer sensitive to nonlinear refraction, but it is still sensitive to nonlinear absorption. Thus, measurement of the transmission as a function of position without the aperture allows for determination of β . Although z-scan does not provide time resolution, it offers a simple setup and straightforward analysis.

Sheik-Bahae et al. developed a theoretical analysis for the z-scan method [113]. The presence of a nonlinear sample will modify both the phase $\Delta\phi$ and intensity I of an incident Gaussian beam, such that

$$\frac{d\Delta\phi}{dz'} = \Delta n(I)k \quad (2.1)$$

and

$$\frac{dI}{dz'} = -\alpha(I)I, \quad (2.2)$$

where $\alpha(I)$ is the intensity-dependent absorption, k is the wavenumber, z' is the propagation distance through the sample, and $\Delta n(I)$ is the intensity-dependent change in refractive index. Here, the sample length L is assumed to be small enough that changes in beam diameter due to diffraction or nonlinear refraction are negligible, with $L < z_0$ typically sufficient, where z_0 is the confocal parameter [113]. For a sample with third-order nonlinearity,

$$\Delta n(I) = n_2 I \quad (2.3)$$

and

$$\alpha(I) = \alpha + \beta I, \quad (2.4)$$

where n_2 is the nonlinear refractive index, α is the linear absorption, and β is the two-photon absorption coefficient. After accounting for the phase and intensity changes due to the sample, the resulting electric field is calculated in the far field. The field is then spatially integrated over the aperture (or over the full cross section) to determine the theoretical z-scan transmission for a closed (or open) aperture z-scan trace. When pulses are used, rather than cw light, the time-dependent field can be time-integrated to obtain the average transmittance. For a Gaussian pulse shape, transmission without the aperture is given by

$$T_{open} = \sum_{m=0}^{\infty} \frac{[-q_0(z)]^m}{(m+1)^{3/2}}, \quad (2.5)$$

for values of $|q_0| < 1$, where

$$q_0 = \frac{\beta I_0 L_{eff}}{(1+x^2)}, \quad (2.6)$$

$$x = \frac{z\lambda}{\pi w^2}, \quad (2.7)$$

z is the distance of the sample from focus, and m is an integer [113]. Here, I_0 is the peak on-axis intensity, w is the beam waist, and λ is the wavelength. The effective sample length is given by

$$L_{eff} = \frac{(1-e^{-\alpha L})}{\alpha}, \quad (2.8)$$

where L is the physical sample length and α is the linear absorption coefficient.

Typically $q_0 \ll 1$ and only the first two terms of Eq. (2.5) contribute significantly to an open aperture z-scan trace. For larger values of q_0 , additional terms in the sum can be added as needed to ensure the desired level of accuracy. The theoretical transmission for a closed aperture z-scan trace can be calculated through a similar process, by accounting for phase and intensity changes from the sample, propagating to the far field, and integrating the field over the aperture. In general, the expression can be extensive and can make fitting challenging. However, for small phase shift $\langle \Delta\phi_0 \rangle \ll 1$ and small absorption changes $\beta I_0 L_{eff} \ll 2$, Dinu et al. [114] and Rhee et al. [115] have shown that the expression for the field can be approximated. Additionally, the aperture radius is assumed to be small so that the condition of on-axis transmittance is satisfied [115]. In this case, using a Fourier transform to propagate to the far field, integrating the field over the aperture, and using a series expansion, Dinu et al. [114] shows that the transmission through a small, partially closed aperture is given by

$$T_{cl} \cong 1 + \frac{4x \langle \Delta\phi_0 \rangle}{(1+x^2)(9+x^2)} - \frac{\beta I_0 L_{eff} (3-x^2)}{2\sqrt{2}(1+x^2)(9+x^2)}. \quad (2.9)$$

Here, for a Gaussian pulse shape, the time-averaged peak on-axis phase shift is given by

$$\langle \Delta\phi_0 \rangle = \frac{2\pi L_{eff} n_2 I_0 (1-S)^{0.25}}{\lambda\sqrt{2}}, \quad (2.10)$$

where S is the aperture transmission [114]. For larger absorption or refractive changes, data can be fit to more terms from a full expression given by Gu et al. [116].

Table 2.1. Typical magnitude and response time of nonlinear refractive index [5].

<i>Mechanism</i>	<i>n_2 (cm²/W)</i>	<i>Response time (s)</i>
Electronic polarization	10 ⁻¹⁶	10 ⁻¹⁵
Molecular orientation (liquids)	10 ⁻¹⁴	10 ⁻¹²
Thermal effects	10 ⁻⁶	10 ⁻³

A number of physical processes, including electronic polarization, thermal effects, and free-carrier effects, can cause a nonlinear change in the refractive index, but their corresponding response times and magnitudes vary greatly, as shown in Table 2.1 [5]. For example, intensity-dependent changes in refractive index from heating can be large, but these changes are relatively slow, \sim ms, given their thermal nature. Electronic-polarization-based changes (due to the Kerr nonlinearity) tend to be significantly smaller in magnitude. However, the electronic polarization has ultrafast fs response times, attractive for high-speed applications such as all-optical processing. Although the z-scan technique can only measure the magnitude and sign of the nonlinearity, measurements using different temporal separation between short pulses can help distinguish the origin of the nonlinearity [117].

While chalcogenides are known for having large optical nonlinearities, most work characterizing the nonlinear optical properties of Ge-Sb-Se glasses has centered on telecom wavelengths. A better understanding of this material over a wider wavelength range in both bulk and waveguide forms is crucial for leveraging its nonlinear properties in broadband device designs, since material properties such as absorption, refractive index, and nonlinear refractive index are all wavelength dependent. The refractive index and linear dispersion have been well characterized for chalcogenide materials [108], but their nonlinear properties were not well studied at 1 μ m.

Although a few models for the dispersion of the nonlinear refractive index have been developed, they have not been rigorously tested for chalcogenide materials over broad bandwidths. Sheik-Bahae developed a model for the dispersion of the nonlinear refractive index and two-photon absorption coefficient, using a Kramers-Kronig analysis relating the real and imaginary parts of the third-order susceptibility [118]. While this uses a two-parabolic band model and fits many semiconductors well, chalcogenide glasses are amorphous and do not exhibit a sharp

absorption edge. As such, chalcogenide glasses exhibit finite two-photon absorption even below the half-gap [65], not well-predicted by the Sheik-Bahae model. Lenz et al. developed a model for the magnitude and dispersion of the Kerr effect in glasses, based on a previous model in ionic crystals [65]. However, this model was not experimentally tested for chalcogenides over broad bandwidths. Dinu et al. offers an alternate model for the dispersion of nonlinearity from bound electrons for the case of indirect semi-conductors [119]. Recent experiments covering broader bandwidths are just starting to test the models by Sheik-Bahae, Dinu, and Lenz for chalcogenides [93]. One final rule commonly used to predict the nonlinearity of a material is Miller's rule, an empirical equation which relates the linear refractive index n_0 to n_2 through

$$n_2 = \frac{0.0395\alpha_{Miller}}{n_0^2} \left[\frac{(n_0^2 - 1)}{4\pi} \right]^4, \quad (2.11)$$

where α_{Miller} is the material-dependent Miller's coefficient. Experiments have shown α_{Miller} of 2.7×10^{-10} for chalcogenide glasses [93]. Miller's rule does not explicitly include wavelength dependence of the nonlinear index. However, from Equation 2.11, a wavelength-dependent linear index would lead to a predicted wavelength-dependent nonlinear index. Through experiments, Miller's rule has been shown to provide a good rough estimate of the nonlinear refractive index of a range of materials, including chalcogenides, tellurites, lead silicates, and silica [93,127,128]. However, this rule requires additional experimental testing to test how well it predicts the wavelength dependence of n_2 over broad bandwidths.

2.3 Z-scan measurements of third-order nonlinearity in Ge₂₈Sb₁₂Se₆₀

The nonlinear refractive index n_2 and two-photon absorption coefficient β of polished Ge₂₈Sb₁₂Se₆₀ bulk samples were measured with the z-scan technique, using the setup illustrated in

Figure 2.2. The light source used in the experiments was a mode-locked Yb-doped fiber laser operating at a 37.4 MHz repetition rate, with ~ 200 fs Gaussian pulses at a central wavelength of $1.03 \mu\text{m}$, modeled after a design by Ilday et al. [120]. A schematic of the Yb-doped fiber laser is shown in Figure 2.3.

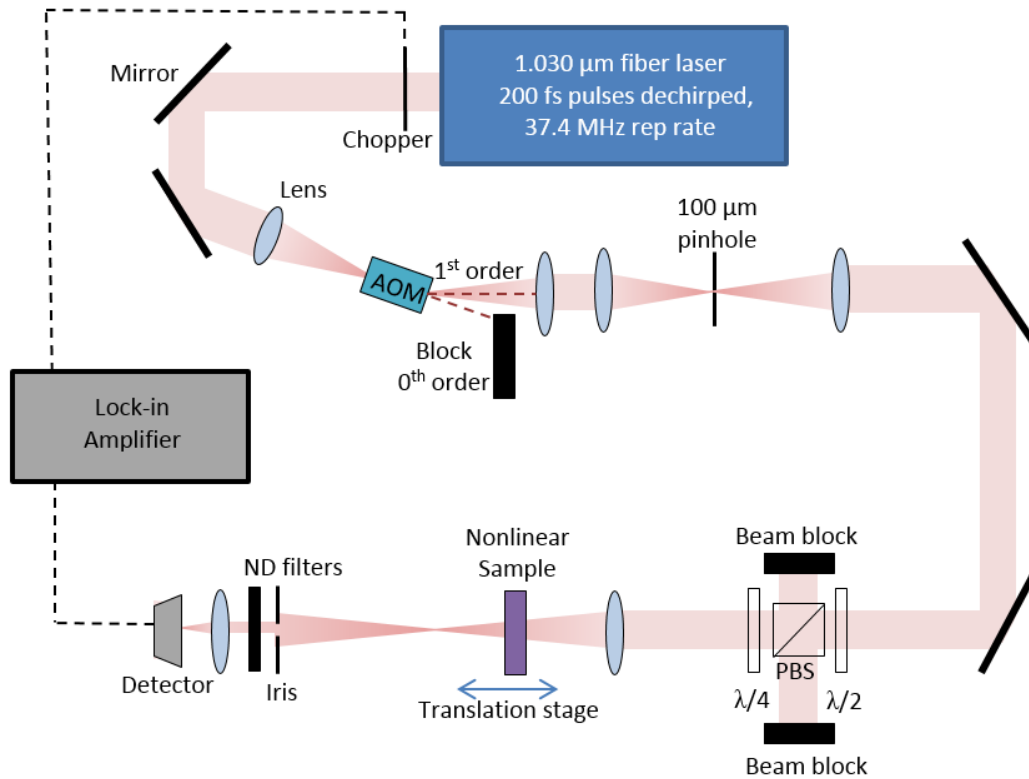


Figure 2.2. Experimental setup for z-scan. 200 fs pulses from a Yb-doped fiber laser are spatially filtered and focused onto a sample. A half waveplate and polarizing beam splitter are used to control the incident power, and a quarter waveplate converts the polarization to circular and serves to prevent back reflections from entering the setup. The sample transmission is recorded as a function of position, both with and without an aperture, to determine the nonlinear properties. The repetition rate is varied by introducing an acousto-optic modulator to pulse pick from 37.4 MHz down to 0.374 MHz.

The $1.03 \mu\text{m}$ laser utilized a unidirectional ring cavity and was pumped by a 980 nm pump diode delivering power through a wavelength division multiplexer (WDM) into a single mode fiber and Yb-doped fiber (Coractive Yb164). Nonlinear polarization rotation was used to mode-lock the laser. By adjusting the separation of the gratings (Thorlabs GR25-610, 600 lines/mm, $1 \mu\text{m}$

blaze), the total group velocity dispersion could be controlled. The laser produced positively chirped pulses, which were dechirped outside of the laser cavity with a second grating pair, external to the cavity. These resulting dechirped pulses were ~ 200 fs in duration, with 37.4 MHz repetition rate and average power of 14 mW (measured after the grating compressor).

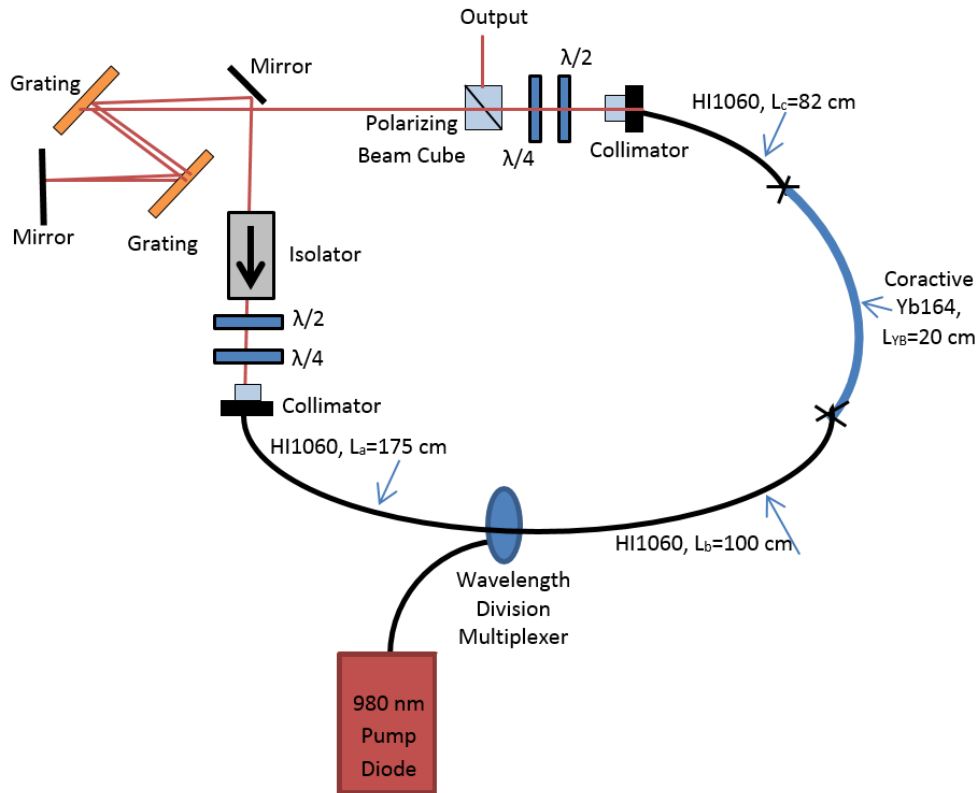


Figure 2.3. Schematic of Yb-doped fiber laser. Experimental setup for mode-locked Yb fiber laser, based on design by Ilday et al. [120]. Ring cavity consists of 20 cm Yb-doped fiber (Coractive Yb164), 357 cm (82 + 100+175 cm) HI1060 fiber, and ~ 110 cm free space (108 cm free space, 2 cm through PBS glass). Through adjustments of the waveplates ($\lambda/2$ and $\lambda/4$), the laser mode-locks using nonlinear polarization rotation.

An acousto-optic modulator (AOM, Gooch & Housego model MM210-.2C2B14-5) was used as a pulse-picker to reduce the repetition rate of the Yb-doped fiber laser to 374 kHz to enable z-scan measurements at different repetition rates. A circuit was designed to provide a fast, low duty cycle trigger signal necessary to drive the AOM safely (See Appendix A). As shown in Figure 2.2, after passing through the AOM, the first order beam is spatially filtered and passed through a

series of polarization optics. A half waveplate and polarizing beam cube provide a simple way to attenuate the beam and adjust the incident power on the sample. These polarization optics, along with the quarter waveplate, also serve as isolation, converting the linear polarization to circular polarization and preventing the reflected beam of the sample surface from re-entering the setup. A nonlinear sample is translated through the focus of the beam, and the transmission vs. position data is recorded, with and without the aperture in place. Data was taken at two repetition rates (37.4 MHz and 374 kHz) with circularly polarized light, on 2 mm-thick polished bulk $\text{Ge}_{28}\text{Sb}_{12}\text{Se}_{60}$ samples.

A series of open and closed aperture z-scan traces were taken over a range of peak intensities from 20 to 95 MW/cm². To account for sample inhomogeneities, z-scan traces were divided by background traces taken at very low intensity levels, where the nonlinearity would produce negligible effects. No changes or degradation to the sample surface were observed in between or after measurements at the different repetition rates. During the experiments, a few technical challenges had to be mitigated. A metal pinhole in a spatial filter before the z-scan setup provided a strong back reflection into the setup. By switching from linear to circular polarization, and providing isolation with a polarizing beam cube and quarter waveplate, as shown in Figure 2.2, this reflection was removed. For amorphous materials, both n_2 and β depend on polarization [5], such that

$$n_2^{circ} = \frac{2}{3} n_2^{lin} \quad (2.12)$$

and

$$\beta^{circ} = \frac{2}{3} \beta^{lin}, \quad (2.13)$$

where n_2^{circ} and β^{circ} are values for circular polarization, and n_2^{lin} and β^{lin} are values for linear polarization [5]. Samples with surfaces relatively parallel surfaces (wedge angle $<0.2\text{mrad}$) were used, such that the amount of beam “walk-off” over the translation of the stage used in the experiments was negligible. As_2Se_3 was used as a reference sample.

Open aperture traces were fit to Equation 2.5, leaving β and w as free parameters, and including nine terms in the sum (m from 0 to 8) to ensure 0.05% accuracy in the fit. Closed aperture traces were fit to the full expression by Gu et. al, which provides more terms for a more accurate determination of n_2 and β than Equation 2.9, given the large observed nonlinear refractive and absorptive changes [116]. Full details of the fitting process and fitting functions used are included in Appendix B.

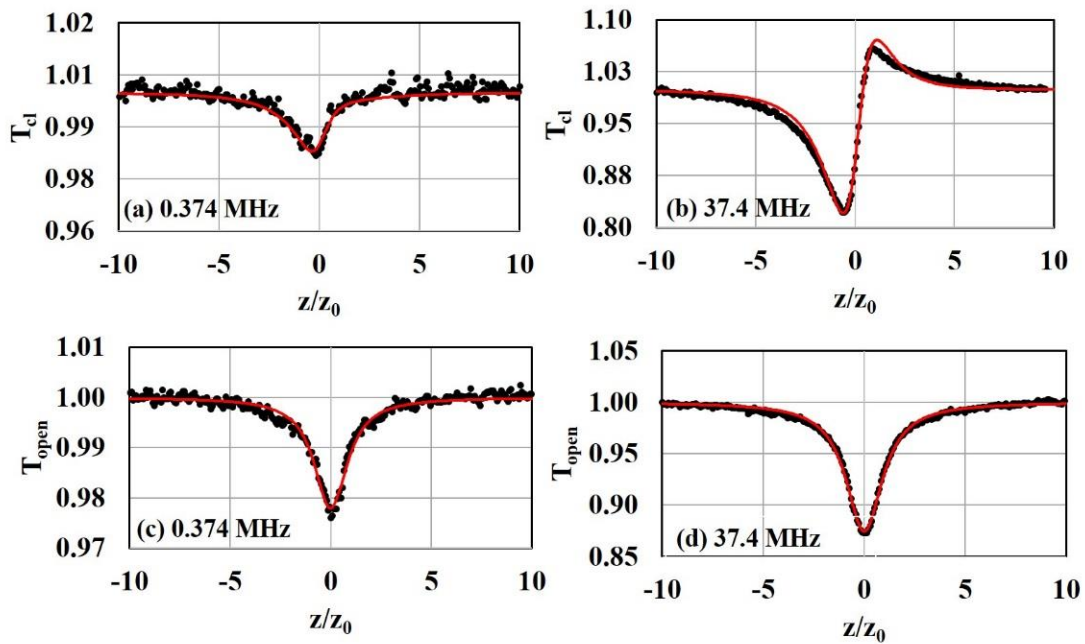


Figure 2.4. Experimental z-scan traces for $\text{Ge}_{28}\text{Sb}_{12}\text{Se}_{60}$. Example closed aperture (a) and (b) and open aperture (c) and (d) z-scan traces taken on $\text{Ge}_{28}\text{Sb}_{12}\text{Se}_{60}$. Note that the traces on the left, (a) and (c), were taken at 0.374 MHz with $I_0=88.5\text{ MW/cm}^2$. The traces on the right, (b) and (d) were taken at 37.4 MHz with $I_0=35\text{ MW/cm}^2$. Data is shown by the black points, and the fits are represented with red lines. Reproduced from [56].

Example z-scan traces at the two different repetition rates are shown in Fig. 2.4. At the lower repetition rate, a noticeably smaller change in transmission was observed for both the open and closed aperture z-scans, and large two-photon absorption obscured the typical valley-peak shape of the closed aperture z-scan. The signal-to-noise ratio (SNR) was limited by laser power fluctuations, which were on the order of 0.2%. The SNR and corresponding detection sensitivity could be improved in the future by adding balanced detection to normalize out power fluctuations, or by averaging.

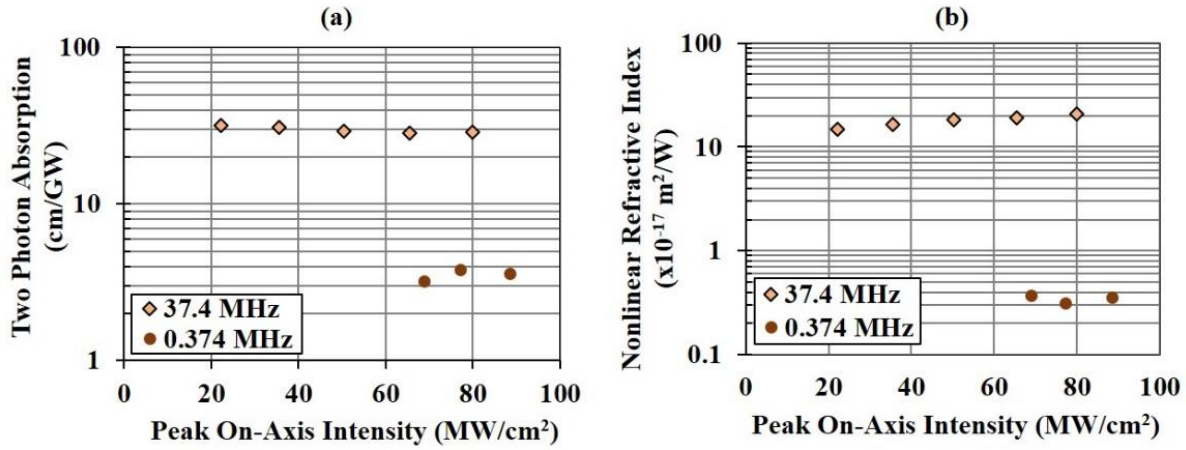


Figure 2.5. Two-photon absorption and nonlinear refractive index for Ge-Sb-Se. Plots of (a) two-photon absorption coefficient, β and (b) nonlinear refractive index, n_2 of $\text{Ge}_{28}\text{Sb}_{12}\text{Se}_{60}$ as a function of peak on-axis intensity, measured by the z-scan technique for two repetition rates, 0.374 MHz and 37.4 MHz. Errors in β and n_2 are approximately 11% and 20%, respectively. At 0.374 MHz, $\beta=3.5 \text{ cm/GW}$ and $n_2=3.4 \times 10^{-18} \text{ m}^2/\text{W}$. Enhanced values of β and n_2 observed at the higher repetition rate are believed to be a cumulative effect caused by the photosensitivity of the material. Reproduced from [56].

The fit values for the data at the two repetition rates, taken over a range of intensities, are summarized in Fig. 2.5. Errors in β and n_2 are approximately 11% and 20%, respectively. The main sources of error in the measurements were laser power fluctuations and uncertainty in the pulse width. At the high repetition rate, n_2 is enhanced, ranging from $15\text{-}21 \times 10^{-17} \text{ m}^2/\text{W}$, and

increases slightly with increasing intensity, while the value of β , roughly 30 cm/GW, also appears significantly enhanced. At the lower repetition rate, both β and n_2 show no dependence on intensity, as expected.

2.4 Discussion of z-scan results

To explore possible causes of the repetition rate dependence of β and n_2 , we first considered thermal effects, where the refractive index changes due to the thermo-optic coefficient and sample heating from absorption. If a laser beam is incident on a sample, the sample will absorb the energy and increase in temperature at an initial linear rate. As described by Hass et al. [121], the temperature change, ΔT of the sample due to linear absorption α is given by

$$\Delta T = \frac{\alpha L_s P_0 t}{MC_p}, \quad (2.14)$$

where L_s is the sample length, P_0 is the incident power, M is the sample's mass, C_p is the specific heat, and t is the bulk heating transit time. For a disk-shaped sample, t is given by $t = r^2 / (6\kappa)$, where r is the radius and κ is the thermal diffusivity [121].

Using Eq. 2.14, along with the material values for our $\text{Ge}_{28}\text{Sb}_{12}\text{Se}_{60}$ sample (α of 0.27 cm^{-1} , L_s of 2 mm, r of 1.27 cm, M of 4.72g, κ of 0.1626 mm^2/s , t of 165.4 s, C_p of 0.33 J/g-K) [122], we calculate ΔT of 0.011-0.057 K for the P_0 of 2-10 mW at the high repetition rate of 37.4 MHz. Additionally, we calculate ΔT of 4.6-6.9 $\times 10^{-4}$ K for the P_0 of 80-120 μW used at the lower repetition rate of 0.374 MHz. Using the thermo-optic coefficient dn/dT of $78.8 \times 10^{-6}/\text{K}$ for $\text{Ge}_{28}\text{Sb}_{12}\text{Se}_{60}$ at 1 μm [123], we estimate corresponding change in refractive index from these absorption-induced temperature changes to be 0.9-4.5 $\times 10^{-6}$ at the high repetition rate, and 4.6-6.9

$\times 10^{-8}$ at the low repetition rate. In comparison, the measured index changes from the z-scan for the high and low repetition rates were $0.3\text{-}1.67 \times 10^{-4}$ and $2.6\text{-}3.2 \times 10^{-6}$ respectively, nearly two orders of magnitude larger than what we would expect from thermal effects.

From these calculations, we conclude that effects due to the thermo-optic coefficient are insignificant, contributing only a few percent of the total measured change in refractive index at both repetition rates. While others have observed cumulative nonlinearities from free-carrier refractive and dispersive contributions in chalcogenide glasses, these are expected to be negligible at both repetition rates due to the short pulse durations used [124].

One possible origin of additional nonlinearities includes effects from photosensitivity. A variety of Ge-Sb-Se glasses and other chalcogenides have been shown to exhibit photodarkening, in which the bandgap red-shifts and absorption and refractive index increase upon illumination close to the bandgap [94,125,126]. Using the commonly used Miller's rule (See Equation 2.11), an increase in n_0 from photodarkening would be expected to increase n_2 [93,129]. Additionally, Sheik Bahae's model for the dispersion of n_2 and β predicts that a decrease in bandgap energy, such as that produced by photodarkening, will increase both n_2 and β [118]. Indeed, an increase in n_2 after photodarkening with a fs laser has been observed in other chalcogenides, such as Ge-Sb-S and As_2S_3 [130,131]. Since the magnitude of the property changes from photodarkening can depend on illumination characteristics, these changes could also produce an effective cumulative nonlinearity [124]. In the case of Ge-Sb-Se glass, one would expect that a red-shift in the band edge would lead to higher two-photon absorption and higher linear and nonlinear refractive indices, consistent with the direction of the shift observed at the higher repetition rate. Given this, along with the magnitudes measured, the enhanced effective n_2 and β at the higher repetition rate were likely caused by a cumulative effect stemming from photosensitivity.

A time-resolved method such as pump-probe spectroscopy is not expected to be able to determine the origin of the nonlinearity, because photodarkening can produce both cumulative nonlinearities, as well as ultrafast nonlinearities due to changes in the bandgap energy, as discussed earlier. Photosensitivity-induced changes can be clearly identified by changes in bond structure [132-134]. Thus, a technique capable of sensing structural changes, such as a Raman spectroscopy or X-ray absorption spectroscopy, may more directly probe the presence of photosensitivity in the future [132-134]. For example, a study of the Raman spectra of samples before and after z-scan measurements could be used to check for permanent changes to the bond structure which would change the resulting energy levels and measured spectra for the material. Similarly, to check for reversible photosensitive effects, one could consider developing a technique to perform *in-situ* spectroscopy with either z-scan or pump-probe measurements simultaneously.

2.5 Linear absorption measurements of $\text{Ge}_{28}\text{Sb}_{12}\text{Se}_{60}$

Accurate fitting of z-scan nonlinearity measurements requires knowledge of the material linear absorption, which will influence the sample's effective length. Weak linear absorption can be a challenge to measure. Given the thin, disk-like geometry of our samples (desired for z-scan), and expected weak absorption in the range $0.05 \text{ cm}^{-1} < \alpha < 1 \text{ cm}^{-1}$, in order to measure the linear absorption of chalcogenide samples, we utilized the Brewster angle technique [135]. In this method, the linear absorption of bulk samples can be determined from measurements of the incident, reflected, and transmitted power at Brewster's angle. A schematic of an experimental setup is shown in Figure 2.6. A half waveplate and polarizing beam splitter are used to change the polarization of the incident beam. The sample is rotated to find the minimum in reflected power, and the transmitted, reflected, and incident powers are recorded at this angle. For small absorption and reflectance, the absorption is given by

$$\alpha = \frac{-\cos\left[\frac{\pi}{2} - \theta_B\right]}{d} \ln \left[\frac{T}{\left(1 - \frac{R}{2}\right)^2} \right], \quad (2.15)$$

where α is the sample thickness, and T and R are the power transmission and reflectance, respectively, all measured at Brewster's angle θ_B [135]. The Brewster angle method utilizes a simple experimental setup, with accuracy depending mainly on uncertainty in power measurements as well as the parallelism and imperfection of the sample surfaces [135].

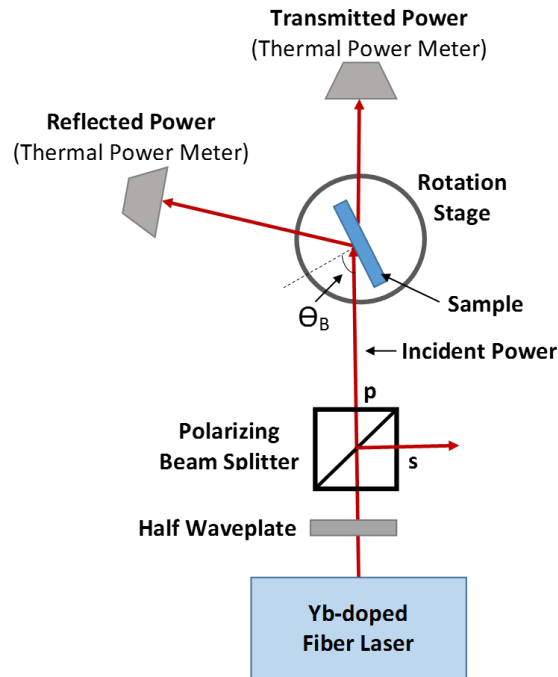


Figure 2.6. Experimental setup for Brewster angle absorption measurement. Linearly-polarized light from a Yb-doped fiber laser is passed through a half waveplate and polarizing beam splitter and optimized for p-polarized light, and directed onto a polished sample. The sample is rotated until the reflected power is minimized to find Brewster's angle θ_B . The angle is recorded, and the reflected, transmitted, and incident power are measured using a thermal power meter.

A schematic of the experimental setup is shown in Figure 2.6. A polished sample is rotated until a minimum in the reflected power is found. The incident, transmitted, and reflected power are measured at this sample angle with a thermal power meter, and the angle is recorded. Using a

cw Yb-doped fiber laser source at a wavelength of 1.03 μm , the linear absorption of bulk $\text{Ge}_{28}\text{Sb}_{12}\text{Se}_{60}$ was determined to be α of $0.27\pm 0.03\text{ cm}^{-1}$, or 1.17 dB/cm. At 1.53 μm , corresponding measurements on $\text{Ge}_{28}\text{Sb}_{12}\text{Se}_{60}$ using a cw Er-doped fiber laser revealed $\alpha=0.07\pm 0.02\text{ cm}^{-1}$, or 0.3 dB/cm. Similar measurements on reference samples As_2Se_3 and $\text{Ge}_{33}\text{As}_{12}\text{Se}_{55}$ agreed with values in literature [136,137].

2.6 Conclusion

From the z-scan data at the 0.374 MHz repetition rate, we measure n_2 to be $3.4\pm 0.4\times 10^{-18}\text{ m}^2/\text{W}$ and β to be $3.5\pm 0.2\text{ cm}/\text{GW}$ in $\text{Ge}_{28}\text{Sb}_{12}\text{Se}_{60}$ for circularly polarized light. The results at 0.374 MHz are independent of intensity, and of the same order of magnitude as those seen for other chalcogenides, even at repetition rates of 1 kHz to 10 Hz [93,94,138]. For example, Petit et al. measured n_2 of $11.5\pm 3\times 10^{-18}\text{ m}^2/\text{W}$ and β of $4.9\pm 0.6\text{ cm}/\text{GW}$ for $\text{Ge}_{28}\text{Sb}_7\text{Se}_{65}$ using the z-scan technique with a 15 ps, 10 Hz Nd:YAG at 1.064 μm [138]. Since photorefractive effects often lead to very strong nonlinear responses and can be intensity-dependent, this comparison and lack of intensity-dependence strongly suggests the 0.375 MHz results include only the two-photon absorption and Kerr effect.

One metric commonly used to evaluate a nonlinear material's performance is its nonlinear figure of merit, $FOM = n_2 / (\beta\lambda)$. For optical switching applications, a $FOM \geq 2$ is desired, and a large FOM indicates that a material has relatively large nonlinear index compared to its nonlinear loss [139]. For $\text{Ge}_{28}\text{Sb}_{12}\text{Se}_{60}$, we calculate a FOM of 0.094 at 1.03 μm . The low measured FOM indicates that the glass is not well-suited for switching applications at 1 μm . However, the high β could hold promise for optical limiting applications in this spectral region. Additionally, this material's high β at 1 μm could be explored as a flexible, compact alternative for two-photon absorption-based autocorrelation detectors for characterizing short pulse durations

at wavelengths $\sim 2 \mu\text{m}$. Finally, we note that multiple studies have shown that the *FOM* of Ge-Sb-Se glasses improves drastically at wavelengths farther from the band edge, ranging from ~ 3 at 1550 nm [65], to >10 at 2500 nm [95].

3. OPTICAL WAVEGUIDE DESIGN AND CHARACTERIZATION

3.1 Overview

Optical chalcogenide waveguides have been studied for operation at wavelengths of 1.0, 1.55, and 3.5 μm . In Section 3.2, basic principles of optical waveguide design and characterization techniques are introduced. In Section 3.3, the design, fabrication, and characterization of chalcogenide strip waveguides at 1.0 μm are described. At this wavelength, waveguides are shown to have average propagation loss of 11.9 ± 1 dB/cm and substantial two-photon absorption of 11.5 ± 0.7 cm/GW, comparable to that observed in the bulk glass. In Section 3.4, the design, fabrication, and testing of chalcogenide waveguides at 1.55 μm is summarized. Here, waveguides are designed for reduced dispersion and larger nonlinear parameter, in order to improve nonlinear interactions and provide more spectral broadening. The waveguides are shown to have propagation loss ranging from 4.0-6.1 dB/cm and significantly reduced two-photon absorption at 1.55 μm . Additionally, the waveguides exhibit average nonlinear parameter of $6/\text{W}\cdot\text{m}$, ~ 5000 x that of standard single mode fiber. In Section 3.5, the design of chalcogenide-on MgF_2 waveguides at 3.5 μm is described.

This work was performed in collaboration with Professor Wounjhang Park and Dr. Sungmo Ahn at the University of Colorado Boulder. Dr. Sungmo Ahn fabricated the waveguides, and Suehyun Cho (University of Colorado Boulder) took scanning electron micrograph (SEM) images. Preliminary waveguide fabrication was performed by Lisa Rengnath and Martin Kronberg at the

University of Colorado Boulder. E-beam lithography was done at the Washington Nanofabrication Facility, a member of the NSF National Nanotechnology Infrastructure Network.

We benefited from technical discussions with Dr. Pete Rakich (Yale) and Dr. Tymon Barwicz (IBM) in building a setup for waveguide coupling. Dr. Milos Popovic (Boston University) provided advice on waveguide design, coupling, and fabrication options. Richard Bojko (University of Washington) provided useful discussions regarding e-beam lithography. A waveguide mode solver from Dr. Milos Popovic was used to simulate guided waveguide modes [141]. A split-step software routine from Dr. Thomas Murphy (University of Maryland) was used to simulate the propagation of optical pulses in nonlinear waveguides [142]. A Picaso phase-retrieval program from Dr. Jeff Nicholson (OFS Laboratories) was used to retrieve electric field phase information from measured spectral and interferometric autocorrelation data [143].

This work was supported in part by NSF Grant EECS-1232077, in part by AFOSR under Grant FA9550-15-1-0506, in part by the DARPA SCOUT Program through ARO under Contract W911NF-15-1-0621, and in part by the Department of Defense through the National Defense Science and Engineering Graduate (NDSEG) Fellowship Program. This chapter is adapted from [56,140].

3.2 Waveguides for nonlinear optics

Optical waveguides can enable nonlinear effects at low thresholds due to their ability to confine light to a sub-micron areas, increasing the intensity that can be maintained over chip-scale lengths. For comparison, consider a free space Gaussian beam, which may be focused to the Abbe diffraction limit, with minimum spot radius of

$$r_{\min} = \frac{\lambda}{2NA}, \quad (3.1)$$

where NA is the numerical aperture and λ is the wavelength. At 1550 nm, assuming $NA \sim 1$, this would roughly correspond to a minimum spot radius of ~ 775 nm. However, due to free space diffraction, the beam spot size will diverge, causing a position-dependent intensity. The corresponding accumulated nonlinear phase shift $\Delta\phi_{NL}$ in a material is given by

$$\Delta\phi_{NL} = \int_0^L \frac{2\pi n_2 I(z) dz}{\lambda}, \quad (3.2)$$

where n_2 is the nonlinear refractive index, λ is the wavelength, $I(z)$ is the intensity, z is the propagation direction, and L is the propagation length. To compare, an optical waveguide can maintain small, constant mode area over longer distances by using materials with high index contrast to tightly confine light. For example, a 5-mm-long waveguide with mode radius of 300 nm at 1550 nm would accumulate ~ 170 times larger nonlinear phase shift than its 5 mm-long free-space, diffraction-limited (~ 775 nm waist) Gaussian-beam counterpart.

Additionally, the small, ≤ 1 cm² footprint of on-chip optical waveguides makes them particularly attractive for compact, lightweight devices. When designing waveguides for nonlinear optical applications, several properties must be considered, including the number of guided modes, effective mode area and nonlinearity, and net dispersion. In particular, lower loss, smaller mode area, and larger nonlinearity are all desired for lower threshold powers. Dispersion also becomes crucial for phase-sensitive effects such as four-wave mixing. Finally, to achieve compact devices with small mode volumes, radiation loss, which limits how tightly a waveguide can be bent, becomes important. In the following sections, key concepts will be introduced, including waveguide loss, dispersion, and nonlinear parameter. Experimental techniques for measuring the

linear loss, nonlinear loss, and nonlinear refractive index of optical waveguides will be summarized.

3.2.1 Waveguide loss

Multiple factors can contribute to loss in an optical waveguide, including scattering loss, due to the rough surfaces and sidewalls of a fabricated waveguide, material absorption, and radiative loss due to tight curves or bends. Loss due to bulk material absorption, $\alpha_{wg,mat}$, can be calculated with an overlap integral of the electric field of the waveguide mode with the spatially varying material absorption $\alpha(x, y)$, such that

$$\alpha_{wg,mat} = \frac{\iint \alpha(x, y) |E(x, y)|^2 dx dy}{\iint |E(x, y)|^2 dx dy}, \quad (3.3)$$

where $E(x, y)$ is the electric field of mode at the location (x, y) in the waveguide cross section. (Note for TE modes, this will be the x-component of the field, and for TM modes, the y-component.) Typically, materials are chosen to minimize loss from material absorption.

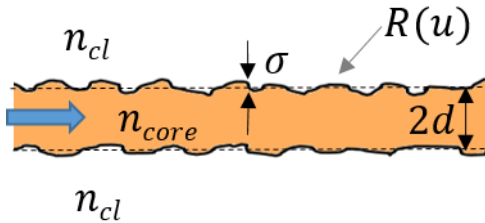


Figure 3.1. Side-view schematic of planar waveguide. Slab waveguide consists of a thin film with index n_{core} and thickness $2d$, surrounded by lower refractive index n_{cl} . The direction of light propagation is indicated with the thick blue arrow. The waveguide surface can be characterized with an autocorrelation function $R(u)$, which has a surface roughness σ and correlation length L_c .

Calculations of scattering loss are more involved. To understand the main factors influencing scattering loss, one can examine analytic theory for scattering loss from surface roughness in a planar, or slab, waveguide, which was developed by Payne and Lacey [144]. A schematic of a slab waveguide, consisting of a high index core film of thickness $2d$, surrounded by lower index cladding material, is illustrated in Figure 3.1.

The surface roughness of such a waveguide can be characterized by an autocorrelation function $R(u)$, with a characteristic RMS surface roughness, σ , and correlation length, L_c . One can compute the radiation in the far field to obtain the scattering loss, using the method of equivalent currents (also called the volume current method) [144,145]. In this method, nonuniformities in the waveguide are treated as induced current sources in a uniform waveguide [145]. The vector potential produced by these induced current sources is then calculated and used to compute the far-field radiation. Assuming the scattering from the top and bottom surfaces are independent, the scattering loss α_{sc} for a slab waveguide is given by

$$\alpha_{sc} = \Phi^2(d) \left[n_{core}^2 - n_{cl}^2 \right]^2 \frac{k_0^3}{4\pi n_{core}} \int_0^\pi \tilde{R}[\beta - n_{cl}k_0 \cos(\theta)] d\theta, \quad (3.4)$$

where $\Phi(d)$ is the modal field at the surface of the waveguide, n_{core} is the core index, n_{cl} is the cladding index, $2d$ is the slab thickness, k_0 is the free-space wavenumber, β is the propagation constant, and θ is the scattering angle [144]. Here, $\tilde{R}(u)$ is the Fourier transform of the autocorrelation function $R(u)$, given by [144]

$$\tilde{R}(u) = \int R(u) \exp[i\omega u] du. \quad (3.5)$$

Here, u is the spatial variable and ω is the spatial frequency. From Equation 3.4, one sees that the scattering loss depends on the modal field at the waveguide surface, the index contrast, the

wavenumber, and the spectral density function for the surface roughness. To simplify, note that many waveguides are well described by an exponential autocorrelation function given by

$$R(u) = \sigma^2 \exp[-|u|/L_c], \quad (3.6)$$

where σ is the RMS surface roughness and L_c is the correlation length [144]. The expression for scattering loss then reduces to

$$\alpha_{sc} = \frac{\sigma^2}{n_{core} d^4 k \sqrt{2}} g(V) f_c(L_c, \gamma), \quad (3.7)$$

where $g(V)$ is a factor determined by waveguide geometry and $f_c(L_c, \gamma)$ is a factor depending on correlation length L_c and the strength of guiding γ , determined by the waveguide geometry and refractive indices of the core and cladding [144]. For a slab waveguide with an exponential autocorrelation function, the scattering loss has a relatively simple analytic expression, which depends primarily on the surface roughness, waveguide thickness, along with factors depending on waveguide geometry, correlation length and guiding strength.

While this theory has been developed for a slab waveguide, no simple analytic expression exists for strip waveguides. (The modes of strip waveguides must be solved for numerically.) However, others have extended this analysis for loss estimates in 3D strip waveguides, where scattering from sidewall roughness dominates [146]. In general, by choosing waveguide designs and fabrication processes which decrease the roughness and reduce the field at the rough surfaces, one can reduce the scattering loss.

Scattering losses can arise from both volume scattering, due to imperfections in the material, as well as interface scattering, due to the rough surfaces and sidewalls. For waveguides, scattering loss is commonly dominated by interface scattering given current fabrication techniques. The wavelength dependence of scattering loss will depend on the geometry and length scale of the

distribution and correlation of scatterers, or how the correlation length compares to the wavelength of light. Tien has shown that for planar waveguides with $L_c > \lambda$, interface scattering scales as $\alpha_{sc} \propto \lambda^{-2}$ [147]. On the other hand, for interface scattering in structures with $L_c \ll \lambda$, Payne and Lacey have predicted $\alpha_{sc} \propto \lambda^{-4}$ using a two-dimensional model [144]. Using a three-dimensional vectorial current method, Ciminelli et al., have predicted that $\alpha_{sc} \propto \lambda^{-4}$ for 3D structures with $L_c \ll \lambda$ [148]. For comparison, in bulk, Rayleigh scattering produces loss which scales as λ^{-4} [149]. For the three-dimensional strip waveguide geometries explored in this thesis, $L_c \ll \lambda$ and interface scattering dominates. As such, the $\alpha_{sc} \propto \lambda^{-4}$ wavelength dependence predicted by Ciminelli et al. is expected to hold [148]. This wavelength scaling is promising, predicting a dramatic reduction in scattering loss as the wavelength is increased from near-infrared to mid-infrared wavelengths.

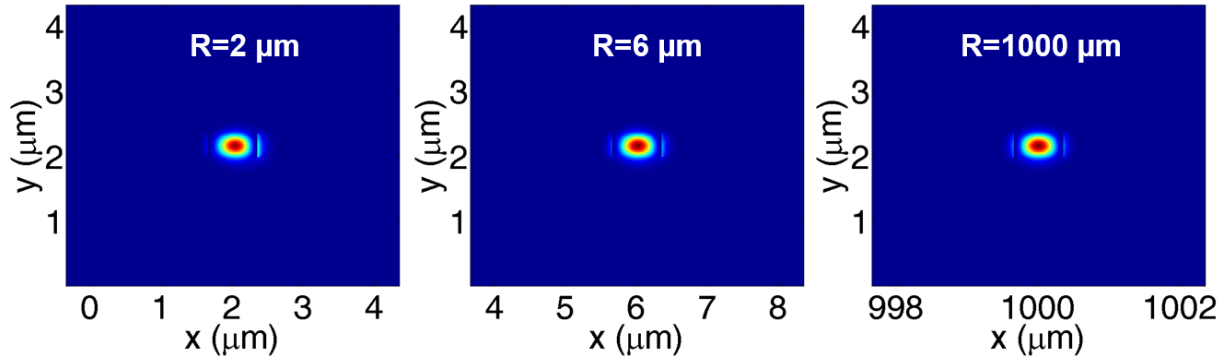


Figure 3.2. Comparison of fundamental waveguide mode profile for various bend radius.

The fundamental mode profile, E_x^2 , is plotted for a 700 nm (W) by 330 nm (H) waveguide for radii of 2, 6, and 1000 μm (left, middle, and right plots, respectively). Note that as the bend radius is reduced from 1000 to 2 μm , the mode shifts outward and the field at the outer sidewall increases, reducing the waveguide confinement to the core from 0.76 to 0.72.

In addition to scattering loss and material loss, radiation loss from bending can also contribute to the total propagation loss. Bending a waveguide distorts the optical field, as

illustrated in Figure 3.2, which shows the mode profile of a waveguide as it is bent with a radii of 2, 6, and 1000 microns. Note that as the bend radius is reduced, the mode shifts outward and the field at the outer sidewall increases, reducing the waveguide confinement to the core from 0.76 to 0.72. To preserve the phase front of the mode, light at the outer radius must travel at higher tangential phase velocity than light at the inner radius. Beyond a certain radius, the phase velocity will be larger than the velocity of unguided light, resulting in radiation loss [150,151].

To calculate the expected radiation loss from bend loss, a mode solver is used to calculate the complex angular propagation constant, ρ , of the desired guided mode for a curved waveguide geometry with given circular bend radius R . Note that the propagation constant is composed of a real and imaginary component

$$\rho = \rho_{real} - j\rho_{im}. \quad (3.8)$$

The propagation constant is related to the electric field by $E \propto \exp[-j\rho\varphi]$, such that

$$E \propto \exp[-j\rho_{real}\varphi]\exp[-\rho_{im}\varphi]. \quad (3.9)$$

Since the intensity is proportional to the square of the electric field, the intensity is given by

$$I \propto \exp[-2\rho_{im}\varphi]. \quad (3.10)$$

Comparing the intensity after propagating around a 90 degree circular bend, $I(\varphi = \pi / 2)$, to the intensity at the start of the waveguide, $I(\varphi = 0)$, one finds the transmission T_{90° is given by

$$T_{90^\circ} = \frac{I(\varphi = \pi / 2)}{I(\varphi = 0)} = \exp[-\pi\rho_{im}]. \quad (3.11)$$

Correspondingly, the radiation loss (with units of 1/length) is given by

$$\alpha_{rad} = \frac{-2}{\pi R} \ln(T_{90^\circ}). \quad (3.12)$$

From simulations, ρ_{im} tends to vary with R , such that $\alpha_{rad} \propto \exp(-c_1 R)$, with the proportionality constant c_1 depending on the waveguide geometry and materials [151].

3.2.2 Chromatic dispersion

Chromatic dispersion describes the wavelength-dependence of the waveguide propagation constant, causing light at different frequencies to travel at different phase velocities. For phase-sensitive effects, such as four-wave mixing, chromatic dispersion becomes important to consider, because it will affect the achievable efficiencies. Additionally, dispersion is important in pulsed applications, as it can dramatically affect pulse durations. One can Taylor expand the propagation constant β as a function of angular frequency ω , such that

$$\beta(\omega) = \beta_0 + \frac{\partial \beta}{\partial \omega} (\omega - \omega_0) + \frac{1}{2} \frac{\partial^2 \beta}{\partial \omega^2} (\omega - \omega_0)^2 + \frac{1}{6} \frac{\partial^3 \beta}{\partial \omega^3} (\omega - \omega_0)^3 + \dots \quad (3.13)$$

Here, the zero-order term describes a common phase shift. The first-order dispersion is described by the group velocity v_g , which describes an overall time delay, not affecting the pulse shape, and related to the first-order term by

$$\frac{\partial \beta}{\partial \omega} = \frac{1}{v_g}. \quad (3.14)$$

The second-order dispersion is described by the group velocity dispersion, or GVD, which is defined as

$$\beta_2 = \frac{\partial^2 \beta}{\partial \omega^2}. \quad (3.15)$$

and has units of s^2/m . A medium is said to have normal dispersion when $\beta_2 > 0$, causing the group velocity to decrease with increasing frequency. Alternatively, when $\beta_2 < 0$, a medium is said to have anomalous dispersion. The fiber optic community also often specifies a dispersion parameter, D_λ , defined as

$$D_\lambda = -\frac{2\pi c}{\lambda^2} \frac{\partial^2 \beta}{\partial \omega^2}. \quad (3.16)$$

Note that the dispersion parameter has units of s/m^2 . While this is directly related to the group velocity dispersion, it is important to note that it has opposite sign. (For example, a material with normal dispersion has $\beta_2 > 0$ and $D_\lambda < 0$.) Higher-order dispersion terms β_n can be defined, such

that $\beta_n = \frac{\partial^n \beta}{\partial \omega^n}$.

In a waveguide, there are two main contributions to the total chromatic dispersion of a given guided mode: material dispersion and waveguide geometry dispersion. The refractive index depends on wavelength, which results in material dispersion. The Lorenz harmonic oscillator model of the atom explains the phenomenon. Here, one can treat the constituent atoms of a material as harmonic oscillators. In the presence of an applied optical field, the positively charged nuclei will be displaced from their negatively charged electron clouds, producing a dipole moment. The motion of the electron in the presence of the applied oscillatory electric field can be described, using a damping term to account for absorption. The corresponding induced atomic polarization can be calculated. In general, one may find several oscillation frequencies for a given material across the spectrum. Figure 3.3 shows the frequency dependence of the refractive index and absorption near a few resonances for an arbitrary medium with loss [152]. Infrared resonances are

often due to vibrational resonances, while visible and ultraviolet resonances are due to electronic transitions within the molecule. Near resonance, the refractive index exhibits strong dispersion.

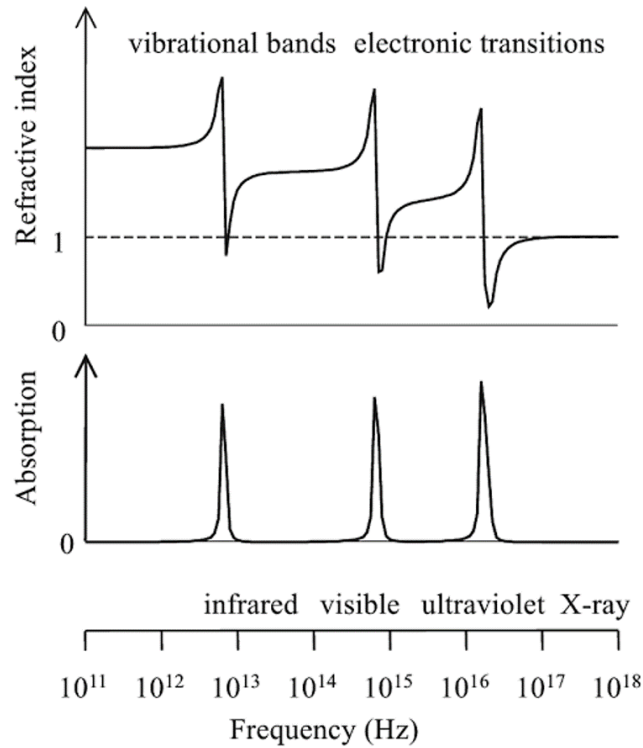


Figure 3.3. Frequency dependence of refractive index (top) and absorption (bottom) for a medium with loss and 3 resonances. Note that near resonance, the refractive index exhibits strong dispersion. Infrared resonances are often due to vibrational resonances, while visible and ultraviolet resonances are due to electronic transitions within the molecule. Figure reprinted with permission from [152], Oxford University Press.

The wavelength-dependent refractive index and group velocity dispersion of bulk $\text{Ge}_{28}\text{Sb}_{12}\text{Se}_{60}$ are plotted in Figures 3.4 and 3.5 [153]. The linear refractive index ranges from 2.60 to 2.66 over the 1.55-12 μm range. The bulk $\text{Ge}_{28}\text{Sb}_{12}\text{Se}_{60}$ material dispersion is normal from 1.0-6.3 μm , and anomalous from 6.3-12 μm (See Figure 3.5).

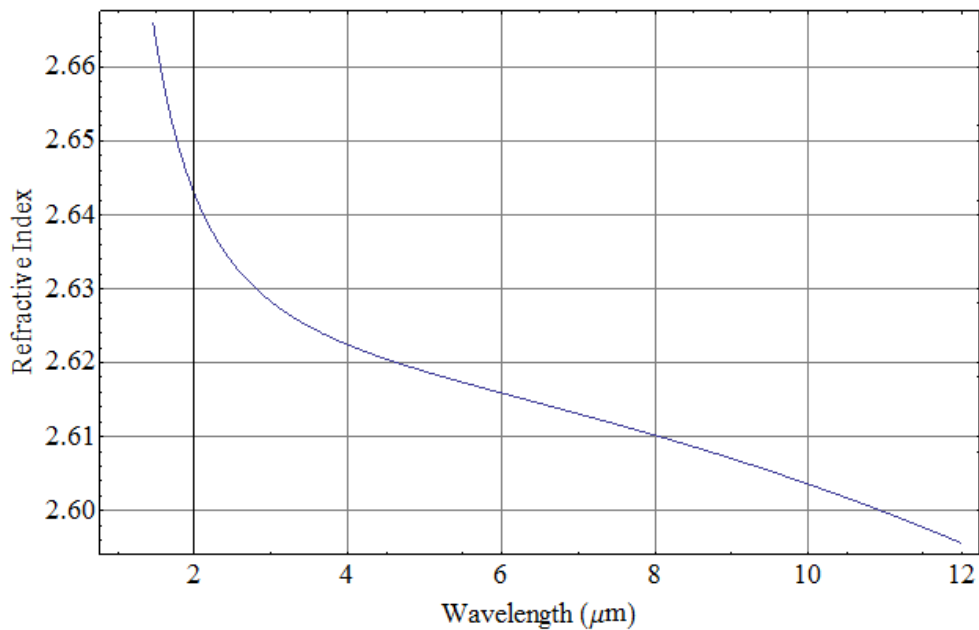


Figure 3.4. Wavelength dependence of refractive index of bulk Ge₂₈Sb₁₂Se₆₀. Over 1 to 12 microns, the refractive index of Ge₂₈Sb₁₂Se₆₀ decreases with increasing wavelength. Note data used is from [153].

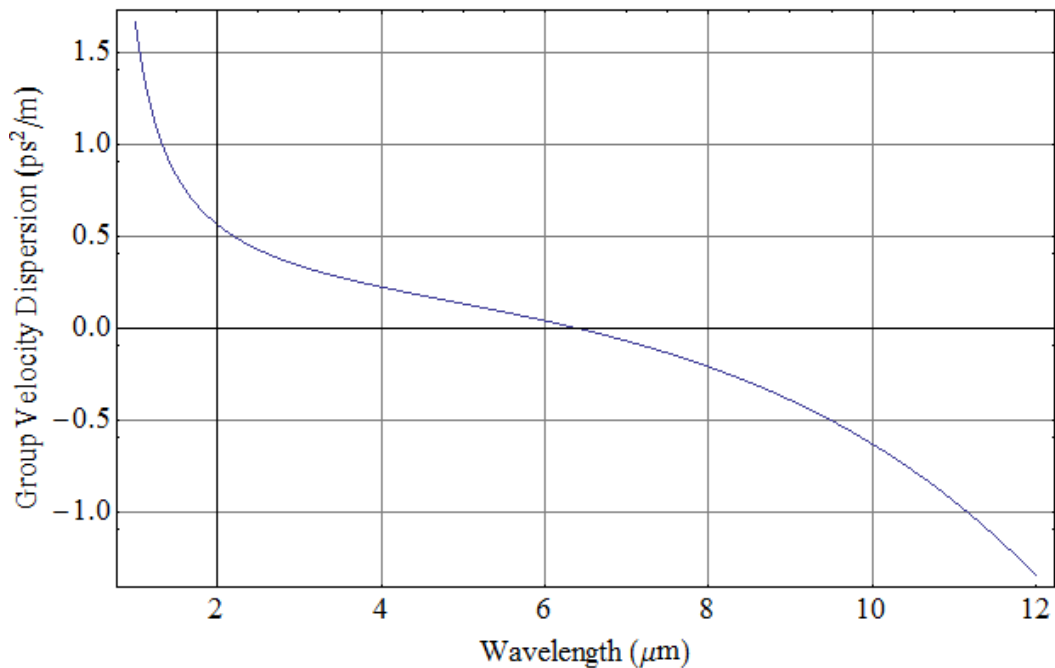


Figure 3.5. Wavelength dependence of material group velocity dispersion (β_2) for bulk Ge₂₈Sb₁₂Se₆₀. Material dispersion is normal from 1.0-6.3 μm, and anomalous from 6.3-12 μm. Note data used is based on refractive index measurements from [153].

In addition to material dispersion, the geometry of a waveguide can also significantly influence a waveguide mode's total chromatic dispersion. Even if material dispersion is set to zero, the propagation constant of a waveguide will vary with wavelength, leading to waveguide geometry dispersion.

To calculate the total chromatic dispersion, one can include material dispersion in the mode solver, updating refractive indices whenever the wavelength is changed, and then calculate the propagation constant as a function of frequency. Using the finite difference method, by running the calculation at the wavelength of interest and nearby wavelengths, one can calculate the total second-order dispersion, as well as higher-order dispersion. For example code showing the dispersion calculation, see Appendix C.2 and C.5.

3.2.3 Waveguide nonlinearity

To describe the nonlinearity of a waveguide, it is common to define a nonlinear parameter

$$\gamma = \frac{2\pi n_2}{\lambda A_{\text{eff}}}, \quad (3.17)$$

where n_2 is the nonlinear refractive index of the waveguide, λ is the wavelength, and A_{eff} is the effective mode area [62]. The nonlinear parameter is a useful quantity for comparing nonlinear waveguides, as it takes into account not only the nonlinearity, but also the effective mode area, which increases local intensity for a given input power.

Although scalar theory is often used to approximate the effective mode area [62], for waveguides with subwavelength dimensions, the z-component of guided modes is no longer negligible (more than a few percent of the total field), and a vectorial model should be used to properly calculate the effective area

$$A_{eff} = \frac{|\int (\mathbf{E} \times \mathbf{H}^*) \cdot \hat{\mathbf{z}} dA|^2}{\int |(\mathbf{E} \times \mathbf{H}^*) \cdot \hat{\mathbf{z}}|^2 dA}, \quad (3.18)$$

where \mathbf{E} and \mathbf{H} are the electric and H fields of the guided mode, and $\hat{\mathbf{z}}$ is a unit vector lying along the length of the waveguide [62,154]. Following the same model, the effective nonlinearity of the waveguide, $n_{2,wg}$ is given by

$$n_{2,wg} = \frac{\varepsilon_0}{\mu_0} \frac{\int n_0^2(x, y) n_2(x, y) [2|\mathbf{E}|^4 + |\mathbf{E}^2|^2] dA}{3 \int |(\mathbf{E} \times \mathbf{H}^*) \cdot \hat{\mathbf{z}}|^2 dA}, \quad (3.19)$$

where n_0 is the linear refractive index, n_2 is the nonlinear refractive index, and ε_0 and μ_0 are the permittivity and permeability of free space, respectively [154]. The vectorial model for effective area and nonlinearity has been experimentally verified in subwavelength waveguides [229]. Additionally, the model has been shown to approach the scalar model for larger waveguides with \geq wavelength-sized dimensions [154,229].

3.2.4 Waveguide design geometries

Cross sections of a few commonly used waveguide geometries offering are illustrated in Figure 3.6. These include slab, strip, rib, and strip-loaded waveguides. Strip waveguides offer the strongest confinement, enabling tight bends with little radiation loss. Additionally, strip waveguides provide good control of dispersion through cross sectional dimensions and can be made to have sub-square-micron mode areas. The main challenge of strip waveguides is stronger field overlap with the rough sidewalls, leading to losses typically on the order of a few dB/cm or higher [88], even utilizing state-of-the-art fabrication technologies. Rib and strip-loaded waveguides provide weaker guiding, leading to substantially higher radiation loss than strip waveguides, for a given radius. Additionally, controlling dispersion through waveguide geometry

can be more of a challenge. Rib and strip-loaded waveguides can also be more difficult to fabricate with liftoff, and, depending on the dimensions chosen, may require etching. However, these two structures offer the advantage of significantly lower propagation loss, $\sim 0.05\text{-}0.8$ dB/cm typically in chalcogenide waveguides [88,106,163], due to less interaction of the optical mode with the rough sidewalls. Finally, slab waveguides also feature low loss, but they can suffer from larger mode areas compared to strip waveguides, and they are not suitable for making ring resonators, given their geometry. Considering the trade-offs of the various waveguide geometries, along with available fabrication methods, strip waveguides were chosen for this work.

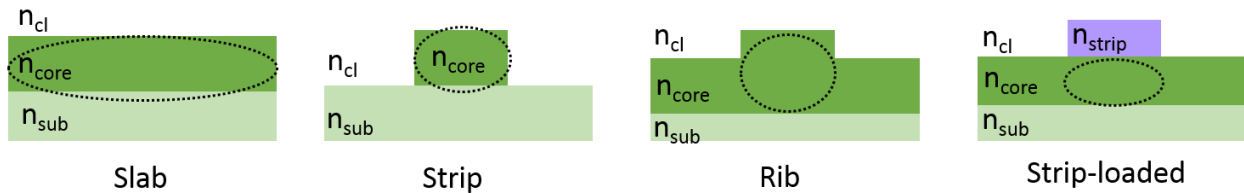


Figure 3.6. Typical waveguide geometries. Cross sections of slab, strip, rib, and strip-loaded waveguides are shown schematically. The general location of the guided mode is shown with a dotted black line. Note that for all geometries, the core refractive index, n_{core} , is larger than the refractive indices of the substrate (n_{sub}), cladding (n_{cl}), or upper strip (n_{strip}), such that $n_{core} > n_{strip} > n_{cl}, n_{sub}$.

3.2.5 Linear loss characterization techniques

A variety of experimental methods exist to measure the linear loss in a waveguide, including cutback [155], Fabry-Perot [156], and scattered light methods [157]. In the cutback method, transmission is measured for a series of waveguides of different lengths. A single long waveguide can be progressively cleaved shorter, measuring the transmission with each new length. Alternatively, multiple waveguides of different lengths can be fabricated on the same chip to reduce unwanted variation from multiple cleaving attempts. Although this method is

straightforward, it requires repeatable coupling efficiency to accurately extract the propagation loss. An alternate loss characterization method is the Fabry-Perot technique, which involves measuring the Fabry-Perot transmission fringes that occur from highly parallel, cleaved facets of a waveguide. This technique is best suited for short, single-mode waveguides based on crystalline semiconductors, which provide smooth, easily cleaved clean facets [156]. From our experience, achieving perfectly parallel facets was a challenge with non-crystalline chalcogenide-based waveguides, making this method difficult for our system.

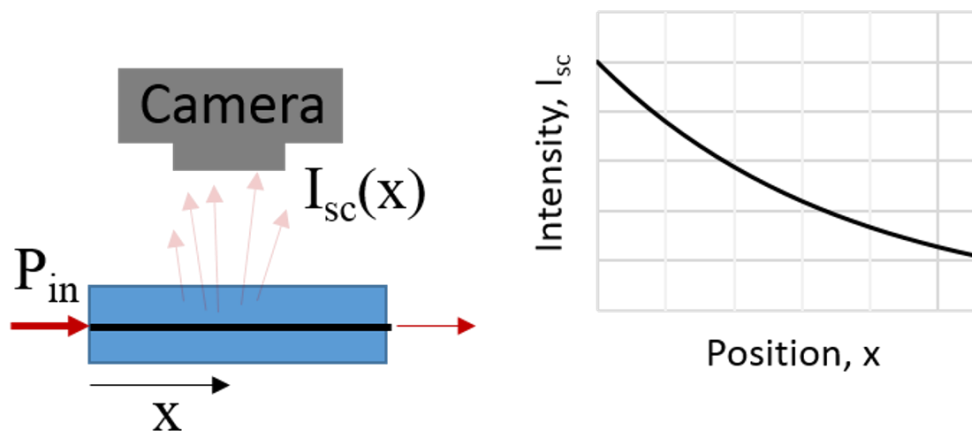


Figure 3.7. Illustration of scattered light waveguide loss method. Light is coupled into a waveguide, and scattered light is imaged from above the waveguide using a camera, as shown on the left. Since the intensity of the scattered light is proportional to the light remaining in the waveguide, one can plot I_{sc} vs. distance x and fit to a decaying exponential to determine propagation loss α_{tot} .

Instead, we focus on the scattered light method [157], which is illustrated in Figure 3.7. In this method, light is coupled into a waveguide, and the scattered light from the waveguide is imaged using a camera. Since the intensity of the scattered light is proportional to the light remaining in the waveguide, one can measure this scattered light intensity as a function of position at a fixed input power, and fit to a decaying exponential to determine the total loss. The advantages

of this method are its simplicity, single-shot nature, and independence from coupling loss. Since waveguide lengths $\geq 1/\alpha$ are desired for an accurate measurement, the main disadvantage is that it requires relatively long waveguides to sensitively measure low loss. As such, the method is best suited for loss measurements on samples with losses \geq a few dB/cm.

3.2.6 Nonlinear loss characterization techniques

To determine the nonlinear loss in a waveguide, one can measure the transmission as a function of incident intensity. Assuming both linear absorption α and two-photon absorption β_{wg} are present in a waveguide, the change in intensity I with distance z is given by

$$-\frac{dI}{dz} = \alpha I + \beta_{wg} I^2. \quad (3.20)$$

Rearranging to separate variables, this can be written as

$$\int \frac{dI}{\alpha I + \beta_{wg} I^2} = \int -dz. \quad (3.21)$$

Integrate both sides. Letting I_f be the output intensity, I be the input intensity, and $z_f - z_i = L_{wg}$, the length of the waveguide, one finds

$$\frac{\ln(I_f) - \ln[\alpha + \beta_{wg} I_f]}{\alpha} - \frac{\ln(I) - \ln[\alpha + \beta_{wg} I]}{\alpha} = -L_{wg}. \quad (3.22)$$

Multiplying both sides by α and then combining ln terms, this can be written as

$$\ln \left[\frac{I_f (\alpha + \beta_{wg} I)}{I (\alpha + \beta_{wg} I_f)} \right] = -\alpha L_{wg}. \quad (3.23)$$

This can be further written as

$$\left[\frac{I_f(\alpha + \beta_{wg} I)}{I(\alpha + \beta_{wg} I_f)} \right] = \exp[-\alpha L_{wg}]. \quad (3.24)$$

The transmission is defined as $T = I_f / I$. Using this to eliminate I_f , one finds

$$T \frac{(\alpha + \beta_{wg} I)}{(\alpha + \beta_{wg} IT)} = \exp[-\alpha L_{wg}]. \quad (3.25)$$

Multiplying through, one finds

$$T(\alpha + \beta_{wg} I) = (\alpha + \beta_{wg} IT) \exp[-\alpha L_{wg}]. \quad (3.26)$$

Combining terms depending on T , one finds

$$T[\alpha + \beta_{wg} I - \beta_{wg} I \exp[-\alpha L_{wg}]] = \alpha \exp[-\alpha L_{wg}]. \quad (3.27)$$

Rearranging, this can be re-written as

$$\frac{1}{T} = \frac{\alpha + \beta_{wg} I(1 - e^{-\alpha L_{wg}})}{\alpha e^{-\alpha L_{wg}}}. \quad (3.28)$$

This can be simplified as

$$\frac{1}{T} = e^{\alpha L_{wg}} + \frac{\beta_{wg} I e^{\alpha L_{wg}} (1 - e^{-\alpha L_{wg}})}{\alpha}. \quad (3.29)$$

After further simplifying, the loss in a waveguide due to both linear absorption and two-photon absorption is described by the following equation:

$$\frac{1}{T} = \frac{[e^{\alpha L_{wg}} - 1] \beta_{wg}}{\alpha} I + e^{\alpha L_{wg}}, \quad (3.30)$$

where $1/T$ is the reciprocal transmission, I is the incident peak intensity, α is the linear absorption of the waveguide, β_{wg} is the two-photon absorption coefficient of the waveguide, and L_{wg} is the length of the waveguide [158]. To avoid future mistakes, note that a later paper commonly cited [159] has an error in the equation relating the reciprocal transmission to two-photon absorption. Both Equation 3.30 and reference [158] provide the correct equation.

At high intensities, saturation of the two-photon absorption has been observed in chalcogenides and other semiconductors [160,161]. Two-photon absorption excites many electrons from lower-energy states to a finite number of higher-energy states, changing the electron population distribution. Once the lower level states are depleted and the upper level states are filled, the nonlinear absorption is reduced, resulting in saturation [161]. Two-photon absorption saturation has been modeled with a saturation intensity I_{sat} and an effective two-photon absorption coefficient [162],

$$\beta_{eff} = \frac{\beta_{wg}}{\left(1 + \frac{I}{I_{sat}}\right)}. \quad (3.31)$$

It can be useful to define a waveguide confinement,

$$\Gamma = \frac{\iint_{core} |E(x, y)|^2 dx dy}{\iint_{\infty} |E(x, y)|^2 dx dy}, \quad (3.32)$$

where $E(x, y)$ is the x -component of the electric field of the TE mode at the location (x, y) in the waveguide cross section. Analogous to the concept of confinement and the calculation of material absorption in a waveguide in Equation 3.3 and 3.32, one can calculate the overlap of the guided mode with the core and cladding layers to estimate the expected two-photon absorption, β_{wg} , of a waveguide structure.

$$\beta_{wg} = \frac{\iint \beta(x, y) |E(x, y)|^2 dx dy}{\iint |E(x, y)|^2 dx dy}, \quad (3.33)$$

where $E(x, y)$ is the x -component of the electric field of the TE mode at the location (x, y) in the waveguide cross section, and $\beta(x, y)$ is the material two-photon absorption coefficient at the location (x, y) .

3.2.7 Nonlinear refractive index characterization techniques

A simple technique to characterize the nonlinear refractive index of a waveguide is to measure the spectral broadening [100,163-166]. A short pulse is coupled into a waveguide, and the corresponding spectra before and after the waveguide are recorded. The nonlinear refractive index will cause self-phase modulation in the waveguide, which can broaden the spectrum as the pulse propagates along the waveguide. Waveguide dispersion can further complicate pulse propagation.

The nonlinear Schrödinger equation describes pulse propagation in a dispersive, nonlinear optical medium. Assuming the field varies slowly in the propagation direction z , and neglecting Raman and self-steepening effects, the nonlinear Schrödinger equation can be written as

$$\frac{dA}{dz} + \frac{\alpha}{2} A + \frac{i\beta_2}{2!} \frac{\partial^2 A}{\partial t^2} - \frac{\beta_3}{3!} \frac{\partial^3 A}{\partial t^3} + \dots + \frac{i^{n-1} \beta_n}{n!} \frac{\partial^n A}{\partial t^n} = i\gamma |A|^2 A, \quad (3.34)$$

where $A(z, t)$ is the slowly-varying field envelope, β_n is the n^{th} order dispersion, t is time, and γ is the nonlinear parameter [62,142,167]. Note that the Fourier transform of the field envelope, $\tilde{A}(z, \omega)$, is related to the Fourier transform of the electric field, $\tilde{E}(x, y, z, \omega)$ by

$$\tilde{E}(x, y, z, \omega) = F(x, y) \tilde{A}(z, \omega) \exp(i\beta_0 z), \quad (3.35)$$

where β_0 is the wave number, ω is the optical frequency of the wave, and $F(x, y)$ is the spatial mode profile. The nonlinear Schrödinger equation can also be modified to include the effects of multi-photon absorption [167,168].

To determine $n_{2,wg}$, experimental spectral measurements can be compared to simulated spectra, generated with code, using the split-step Fourier method to solve the scalar nonlinear Schrödinger equation and calculate pulse propagation in a nonlinear waveguide. In the split-step method, the field is propagated over a series of small steps, approximating that dispersion and nonlinearity act roughly independently over short steps [62]. Taking advantage of the fast Fourier transform (FFT) algorithm, the split-step method is a relatively fast method to numerically solve the scalar nonlinear Schrödinger equation [62]. Although analysis is somewhat complex for dispersive waveguides, the spectral broadening method requires little specialized equipment, aside from a pulsed source.

3.3 Waveguides at 1.0 μm

3.3.1 Waveguide design and fabrication at 1.0 μm

For thin film devices, chalcogenides are prepared in bulk glass form and then deposited onto a substrate using thermal evaporation [169], pulsed laser deposition [170], or sputtering [171]. Although pulsed laser deposition can be used to quickly fabricate few- μm -thick films, films can suffer from poor uniformity and quality [172]. RF-sputtering produces films with stoichiometry in good agreement with bulk [173], but this deposition method can be slow and more difficult to combine with a lift-off process [226]. Thermal evaporation is a particularly attractive, simple technique that yields high quality films. Although it suffers from shadowing effects, thermal

evaporation provides good surface roughness, is relatively inexpensive, and allows for uniform deposition over a few cm^2 .

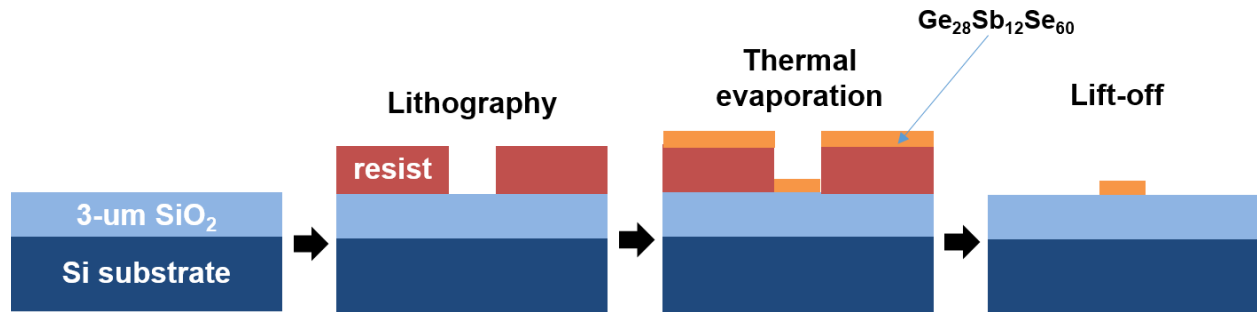


Figure 3.8. Fabrication process flow for strip waveguides. Photolithography was used to form a resist pattern on a substrate, consisting of a Si wafer with a 3 micron-thick oxide layer. A thin layer of Ge-Sb-Se glass was thermally evaporated, and then lift-off was used to remove the resist and pattern strip Ge-Sb-Se waveguides.

To fabricate waveguides, $\text{Ge}_{28}\text{Sb}_{12}\text{Se}_{60}$ glass was thermally evaporated onto a Si wafer with a $3\ \mu\text{m}$ oxide layer, and lift-off was used to pattern strip Ge-Sb-Se waveguides of $2.2\ \mu\text{m}$ width and $45\ \text{nm}$ height. The fabrication process flow is shown in Fig. 3.8.

Energy Dispersive X-ray Spectroscopy (EDX or EDS) measurements on thin Ge-Sb-Se films confirmed that the stoichiometry of the fabricated thin films is within 4 atomic % of the bulk material, as shown in Fig. 3.9(a). Figure 3.9(b) shows a scanning electron micrograph (SEM) of the fabricated waveguides. The surface roughness was measured to be $0.8\ \text{nm}$ using atomic force microscopy (AFM). The average sidewall roughness was measured to be $11.8\ \text{nm}$ using data from high resolution SEMs. These measured roughness values are comparable to values obtained by other groups using a similar fabrication process [88].

Waveguide modes were simulated using a 2D finite-difference vectorial mode solver developed by Dr. Milos Popovic [141]. The mode solver solves for the modes of a given two-dimensional dielectric distribution, using the finite-difference approximation of the transverse-E wave equation [141]. The use of photolithography set a limit on the waveguide width, requiring

$w \geq 2 \mu\text{m}$ for successful fabrication. Given this constraint, initial waveguide dimensions were chosen to ensure single-mode operation at $1.03 \mu\text{m}$. The simulated TE mode profile for the $2.2 \mu\text{m}$ wide (W) by 45 nm tall (H) waveguide at $1.03 \mu\text{m}$ is shown in Figure 3.9(c). Although the guided mode is not well confined to the chalcogenide core material, having 13% confinement, the highly asymmetric dimensions do provide an advantage. Given the wide, flat waveguide design, the field at the sidewalls of the waveguide is weak, desirable for reduced sidewall scattering.

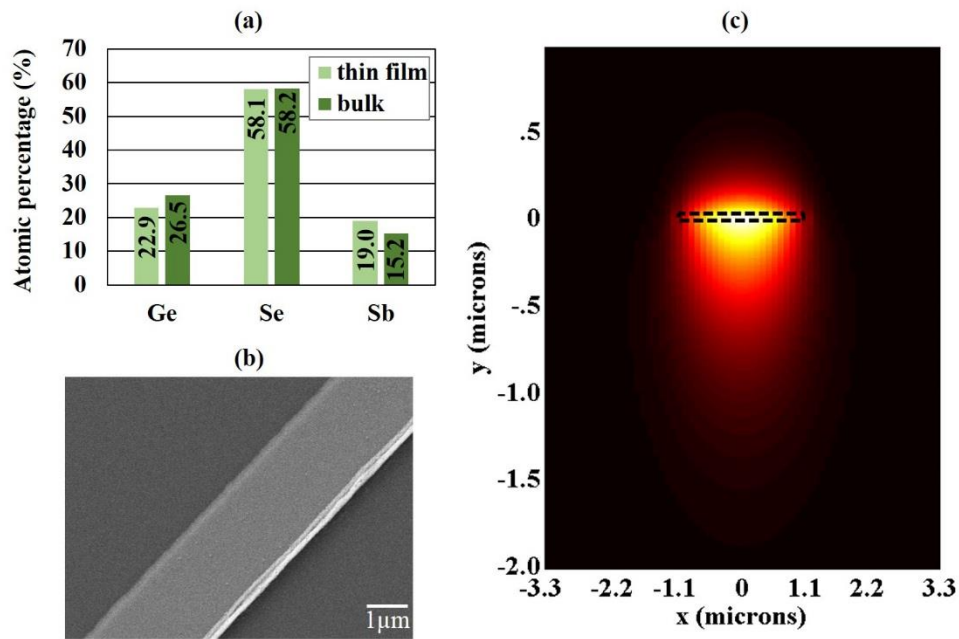


Figure 3.9. Atomic composition, SEM image, and mode profile of thin-film Ge-Sb-Se devices. (a) Atomic composition of thin film and bulk Ge-Sb-Se samples. (b) Scanning electron micrograph (SEM) of a chalcogenide strip waveguide, consisting of silicon substrate, $3\text{-}\mu\text{m}$ -thick SiO_2 , a $2.2\text{-}\mu\text{m}$ -wide and 45-nm -thick Ge-Sb-Se layer, and air upper cladding. (c) Simulated mode profile for the single-mode Ge-Sb-Se strip waveguide. The black dotted rectangular outline indicates the x and y position and size of the Ge-Sb-Se core relative to the mode. Figure reprinted with permission from [56], Optical Society of America.

3.3.2 Linear waveguide characterization at $1.0 \mu\text{m}$

Waveguides were characterized at $1.0 \mu\text{m}$ by measurements of linear and nonlinear loss.

A schematic of the waveguide characterization setup is shown in Figure 3.10. Light was coupled

in and out of the Ge-Sb-Se waveguides using high numerical aperture fibers (Nufern UHNA3, NA=0.35) mounted on piezo-actuated three-axis stages (Thorlabs MAX312D and MDT693A) for precise alignment. Fibers were chosen for improved coupling efficiency for the given waveguide structures, with efficiencies.

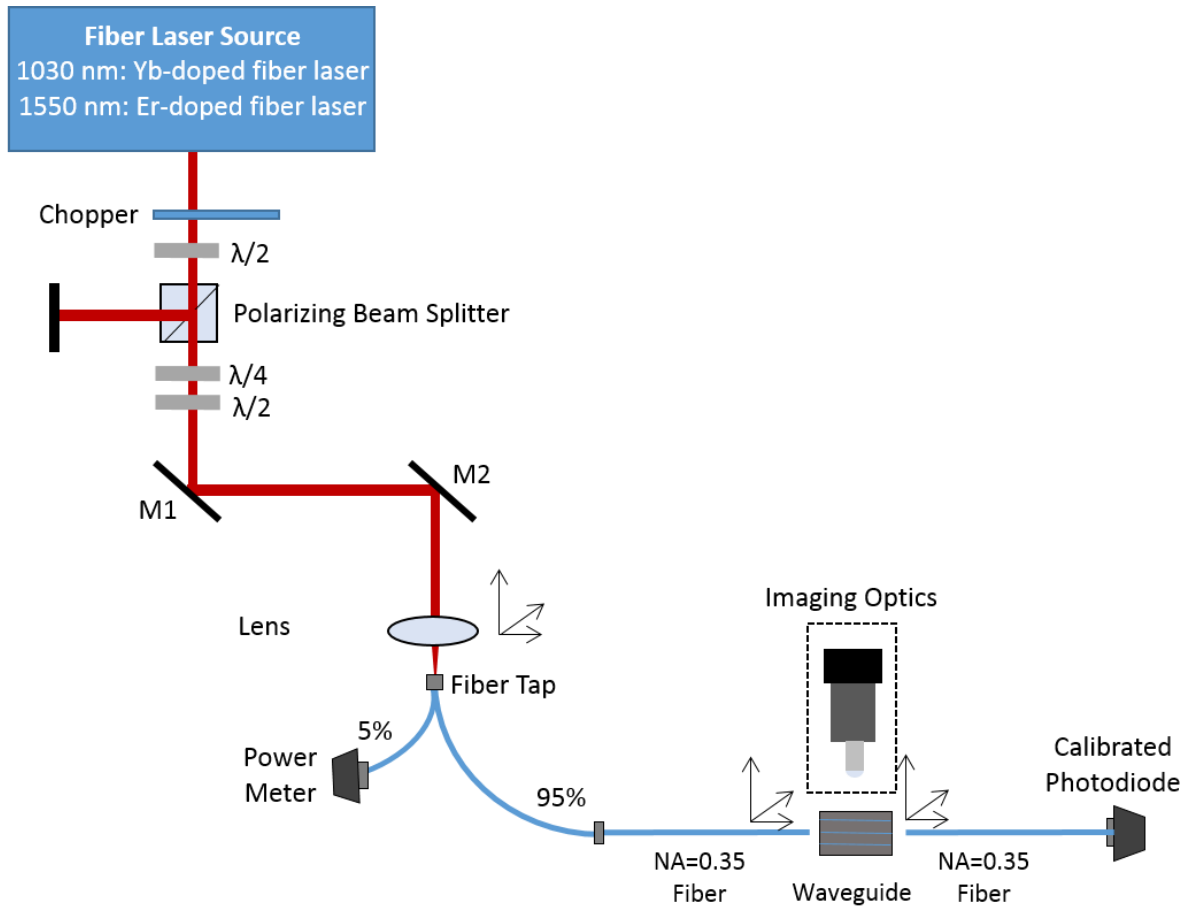


Figure 3.10. Waveguide characterization setup. Light is coupled from an Er- or Yb-doped fiber laser into a fiber tap coupler and high numerical aperture (Nufern UHNA3, NA=0.35) fiber. A half waveplate and polarizing beam splitter are used to control the input power, and another half and quarter waveplate are used to control the launched polarization. The ends of the fiber are mounted on precision piezo-actuated 3-axis stages for alignment to the optical waveguides. Imaging optics, consisting of a camera, zoom lens, and 32X objective, are mounted above the waveguide to aid in alignment. For work at 1030nm, a CCD is used, and at 1550 nm, an InGaAs array is used. Light is coupled out of the waveguides with another high NA fiber, and sent to a calibrated photodiode. For more sensitive detection, the beam is chopped, and a lock-in amplifier is used. For sub-micron waveguides, the high NA fiber is replaced with lensed fiber (Lase Optics, 1 μm spot diameter, 12-14 μm working distance) for improved coupling efficiency.

Horizontally polarized light was used to match the polarization of the guided TE mode. End-fire coupling was used, as it can provide reasonable efficiency $\sim 10 - 25\%$ per facet with less alignment complexity than techniques such as prism coupling. Additionally, unlike grating coupling, end-fire coupling requires no special design or fabrication to function over broad bandwidths, which is important when performing measurements of nonlinear properties using short-pulsed sources. Using the end-fire coupling method, coupling efficiencies of $\sim 10-25\%$ per facet were routinely achieved. This could be further improved with inverse tapers at the output facets, to expand the mode size and provide better overlap with the coupling fiber mode. For example, Almeida et al. demonstrated inverse tapers in silicon waveguides, showing coupling efficiencies up to $\sim 89\%$ (-0.5 dB loss) [230].

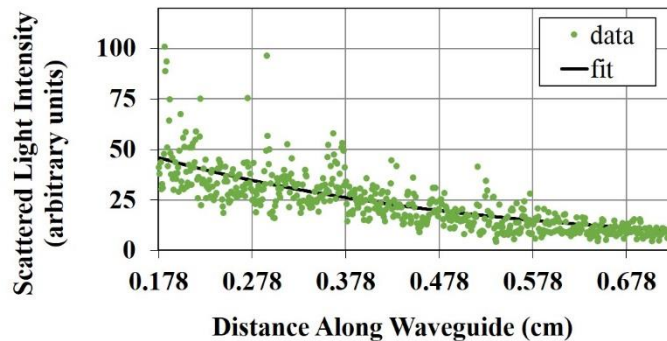


Figure 3.11. Ge-Sb-Se waveguide propagation loss at 1.03 μm . Plot of scattered light intensity vs. distance for a single-mode Ge-Sb-Se waveguide at a wavelength of 1.03 μm . A fit to a decaying exponential yields a total loss of $2.8 \pm 0.3 \text{ cm}^{-1}$, or 12.2 dB/cm, for the waveguide illustrated. An average total loss of 11.9 ± 1 dB/cm is obtained for measurements on six adjacent waveguides. Reprinted with permission from [56], Optical Society of America.

The linear loss of the Ge-Sb-Se waveguides was measured by coupling low power, cw light into a given waveguide, and recording the intensity of the light scattered above the waveguide surface as a function of distance along the waveguide using a CCD image sensor. The intensity of the scattered light is proportional to the intensity of the light remaining in the waveguide, and thus a fit of the scattered light intensity vs. distance curve to a decaying exponential will yield the

total loss. A linear loss measurement on one waveguide is shown in Fig. 3.11. Averaging over measurements on six adjacent waveguides, the linear loss was determined to be 11.9 ± 1 dB/cm. Scatter in the data comes primarily from imperfections (scatterers) in the sample itself, not noise on the camera. To improve the sensitivity and enable measurement of lower losses, longer samples with length $\geq 1/\alpha$ would be desired. Note that the loss measurement includes material absorption, as well as scattering loss from the surface and sides of the waveguide.

Since the fabricated thin films appear to have similar composition to the bulk glass, the material absorption of the waveguide core material is expected to be similar to that of the bulk glass, 0.27 cm^{-1} or 1.17 dB/cm. The under cladding SiO_2 material has negligible absorption at 1.03 μm . By simulating the electric field of the guided TE mode [141] and calculating the overlap integral of the field with the linear absorption using Equation 3.3, the loss in the waveguide from material absorption is estimated to be 0.15 dB/cm, leaving ~ 11.75 dB/cm of loss due to scattering. Note that the contribution of material loss to the total waveguide loss is low due to the weak $\sim 13\%$ confinement of the mode to the core material.

Due to the asymmetric waveguide geometry, the electric field of the guided mode is very weak near the sidewalls of the waveguide, but it is ~ 3 times stronger near the surface, as illustrated in Fig. 3.9(c). Additionally, the 2200 nm waveguide width provides ~ 49 times longer interaction surface than the 45-nm sidewall length. Thus, scattering loss due to surface roughness, rather than sidewall roughness, is expected to dominate. Approximating the waveguide as a slab waveguide and following the theory of Payne and Lacey [144], the scattering loss due to 0.8 nm surface roughness is expected to be on the order of 13 dB/cm, consistent with our measurements. (This calculation uses the half-waveguide thickness of 22.5 nm, core index of 2.718, average surrounding cladding index of 1.225, effective mode index of 1.4843, wavelength of 1030 nm, 0.8

nm RMS surface roughness, and assumes a correlation length of 50 nm.) For comparison to other work, etched high-contrast, chalcogenide-based embedded strip waveguides have been shown to have losses $\sim 10\text{-}15$ dB/cm [174]. Additionally, measurements made by Hu et al. at 1550 nm on single-mode thermally-evaporated chalcogenide waveguides with significantly smaller core aspect ratios suggest that lower losses on the order of 2-6 dB/cm for strip waveguides and < 0.5 dB/cm for rib waveguides are possible [88]. While our measured loss is reasonable for the given design, we expect the scattering loss of Ge-Sb-Se waveguides can be similarly reduced by optimizing the design of the strip waveguide cross section dimensions to decrease the field at the surface and thereby decrease scattering loss, or by using a rib waveguide design.

3.3.3 Nonlinear waveguide characterization at 1.0 μm

The nonlinear loss of Ge-Sb-Se waveguides was measured by coupling linearly polarized, 7 ps-long pulses from a Yb-doped fiber laser at a 37.4 MHz repetition rate into 6 mm-long waveguides and measuring the output intensity as a function of input intensity. To determine the coupling loss at the input and output waveguide facets, measurements were made launching light forwards through the waveguide, and then backwards, switching input and output fiber patch cord connectors while leaving the high numerical aperture coupling fibers fixed in position. Figure 3.12 shows the reciprocal transmission as a function of incident peak intensity. Since saturation became noticeable at intensities around 1 GW/cm^2 , data was fit to Eq. 3.30, replacing β_{wg} by β_{eff} with Eq. 3.31 and using β_{wg} , α , and I_{sat} as fitting parameters. Earlier independent measurements of α for the waveguides agreed with values from fits. An average of fits to three data sets yields $\beta_{wg}=11.5\pm 0.7 \text{ cm/GW}$ and $I_{sat}=4.3\pm 0.7 \text{ GW/cm}^2$ for the waveguides. The main sources of uncertainty are the measured output power and coupling efficiency.

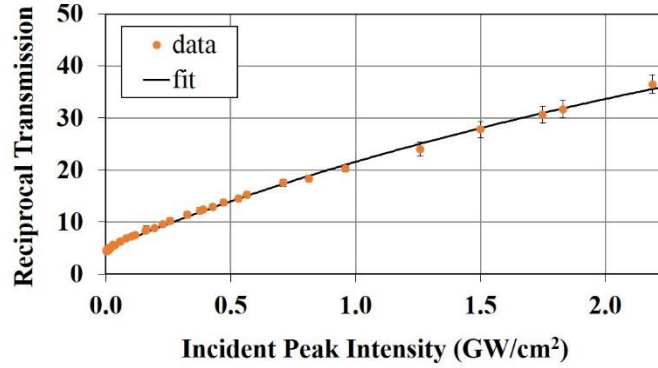


Figure 3.12. Nonlinear loss in Ge-Sb-Se waveguide at 1.03 μm . Plot of reciprocal transmission as a function of incident peak intensity for a single-mode Ge-Sb-Se waveguide. The average effective two-photon absorption coefficient of the waveguide is measured to be 11.5 ± 0.7 cm/GW. Reprinted with permission from [56], Optical Society of America.

Aside from saturation, one other suggested cause of the roll-off observed in the reciprocal transmission in Figure 3.12 is a change in pulse shape induced by strong nonlinear absorption, which has been discussed by J. J. Wathen et al. [175]. In particular, as a pulse propagates through a material with significant two-photon absorption, the peak will be preferentially absorbed relative to the weaker sides of the pulse, effectively broadening the pulse and reducing the peak intensity as the pulse travels. P. Apiratikul has derived this effect for pulses having intensity $I(t) = I_0 \text{sech}^2(t/t_0)$ [176], but for Gaussian pulses, this effect does not have an analytic solution. To check for this effect in our data, the time-average output power per area was numerically calculated with a temporal integral of the time-dependent intensity. Additionally, split-step code was used to iteratively account for changes in the output pulse width for a given two-photon absorption and intensity. We found that this model alone does not fit the shape of our data well.

The expected nonlinearity of the waveguide structure was calculated using Equation 3.33, using the value for β measured in bulk glass under similar 37.4 MHz repetition rate illumination conditions. The effect of linear (vs. circular) polarization was also taken into account with Equation 2.13. β_{wg} is expected to be 5.8 cm/GW, within a factor of 2 of our measured value. It

is important to note that small changes in composition of Ge-Sb-Se glasses have been shown to greatly affect the two-photon absorption coefficient near 1 μm , with β increasing with increasing Sb content [94]. Given the small but measurable differences in stoichiometry, shown in Fig. 3.9(a), the difference in β could be explained by the slight increase in Sb-content and decrease in Ge-content in our fabricated waveguides compared to the bulk.

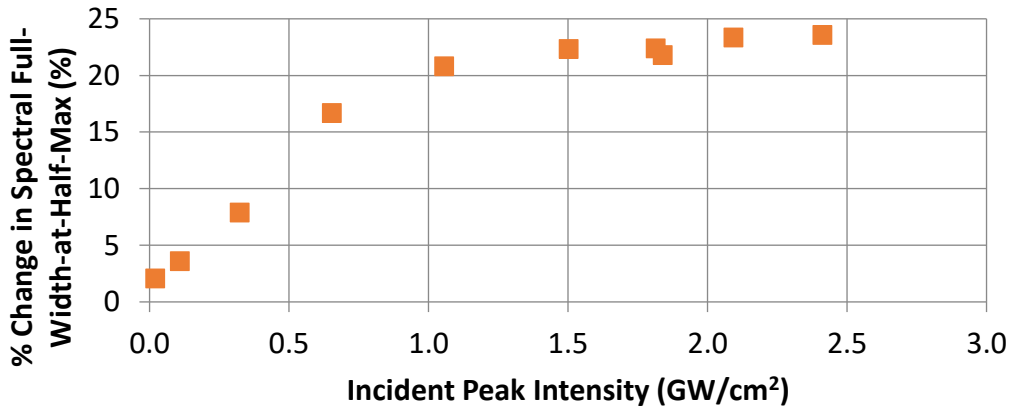


Figure 3.13. Spectral broadening in Ge-Sb-Se waveguide at 1.03 μm . Plot of percentage increase in measured spectral full-width-at-half-max (FWHM) as a function of incident coupled peak intensity, measured after propagation through 6 mm-long Ge-Sb-Se waveguide using 6.59 ps pulses at 37.4 MHz repetition rate at 1.03 μm .

The input and output spectra from our waveguides were also measured, revealing a very weak, power-dependent broadening of the spectral full-width at half-maximum (FWHM). A plot of the percent change in the full width half max of the spectra, as a function of incident intensity, is shown in Figure 3.13. Estimates of spectral broadening from split-step numerical solutions to the nonlinear Schrödinger equation, using the expected effective n_2 for the waveguide and measured β_{wg} with saturation, suggest the changes in FWHM are predominately due to β selectively decreasing the high-intensity peak of the pulses. This, coupled with the small magnitude of spectral changes, made accurate determination of n_2 for the waveguide difficult at this wavelength.

3.4 Waveguides at 1.55 μm

3.4.1 Motivation

Our first designs and measurements were performed at 1.03 μm to leverage existing equipment and provide characterization of Ge-Sb-Se waveguides at a relatively unexplored wavelength. However, Ge-Sb-Se glass is better suited for operation at telecom and mid-infrared wavelengths, where two-photon absorption becomes negligible [93]. Although bulk Ge-Sb-Se shows excellent nonlinearity at 1550 nm [93], to the best of our knowledge, no work had been reported characterizing or demonstrating the nonlinearity of Ge-Sb-Se waveguides in this regime. Studies on Ge-Sb-Se waveguides had characterized only linear optical properties and utilized relatively large mode areas $\geq 4 \mu\text{m}^2$ [177,178]. In our work, sub-micron Ge-Sb-Se waveguides are designed, and both the nonlinear and linear optical properties are characterized at 1.53-1.55 μm . The waveguides exhibit large nonlinearity and weak nonlinear absorption, showing potential for applications such as ultrafast optical switching at telecom wavelengths.

3.4.2 Waveguide design at 1.55 μm

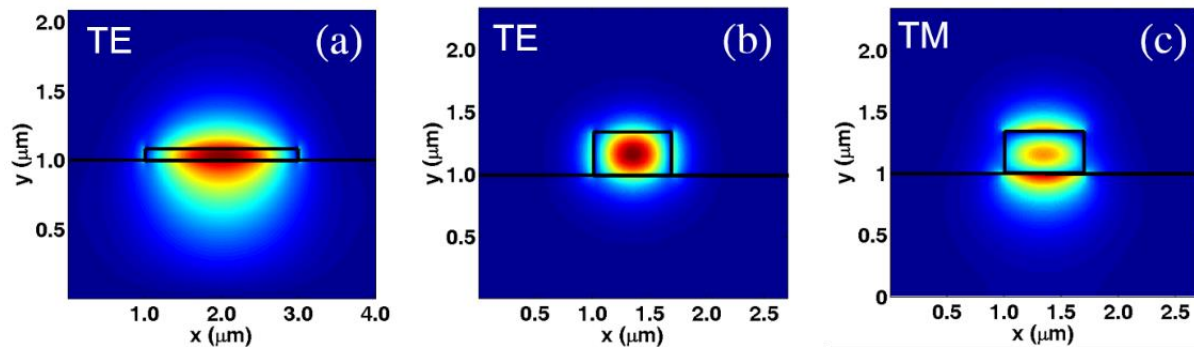


Figure 3.14. Mode profiles of Ge-Sb-Se waveguides at 1550 nm. Simulated TE and TM mode profiles, $|E_x|^2$ and $|E_y|^2$ respectively, for the a) 2000 nm by 90 nm and b) 700 nm by 340 nm Ge-Sb-Se strip waveguides [141]. The black solid outline indicates the x and y position and size of the Ge-Sb-Se core and lower SiO_2 substrate relative to the mode.

Strip, air-clad $\text{Ge}_{28}\text{Sb}_{12}\text{Se}_{60}$ waveguides on a SiO_2 substrate were designed. Two different cross-sections were chosen: (a) $2\ \mu\text{m}$ width (W) x $90\ \text{nm}$ height (H), and (b) $700\ \text{nm}$ (W) x $340\ \text{nm}$ (H). The $2\ \mu\text{m}$ x $90\ \text{nm}$ design supported a single TE mode and could be patterned with photolithography, a relatively inexpensive technique offering high throughput. This design supported one TE mode, as illustrated in Figure 3.14(a). The second design, featuring sub-micron dimensions, was chosen to provide anomalous dispersion for the TE mode through the waveguide geometrical contribution to dispersion. The improved control of dispersion enabled more spectral broadening for measurement of the nonlinearity in the waveguide, $n_{2,\text{wg}}$, at reasonable peak power levels \sim a few hundred W. Additionally, the reduced effective mode area A_{eff} [86] in the second design yielded a large nonlinear parameter, increasing local intensity for a given input power. As shown in Fig. 3.14(b-c) [141], at $1.55\ \mu\text{m}$, the $700\ \text{nm}$ x $340\ \text{nm}$ design supported one TE and one TM mode, which had A_{eff} of $0.2148\ \mu\text{m}^2$ and $0.3156\ \mu\text{m}^2$, respectively. Furthermore, these dimensions allowed for tight bend radii of $\sim 3\ \mu\text{m}$ with negligible calculated radiation loss and anomalous dispersion of $-0.556\ \text{ps}^2/\text{m}$ (TE mode).

Dispersion is calculated using a mode solver to calculate the effective index at nearby wavelengths, including the effect of material dispersion on the substrate, core, and cladding indices, and using finite-difference formula to calculate the desired derivatives. Code for using a mode solver to calculate various waveguide mode properties is included in Appendix C. While the dispersion depends on exact waveguide dimensions [See Fig. 3.15(a)], using fabrication tolerances of $\pm 10\ \text{nm}$ for waveguide heights and $\pm 40\ \text{nm}$ for waveguide widths, the targeted dispersion is expected to be within $\pm 0.18\ \text{ps}^2/\text{m}$.

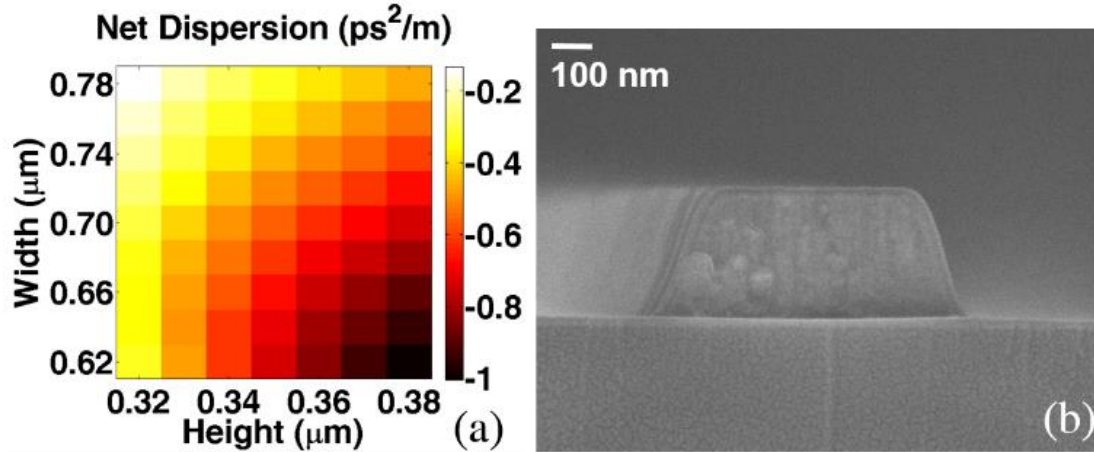


Figure 3.15. Dispersion and SEM of Ge-Sb-Se waveguide at 1550 nm. (a) Simulated net dispersion (in ps^2/m) at 1550 nm for the TE mode of strip, air-clad $\text{Ge}_{28}\text{Sb}_{12}\text{Se}_{60}$ waveguides on a SiO_2 substrate for various core dimensions. (b) Scanning electron micrograph of a strip waveguide cross section, consisting of a Si substrate (not pictured), a 3- μm -thick SiO_2 layer, a 700 nm x 340 nm Ge-Sb-Se layer, and an air upper cladding. Figure reproduced with permission from [140], copyright IEEE 2016.

3.4.3 Waveguide fabrication at 1.55 μm

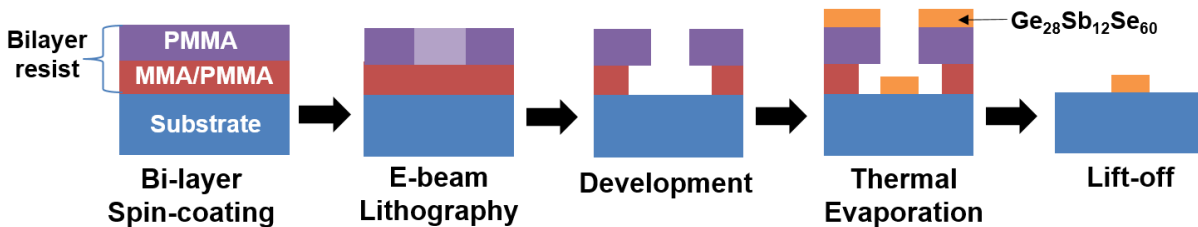


Figure 3.16 Schematic illustrating sub-micron waveguide fabrication flow. A bilayer resist consisting of PMMA and MMA/PMMA is spun onto a substrate. Following e-beam lithography and development, Ge-Sb-Se is thermally evaporated, and lift-off is used to remove the resist and produce strip waveguides 700 nm (W) by 340 nm (H).

To fabricate waveguides, a resist pattern is first formed on a substrate, consisting of a 3 μm -thick oxide layer on top of a Si wafer. $\text{Ge}_{28}\text{Sb}_{12}\text{Se}_{60}$ is then thermally evaporated onto the patterned wafer, and lift-off is used to produce strip Ge-Sb-Se waveguides. Conventional photolithography was used to pattern the wider 2 μm x 90 nm waveguides (See Figure 3.8). Sub-micron waveguides were patterned with e-beam lithography (See Figure 3.16), which offered

improved resolutions of ~10 nm and reduced sidewall roughness, compared with photolithography. To further improve the lift-off process for thicker films, a bilayer resist composed of PMMA and PMMA-MMA copolymer was used [179,180]. Due to the difference in molecular weight, more of the underlying PMMA-MMA layer is removed than the PMMA overlayer, creating a slight overhang desired for subsequent lift-off. The fabrication process flow with e-beam lithography is shown in Fig. 3.16. E-beam lithography was performed by Richard Bojko at the Washington Nanofabrication Facility, using the JEOL JBX-6300FS Electron Beam Lithography System, with e-beam current of 8 nA and writing grid size of 8 nm.

3.4.4 Linear waveguide characterization at 1.55 μm

To measure the bandedge of thin films, transmission measurements were performed by Dr. Sungmo Ahn on a 4.35 μm -thick, thermally evaporated Ge-Sb-Se thin film using a spectrophotometer. Data and corresponding fits for bulk Ge-Sb-Se and the thin film are shown in Figure 3.17. For materials lacking a sharp absorption edge, the point at which the absorption changes from a quadratic dependence on energy to an exponential dependence (Urbach tail region [181]) can be defined as the bandedge [65]. In the Urbach region, the absorption α can be fit to

$$\alpha(h\nu) = \alpha_0 \exp\left[\frac{(h\nu - E_g)}{E_u}\right], \quad (3.36)$$

where ν is the frequency, E_g is the energy gap, $h\nu$ is the energy of the incident photons, and E_u is a measure of the slope of the absorption edge [182]. Here, one can define the optical bandgap as the point at which the [65].

It can also be useful to fit to the strong absorption, or Tauc regime, where the absorption depends quadratically on energy, such that

$$\alpha(h\nu) \propto \frac{(h\nu - E_g)^2}{h\nu}, \quad (3.37)$$

where E_g is the energy gap and $h\nu$ is the energy of the incident photons. To determine the band edge in the strong absorption regime, one can fit to Equation 3.37, and extrapolate where the $\alpha(h\nu) = 0 \text{ cm}^{-1}$.

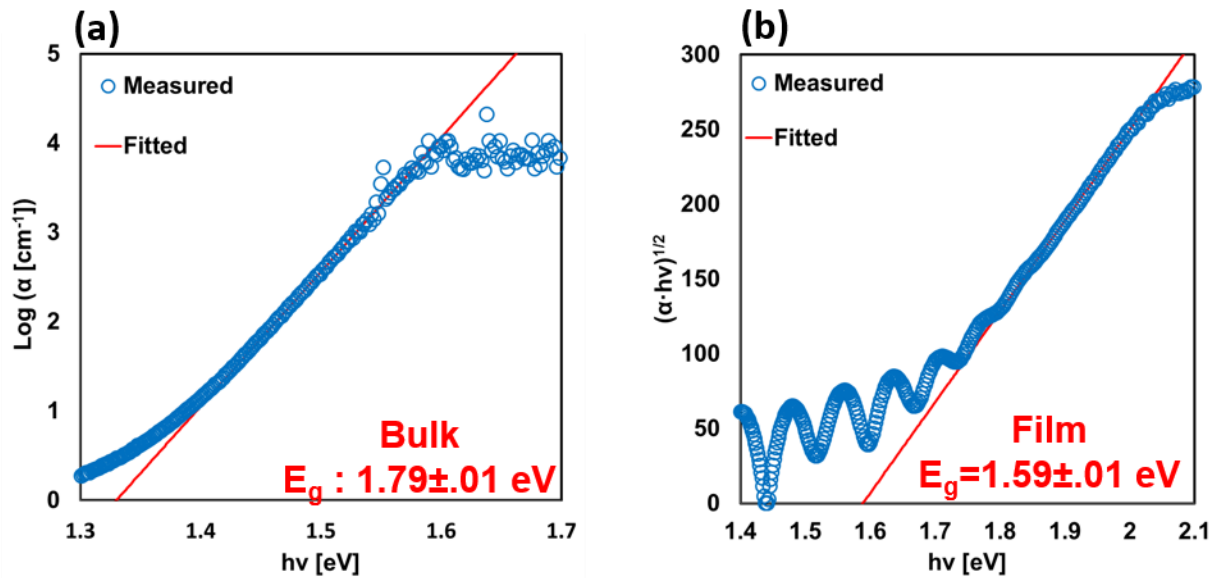


Figure 3.17 Band edge measurements of bulk and thin-film Ge-Sb-Se. a) Bulk band edge of $\text{Ge}_{28}\text{Sb}_{12}\text{Se}_{60}$ fit to be $1.79 \pm 0.01 \text{ eV}$, fitting to Urbach tail. b) Tauc band edge of Ge-Sb-Se thin film determined to be $1.59 \pm 0.01 \text{ eV}$ from fit to strong absorption (Tauc) regime.

As noted, two regimes are commonly used to extract a value for the band edge: the Urbach regime, and the strong absorption, or Tauc, regime. For data on the bulk material, the strong absorption region was severely limited by detector sensitivity and could not be accurately fit. As a result, the bulk material transmission data was fitted to the Urbach region, shown in Figure 3.17(a). The bulk Urbach band edge of $1.79 \pm 0.01 \text{ eV}$ is in good agreement with the 1.8 eV Urbach band edge from literature [65]. For the thin Ge-Sb-Se film, the Urbach region was obscured by strong interference fringes, so the thin film data could only be accurately fit to the high absorption

region, yielding a Tauc bandedge of 1.59 ± 0.01 eV. The measured value on the thin film is close to the 1.62 eV Tauc bandedge of bulk $\text{Ge}_{28}\text{Sb}_{12}\text{Se}_{60}$ reported in literature [108]. Energy Dispersive X-ray Spectroscopy measurements on thin Ge-Sb-Se films confirmed that the stoichiometry of the fabricated thin films is within 4 atomic % of the bulk material [56].

A scanning electron micrograph (SEM) of a fabricated waveguide is shown in Fig. 3.15(b). Using SEM images of the waveguide edges, the RMS sidewall roughness was ~ 12 nm and 4 nm for the waveguides fabricated with photo- and e-beam lithography, respectively [140]. The top RMS surface roughness was measured to be 0.8 nm using atomic force microscopy (AFM).

To characterize propagation loss, light at a wavelength of $1.53 \mu\text{m}$ was coupled into and out of the Ge-Sb-Se waveguides using high numerical aperture (Nufern UHNA3, $\text{NA}=0.35$) fibers or tapered fibers (Lase Optics, $1 \mu\text{m}$ spot diameter, 12-14 μm working distance) mounted on piezo-actuated three-axis stages for precise alignment, as illustrated in Fig. 3.10. Fibers were chosen to provide the best mode overlap and coupling efficiency for the given waveguide designs. Linearly polarized light was used to match the polarization of the desired guided mode. Using low, 1-2 mW coupled cw power, the intensity of the light scattered above the waveguide surface was measured as a function of distance along the waveguide using a cooled InGaAs detector array. The resulting data was fit to a decaying exponential to determine the total loss. To account for the background noise of the InGaAs camera, measurements without the laser were subtracted from those with the laser. Note that this background is roughly constant, around 6% of the maximum signal level before subtraction, and that the scatter in the data is predominately from imperfections (scatterers) in the waveguide sample itself. Data from the first ~ 3 mm of the waveguide near the input facet was excluded from fitting, due to non-negligible background from uncoupled light from the input fiber. The InGaAs camera was confirmed to respond linearly for the experimental settings.

Background light from slab-guided light was verified to be negligible, by slightly misaligning the input fiber and confirming that no visible signal on the camera was produced.

Loss measurements were made on 3-5 adjacent waveguides for each mode, and then averaged to obtain the loss, as summarized in Table 3.1 [140]. Given the low material absorption of $\text{Ge}_{28}\text{Sb}_{12}\text{Se}_{60}$ and SiO_2 , propagation loss is dominated by scattering loss. The measured linear loss in our Ge-Sb-Se waveguides is comparable to loss measured in other chalcogenide ($\text{Ge}_{23}\text{Sb}_7\text{S}_{70}$) strip waveguides of similar dimensions [88]. Although strip waveguides have higher loss than rib designs (typically by \sim one order of magnitude), the strip geometry enables broader dispersion engineering and significantly reduced bend radii for resonator-enhanced nonlinear photonics.

Table 3.1 Average Loss for Ge-Sb-Se Waveguides at 1.53 μm [140]

<i>Fabrication method</i>	<i>Fabrication parameters</i>	<i>Waveguide dimensions</i>	<i>Average TM loss (dB/cm)</i>	<i>Average TE loss (dB/cm)</i>
Photo-lithography	NA	2000 nm x 90 nm	no TM mode	4.0 \pm 0.9
E-beam lithography	8 nA current, 8 nm grid	700 nm x 340 nm	5.6 \pm 1.0	6.1 \pm 0.8

3.4.5 Nonlinear waveguide characterization at 1.55 μm

To measure the nonlinear properties of waveguides, a mode-locked Er-doped fiber laser was constructed. A schematic of the home-built laser, based on the designs by H. Liu et al. [183] and B. Oktem et al. [184], is shown in Figure 3.18. The laser operates at a center wavelength \sim 1555 nm and provides an average power \sim 15-20 mW (measured at the polarizing beam splitter output). A typical autocorrelation trace and spectrum of the laser are shown in Figure 3.19. The laser produces \sim 170 fs pulses (measured after compression with external grating pair) at a 17.8 MHz repetition rate.

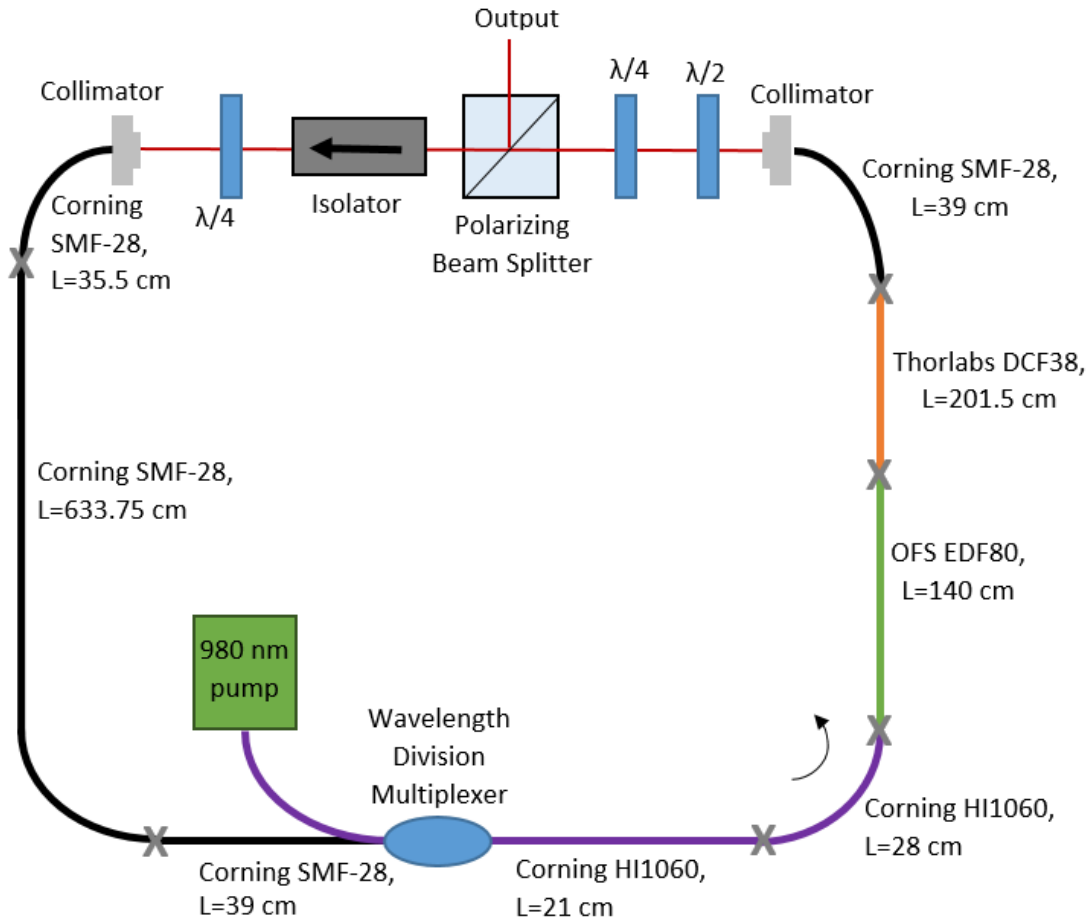


Figure 3.18. Er-doped fiber laser schematic. The mode-locked Er-doped fiber laser operates ~ 1555 nm with a slightly normal net cavity dispersion of $\sim +0.0136$ ps². The laser design is based on designs by H. Liu et al. [183] and B. Oktem et al. [184].

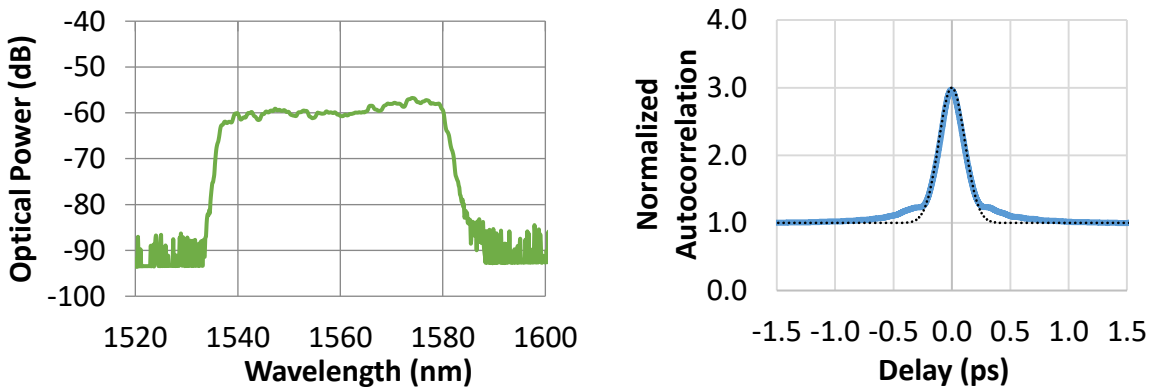


Figure 3.19. Er-doped fiber laser optical spectrum and intensity autocorrelation. Optical spectrum (left) reveals full-width-at-half-maximum (FWHM) spectral width of ~ 15 nm, and -30 dB width of ~ 52 nm. Autocorrelation (right) compares data (blue line) to fit (dotted black line), with FWHM pulse duration of 170 fs.

As noted in Section 3.2.6, the loss in a waveguide due to both linear absorption and two-photon absorption is given by Equation 3.30. The nonlinear loss of 700 nm x 340 nm Ge-Sb-Se waveguides was determined by measuring the output intensity as a function of input intensity. Vertically-polarized (P-polarized), 170 fs-long pulses from an Er-doped fiber laser at a 17.8 MHz repetition rate were coupled into the TM mode of 10 mm-long waveguides. To verify the coupling loss, measurements were made launching light forwards through the waveguide, and then backwards, switching fiber patch cord connectors while leaving the lensed coupling fibers fixed in position. Waveguides were illuminated with peak intensity up to 65 GW/cm² over 10 minutes. Data taken with increasing and decreasing power agreed and was repeatable.

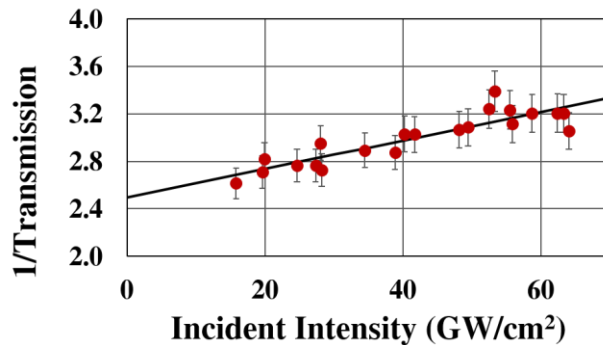


Figure 3.20. Nonlinear absorption in Ge-Sb-Se waveguides at 1550 nm. Plot of reciprocal transmission as a function of incident peak intensity for the TM mode of the 700 nm by 340 nm Ge-Sb-Se waveguide. The average effective two-photon absorption coefficient is 0.0055 ± 0.0004 cm/GW [231].

Figure 3.20 shows the reciprocal transmission vs. incident peak intensity. The data is linear, showing no saturation effects, as one would expect, considering the weak linear and nonlinear absorption at this wavelength. Additionally, given the extremely low two-photon absorption, no roll-off due to nonlinear-absorption-driven pulse broadening is observed. An average of fits to three data sets yields $\beta_{wg}=0.0055\pm0.0004$ cm/GW for the TM mode of the waveguides [231]. The main sources of error are the uncertainty in pulse shape and coupling efficiency, leading to uncertainty in the coupled peak power. The measured value for β is in line

with values measured for bulk Ge-Sb-Se near 1550 nm, which from negligible values to 0.04-0.2 cm/GW, depending on exact composition [65,93-95]. Theory by Lenz et al. can be used to predict the expected two-photon absorption, using the material's bandedge, wavelength, and the field of the guided mode [65]. However, this calculation is exquisitely sensitive to bandedge position relative to the measurement wavelength. For example, a shift in bandedge from 1.59 eV to 1.62 eV results in predicted β of 0.015 to 0 cm/GW at 1555 nm. The measured β is found to be within the range predicted by theory, taking into account this uncertainty.

The input and output spectra from the 700 nm x 340 nm Ge-Sb-Se waveguides were also measured, revealing a power-dependent broadening of the output spectral width. 170 fs-long pulses at a 17.8 MHz repetition rate were coupled into the waveguide. Using coupled input peak powers ranging from 60-140 W, the corresponding -30 dB spectral width increased by ~26% to 200% from the input spectral width.

To analyze our experimental results, simulations using the symmetrized split-step Fourier method [142] were employed to solve the scalar nonlinear Schrödinger equation, which included the effects of group velocity dispersion, higher order dispersion, linear and two-photon absorption, and self-phase modulation. A complete description of the split step method is in Section 3.2.7. The initial electric field amplitude and phase were determined with the PICASO phase retrieval algorithm, with experimental data of the spectrum and interferometric autocorrelation [143]. The PICASO phase retrieval method iteratively guesses the electric field amplitude and phase that best fits experimental data. The algorithm begins with an initial guess of the complex field spectrum, including the spectral phase. The routine computes an inverse Fourier transform to calculate the field in the time domain. The corresponding interferometric autocorrelation and RMS deviation from the experimental data are calculated. The program generates a new guess for the spectral

phase, and after thousands of iterations, can retrieve the spectral phase [143]. While other techniques such as frequency-resolved optical gating (FROG) or spectral phase interferometry for direct electric-field reconstruction (SPIDER) also exist to characterize short pulses [143], the PICASO algorithm offers the advantages of a relatively simple, inexpensive set up. One main challenge of using the PICASO algorithm includes being able to resolve interferometric autocorrelations well enough for relatively longer ps pulses

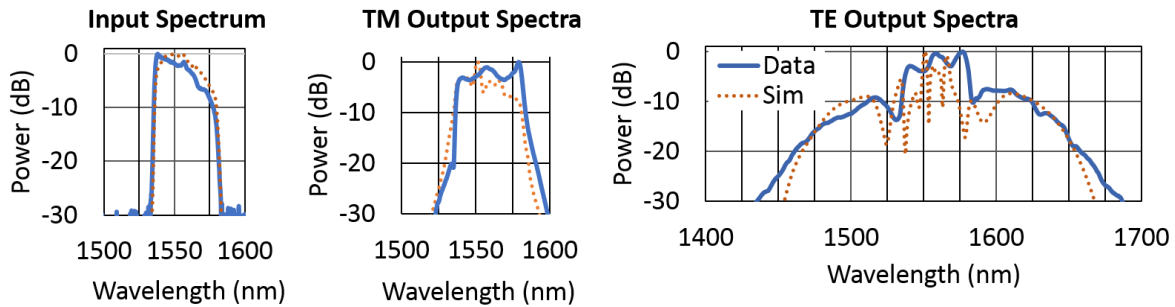


Figure 3.21. Spectral broadening experiment and simulation for Ge-Sb-Se waveguides. Comparison of experimental data (solid blue line) and simulation (dashed orange line) of input and output spectra of the 10 mm-long, 700 nm by 340 nm Ge-Sb-Se waveguide, using coupled peak power of 87 W and 109 W for the TM and TE mode, respectively. The TE mode produces significantly more broadening than the TM mode due to its relatively low, anomalous dispersion of $-0.556 \text{ ps}^2/\text{m}$ (vs. $6.23 \text{ ps}^2/\text{m}$ for TM). Reproduced from [231].

To determine $n_{2,\text{wg}}$ from the broadened spectra, experimental spectra were compared to simulations. Measured parameters corresponding to the experimental setup, including α , β_{wg} , L_{wg} , A_{eff} , the coupling efficiency, the input field, and the dispersion (up to 4th order) were fixed in the simulations, and $n_{2,\text{wg}}$ was used as a free parameter to find a best fit to the experimentally measured spectral widths. A set of input and output spectra, along with corresponding simulation results, are shown in Fig. 3.21 [231]. While the simulations do not capture all the fine spectral features, they reproduce the general spectral shapes well. From measurements on the TM mode taken at various coupled peak power levels from 60-140 W, the average $n_{2,\text{wg}}$ was found to be

$4.4 \pm 1.4 \times 10^{-19} \text{ m}^2/\text{W}$. This corresponds to a nonlinear parameter, γ of $5.6 \pm 1.7 \text{ W}^{-1}\text{m}^{-1}$ ($\sim 4500 \times \gamma$ of single-mode SiO_2 fiber) and a figure of merit, $FOM = (n_{2,\text{wg}} / \beta_{\text{wg}} \lambda)$ of 5.2 ± 1.6 . The main sources of error in $n_{2,\text{wg}}$ are due to uncertainty in the initial pulse shape and temporal phase.

The measurements of the waveguide nonlinearity are not time-resolved. Low throughput from the waveguides, primarily due to coupling loss, limits us from performing a pump-probe experiment with significantly weaker probe beam to study the time constant of the nonlinear response. These measurements are performed at wavelengths far from the bandedge, where both linear and two-photon absorption are weak. This makes photosensitivity-induced changes less likely, though still possible, given observation of defect absorption-driven photosensitivity in other chalcogenides [185]. Note that the measurements of the transmission were stable and reproducible, indicating the Ge-Sb-Se waveguides are photostable under these conditions. Furthermore, no degradation of waveguide samples has been observed for over two years.

The waveguide FOM is the same order-of-magnitude as values measured on bulk samples of Ge-Sb-Se with slightly different composition, typically $\sim 1-8$ at 1550 nm [65,93-95]. However, our values for $n_{2,\text{wg}}$ are roughly an order of magnitude lower than what is typically measured on bulk Ge-Sb-Se of similar composition [65,93-95]. Additionally, the predicted n_2 of $8.22 \times 10^{-18} \text{ m}^2/\text{W}$ for the material, calculated from Miller's rule [65] using the linear refractive index of 2.66, is $\sim 16 \times$ larger than that measured in our waveguides, after accounting for a $0.867 \times$ enhancement factor from waveguide geometry for the TM mode [154]. While studies have shown that variations in composition can lead to changes in n_2 by $\sim 2-3 \times$ [93,95], this cannot fully explain the large difference observed between bulk and waveguide. Some laser-written chalcogenide waveguides have been shown to exhibit significantly lower n_2 than bulk [186], but reports of

As₂S₃ and Ge-As-Se chalcogenide waveguides fabricated with lithography and etching show n_2 similar to bulk [163,187].

Nonlinear optical measurements were also performed with the TE mode of 2 μm x 90 nm Ge-Sb-Se waveguides. These waveguides had A_{eff} of 0.9241 μm^2 , group velocity dispersion of 3.42 ps²/m, and a 1.12x enhancement factor of n_2 from waveguide geometry [154]. Intensity-dependent transmission measurements revealed an average β_{wg} of 0.012 \pm 0.002 cm/GW. Similarly, spectral broadening measurements indicated an average $n_{2,\text{wg}}$ of 7.9 \pm 2.5 $\times 10^{-19}$ m²/W, corresponding to FOM of 4.2 \pm 1.3. These values for the waveguides made using photolithography are the same order-of-magnitude as those for the waveguides fabricated using e-beam lithography (average $n_{2,\text{wg}}$ of 4.4 \pm 1.4 $\times 10^{-19}$ m²/W and FOM of 5.2 \pm 1.6). This suggests that the writing process alone is not the main cause of the nonlinearity discrepancy between bulk and waveguides. The two samples, in addition to having different patterning methods (photo- vs. e-beam lithography) are also from two different chalcogenide evaporations. This indicates the low nonlinearity compared to bulk is a relatively consistent issue. Additional study is required to better understand the source of our observed difference between waveguide and bulk. We are aware that this issue is a challenge for the broader chalcogenide community, probably not limited to our chosen material.

Ellipsometry measurements have revealed a small difference in linear index between bulk and film, and we are exploring annealing as a potential way to improve the nonlinearity of films. In particular, during thermal evaporation, the non-equilibrium conditions under which thin films are formed can cause both structural disorder and defective bonds, which alter thin film properties [188]. Additionally, chalcogenide and silica have a thermal expansion mismatch [153,189],

leading to thermal stress which can also produce changes in refractive index [232]. Annealing can be used to relax stresses and reduce defects, bringing thin film properties closer to those of bulk in various chalcogenides [188,190-191]. In spite of the lower nonlinearity currently observed in the waveguides, the measured *FOM* suggests that Ge-Sb-Se still holds promise as a nonlinear integrated optics platform at telecom wavelengths and beyond.

3.5 Waveguides at 3.5 μm

Initial Ge-Sb-Se waveguide demonstrations in the near-infrared successfully leveraged existing equipment, but most interest in chalcogenide glasses stems from their excellent transparency and nonlinearity in the mid-infrared, where other optical materials are lacking. To further explore Ge-Sb-Se in the mid-infrared, we have designed waveguides at 3.5 μm . Single-mode chalcogenide waveguides were designed for operation at 3.5 μm , taking into account dispersion, mode area, and effective nonlinearity. A range of substrate materials were considered. ZnSe, ZnS, and Al₂O₃ (sapphire) were all found to be unsuitable due to the limited achievable dispersion ranges, given the reduced index contrast. However, the stronger index contrast provided by MgF₂ substrates yielded a wider range of waveguide geometry dispersion, sufficient for our designs.

A schematic of a waveguide and the corresponding dispersion plot is shown in Figure 3.22. For straight, air-clad Ge-Sb-Se strip waveguides on MgF₂ substrates, cross-sectional dimensions of 1.44 μm (W) x 580 nm (H) provide a single TE and TM mode. The TE mode has near zero, -0.0687 ps²/m net dispersion, small effective area of 1.03 μm^2 , and an expected nonlinear parameter of $\sim 9.35/W\text{-m}$, using the definitions in Equations 3.17-3.19. For the calculation of the nonlinear parameter, a nonlinear refractive index in bulk of 4.2×10^{-18} m²/W is assumed (roughly

0.45 times the bulk nonlinearity at 1550 nm), using the prediction from Lenz et al. [65] for $\text{Ge}_{28}\text{Sb}_{12}\text{Se}_{60}$ at a wavelength of 3.5 μm .

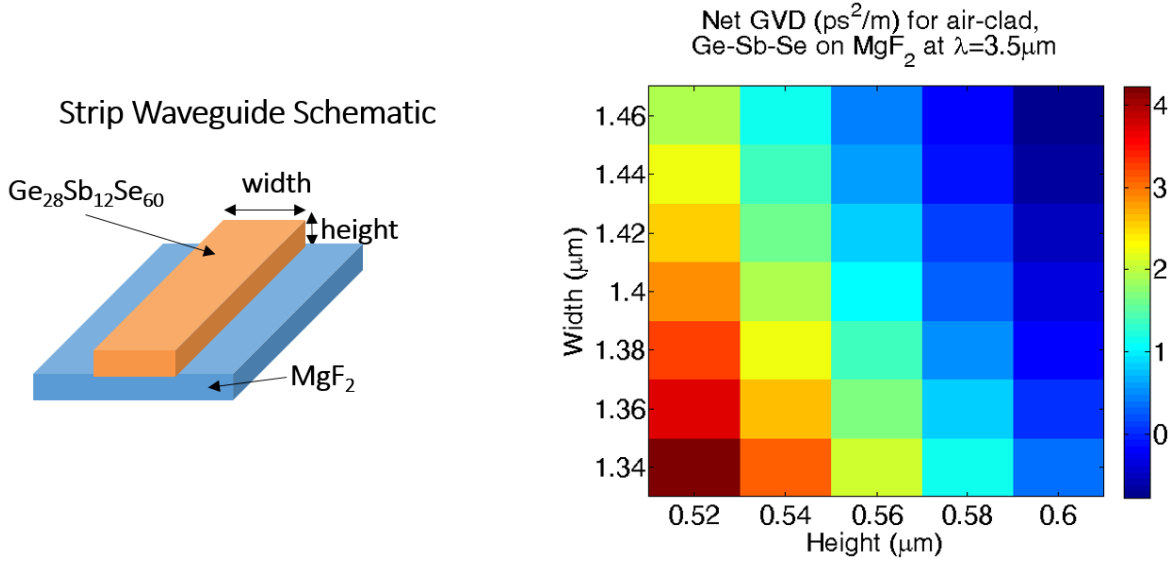


Figure 3.22. Strip waveguide schematic and simulated dispersion at 3.5 μm . Left: Schematic of Ge-Sb-Se waveguide. Right: Plot of dispersion (in ps^2/m) as a function of straight waveguide height and width. Near-zero, slightly anomalous dispersion (deep blue) is achieved for cross section of 1.44 μm (w) x 580 nm (h) for a straight waveguide.

3.6 Conclusion

Ge-Sb-Se waveguides were designed, fabricated, and characterized over a range of wavelengths, from 1.03 to 3.5 μm . At 1.03 μm , Ge-Sb-Se waveguides, fabricated by photolithography and lift-off, had an average linear propagation loss of 11.9 dB/cm in agreement with theory, and a large two-photon absorption coefficient of $\beta_{\text{wg}}=11.5\pm0.7$ cm/GW.

As expected, the linear loss and nonlinear optical properties of Ge-Sb-Se waveguides improved greatly at telecom wavelengths of 1.53-1.55 μm . Ge-Sb-Se waveguides, fabricated by photolithography and lift-off, had an average linear loss of 4.0 dB/cm at 1.53 μm . Additionally, the average linear loss for 700 nm (W) by 340 nm (H) waveguides, fabricated by e-beam

lithography, was 5.6 ± 1.0 for the TM mode, and 6.1 ± 0.8 dB/cm for the TE mode. The nonlinear loss of the waveguides fabricated with e-beam lithography was 0.0055 ± 0.0004 cm/GW, reasonable considering other Ge-Sb-Se bulk measurements in literature. Corresponding spectral broadening measurements revealed a nonlinear figure of merit of 5.2 ± 1.6 and a nonlinear parameter of 5.6 ± 1.7 $W^{-1}m^{-1}$, indicating preliminary promise for nonlinear applications such as ultrafast switching at telecom wavelengths. Finally, single-mode Ge-Sb-Se waveguides were designed for operation at $3.5\ \mu m$, with near-zero dispersion for improved spectral broadening.

4. GE-SB-SE RING RESONATORS

4.1. Overview

Chalcogenide ring resonators are designed, with dimensions optimized for four-wave mixing at wavelengths of 1.55 and 3.5 μm . In Section 4.2, background on ring resonators for nonlinear optics is provided. Specifically, the motivation for exploring ring resonators is discussed, and concepts useful for design are described, including basic ring resonator properties, four-wave mixing, resonant enhancement, and bus waveguide-to-ring coupling. Section 4.3 describes the design process and final Ge-Sb-Se ring resonator designs, optimized for four-wave mixing at wavelengths of 1.55 and 3.5 μm . Additionally, this section provides basic characterization of first-generation ring resonators at 1.55 μm .

This work was performed in collaboration with Professor Wounjhang Park, Dr. Gumin Kang, and Michael Grayson at the University of Colorado Boulder. In particular, Dr. Gumin Kang and Michael Grayson provided fabrication process development, fabricated the ring resonators, and provided SEM images. For all devices described in this chapter, e-beam lithography was performed by Kevin Roberts and Dr. Greg Cibuzar at the Minnesota Nano Center at the University of Minnesota.

We benefited from technical discussions with Professor Milos Popovic, YangYang Liu, and Cale Gentry at the University of Colorado Boulder. A waveguide mode solver from Professor Milos Popovic was used to simulate guided waveguide modes [141].

This work was supported in part by NSF Grant EECS-1232077, in part by AFOSR under Grant FA9550-15-1-0506, in part by the DARPA SCOUT Program through ARO under Contract W911NF-15-1-0621, and in part by the Department of Defense through the National Defense Science and Engineering Graduate (NDSEG) Fellowship Program. Additionally, equipment funding was provided in part by the Defense University Instrumentation Program (DURIP) Award ONR N00014-16-1-2544.

4.2 Ring resonators for nonlinear optics

4.2.1 Ring resonator motivation and applications

A ring resonator consists of a waveguide wrapped around on itself to form a circle, along with a mechanism to couple light to the structure, as illustrated in Figure 1.4. Given their ability to trap light in small volumes, ring resonators have been used for intriguing applications in a broad range of fields [52]. For example, they have served as important building blocks for optical signal processing [192], including wavelength-selective filters [193] and modulators [194]. Ring resonators have also found use in biology for biosensing applications such as protein detection [195] and as refractometric sensors for lab-on-chip development [196]. Finally, ring resonators have provided compact platforms for novel sources, including quantum-correlated photon pair sources [197], Raman lasers [198], Brillouin lasers [199], and optical frequency combs [9].

Achieving high quality factor, Q , in micron-scale ring resonators can be a challenge, given loss resulting from standard fabrication processes. To date, state-of-the-art ring resonators exhibit Q s from 3×10^6 for μm -scale radii [50,51], to Q s of 8×10^7 for mm-scale radii [49]. However, compared to other microresonator geometries shown in Figure 1.4, ring resonators offer three key advantages. Ring resonators can be easily integrated, they can be designed to eliminate higher

order modes, and their geometry offers simple changes to better control the dispersion through waveguide geometry. These features make ring resonators a promising platform for robust, chip-scale nonlinear photonics. Ring resonators have been demonstrated in many materials, including silicon [200], silicon nitride [46], doped silica [201], gallium arsenide [202], and chalcogenide glasses such as Ge-As-Se [203] and As₂Se₃ [204]. To push development of ring resonator-enhanced nonlinear optics in the near- and mid-infrared, this research explores Ge₂₈Sb₁₂Se₆₀-based ring resonators. In addition to the excellent nonlinear material properties and broad transparency found in chalcogenide glasses, Ge₂₈Sb₁₂Se₆₀ is arsenic free and commercially available.

Chalcogenide-based ring resonators are designed with dimensions optimized for cavity-enhanced four-wave mixing efficiency. First-generation ring resonators are fabricated and quality factors are characterized.

4.2.2 Ring resonator properties

Two common ring resonator and bus waveguide geometries, including the all-pass and add-drop ring resonators, are illustrated schematically in Figure 4.1. In general, resonance is achieved when the round trip accumulated phase is an integer multiple of 2π , such that the circulating waves constructively interfere. This occurs when an integer m number of wavelengths match the cavity length L , such that

$$\lambda_{res} = \frac{n_{eff}(\lambda)L}{m}, \quad (4.1)$$

where $n_{eff}(\lambda)$ is the effective index of the ring resonator, which depends on the wavelength λ .

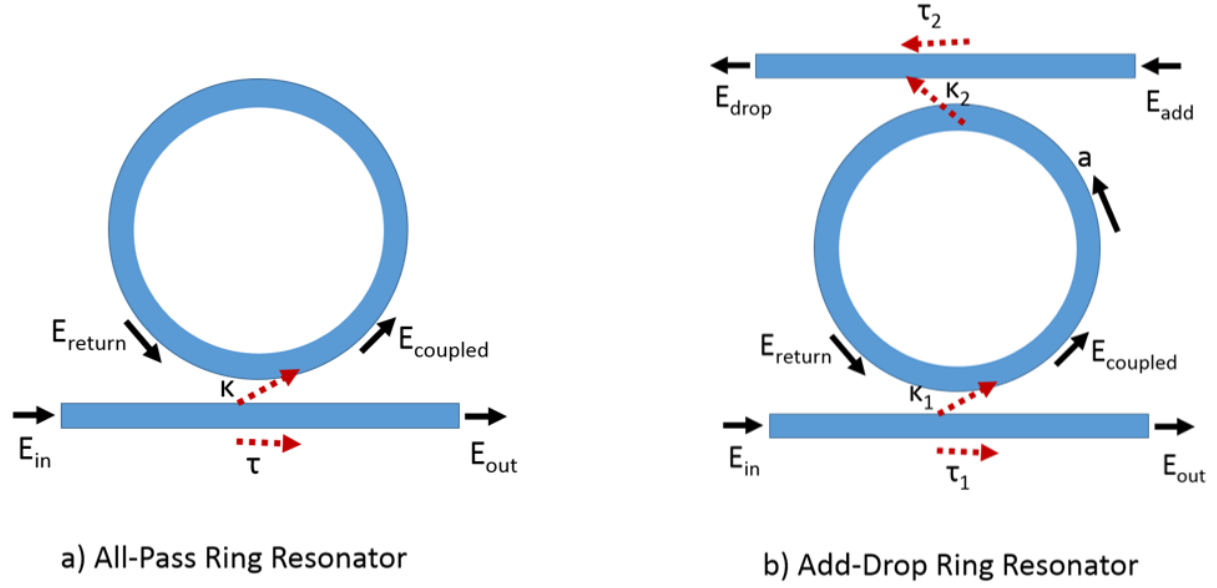


Figure 4.1. Schematic of all-pass ring resonator and add-drop ring resonator. (a) An all-pass ring resonator consists of a single bus waveguide and ring resonator. E_{in} is the input field, E_{out} is the output field, E_{return} is the return field, $E_{coupled}$ is the coupled field, κ is the cross-coupling coefficient, τ is the self-coupling coefficient, and a is the power attenuation coefficient. (b) An add-drop ring resonator consists of a ring resonator with two coupled bus waveguides. Here, E_{add} is the added field, and E_{drop} is the dropped field. Both the input and output bus waveguides have cross-coupling coefficients κ_1 and κ_2 , as well as cross-coupling coefficients τ_1 and τ_2 .

At the coupling point between the bus waveguide and ring resonator, one can use scattering matrix formalism [208] to write the relationship between the input, output, and circulating fields, as illustrated in Figure 4.1(a), as

$$\begin{pmatrix} E_{coupled}(\omega) \\ E_{out}(\omega) \end{pmatrix} = \begin{pmatrix} \tau & -i\kappa \\ -i\kappa & \tau \end{pmatrix} \begin{pmatrix} E_{return}(\omega) \\ E_{in}(\omega) \end{pmatrix}, \quad (4.2)$$

where τ and κ are the self- and cross-coupling coefficients, which satisfy the relation $|\tau|^2 + |\kappa|^2 = 1$. Here, E_{in} is the input field, E_{out} is the output field, E_{return} is the return field, and $E_{coupled}$ is the coupled field [See Figure 4.1(a)].

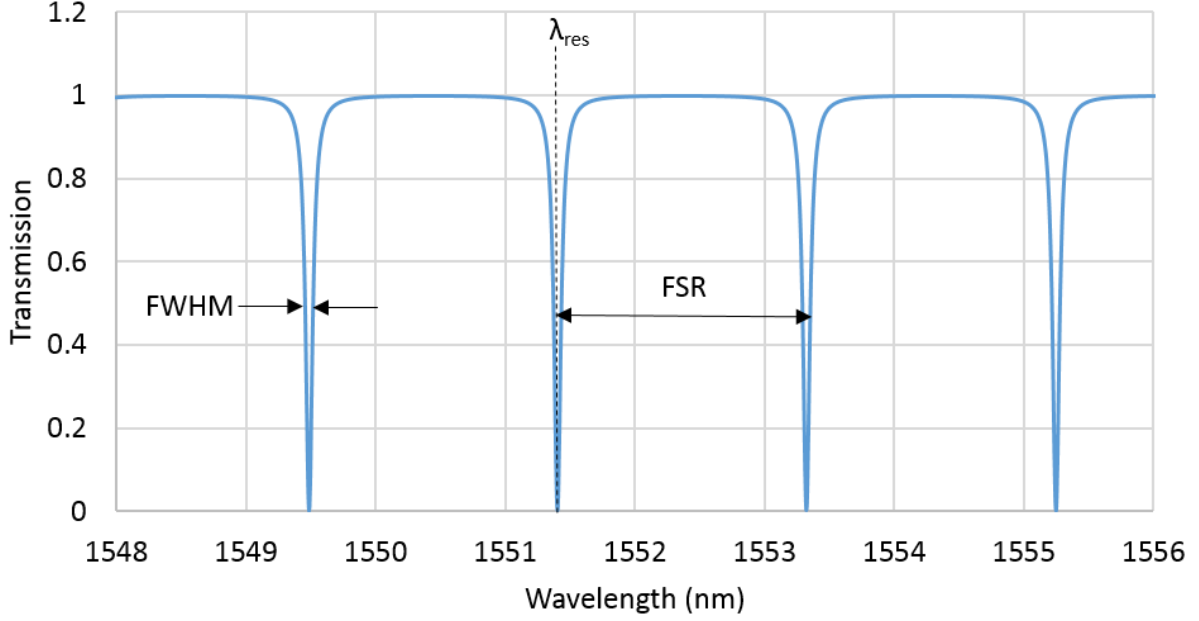


Figure 4.2. Example transmission spectra for an all-pass ring resonator. An example resonant wavelength, full width at half max (FWHM), and free spectral range (FSR) are illustrated on the plot. Plot generated using $\tau=a=0.95$, n_{eff} of 2, and ring radius of $100 \mu\text{m}$.

Using Equation 4.2 to calculate $|E_{out} / E_{in}|^2$, the transmission for an all-pass ring resonator, consisting of a single bus waveguide and ring resonator, is given by [205]

$$T_{all-pass}(\lambda) = \frac{a^2 - 2\tau a \cos\left(\frac{2\pi n_{eff} L}{\lambda}\right) + \tau^2}{1 - 2\tau a \cos\left(\frac{2\pi n_{eff} L}{\lambda}\right) + (\tau a)^2}, \quad (4.3)$$

where τ is the self-coupling coefficient, and α is related to the power attenuation coefficient a by [205]

$$a^2 = \exp[-\alpha L]. \quad (4.4)$$

Coupling will be described in more detail in Section 4.2.4. From the transmission, the full width at half maximum (FWHM) for an all-pass ring is given by

$$FWHM_{all-pass} = \frac{(1-\tau a)\lambda_{res}^2}{\pi n_g L \sqrt{\tau a}}, \quad (4.5)$$

where n_g is the group index [205]. The wavelength spacing between two adjacent resonances, or free spectral range (FSR) is given by [205]

$$FSR = \frac{\lambda^2}{n_g L}. \quad (4.6)$$

Finally, the quality factor, Q , is a measure of the resonance sharpness, relative to its central wavelength:

$$Q = \frac{\lambda_{res}}{\Delta\lambda_{FWHM}}, \quad (4.7)$$

where $\Delta\lambda_{FWHM}$ is the full width at half maximum spectral width. Another equivalent definition for Q is 2π times the ratio of the stored energy in the oscillator to the dissipated energy per cycle. For an all-pass ring, one can re-write Q as [205]

$$Q_{all-pass} = \frac{\pi n_g L \sqrt{\tau a}}{\lambda_{res} (1-\tau a)}. \quad (4.8)$$

The transmission and corresponding spectral features of an all-pass ring resonator are illustrated in Figure 4.2.

As noted earlier, one other common ring geometry is called an add-drop filter, which consists of a ring resonator, input bus waveguide, and output bus waveguide [See Figure 4.1(b)]. Corresponding transmission and spectral properties for the add-drop geometry can be derived in a

similar fashion, assuming cw operation and using scattering matrix formalism, as described in [208].

4.2.3 Four-wave mixing and resonant enhancement

High-Q ring resonators are particularly attractive for nonlinear optical applications, given their tight confinement and resonant enhancement of efficiencies. Four-wave mixing is a third-order nonlinear process which has drawn significant interest with the ability to efficiently generate light at new frequencies [62]. For example, four-wave mixing and corresponding cascaded processes are central to generating optical frequency combs, which are illustrated in Figure 1.5.

Degenerate four-wave mixing is a $\chi^{(3)}$ -based nonlinear optical process in which two pump photons are annihilated to create a signal and idler photon at frequencies obeying energy and momentum conservation. From energy conservation,

$$2E_p = E_s + E_i, \quad (4.9)$$

where E_p , E_s , and E_i are the photon energies at the pump, signal, and idler, respectively, given by

$$E_x = hf_x. \quad (4.10)$$

Here, E_x is the photon energy and f_x is the frequency for the corresponding pump, signal, or idler beam. To obey momentum conservation,

$$2k_p = k_s + k_i, \quad (4.11)$$

where k_p , k_s , and k_i are the propagation constants at the pump, signal, and idler, respectively, given by

$$k_x = \frac{2\pi n_x}{\lambda_x}. \quad (4.12)$$

Here, λ_x is the wavelength and n_x is the effective index for the corresponding pump ($x = p$), signal ($x = s$), or idler beam ($x = i, c$). In *seeded* four-wave mixing, this process is initiated by launching a strong pump beam and weak signal beam into a $\chi^{(3)}$ -based nonlinear material, to generate output light at the pump, signal, and idler wavelengths, obeying energy and momentum conservation. This is illustrated schematically in Figure 4.3.

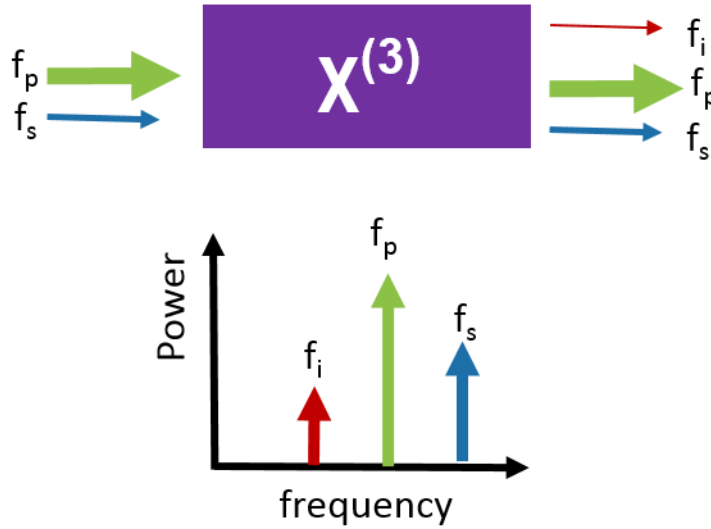


Figure 4.3. Illustration of degenerate four-wave mixing. A strong pump beam and weak signal beam are launched into a $\chi^{(3)}$ -based nonlinear material, to generate output light at the pump, signal, and idler frequencies (f_p , f_s , and f_i respectively). In degenerate four-wave mixing at the photon level, two pump photons are annihilated to generate a signal and idler photon at frequencies obeying energy and momentum conservation.

Given an intense pump and weak signal at frequencies f_p and f_s , respectively, an idler (also called converted) wave is generated at a frequency f_c . The derivation for four-wave mixing theory is outlined by Agrawal in [62]. Beginning with the wave equation for the various frequencies, one finds that the evolution of the field is governed by a set of coupled differential

equations [62]. Assuming a slowly varying envelope, undepleted pump, small signals, lossless media, and negligible self-phase modulation and cross phase modulation effects, the output converted wave power P_c will satisfy [62]

$$P_c(z) = \gamma^2 P_p^2 z^2 P_s \text{sinc}^2\left(\frac{z\Delta k}{2}\right), \quad (4.13)$$

where P_p is the input pump power, P_s is the input signal power, z is the distance propagated in the nonlinear medium, γ is the nonlinear parameter, and Δk is the phase mismatch, given by

$$\Delta k = 2k_p - k_s - k_c. \quad (4.14)$$

Recall k_x is given by Equation 4.12. Note that the maximum power transfer from the pump to the converted wave in Equation 4.13 is limited by the phase mismatch [206]. It is useful to define a four-wave mixing conversion efficiency, which is equal to the output idler power, divided by the input signal power as shown:

$$\eta_{FWM} = \frac{P_c}{P_s}. \quad (4.15)$$

Combining Equations 4.13 and 4.15, the theoretical four-wave mixing efficiency is given by

$$\eta_{FWM} = \gamma^2 P_p^2 z^2 \text{sinc}^2\left(\frac{z\Delta k}{2}\right). \quad (4.16)$$

Thus, the four wave mixing efficiency depends on the square of the nonlinear parameter, pump power, and length. With the use of a straight, 5 mm-long Si nanocrystal-embedded silicon slot waveguide with large nonlinear parameter $\sim 1100\text{W}^{-1}\text{m}^{-1}$, A. Trita et al. demonstrated four-wave mixing efficiency of -28.9 dB and -43 dB for the quasi-TM and quasi-TE mode with 5 mW pump power and 4 mm effective length (taking into account loss) [207]. While this result is impressive, it requires sophisticated fabrication techniques and materials to achieve large nonlinear parameter.

Alternatively, the four-wave mixing efficiency can be significantly enhanced with the use of ring resonators. One can assume that a ring resonator is pumped with a strong pump beam with power P_p , and seeded with a weak signal beam with power P_s , such that $P_p \gg P_s$. Combining Equation 4.2 for the fields with four-wave mixing theory, applying small-signal analysis by assuming $|E_p| \gg |E_s| \gg |E_c|$, Absil et al. showed that conversion efficiency in a ring resonator is given by

$$\eta_{FWM} = |\gamma P_p L'|^2 FE_p^4 FE_s^2 FE_c^2, \quad (4.17)$$

where γ is the effective nonlinearity, P_p is the pump power [202]. Here, L' and FE_i are the effective length and field enhancement factors at the pump (p), signal (s) and converted idler (c) wavelengths, given by the following

$$FE_i = \left| \frac{\kappa}{1 - \tau \exp[-\alpha L / 2 + jLk_i]} \right|^2 \quad (4.18)$$

$$L'^2 = L^2 \exp[-\alpha L] \left| \frac{1 - \exp[-\alpha L + jL\Delta k]}{\alpha L - jL\Delta k} \right|^2. \quad (4.19)$$

Here, κ is the ring coupling (cross-coupling) coefficient, τ is the ring transmission (self-coupling) coefficient, L is the ring circumference, α is the loss, k_i is the propagation constant (also called β) of the pump, signal, or converted idler, and Δk is the phase mismatch, equal to $2k_p - k_s - k_c$ [202].

Ring resonators improve the four-wave mixing efficiency through resonant enhancement, with maximum efficiency for critical coupling, where the power coupled to the ring is equal to the power lost such that $\tau = \alpha$. However, dispersion can cause unequal spacing in the resonances, leading to phase mismatch that can decrease this enhancement. This is illustrated in Figure 4.4.

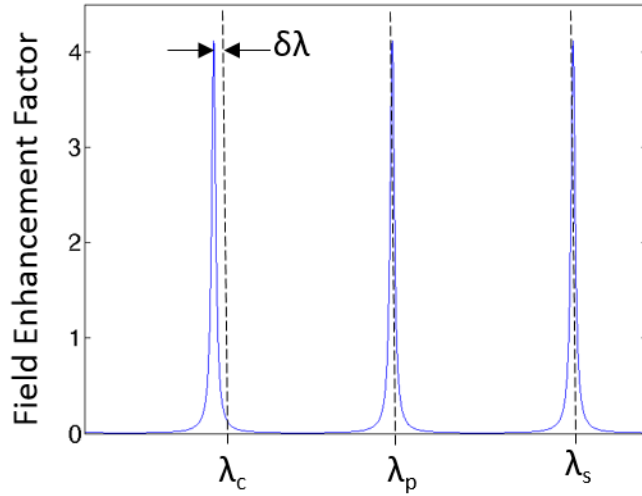


Figure 4.4 Field enhancement factor as a function of wavelength. Dispersion causes uneven spacing in resonance frequencies at the pump λ_p , signal λ_s , and idler, leading to reduced enhancement at the converted wavelength λ_c [202]. The shift from optimum enhancement is given by $\delta\lambda$.

In our design, ring waveguide dimensions are optimized to provide maximize four-wave mixing efficiency. To simplify the calculations of four-wave mixing efficiency, we assume critical coupling, with both pump and signal on-resonance, and we assume equal losses across the signal, idler, and pump waves. Under these assumptions, the four-wave mixing efficiency in a ring resonator is given by

$$\eta = \gamma^2 P_p^2 \frac{e^{-\alpha L}}{(1 - e^{-\alpha L})^2} \frac{1}{\alpha^2 + \Delta k^2}. \quad (4.20)$$

In general, multiple effects contribute to phase mismatch, including material dispersion, waveguide geometry dispersion, as well as self- and cross-phase modulation, nonlinear effects which shift the resonant wavelengths. The resonant shift from nonlinear effects is negligible when it is small compared to the resonance wavelength, such that [202]

$$\frac{L\gamma(FE)^2 P_p}{2\pi m} \ll \frac{\Delta\lambda_{FWHM}}{\lambda_{res}}. \quad (4.21)$$

In practice, this constraint can be satisfied by using suitably low power levels and small cavity lengths. In this case, it can be useful to write the phase mismatch in terms of the effective index, such that

$$\Delta k = \frac{(m_p - 1)}{R} - \frac{2\pi n_{eff,c}}{\lambda_c}. \quad (4.22)$$

Here, R is the ring radius, $n_{eff,c}$ is the effective index at the converted idler wavelength λ_c , and m_p is the resonance integer at the pump wavelength.

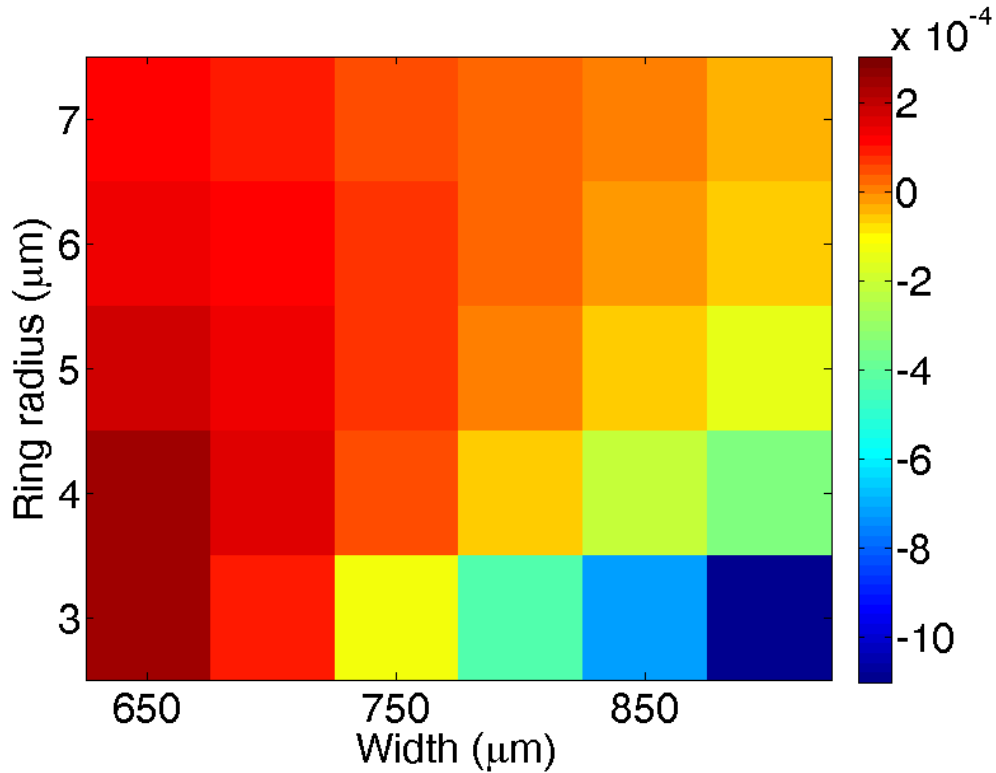


Figure 4.5 Phase mismatch for air-clad, Ge-Sb-Se ring resonators on SiO₂ at 1550 nm. Simulated phase mismatch is plotted in color (in 1/μm) as a function of ring resonator radius and waveguide width. For simulations, a fixed height of 350 nm and air cladding are assumed.

A plot of the simulated phase mismatch at 1550 nm for various Ge-Sb-Se ring resonator waveguide dimensions is shown in Figure 4.5, neglecting nonlinear resonant shifts. Although the Ge-Sb-Se material has normal dispersion at 1550 nm (see Figure 3.5), the anomalous dispersion from the

wider, curved waveguide geometry can be used to compensate, reducing the overall phase mismatch.

The theoretical four-wave mixing efficiency is plotted in Figure 4.6. By calculating the phase mismatch (caused by dispersion) for various ring radii and cross sectional dimensions, one can use Equation 4.20 to find which dimensions optimize this efficiency, assuming a fixed loss, nonlinearity and pump power.

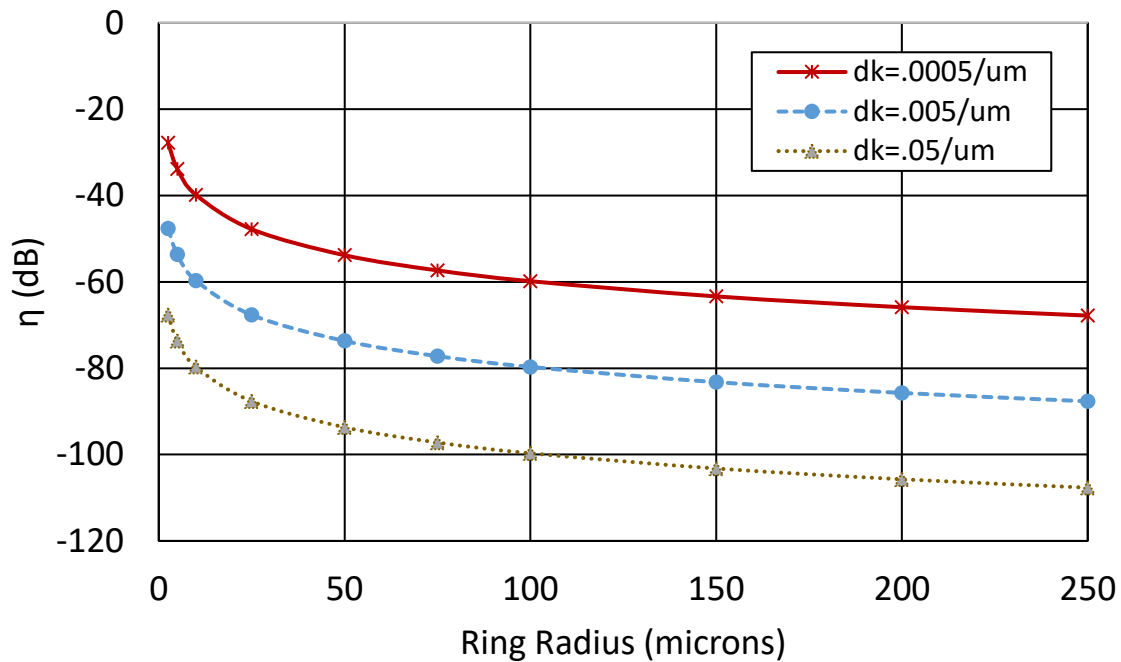


Figure 4.6. Theoretical four-wave mixing efficiency. The theoretical four-wave mixing efficiency is plotted as a function of ring radius, for various values of phase mismatch dk . Calculations assume loss of 4 dB/cm, nonlinear parameter of 6/W-m, and 5 mW pump power.

In general, experimental four-wave mixing efficiencies demonstrated in ring resonators tend to match predictions from the theory by Absil et al. [197,202,225], though some deviation at high power, due to free carriers, nonlinear absorption, and thermal effects have been observed [197]. Example code to optimize ring resonator geometry for four-wave mixing efficiency is given in Appendix E.

4.2.4. Ring coupling design

A resonator can be characterized through measurements of its quality factor. Physically, the quality factor represents the number of field oscillations before the energy decays to $1/e$ of its initial value [205]. Note that the total (or loaded) quality factor Q is given by

$$Q^{-1} = Q_{\text{int}}^{-1} + Q_{\text{ext}}^{-1}, \quad (4.23)$$

where Q_{ext} represents the extrinsic coupling losses, and Q_{int} is due to intrinsic loss in the ring from scattering and absorption, given by [210]

$$Q_{\text{int}} = \frac{2\pi n_g}{\alpha \lambda}. \quad (4.24)$$

Here, n_g is the group index, α is the absorption, and λ is the wavelength.

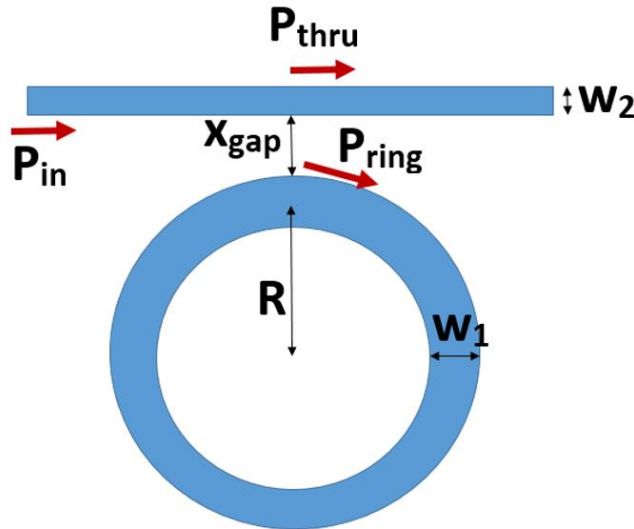


Figure 4.7. Schematic of bus-to-ring coupling and coupling strength. A fraction of power from a bus waveguide with width w_2 , spaced a distance x_{gap} from a ring resonator with radius R and width w_1 , is coupled to the ring. P_{in} the input power to the bus waveguide, P_{thru} is the power that remains in the bus waveguide, and P_{ring} is the power coupled to the ring.

For extrinsic coupling loss, it is useful to first define the power coupling coefficient,

$$\kappa^2 = P_{\text{ring}}/P_{\text{in}}, \quad (4.25)$$

where P_{in} is the power launched into the waveguide, and P_{ring} is the power coupled to the ring, as illustrated in Fig. 4.7. For small coupling loss, where the coupling coefficient $|\kappa^2| \ll 1$,

$$Q_{ext} = \omega_0 \tau / |\kappa^2|, \quad (4.26)$$

where τ is the round-trip time [210].

Two coupling regimes were examined: weak coupling and critical coupling. To characterize the intrinsic loss of a resonator, one can use the ‘weakly coupled cavity’ method described in [211]. In this method, coupling into and out of the ring is intentionally designed to be weak, so that $Q_{ext} \gg Q_{int}$, and intrinsic loss dominates the linewidth. In this case, $Q \sim Q_{int}$, and a measure of the linewidth is $\sim Q_{int}$. For a measurement with enough power, yet reasonably low error, $10 < Q_{ext}/Q_{int} < \sim 30$ is suggested [211]. By including a range of coupling gaps on a chip and testing to find the smallest gap that provides measurable signal, this method provides a quick, accurate estimate of the intrinsic loss. For the ‘weakly-coupled cavity’ method, if intrinsic losses ~ 1 -10 dB/cm are expected, and an add-drop configuration (See Figure 4.1b) with equal coupling gaps is used, coupling strengths of roughly $-4.7 < \log_{10}(\kappa^2) < -3.7$ would be desired.

Four-wave mixing is most efficient under critical coupling, where the power coupled to the ring is equal to loss in the ring, such that the coupling strength is given by

$$\kappa^2 = 1 - \alpha^2, \quad (\text{for critical coupling}) \quad (4.27)$$

Here, α is the power attenuation coefficient given by Equation 4.4, and L is the length of the resonator, $2\pi R$ for a ring [205]. Depending on the range of expected loss of the ring, there will be a corresponding range of values for κ^2 to achieve critical coupling. For example, for a 6 μm -radius ring with 1 to 10 dB/cm loss would require coupling strength of $-3.1 < \log_{10}(\kappa^2) < -2.1$ is desired, depending on the exact loss.

Sometimes, strong enough coupling cannot be obtained with simple straight bus waveguides due to fabrication constraints. In particular, although smaller coupling gaps increase coupling strength, gaps less than a few hundred nanometers are challenging to fabricate successfully. Two possible solutions to increase the required coupling gap are illustrated in Figure 4.8. One option is to use racetrack resonators, effectively increasing the coupling length. However, racetrack resonators require additional design to mitigate loss from modal mismatch at the curved and straight waveguide junctions. An alternate solution is to use curved waveguide structures, called pulley couplers. This increases the coupling length and decreases the required gap sizes.

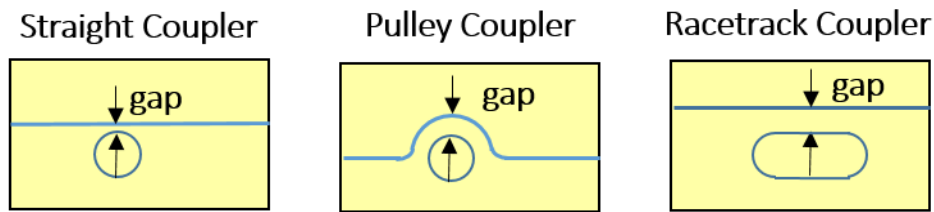


Figure 4.8. Schematic of alternative coupling schemes. A pulley coupler, consisting of a curved bus waveguide, can be used to increase the effective coupling length and reduce the gap required to achieve a particular coupling strength, compared to a straight coupler. Alternatively, a racetrack coupler, consisting of a straight bus waveguide coupling to a stretched ring “racetrack” resonator can be used to increase the coupling length.

For these longer coupling lengths, it is important to design the width of the bus waveguide to be ‘phase-matched’ to the ring resonator waveguide to ensure proper coupling [208]. A bent mode solver was used to simulate two concentric rings: the inner with the fixed ring waveguide width, and the outer with a width w_2 and given gap distance. The propagation constants of the first two modes were calculated as a function of w_2 for a single gap x_{gap} and plotted, as shown in Fig.

4.9. If straight lines are fit to the asymptotes, then the phase-matched width will occur at the intersection of these two lines. This process can be repeated for a range of different gap sizes, yielding a plot of phase-matched w_2 vs. x_{gap} . The result can be used in ring design with curved pulley couplers (See Fig. 4.10). Example code for phase-matching the widths of a coupler waveguide to a particular ring resonator is given in Appendix E.

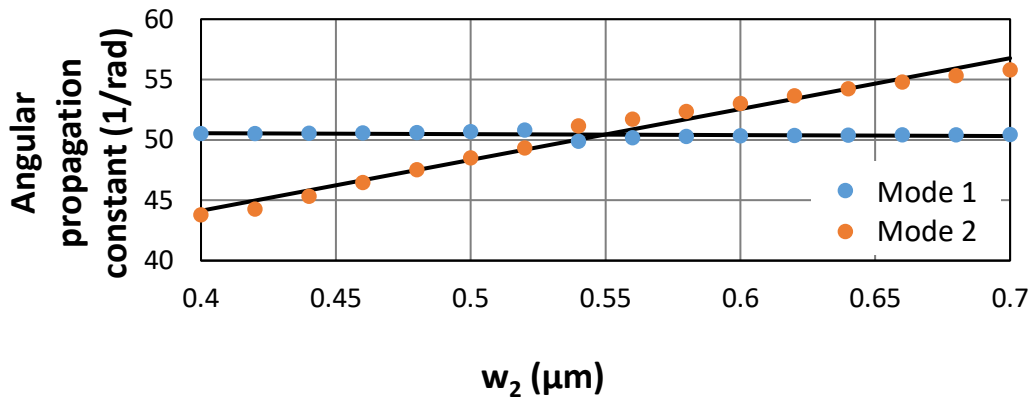


Figure 4.9. Propagation constant vs. bus width for concentric (pulley) coupler. This shows the angular propagation constants of 2 supermodes vs. the outer waveguide width w_2 . For this plot, the waveguide height was 330 nm, and the inner waveguide width was 800 nm, with 6 μm radius and fixed gap of $x_{gap}=100$ nm. The waveguides are phase-matched for $w_2=0.55$ μm , where the propagation constants of the two modes are approximately equal.

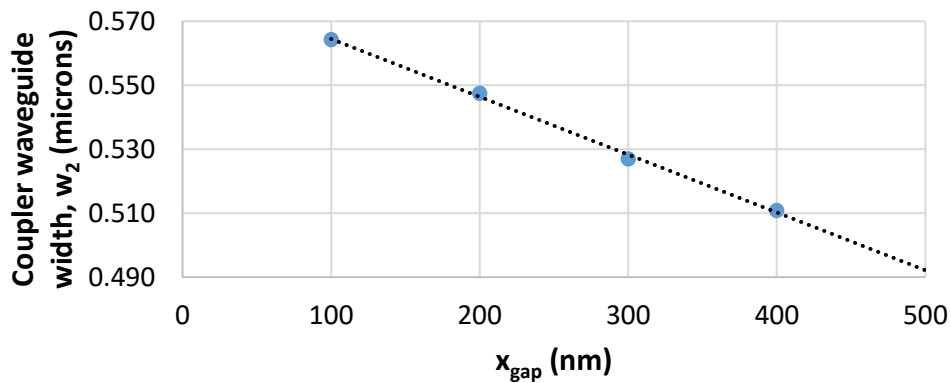


Figure 4.10. Phase-matched width vs. gap distance for concentric (pulley) coupler. Example plot of the phase-matched outer waveguide width, w_2 as a function of bus-to-ring gap x_{gap} , calculated for phase-matching to a 6-micron radius inner ChG-on-SiO₂ ring with 800 nm width and 330 nm height at 1550 nm.

4.3 Ge-Sb-Se ring resonators for four-wave mixing

4.3.1 Near-infrared ring resonator design

Chalcogenide microring resonators were designed for operation at near-infrared wavelengths and optimized for four-wave mixing efficiency. The resonances and dispersion were simulated over a range of waveguide cross-sectional dimensions and ring radii. Using these results, the theoretical four-wave mixing efficiency was calculated, and the optimal waveguide dimensions, within fabrication and source constraints, were determined. The coupling region between bus waveguides and ring resonators was also designed to enable measurements of the Q factor and nonlinear effects such as four-wave mixing. A flow chart of the general process used to design ring resonators is shown in Figure 4.11.

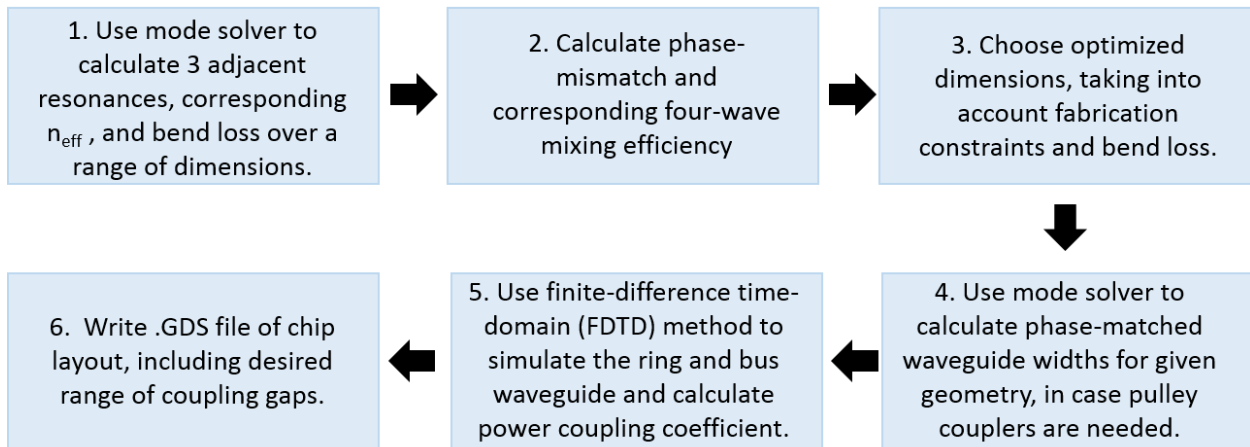


Figure 4.11. Design process for ring resonators optimized for four-wave mixing. A mode solver is first used to calculate bend loss, resonances, and effective index n_{eff} over a range of dimensions. The corresponding four-wave mixing efficiency is calculated, and optimal ring dimensions are chosen. Coupling is then designed, and a .GDS file for chip layout is written.

For a range of waveguide cross sections and ring radii, the four-wave mixing efficiency was predicted, using calculated resonance locations and dispersion, along with a fixed estimate of

waveguide loss, nonlinearity, coupled pump power, and critical coupling. An example plot of the four wave mixing efficiency for various waveguide dimensions and radii is shown in Figure 4.12. In general, four-wave mixing efficiency improves with decreasing ring radius due to decreased mode volume. At small radii, where resonances are spaced farther apart, dispersion becomes increasingly important, causing the efficiency to also depend on waveguide width.

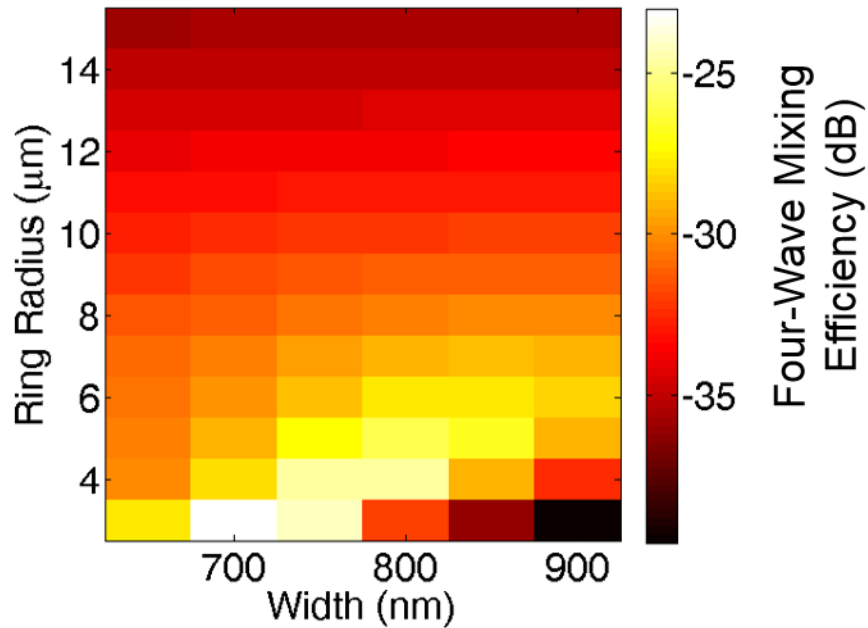


Figure 4.12 Four-wave mixing efficiency for various chalcogenide waveguide dimensions. Color plot shows the four wave mixing efficiency (color scale, in dB, defined in Eqn. 4.15) for an air-clad chalcogenide ring resonator on SiO₂ near 1550 nm, as a function of waveguide width and ring radius. Calculations assume 350 nm waveguide height, fixed loss of 6 dB/cm, nonlinearity of 6/W-m, and pump power of 5 mW.

A plot of the simulated radiation loss due to bending is shown in Figure 4.13. Bend loss decreases exponentially with increasing radius. At radius of 3.3 μm, bending loss becomes comparable to the measured 0.07 cm⁻¹ material absorption loss. At radius $R \geq 3.93 \mu\text{m}$, radiative loss becomes negligible compared to material loss. As illustrated in Figure 4.12, while smaller radii rings provide best four-wave mixing efficiency, they also produce larger free spectral range

(FSR), which requires larger laser tunability for characterization. Additionally, tighter bend radii lead to increased field strength at the rough outer waveguide sidewall, as illustrated and discussed in Section 3.2.1 and Figure 3.2. The final chosen design dimensions used 800 nm (W) by 330 nm (H) cross section with small 6 micron-radius rings, which still provide a few resonances within the tuning range of available lasers for thorough characterization.

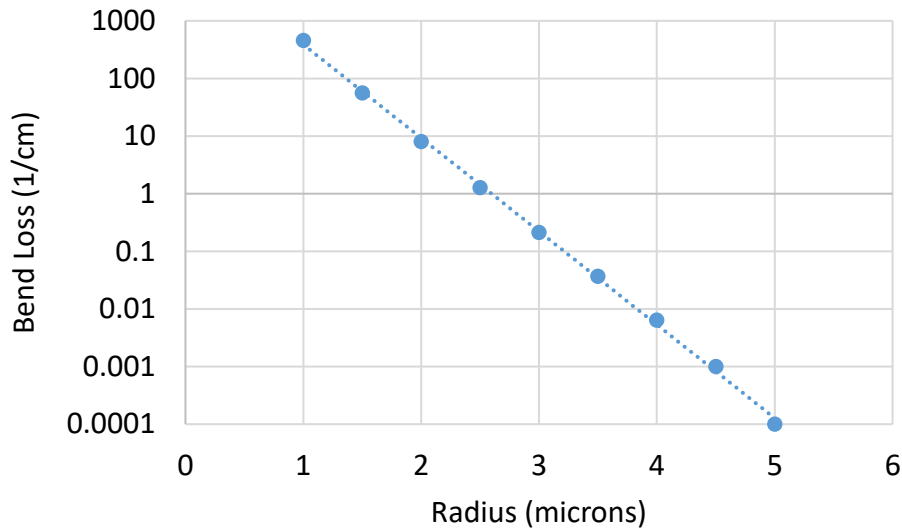


Figure 4.13 Simulated bend loss vs. radius and corresponding fit for Ge-Sb-Se waveguide. Calculations assume 800 nm (W) x 330 nm (H) air-clad Ge-Sb-Se waveguide on SiO₂ substrate at 1550 nm. Bend loss decreases exponentially with increasing ring radius, and radiative loss is comparable to or less than material loss for radii $R \geq 3.3 \mu\text{m}$.

The bus-to-ring coupling coefficient was also calculated for various bus waveguide geometries as a function of the gap distance between the ring resonator and bus waveguide. Structures were simulated using Lumerical’s Mode Solutions variational finite difference time domain (varFDTD) and full 3D finite difference time domain (FDTD) simulations. The chalcogenide material dispersion was imported into Lumerical and the desired structures were drawn using Lumerical’s graphical user interface. An optical mode source was launched into the bus waveguide, and monitors were used to check the input power and output power at the bus and

ring (See Fig. 4.14). Based on the power splitting fraction between the bus and the ring, the coupling coefficient κ^2 was calculated.

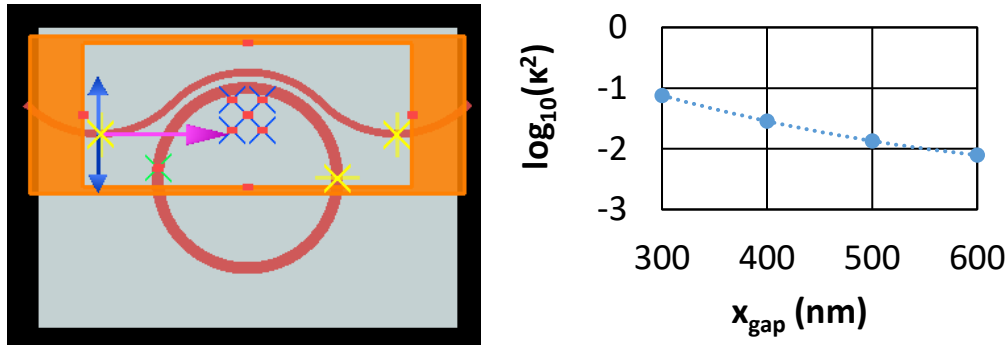


Figure 4.14. Example Lumerical varFDTD simulation of pulley coupler. The mode is launched at the start (left) of the waveguide, propagating towards the right. Yellow power monitors are placed at the input, as well as the output bus and ring waveguides, and data of the power and transmission at these points as a function of wavelength is recorded over the range of interest. Note that the simulated region, indicated by the orange box, only includes half of the ring, in order to decrease run time and while still extracting meaningful power coupling results. The graph on the right shows example extracted coupling strength κ^2 for phase-matched curved structures as a function of bus-ring gap distance, x_{gap} , for 6-micron rings.

By varying the gaps, as well as the bus waveguide widths and straight vs. curved bus geometry, a range of acceptable coupler designs were found for the expected range of waveguide losses. Note that to significantly decrease computation time, only half-ring, rather than full ring, structures were simulated. As discussed in Section 4.2.4, propagation constants of pulley couplers were simulated with a mode solver as a function of gap size, to find the proper phase-matched waveguide width. Results of the phase-matching simulations are shown in Figure 4.10. Additional coupling simulation results for larger-radii ring resonators at 1550 nm are shown in Figure 4.15. Coupling strength decreases with increasing bus-ring gap distance.

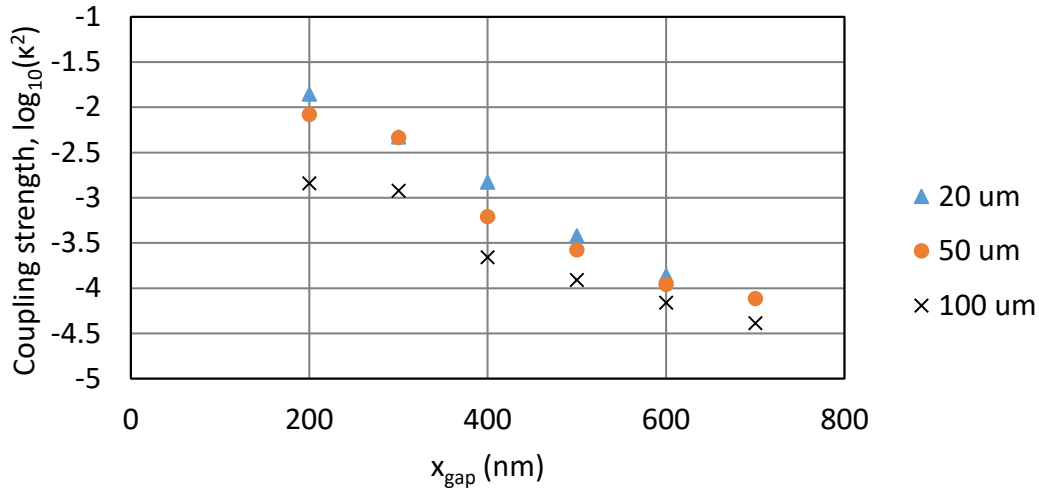


Figure 4.15. Coupling strength vs. gap for straight coupler with various ring radii. Coupling strength κ^2 is plotted as a function of bus-ring gap distance, x_{gap} , for rings of 20, 50, and 100 micron radii. Using Lumerical MODE Solutions, the ChG ring waveguide cross section used is 800 nm (W) by 330 nm (H), with 65 degree base angle and SiO₂ substrate. The straight bus waveguide width is fixed at 700 nm.

Our final designs are summarized in Table 4.1. They featured add-drop rings with 6 micron radius, along with larger rings of radii of 20, 50, and 100 microns, and variety of coupling gaps to cover a range of possible losses. (Larger rings were included to examine the radius-dependence of loss.) For the smallest add-drop rings with 6 μm radius, curved couplers for critical coupling were also designed for four-wave mixing, using a phase-matched bus width of 520 nm, and 90 degree section with constant coupling gaps of 350, 370, and 390 nm. Additionally, alternate all-pass ring resonators with straight critical couplers were included, using a bus waveguide width of 530 nm and coupling gaps of 300, 400, and 500 nm.

Table 4.1 Summary of ring design for 800 nm (w) x 330 nm (h) Ge-Sb-Se rings at $\lambda=1.55\mu m$.

<i>Radius</i> (μm)	<i>FSR</i> (GHz)	<i>Straight Coupler x_{gap}</i> (nm)	<i>FWM Efficiency</i> (dB)
6	2580	380-660	-28
20	777	480-760	-38
50	311	450-730	-46
100	155	300-700	-52

Straight waveguides and ring resonators were laid out using KLayout to create a .GDS file for e-beam lithography. An image of the chip layout is shown in Figure 4.16. As shown, each chip includes a series of straight waveguides, waveguides with fixed number of bends, and ring resonators with radii of 6, 20, 50, and 100 μm .

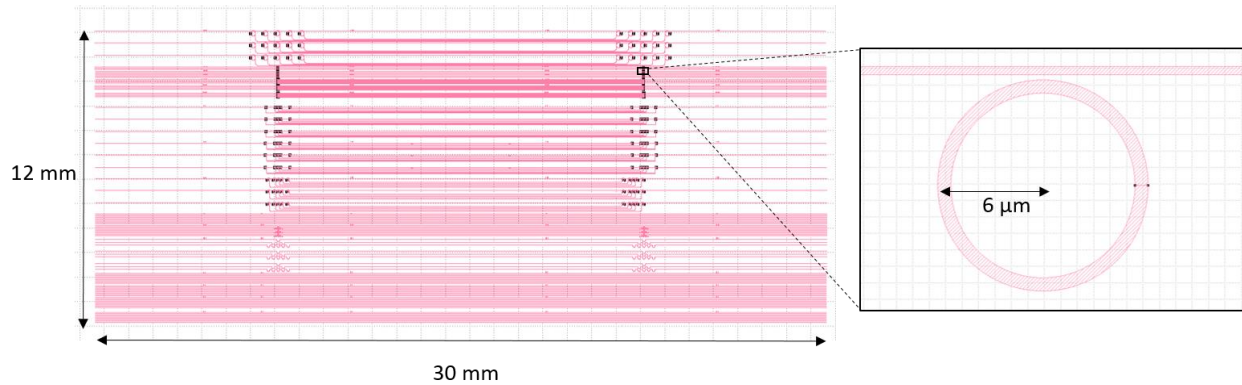


Figure 4.16. Chip layout for ring resonators at 1550 nm. KLayout is used to create a .GDS file of the chip layout for e-beam lithography. Left: two mirror-image, 15 mm-long chips are placed side-by-side. Each chip includes a series of straight waveguides, waveguides with fixed number of bends, and ring resonators with radii of 6, 20, 50, and 100 μm . After fabrication, the side-by-side chips are cleaved apart to provide two samples for testing. Right inset: Zoomed-in view of ring resonator on chip.

4.3.2 Mid-infrared ring resonator design

Chalcogenide (ChG) microrings were also designed for operation at a mid-infrared wavelength of 3.5 μm , applying the same design methods. This design work was based on an air-clad, ChG-on-MgF₂ platform. For a range of waveguide cross-sections and ring radii, the four-wave mixing efficiency was predicted, using calculated resonance locations, dispersion, and nonlinearity, along with a fixed estimate of waveguide loss, coupled pump power, and critical coupling.

An example plot of predicted four-wave mixing efficiency as a function of radius is shown in Figure 4.17, using a fixed waveguide height of 580 nm, a calculated nonlinear parameter based on estimate from Lenz et al. [36], and assuming 5 mW pump power and 4 dB/cm loss. Four-wave mixing efficiency tends to increase with decreasing radius. However, at very small bend radii, the enhancement from smaller mode volume begins to compete with the phase-matching constraint from dispersion. (Recall that the dispersion shifts as the waveguide is bent more tightly.) For 580 nm-thick ChG-on-MgF₂ waveguide, maximum four-wave mixing efficiency is achieved with a waveguide width of 1120 nm.

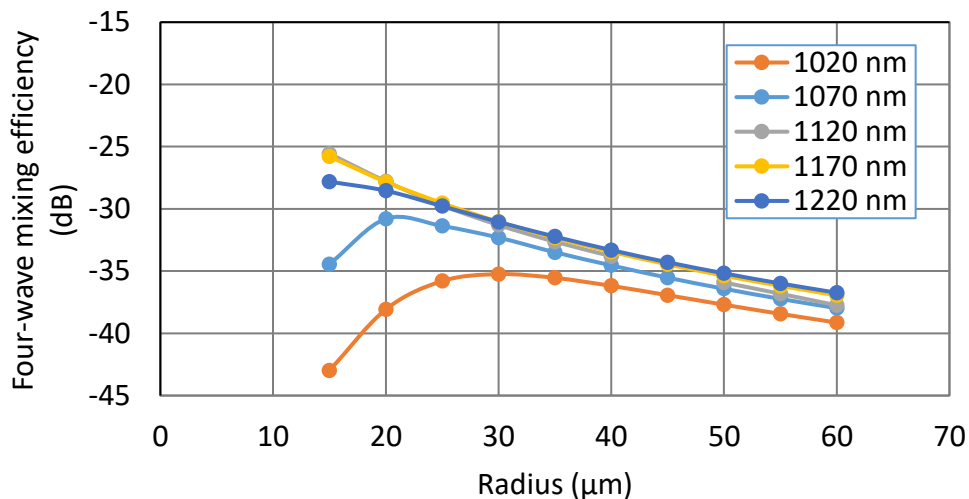


Figure 4.17 Four-wave mixing efficiency vs. radius for chalcogenide (ChG) ring at 3500 nm. Efficiency calculated for air-clad 580 nm-thick ChG-on-MgF₂ waveguide at 3500 nm, for various waveguide widths. Calculations assume input pump power of 5 mW and 4 dB/cm loss. At large radii, four-wave mixing efficiency tends to decrease with increasing radius. For 580 nm-thick waveguide, maximum four-wave mixing is achieved with waveguide width of 1120 nm.

Simulations for a few different waveguide heights were compared. For a given height, a corresponding optimal width could be found to compensate for dispersion and provide comparable efficiency, as illustrated in Figure 4.18. However, our bilayer resist and liftoff process is limited

to making ChG films <600 nm thick, due to the available resists and achievable resist thickness. Considering this constraint, cross-sectional dimensions of 1220 nm (W) x 520 nm (H) provided good four-wave mixing efficiencies ~ -25 to -38 dB at 3.5 μm in the curved geometry while maintaining single mode operation and falling well within the fabrication constraint.

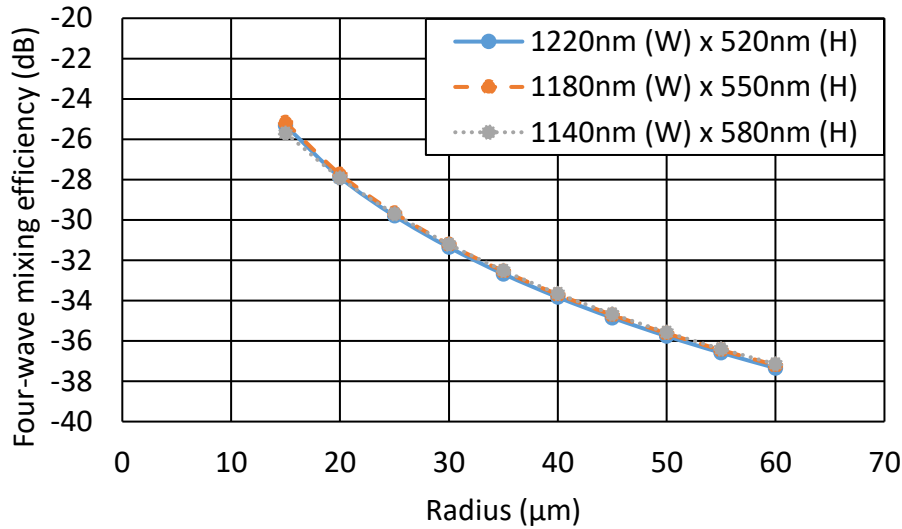


Figure 4.18. Four-wave mixing efficiency vs. radius for ChG rings, for optimized dimensions. Structures simulated are air-clad Ge-Sb-Se rings on MgF_2 , at 3500 nm wavelength. Calculations assume input pump power of 5 mW and 4 dB/cm loss. At large radii, four-wave mixing efficiency decreases with increasing radius.

In the mid-infrared, larger bend radii $\geq 16.9 \mu\text{m}$ are required for radiation loss comparable to material loss, and radii $\geq 20 \mu\text{m}$ are needed for negligible loss relative to material loss (See Fig. 4.19). Additionally, as discussed in Section 4.3.1, although smaller radii rings provided best four-wave mixing efficiency, they also produced larger *FSR*. For example, at 3.5 μm wavelength, with a group index of 3.14, the radii of 20 μm and 30 μm correspond to *FSR* of 31.0 nm and 20.7 nm, respectively. The final chosen design dimensions utilize mid-sized 30 μm radius rings with ~20.7 nm *FSR*, which still provide multiple resonances within the tuning range of available sources for thorough characterization.

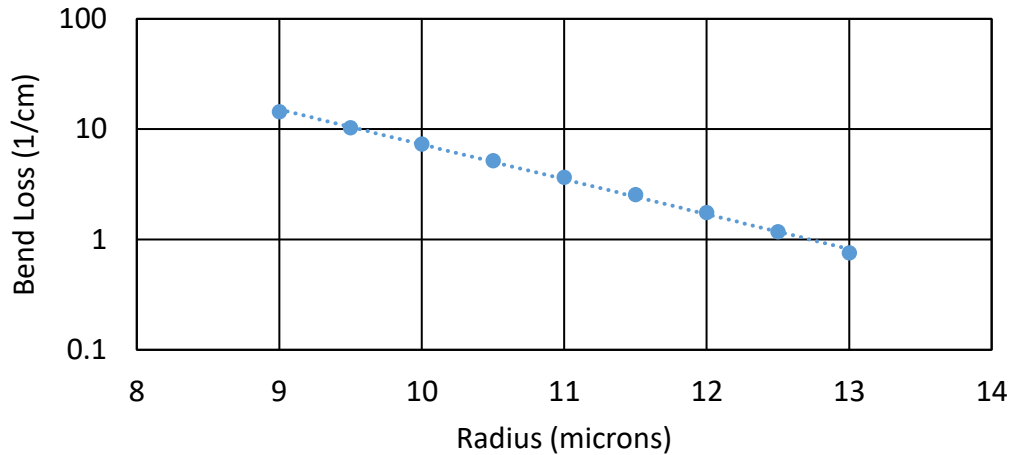


Figure 4.19. Simulated bend loss vs. radius and corresponding fit for ChG-on-MgF₂ at 3500 nm. The bend loss is simulated for 1220 nm (W) x 520 nm (H) air-clad Ge-Sb-Se waveguide on MgF₂ substrate. The bend loss decreases exponentially with increasing ring radius. Extrapolating from the fit, radiative loss is comparable to or less than material loss of 0.05 cm⁻¹ at 3500 nm for radii $R \geq 16.9 \mu\text{m}$.

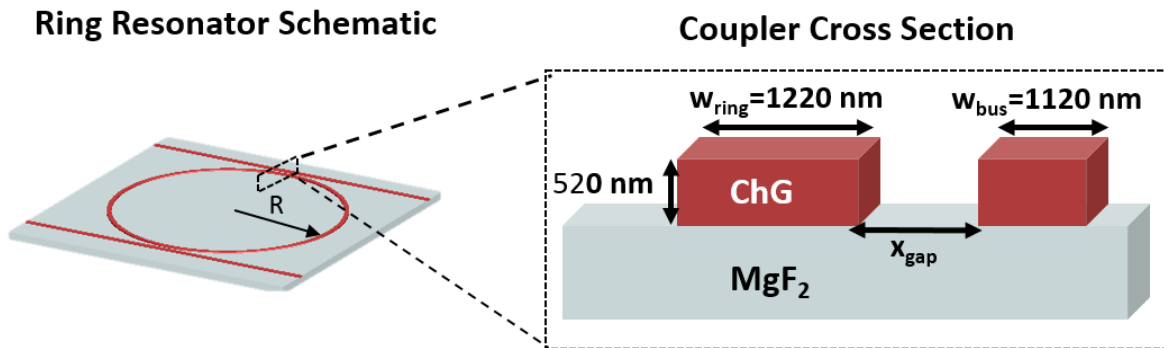


Figure 4.20. Example straight coupler simulated using Lumerical varFDTD. Left: Schematic of simulated add-drop ChG-on-MgF₂ ring resonator. Right inset: Cross section of a coupling region showing waveguide dimensions, with gap distance x_{gap} .

The bus-to-ring power coupling coefficient was calculated as a function of the gap distance between the ring resonator and bus waveguide, using Lumerical's varFDTD solver in the MODE Solutions package. (The ring resonators, $\geq 100 \mu\text{m}^3$, were too large for efficiency 3D FDTD, given the large simulation volume required.) By varying the gaps for given bus waveguide widths, a

range of acceptable coupler designs were found for the anticipated possible range of waveguide losses (See Figures 4.20 and 4.21).

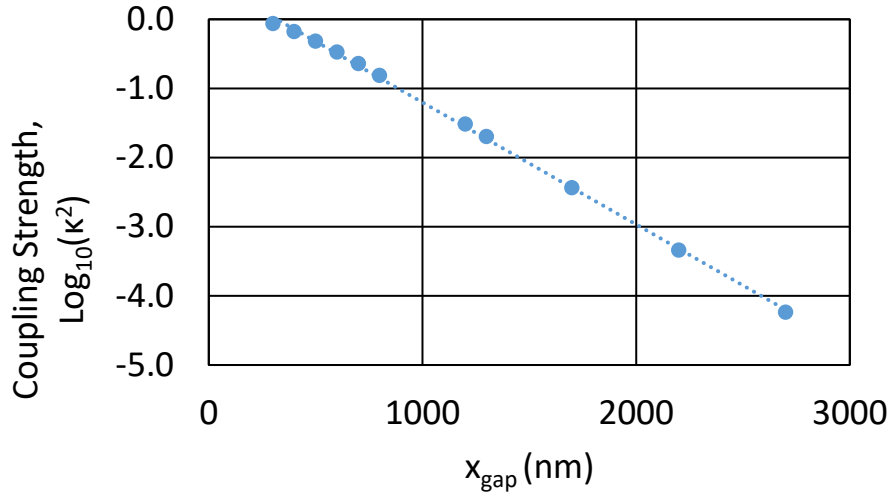


Figure 4.21. Plot of extracted coupling strength a function of bus-ring gap distance at $\lambda=3.5\mu\text{m}$. Coupling strength is simulated as a function of bus-ring gap, using ring radius $R=30\mu\text{m}$, $1220\text{ nm (W)} \times 520\text{ nm (H)}$ ring cross section, and 1120 nm bus waveguide width.

Table 4.2. Summary of coupling gap designs for $1220\text{ nm (W)} \times 520\text{ nm (H)}$ Ge-Sb-Se rings at $\lambda=3.5\mu\text{m}$

<i>Radius</i> (μm)	<i>FSR</i> (GHz)	<i>Weak x_{gap}</i> (μm)	<i>Critical x_{gap}</i> (μm)
30	507	2.02-2.76	1.13-1.46
60	253	1.96-2.68	1.09-1.40
100	152	1.84-2.57	1.04-1.43

Our final mid-infrared designs featured rings with 30 micron radius, along with larger rings of radii of 60 and 100 microns, and variety of coupling gaps to cover a range of possible losses (see Table 4.2).

4.3.3 Ring resonator fabrication

The ring resonators designed for operation at 1550 nm (described in Section 4.3.1), were fabricated in collaboration with Dr. Wounjhang Park, Dr. Gumin Kang, and Michael Grayson at

the University of Colorado Boulder. The process flow for fabrication of ring resonator samples was analogous to the earlier process used for fabrication of sub-micron waveguides, and is illustrated in Figure 3.16. A bilayer resist consisting of PMMA and MMA/PMMA is spun onto a substrate, consisting of a 300 μm -thick Si wafer with 3 μm -thick SiO_2 layer on top, from University Wafer. Glass pipettes, compatible with PMMA, are used and e-beam exposure conditions were optimized (1500 $\mu\text{C}/\text{cm}$) to yield a clean pattern and reduce contaminants. Following e-beam lithography and development, Ge-Sb-Se is thermally evaporated, and lift-off is used to remove the resist and produce ring resonators with cross-sectional dimensions of 800 nm (W) by 330 nm (H). E-beam lithography was carried out using a Vistec EBPG5000 e-beam lithography system at the Minnesota Nano Center at the University of Minnesota out by Kevin Roberts and Dr. Greg Cibuzar. The fabricated sample included ring resonators, as well as straight waveguides of various widths, in order to compare losses to previous samples fabricated at the University of Washington.

4.3.4 Ring resonator characterization

Near-infrared ring resonators and waveguides, fabricated by e-beam lithography, thermal evaporation, and liftoff, were characterized from 1500-1630 nm. The experimental setup for optical characterization is illustrated in Figure 4.22. To characterize the Q of the ring resonators, light from a sub-MHz linewidth, tunable laser (Yenista TUNICS, $1500 \leq \lambda \leq 1630$ nm) is coupled on and off chip using lensed fibers (Lase Optics, 1 μm spot diameter, 12-14 μm working distance, part # LF-SM-SC-01-SMF-28-FC/APC), and the transmission is monitored as a function of wavelength using a swept-wavelength interferometer system (Yenista CT400). The polarization of the input light is controlled using fiber polarization paddles (Thorlabs FPC562). Both the taper and wedge resonator are mounted on 3-axis piezo-actuated stages (Thorlabs MAX312D) with 20 nm resolution, and imaged from above using a microscope (See Appendix G for components).

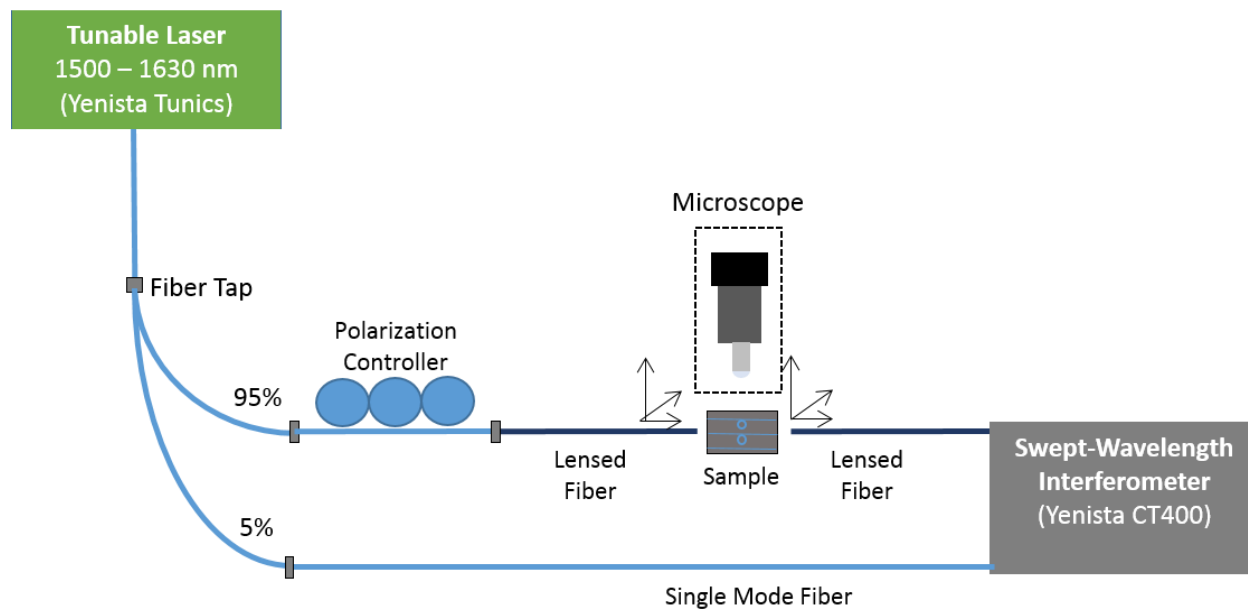


Figure 4.22. Ring resonator coupling schematic. Light from a tunable, narrow-linewidth laser is coupled to and from the chip using lensed fibers, mounted on a piezo-actuated 3-axis stage and positioned one working distance (12-14 μm) from the chip. A polarization controller is used to optimize the polarization. The transmission vs. wavelength is monitored using a swept-wavelength interferometer system.

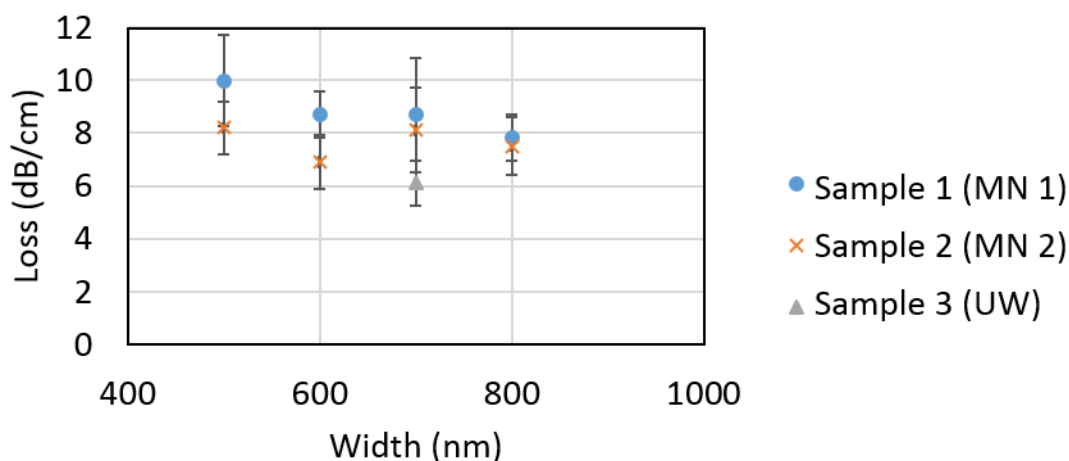


Figure 4.23. Average TE propagation loss vs. waveguide width for various samples. E-beam lithography was performed at the University of Minnesota for samples 1 and 2 (same conditions), and at the University of Washington for sample 3. Chalcogenide waveguide samples (height of 330 nm) from two different batches, fabricated at the University of Minnesota, exhibit losses ranging from 7-10 dB/cm. Errors are estimated from the standard deviation. This loss is within the uncertainty of loss from earlier sample (height of 340 nm) fabricated at the University of Washington, using normal writing conditions.

Linear propagation loss of straight waveguides was measured using the scattered light method. The TE propagation loss is shown in Figure 4.23 as a function of waveguide width (for fixed height of 330 nm), averaging over 8-9 waveguides for each data point. Error bars are estimated using the standard deviation of the measurements. For comparison, the loss of a previous waveguide sample fabricated at the University of Washington (with fixed height of 340 nm) is also shown. Average propagation losses for the samples consistently range from 7-10 dB/cm, even for two different fabrication runs at the University of Minnesota. Additionally, taking the uncertainty into account, the measured loss is comparable to the loss of previous samples fabricated at the University of Washington.

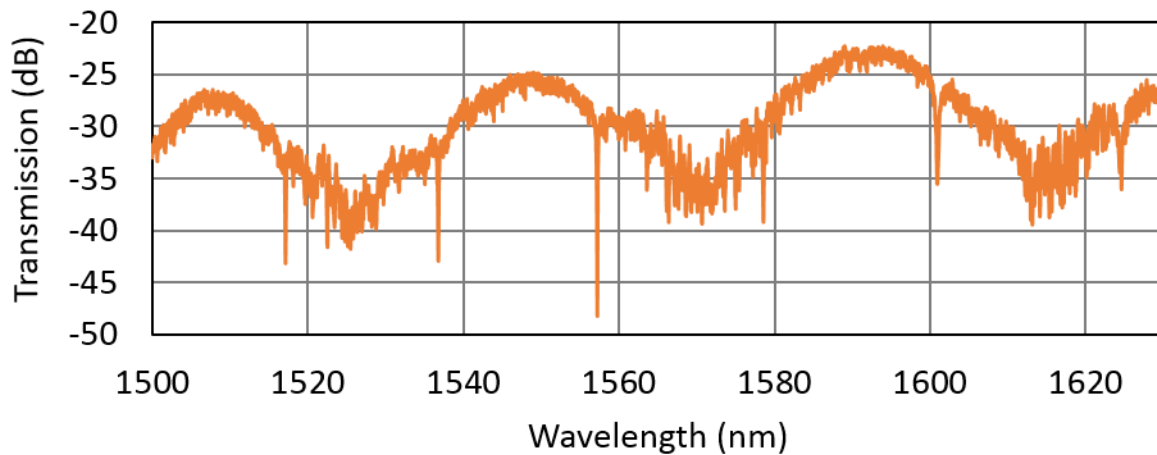


Figure 4.24. Near-infrared transmission vs. wavelength for Ge-Sb-Se ring with 6 μm radius. Six resonances are observed over the transmission scan, with a free spectral range (FSR) of roughly 21 nm. Large, oscillatory parasitic background with ~ 40 nm period is likely caused by wavelength-dependent polarization effects in the experimental setup.

The quality factor of fabricated ring resonators was characterized through measurements of transmission vs. wavelength. Here, all-pass resonator structures consisting of a single bus waveguide and ring resonator with 6 μm radius, were utilized. An example transmission plot for a 6 μm radius ring is shown in Figure 4.24. Although there is substantial oscillatory background,

six resonances can be observed, with free spectral range (FSR) of roughly 21 nm. The magnitude of the background ripple and shape do not fit well to a Fabry-Perot effect. Instead, the background is likely due to wavelength dependent polarization in the setup. We are exploring options to resolve this. One additional cause of background ripple may be due to parasitic modal coupling to a higher order mode [224]. Although the ring dimensions were designed to support one TE and one TM mode, the design assumed the bulk refractive index. Updating the calculations to use Ge-Sb-Se thin film material dispersion from ellipsometry measurements instead of bulk material dispersion, the 800 nm x 330 nm dimensions support two TE modes and one TM modes, though the second TE mode is very weakly guided, resulting in high bend loss.

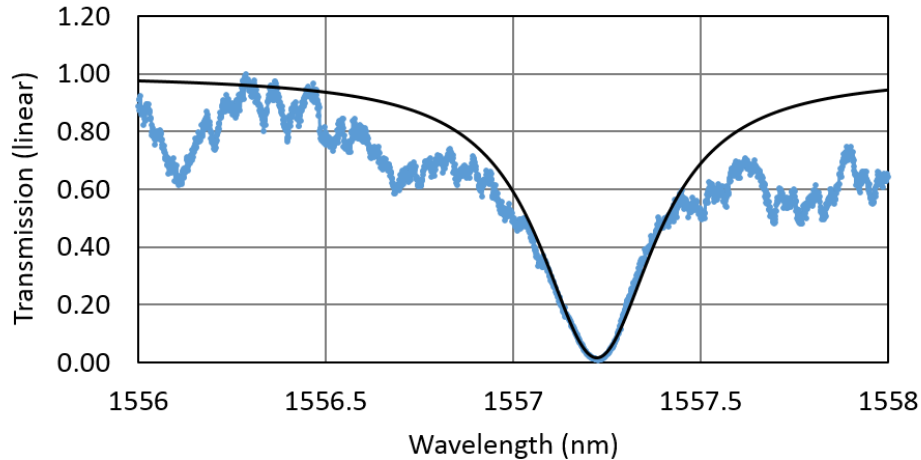


Figure 4.25. Lorentzian fit to resonance for an all-pass ChG ring with 6 μm radius. An all-pass ring resonator configuration was used, with a single straight bus waveguide. From the fit, Q_{loaded} is 6.0×10^3 , the coupling coefficient τ is 0.9837, and the power coupling coefficient a is 0.9788.

A resonance and corresponding Lorentzian fit are illustrated in Figure 4.25. From fits to multiple resonances from multiple samples, Q_{loaded} ranges from 0.5 to 1×10^4 and Q_{int} ranges from 1 to 2×10^4 are obtained. These measurements were consistent between two different sample

batches (using same fabrication conditions) with multiple ring resonators. Note that the measured intrinsic Q corresponds to losses $\sim 25\text{-}50$ dB/cm, roughly 3-6x higher than measured loss in straight waveguides. Calculations suggest radiative loss due to bending is negligible, $\sim 3 \times 10^{-6}$ /cm, corresponding to radiation Q of 4×10^{10} . There are a few possible causes of the increased loss observed in the ring resonators, including pattern discretization and fabrication issues, as well as changes in mode profile from bending.

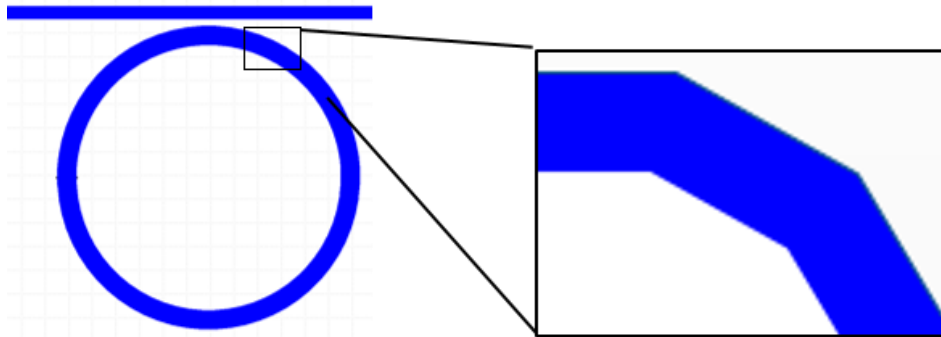


Figure 4.26. Schematic of pattern discretization in a ring resonator. Curved patterns can become discretized and less smooth if not enough vertices are used in the .GDS file, or if e-beam conditions (such as beam size and step size) are not optimal [167].

Pattern discretization is illustrated in Figure 4.26. In particular, curved patterns can become discretized if too few vertices are used in the .GDS file, or if e-beam conditions (such as beam size and step size) are not optimal [167]. This discretization effect could cause rougher edges, increasing the scattering loss for curved structures. To explore discretization in the samples, SEM images of rings were examined (See Figure 4.27). Although clear examples of discretization were not observed, small residue $\sim 30\text{-}100$ nm in diameter was noted near the rings. This residue may lead to increased roughness, thereby increasing scattering loss. The residue was not observed

near the simple straight waveguides on the sample. An investigation to better understand the cause of the residue, and how to best remove it, is ongoing.

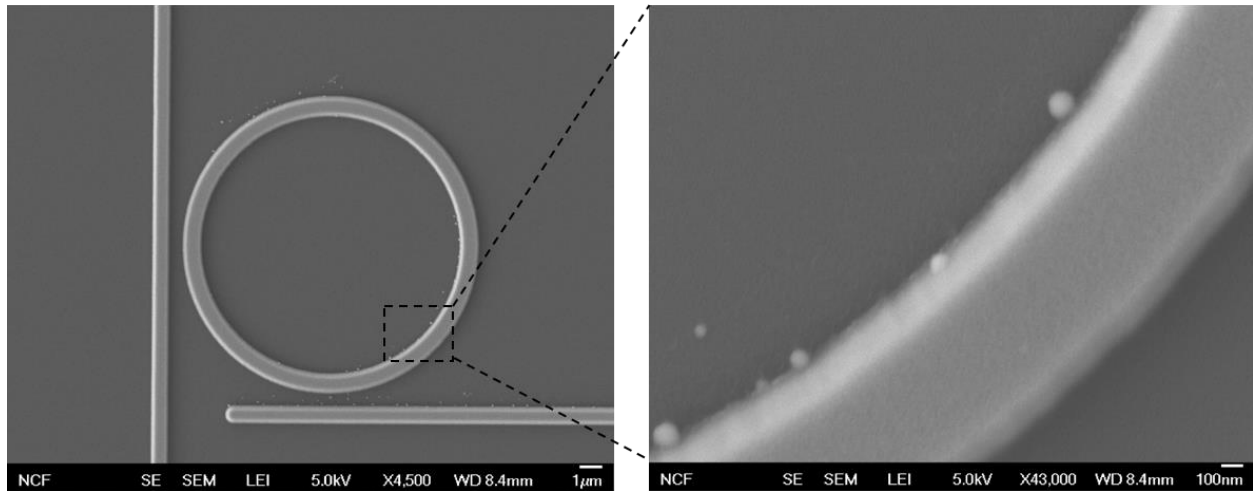


Figure 4.27. Scanning electron micrographs (SEMs) of ring resonator sample. Left: Ring resonator SEM. Right: High-magnification SEM of portion of ring. No clear evidence of discretization exists. Undesired residue, in the form of small dots with ~30-100 nm diameter, is observed near ring structures on the sample.

Changes in mode profile from bending can also cause increased loss in rings compared to straight waveguides. As a waveguide is bent, the mode profile shifts, increasing the strength of the electric field at the outer edge of the waveguide as the waveguide is bent more tightly. This effect is illustrated in Figure 3.2. This enhanced field at the rough sidewall would cause more scattering loss, resulting in higher propagation loss. To explore this mode profile effect, larger ring resonators on the same chip were also examined. Preliminary data on a larger add-drop ring resonator with radius of 20 μm is shown in Figure 4.28. A fit to the transmission spectra at 1616.57 nm yields Q_{loaded} of 3.4×10^4 and Q_{int} of 8.3×10^4 , corresponding to a propagation loss of 6 dB/cm, within the error of the loss measured in comparable straight waveguides. The higher quality factor

measured in 20 μm rings suggests that the bent waveguide mode profile may be the cause of the reduced Q in the 6 μm rings.

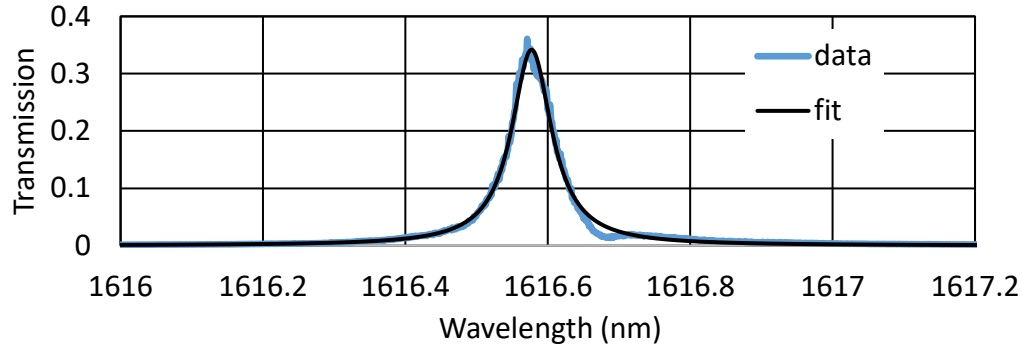


Figure 4.28. Transmission spectra from drop port of 20 μm add-drop ring resonator. Ring resonator has 20 μm radius with cross section dimensions of 800 nm (W) by 330 nm (H). Coupling gap distance is 550 nm, and bus waveguide dimensions are 700 nm (W) by 330 nm (H). Fit to data yields Q_{loaded} of 3.4×10^4 and Q_{int} of 8.3×10^4 corresponding to a propagation loss of 6 dB/cm. Propagation loss in ring is within error of measured loss in 800 nm (W) by 330 nm (H) straight waveguides.

4.4 Conclusion

To summarize, chalcogenide ring resonators were designed with dimensions optimized for four-wave mixing efficiency at 1.55 and 3.5 μm . The coupling between bus waveguides and ring resonators was simulated and designed for weakly coupled resonators for quick Q measurements, as well as critically coupled resonators for optimal power transfer for nonlinear effects. First-generation ring resonators with 6- μm radius are shown to have Q_{loaded} of $0.5-1 \times 10^4$ and Q_{int} of $1-2 \times 10^4$. The measured Q_{int} corresponds to losses $\sim 25-50$ dB/cm, $\sim 3-6$ times higher than propagation losses measured in straight waveguides on the same chip. The larger measured loss in the small ring structures is likely due to stronger electric field at the rough sidewalls for tightly bend waveguides, given higher $Q_{int} \sim 8.3 \times 10^4$ measured in larger rings with 20- μm radius. Scanning

electron micrographs also reveal residue near some of the ring structures, a possible cause of increased roughness. Low Q in the small ring resonators prohibited initial four-wave mixing measurements. In the future, one could optimize fabrication conditions to remove this residue and improve Q_{int} , or explore larger ring resonators using more power, in order to enable nonlinear optical demonstrations in chalcogenide ring resonators.

5. GE-SB-SE WEDGE RESONATORS

5.1. Overview

High- Q , hybrid chalcogenide-silica wedge resonators were designed, fabricated, and characterized at 1.55 μm . Section 5.2 introduces wedge resonators and provides motivation for this work. Section 5.3 describes the design and fabrication of hybrid chalcogenide-silica wedge resonators, and Section 5.4 summarizes Q measurements in the hybrid wedge resonators. Large 46.5 μm diameter resonators exhibited loaded Q s up to 1.5×10^5 . Section 5.5 describes thermal characterization of the wedge resonators with an average thermal resonant wavelength shift of 60.5 pm/C, in good agreement with theoretical predictions.

This work was performed in collaboration with Professor Wounjhang Park, Dr. Gumin Kang, and Michael Grayson at the University of Colorado Boulder, along with Dae-Gon Kim and Dr. Hansuek Lee at Korea Advanced Institute of Science and Technology. In particular, Dr. Gumin Kang designed the wedge and athermal microresonators. Dae-Gon Kim, Dr. Gumin Kang and Michael Grayson fabricated the microresonators. Additionally, Dr. David Carlson and Dr. Scott Papp at NIST generously provided silica fiber tapers and a mount to couple to the microresonators.

This work was supported in part by AFOSR under Grant FA9550-15-1-0506, in part by the DARPA SCOUT Program through ARO under Contract W911NF-15-1-0621, and in part by the Asian Office of Aerospace R&D (FA2386-16-1-4139). Additionally, equipment funding was

provided in part by the Defense University Instrumentation Program (DURIP) Award ONR N00014-16-1-2544. This chapter is adapted from [212].

5.2 Wedge resonator motivation

Given the lack of mature chalcogenide fabrication technologies, particularly etching recipes, obtaining ultrahigh- Q , chip-compatible microresonators can be a considerable challenge. To date, the highest Q obtained in a chalcogenide microresonator was $\sim 7 \times 10^7$, which utilized laser reflow on high purity As_2S_3 fiber [235]. However, these devices are not integrated and lack options for dispersion engineering. Our first generation ring resonators exhibited intrinsic Q s up to 8.3×10^4 . In the near-infrared, state-of-the-art chalcogenide ring resonators have revealed intrinsic Q s up to 7.5×10^5 in $50 \mu\text{m}$ radii Ge-Sb-S microrings [236]. However, these devices require careful optimization of fluorine plasma dry etching conditions, which is material dependent.

One promising microresonator geometry is the wedge resonator, which is illustrated in Figure 1.4. By optimizing the etching process and oxide growth conditions, ultrahigh- Q silica wedge resonators have been demonstrated with Q s up to 8.75×10^8 [42]. Importantly, the fabrication process for high- Q wedge resonators offers precise dimensional control since it does not rely on a reflow technique, which can deform the resonator [42]. Control of dimensions, such as wedge angles, has been shown to be a useful tool to engineer the wedge resonator dispersion [42,213]. A main disadvantage of the wedge resonator geometry is that fabricating side-coupled waveguides can be a challenge. As a result, to couple to wedge resonators, tapered fiber coupling schemes are often used, which are not particularly robust and require precise alignment. However, tapered fiber coupling can enable tunable coupling gaps and strengths. Additionally, Ramiro-Manzano et al. have demonstrated that fabricating vertically-coupled waveguides, integrated with

wedge resonators is feasible [214], offering more stable coupling at the cost of increased fabrication complexity.

In order to improve Q in chalcogenide (ChG) microresonators, a new type of hybrid resonator is developed by extending the process that had been developed for ultrahigh- Q silica wedge resonators [42]. For these devices, a layer of Ge-Sb-Se glass is thermally evaporated on silica wedge resonators, utilizing the smooth surface obtained from the optimized silica etching process for reduced roughness. We demonstrate high- Q hybrid chalcogenide-silica wedge resonators, operating at near-infrared wavelengths.

5.3 Wedge resonator design and fabrication

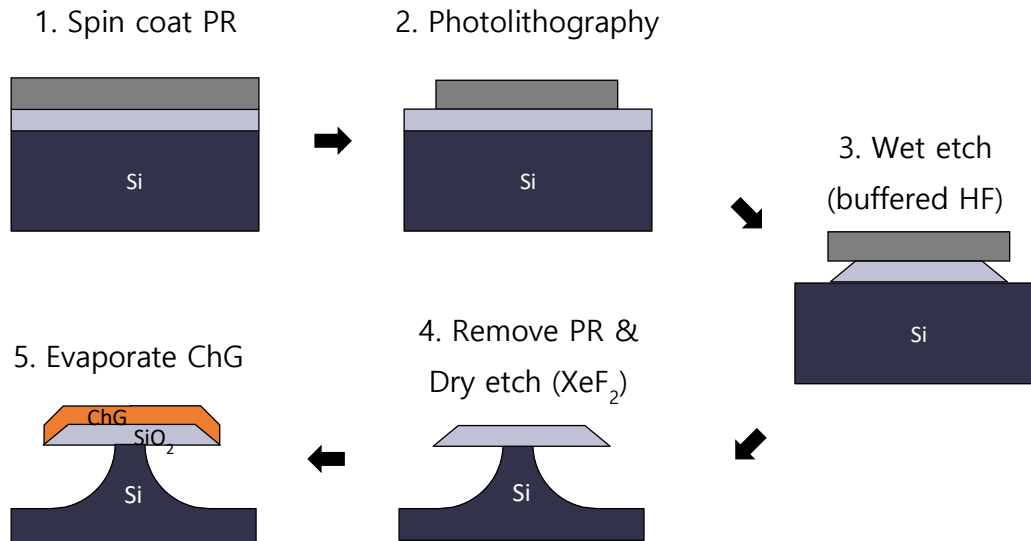


Figure 5.1 Fabrication process flow for hybrid chalcogenide-silica wedge resonators. Photoresist is spin-coated onto a SOI wafer, and disks are patterned with photolithography. Wet etch (using buffered hydrofluoric solution) is used to etch the sides of the silica resonator. Photoresist is removed, and the Si is undercut using dry etch. A thin, 125-nm-thick film of chalcogenide (ChG) is thermally evaporated to form a hybrid chalcogenide-silica wedge resonator.

Hybrid wedge resonators were fabricated as a collaboration between Professor Hansuek Lee's group at KAIST and Professor Wounjhang Park's group at the University of Colorado

Boulder. The fabrication process flow is illustrated in Figure 5.1. Two-micron-thick silica wedge resonators of various diameters were prepared by Professor Hansuek Lee's group at KAIST. Disk-shaped photoresist patterns are first defined by photolithography on the silicon wafer with 2 μm -thick thermal oxide. Then, the sample is immersed in a buffered oxide etchant (BOE) to produce circular silica wedges. This wet etch step ensures that the silica surface is extremely smooth. (With optimized processing, RMS roughnesses of 0.46 to 0.75 nm have been achieved on the wedge part of the resonators [42].) After removing the photoresist using organic solvent, the silicon substrate is dry-etched with xenon difluoride (XeF_2) to create air-suspended wedge structures. Finally, a 125 nm-thick chalcogenide glass film is thermally evaporated onto the silica wedge at a base pressure of 3×10^{-7} Torr, resulting in hybrid chalcogenide-silica wedge resonators as illustrated in Figure 5.1 [212].

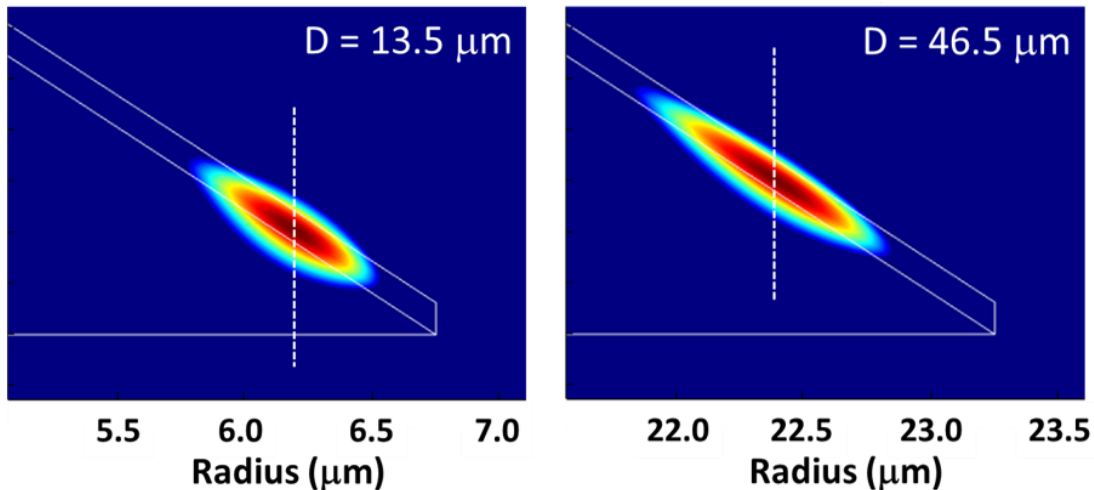


Figure 5.2 Simulated fundamental mode profiles of hybrid wedge resonators. The white solid outline indicates the silica wedge and ChG film. Left: Fundamental mode profile for wedge resonator with 13.5 μm diameter. Right: Fundamental mode profile for wedge resonator with 46.5 μm diameter. Note that the larger resonator provides better confinement of the mode to the chalcogenide layer. Modified from [212].

Hybrid resonators with two outer diameters were fabricated: 46.5 μm and 13.5 μm . The 46.5 μm -diameter resonators supported over eight TE radial mode families, and the 13.5 μm -diameter resonators supported just two TE radial mode families. The 125 nm chalcogenide film thickness was chosen to reduce the effective mode index, allowing for phase-matching and efficient coupling with relatively standard silica fiber tapers. (Coupling efficiency depends on the field overlap of the fiber mode with the resonator mode, along with the phase-mismatch between these modes [216]. Since efficiency decreases exponentially with the square of the phase mismatch, similar effective indices are desired for efficient coupling [216,217].) Given the very thin chalcogenide layer, the hybrid resonators did not support TM radial mode families and only supported TE radial mode families. The fundamental optical mode profiles for the two hybrid resonators, shown in Figure 5.2, were simulated by 2D axisymmetric eigenmode analysis by Dr. Gumin Kang using COMSOL. Scanning electron micrograph (SEM) images of the hybrid wedge resonators are shown in Figure 5.3, showing a tilted view as well as the cross section of the wedge resonator [212].

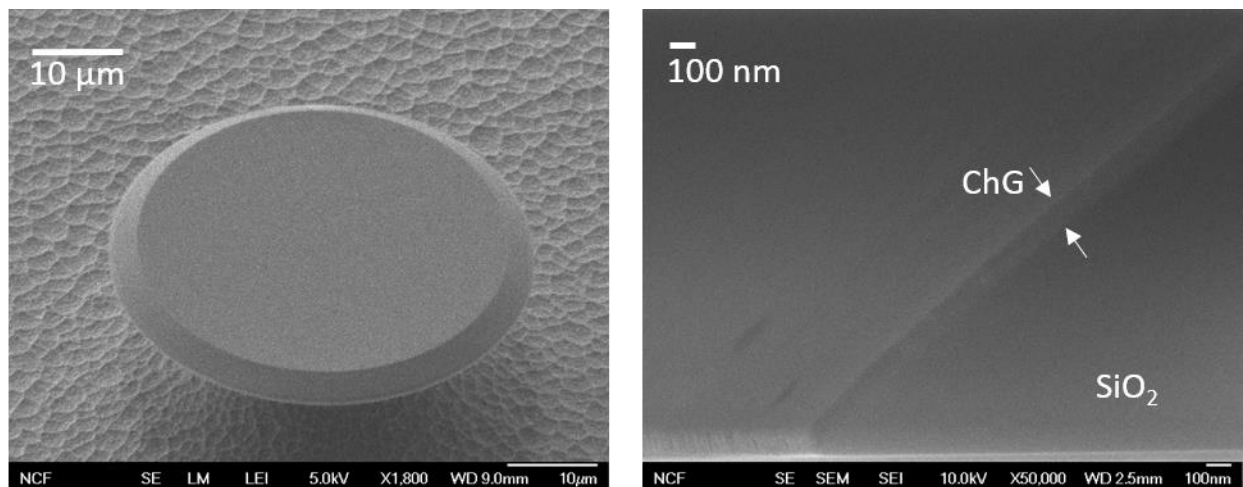


Figure 5.3 Scanning electron micrographs (SEMs) of hybrid wedge resonators. Left: Tilted SEM of a hybrid chalcogenide-silica wedge resonator, with 46.5 μm diameter. Right: SEM of cross section of wedge resonator. From [212].

5.4 Q measurements in wedge resonators

A schematic of the setup used to couple to wedge resonators is shown in Figure 5.4. Tapered fibers, which can be fabricated by heating and pulling standard SMF-28 fiber down to diameters $\sim 1\text{-}3$ microns, are used to couple to the chalcogenide wedge resonators. Tapering the fiber produces a mode which is less well confined to the optical, fiber, allowing light to evanescently couple to a resonators when placed in close proximity to the fiber. The efficiency of this coupling will depend on the spatial mode overlap and the change in effective index, or phase mismatch, between the fiber and resonator modes [216,217]. For this project, silica fiber tapers were generously provided by Dr. Scott Papp and Dr. David Carlson at NIST Boulder. To couple to the wedge samples, the requested fiber taper dimensions were minimum diameter of $1\text{-}2\ \mu\text{m}$, and $1\ \text{cm}$ length with diameter $<10\ \mu\text{m}$ to accommodate the sample geometry.

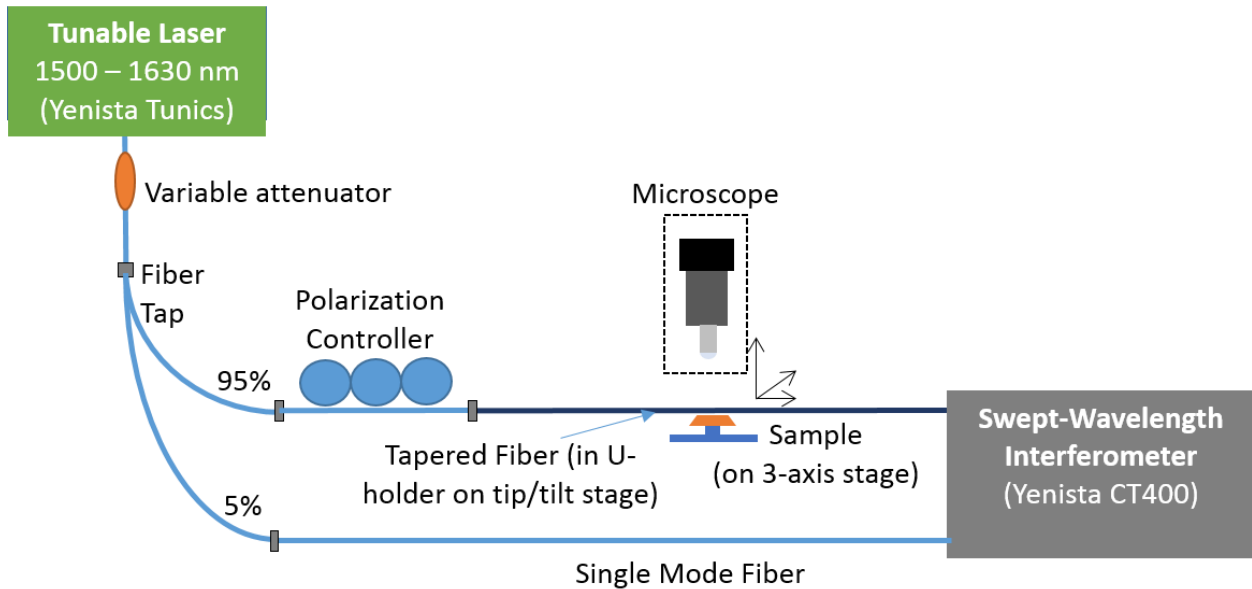


Figure 5.4 Wedge resonator coupling schematic. Light from a tunable, narrow-linewidth laser is polarization-controlled and launched into a tapered fiber, positioned within μm of a wedge resonator, mounted on a piezo-actuated 3-axis stage for precise alignment. Light couples to the wedge resonator, and the transmission vs. wavelength is monitored using a swept-wavelength interferometer system. The setup is placed in an enclosure to prevent drift from air currents.

To characterize the Q of a wedge resonator, light from a sub-MHz linewidth, tunable laser (Yenista TUNICS, $1500 \leq \lambda \leq 1630$ nm) is coupled into a fiber taper positioned hundreds of nm from a wedge resonator, and the transmission is monitored as a function of wavelength using a swept-wavelength interferometer system (Yenista CT400). The polarization of the input light is controlled using fiber polarization paddles. Both the taper and wedge resonator are mounted on 3-axis piezo-actuated stages with 20 nm resolution, and imaged from above using a microscope (See Appendix G for components). The coupling setup is surrounded by a sealed plastic enclosure to block air currents and reduce taper fiber drift. A photo of the setup, along with a microscope image of a wedge resonator and fiber taper, are shown in Fig. 5.5.

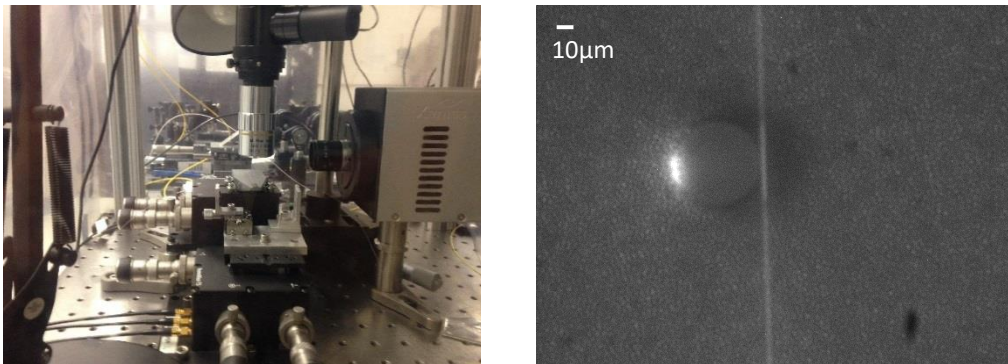


Figure 5.5. Coupling setup and wedge resonator. Left: Photo of coupling setup. Both wedge resonator sample (mounted on aluminum mount) and fiber taper (mounted to U-shaped aluminum mount) are on 3-axis piezo-controlled stages for precise alignment. Right: Microscope image of wedge resonator (46.5 μm diameter) and fiber taper (2.8 μm diameter).

Light was coupled to larger wedge resonators with 46.5 μm diameter. An example transmission spectrum and rough fit to resonance are shown in Figures 5.6 and 5.7. From fits to resonances, loaded Q s up to $\sim 1.5 \times 10^5$ are measured. The average loaded Q is $\sim 6.4 \times 10^4$, based on measurements on 3 adjacent resonators, using ~ 12 fitted resonances each. Intrinsic Q s up to $\sim 1.6 \times 10^5$ are measured. However, identifying the modes is challenging given the presence of

over eight nearby mode families. As such, smaller wedge resonators with 13.5 μm diameter, which feature only two radial mode families, were also characterized.

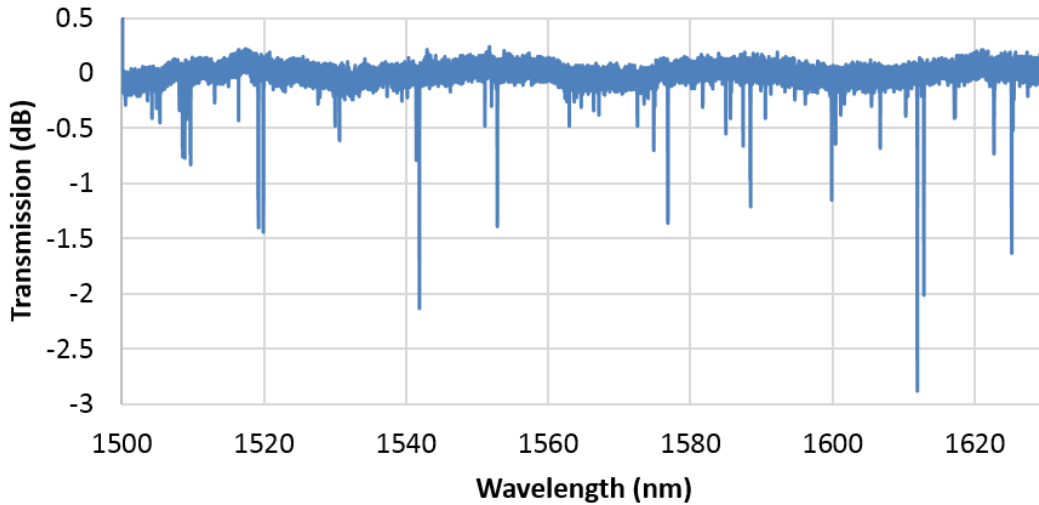


Figure 5.6. Transmission vs. wavelength for 46.5 μm diameter hybrid wedge resonator. While the FSR of the fundamental mode family is expected to be ~ 8 nm, multiple nearby higher order modes are also observed in the scan.

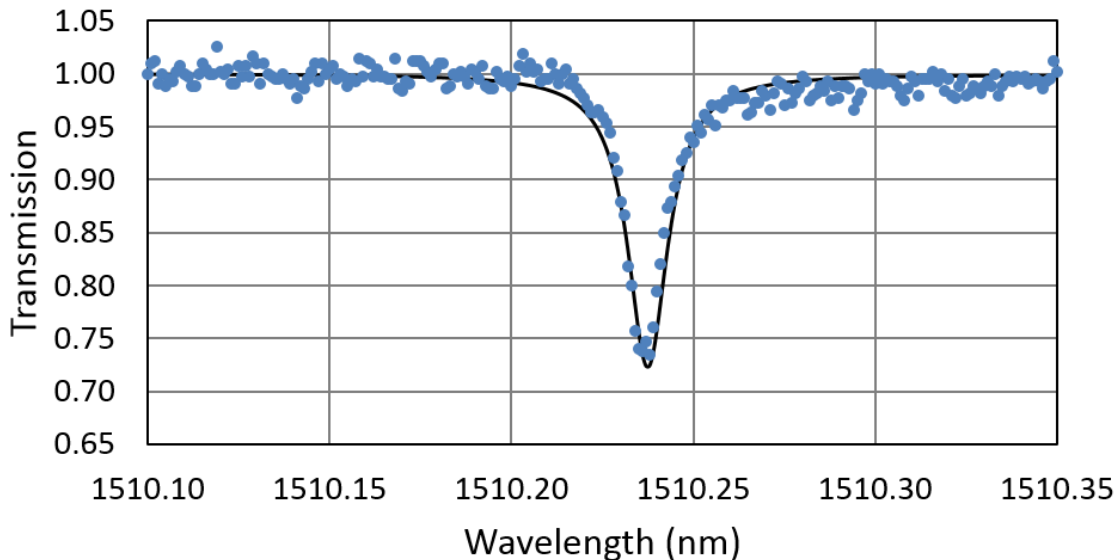


Figure 5.7. Fit for one resonant mode from the 46.5 μm diameter hybrid wedge resonator. From measurement of the resonant wavelength and full-width-half-max (FWHM), a total Q factor of $\sim 2.1 \times 10^4$ is obtained.

Coupling to the smaller resonators with 13.5 micron diameter proved to be difficult, because the small resonators were $\sim 4.8 \mu\text{m}$ from the substrate, leaving less clearance for positioning the fiber taper. (For comparison, the larger $46.5 \mu\text{m}$ -diameter resonators were $\sim 14.6 \mu\text{m}$ from the substrate.) To mitigate this issue, the fiber taper was mounted on a tip/tilt mount for more precise fiber angle adjustments, and the substrate was cleaved from its initial 5 mm width to a 1.2 mm width. This enabled positioning of the fiber close enough to allow light to couple to the resonator.

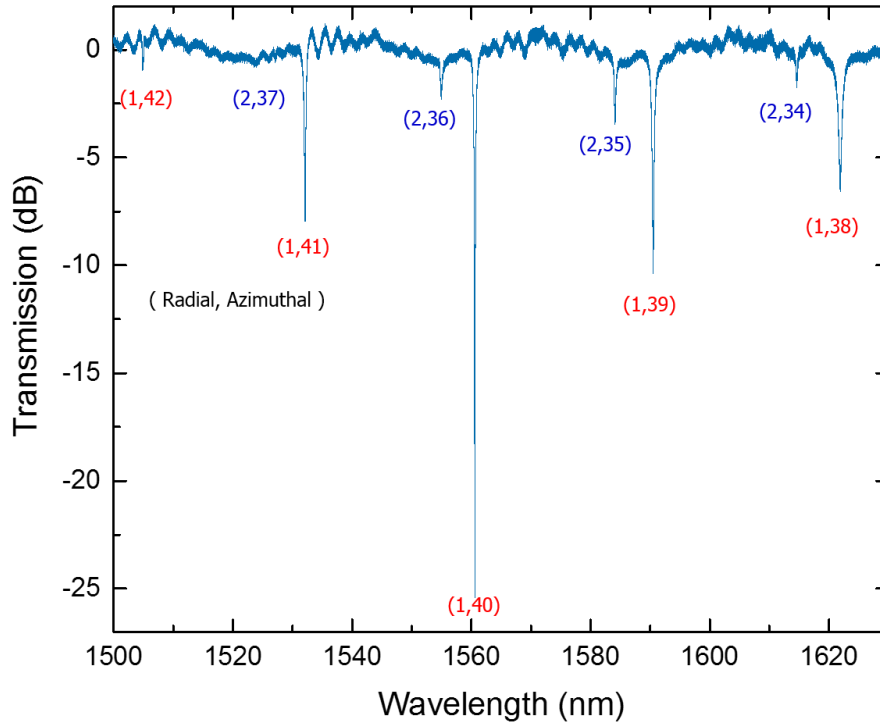


Figure 5.8. Transmission vs. wavelength for 13.5 μm diameter chalcogenide wedge resonator. Both the first-order and (weaker) second-order radial mode families are observed. The FSR of the fundamental mode family is expected to be $\sim 30.6 \text{ nm}$, close to the measured FSR of $\sim 30 \text{ nm}$.

A full transmission spectra from a smaller resonator is shown in Fig. 5.8. Coupling is achieved for two main mode families, the first- and second-order radial modes. From fits on these smaller devices (See Fig. 5.9), loaded Q s up to $\sim 4.8 \times 10^3$ are measured. Averaging over multiple

critically-coupled resonances, the average intrinsic Q is found to be $\sim 9.2 \times 10^3$. Simulations indicate radiation $Q_s > 10^7$, and the bulk $\text{Ge}_{28}\text{Sb}_{12}\text{Se}_{60}$ absorption limited Q factor is 1.6×10^6 , using the 0.3 dB/cm linear absorption measured at 1550 nm [140]. Given the significantly lower Q_s measured for the wedge resonators with diameters of 13.5 μm , Q_s are likely limited by scattering loss. The two different resonators exhibit a similar level of RMS edge roughness, 2.2 nm and 1.6 nm, as measured from SEM images of the large and small resonators, respectively. However, the 13.5 μm wedge resonators are expected to be more influenced by scattering loss than the 46.5 μm resonators, given the stronger electric field of the mode at the chalcogenide-silica and chalcogenide-air interfaces (See Figure 5.2). Moreover, the optical field is shifted away from the lithographically defined rough edges as the size increases, which leads to reduced edge scattering loss [218]. Fabrication of second-generation wedge resonators, which will optimize fabrication conditions to reduce surface roughness, is currently underway.

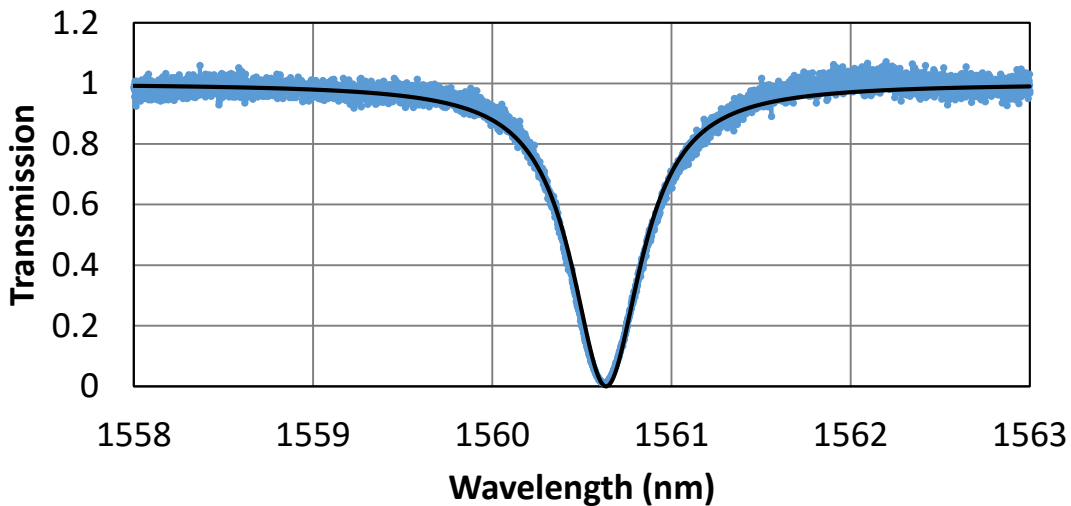


Figure 5.9. Fit for critically-coupled mode from the 13.5 μm diameter hybrid wedge resonator. The fit yields a total (loaded) Q factor of $\sim 4.6 \times 10^3$, and coupling parameter τ of 0.9826, and power attenuation coefficient a of 0.9826. The intrinsic Q is 9.2×10^3 .

We note that nonlinear device efficiencies have an important tradeoff between loss and nonlinearity. For example, the seeded four-wave mixing efficiency scales roughly as the square of both n_2 and Q . At 1550 nm, since Ge-Sb-Se bulk glass has ~ 360 times higher n_2 than fused silica, we would require $Q \sim 2.43 \times 10^6$ in chalcogenide devices to match efficiencies predicted in silica devices with $Q \sim 8.75 \times 10^8$, assuming dispersion has been engineered for phase-matching. Achieving such Q s in chalcogenide may require not only optimized silica wedge etching, but also reduction of impurities which contribute to intrinsic absorption in chalcogenide glass [235].

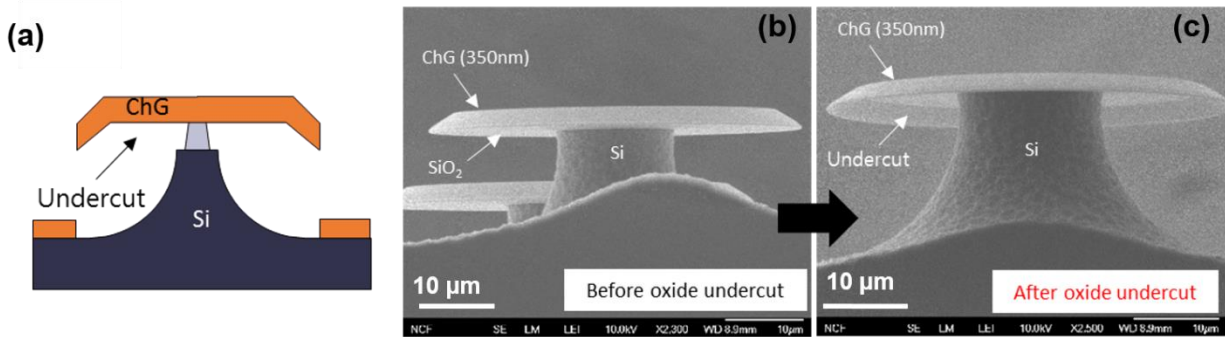


Figure 5.10. Inverted-plate ChG resonator for mid-infrared operation. (a) Schematic of inverted-plate ChG resonator, fabricated by undercutting the SiO₂ layer of hybrid ChG-silica wedge resonators. (b) Scanning electron micrograph (SEM) of wedge resonator before oxide undercut. (c) SEM of inverted-plate ChG resonator after oxide undercut, for mid-infrared operation.

Although first generation hybrid resonators were demonstrated in the near-infrared, chalcogenide-based devices have attracted most interest in the mid-infrared, where many other materials lack transparency. However, the SiO₂ layer in the hybrid structures becomes lossy beyond $\sim 3.4 \mu\text{m}$. To extend our ChG-based wedge structures to operation in the mid-infrared, we can remove the lower oxide layer to create inverted-plate resonators, as shown in Figure 5.10. To fabricate these structures, we begin with our standard hybrid wedge resonator fabrication process, as shown in Figure 5.1, and add a final oxide undercut step to remove the SiO₂ [See Figure 5.10(a)].

We employed vapor phase HF etching method with optimized processing conditions to selectively remove underlying oxide without breaking the thin and brittle ChG layer. A scanning electron micrograph (SEM) of the inverted-plate resonator after the final oxide undercut is shown in Figure 5.10(c).

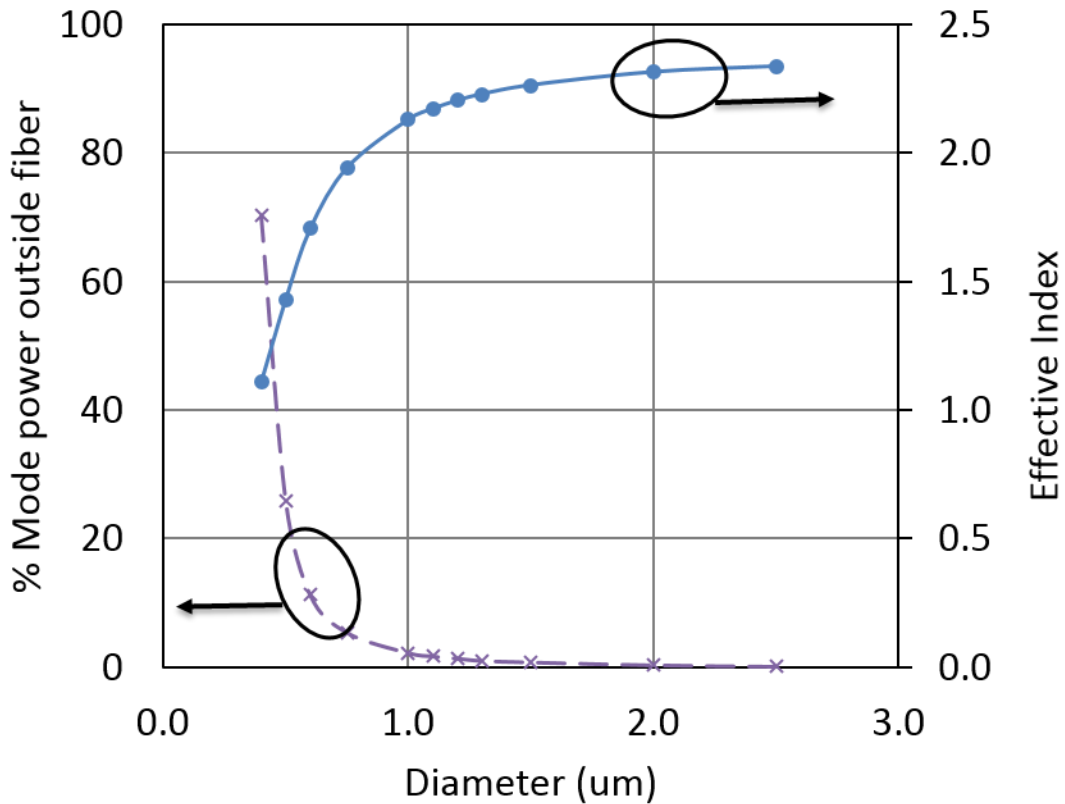


Figure 5.11. Simulated fundamental mode properties of As_2S_3 chalcogenide fiber. Plot of effective index and percentage of power of mode outside of fiber as a function of fiber diameter for As_2S_3 fiber at 1550 nm. As_2S_3 fibers can provide high effective index and reasonable power available for coupling for diameters $\sim 0.6\text{-}1.2\ \mu\text{m}$.

In the future, other fiber and sample geometries, such as U-shaped fiber tapers and pedestal strips, are under consideration to reduce taper-resonator coupling challenges presented. Additionally, we are collaborating with Dr. Tobias Kippenberg's lab to obtain chalcogenide fiber tapers with high effective index to enable phase-matching to future high-index resonators. Chalcogenide-based fibers also offer good transparency for future mid-infrared demonstrations.

A mode solver from Lumerical was used to calculate the effective index and percentage of mode power located outside the fiber for various chalcogenide As_2S_3 taper diameters. The results from these simulations are plotted in Figure 5.11. Simulations show that As_2S_3 fibers can provide high effective index and reasonable power available for coupling for diameters $\sim 0.6\text{-}1.2\ \mu\text{m}$.

5.5 Thermal characterization of wedge resonators

The thermal response of the wedge resonators was characterized by measuring the shift in resonant wavelength as a function of temperature. The sample was attached to a thermo-electric cooler (TEC)-based temperature-controlled mount using thermally conductive tape, and a thermistor was used to monitor the temperature of the mount (and Si substrate). Light was coupled to a wedge resonator (diameter of $46.5\ \mu\text{m}$) using a silica tapered fiber, and transmission spectra were recorded as a function of temperature.

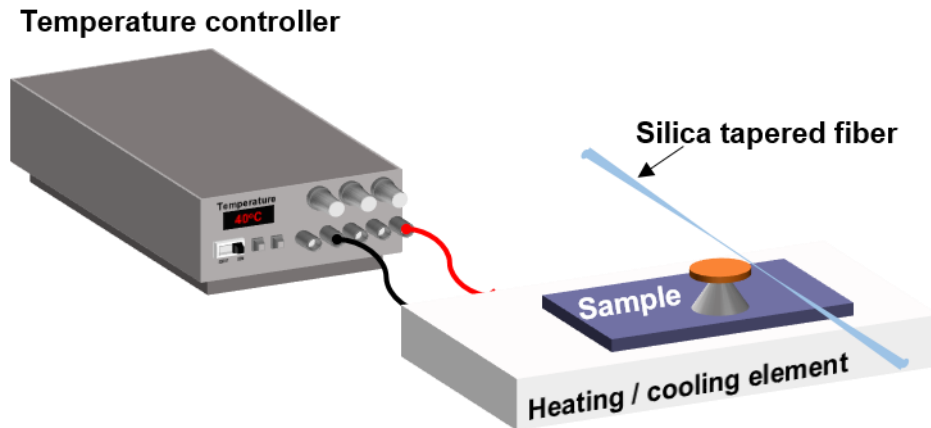


Figure 5.12. Thermal characterization setup for wedge resonators. The sample is mounted on a TEC heating/cooling element with thermally conductive tape. The temperature of the TEC is controlled through a temperature controller. A silica tapered fiber is used to couple light to and from the wedge resonator. Figure reproduced from [212].

A schematic of the experimental setup is illustrated in Fig. 5.12. Although the thermistor measured the temperature of the mount and base of sample, COMSOL simulations showed the difference in temperature between the base of the sample and the edge of the resonator was negligible over the range of temperatures studied, $\sim 20^{\circ}\text{C}$ - 42°C .

The resonant wavelength increases as the temperature increases, as shown in Figure 5.13. A plot of the corresponding shift in resonant wavelength as a function of temperature reveals a thermal resonant shift $d\lambda/dT$ of $60.5 \text{ pm}/^{\circ}\text{C}$, corresponding directly to the slope of a linear fit to the data, as shown in Figure 5.14.

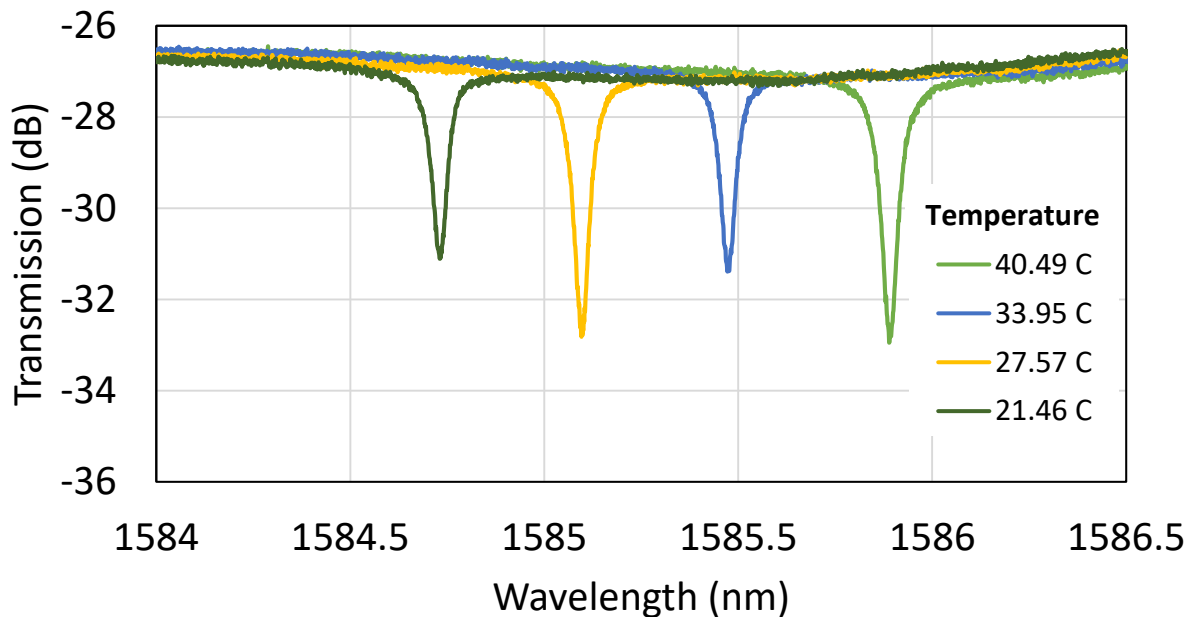


Figure 5.13. Wedge resonator transmission spectra, taken at various temperatures. Transmission spectra were measured for a $46.5 \mu\text{m}$ -diameter hybrid chalcogenide-silica wedge resonator, at various temperatures. The resonant wavelength increases as the temperature increases.

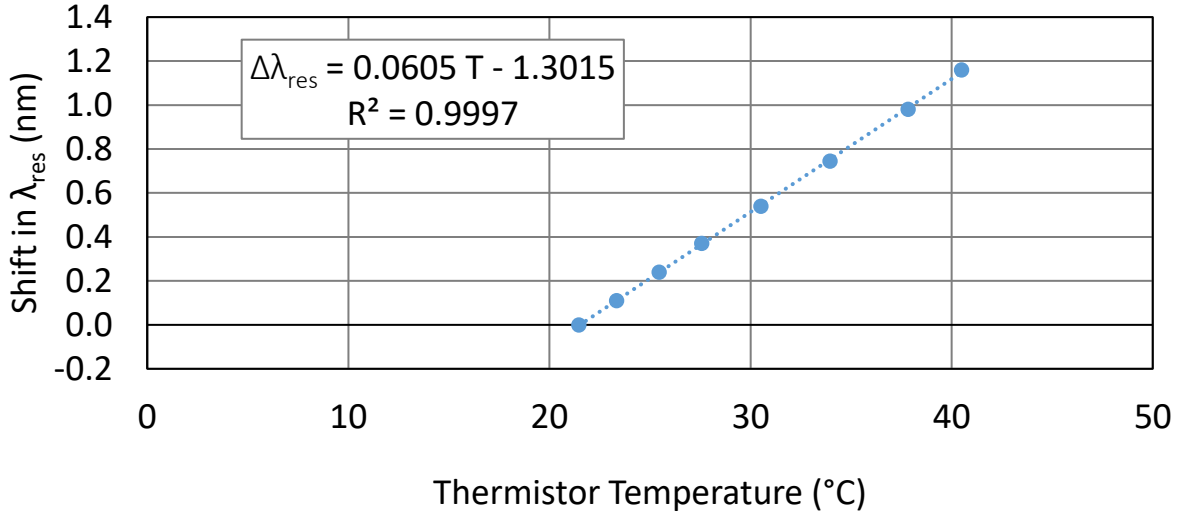


Figure 5.14. Shift in resonant wavelength as a function of temperature. As the hybrid resonator is heated, the resonant wavelength increases linearly. A linear fit to the data yields $d\lambda/dT$ of 60.5 pm/°C.

The resonant wavelength is given by

$$\lambda_{res} = \frac{2\pi R n_{eff}}{m}, \quad (5.1)$$

where R is the radius, n_{eff} is the effective index, and m is the mode index. In general, both the thermo-optic coefficient and thermal expansion can cause a shift in resonant wavelength from heating. By simply differentiating Equation 5.1 with respect to temperature, one finds that the temperature-dependent wavelength shift is expressed as

$$\frac{d\lambda_{res}}{dT} = \frac{2\pi}{m} \left[R \frac{dn_{eff}}{dT} + n_{eff} \frac{dR}{dT} \right], \quad (5.2)$$

where T is the temperature, $\frac{dn_{eff}}{dT}$ is the thermo-optic coefficient of the resonator, and $\frac{dR}{dT}$ is the thermal expansion coefficient. Given the low thermal expansion coefficient of silica and the small

thickness of chalcogenide layer in our resonator geometry, the contributions from thermal expansion of these materials are found to be negligible [153,189]. Therefore, the temperature dependence of refractive index can be approximated as

$$\frac{dn_{eff}}{dT} \approx \frac{m}{2\pi R} \frac{d\lambda}{dT}. \quad (5.3)$$

For full calculations of the contributions to a resonant wavelength shift from heating, see Appendix F. Using Equation 5.3 and the results of the temperature-dependent measurements, an average thermo-optic coefficient of the resonator, $\frac{dn_{eff}}{dT}$ of $5.5 \pm 0.4 \times 10^{-5}/K$ is calculated. This is reasonable, considering the thermo-optic coefficients of $Ge_{28}Sb_{12}Se_{60}$ ($7.44 \times 10^{-5} / K$) and fused silica ($\sim 1 \times 10^{-5}/K$) [153,219]. Based on the fraction of modal power in the chalcogenide, silica, and air layers of the resonator, $\frac{dn_{eff}}{dT}$ of $5.2 \times 10^{-5}/K$ is predicted theoretically, which is in good agreement with the average measured value.

Although a thermal resonant wavelength shift could be used as a temperature sensor, for other applications, this effect is undesirable. To reduce the thermal resonant wavelength shift, an athermal, three-layer hybrid wedge resonator design has been explored. Since both $Ge_{28}Sb_{12}Se_{60}$ and fused silica have a positive thermo-optic coefficient, including a third top layer material with a negative thermo-optic coefficient can help counter the thermal shift, compensating for thermal fluctuations from the environment or incident laser powers. Some polymers such as PDMS, PMMA, and polystyrene have been used as a cladding layer to eliminate thermal effect [220,221]. However, polymers have low thermal stability and suffer from poor thickness control. In contrast, inorganic titanium dioxide (TiO_2) is very stable at high temperatures and precise thickness control can be obtained with CMOS compatible technologies. Moreover, at 1550 nm TiO_2 has a relatively

high refractive index ~ 2.4 , which can pull the optical mode from the lower layers towards the upper TiO₂ cladding layer, reducing the thermal fluctuation significantly [222].

The optical mode profile of 3-layer hybrid resonator with TiO₂ cladding layer was simulated by Dr. Gumin Kang using COMSOL (See Figure 5.15). The light confinement factors, Γ_x , of air, ChG, TiO₂, and SiO₂ were calculated by integrating the computed light energy over each layer. The effective thermo-optic coefficient and temperature dependent resonance shift of the device can be derived based on these simulations and Eq. (5.4), taking bulk thermo-optic properties into account.

$$\frac{dn_{eff}}{dT} = \Gamma_{air} \left(\frac{dn}{dT} \right)_{air} + \Gamma_{ChG} \left(\frac{dn}{dT} \right)_{ChG} + \Gamma_{TiO_2} \left(\frac{dn}{dT} \right)_{TiO_2} + \Gamma_{SiO_2} \left(\frac{dn}{dT} \right)_{SiO_2}, \quad (5.4)$$

where Γ_x is the power confinement in material x , and $\left(\frac{dn}{dT} \right)_x$ is the thermo-optic coefficient of material x [223]. Figure 5.15(b) shows the calculated thermal drift of the resonance wavelength for different TiO₂ cladding thickness. The simulation results show that the thermo-optic properties of the resonator can be effectively engineered by changing the thickness of TiO₂ cladding layer. For the resonator without TiO₂ cladding layer, thermal shift of the resonant wavelength is 5.4×10^{-2} nm/K. However, the thermal shift can be reduced to 1.7×10^{-4} nm/K in the device with 135 nm TiO₂ cladding layer. The result shows that with the addition of TiO₂, the temperature insensitivity of the device can be improved by more than two orders of magnitude.

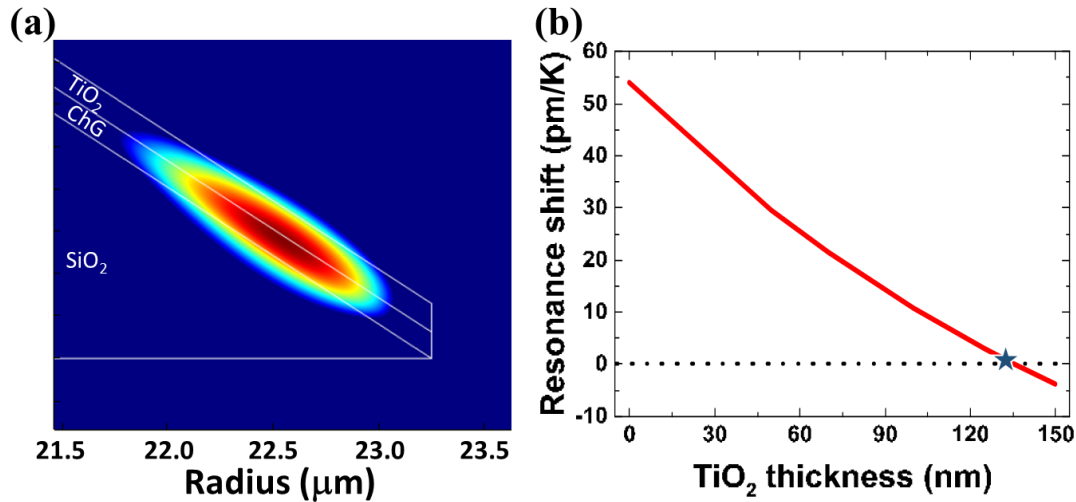


Figure 5.15 Athermal three-layer hybrid wedge simulation. (a) Cross-sectional mode profile in the athermal 3-layer hybrid resonator, consisting of lower SiO₂ layer, 125 nm-thick Ge-Sb-Se chalcogenide layer, and TiO₂ upper cladding. (b) Thermal shift of the resonant wavelength for the device with different TiO₂ thickness. The thermal resonance shift is minimized for TiO₂ thickness of 135 nm. Reproduced from [212].

5.6 Conclusion

A simple hybrid resonator design was reported, composed of a thin ChG layer deposited on a silica wedge resonator. The well-developed etch recipes for silica enable an extremely smooth surface of a silica wedge can be obtained, and the ChG overlayer deposited on it naturally forms a smooth surface. High- Q chalcogenide-silica hybrid wedge resonators were demonstrated, achieving intrinsic Q s up to 1.6×10^5 . Smaller wedge resonators were shown to have significantly lower Q than larger wedge resonators, likely due to mode profile differences resulting in increased scattering. The temperature dependence of the resonances was also characterized. A thermal resonant wavelength shift of 60.5 pm/C was measured, primarily due to the thermo-optic coefficient and in good agreement with theoretical predictions. To mitigate thermal effects in future devices, athermal 3-layer hybrid resonator designs were explored, featuring a TiO₂ coating with negative thermo-optic coefficient to reduce the thermal resonant shift by over two orders of

magnitude. Additionally, a modification of the hybrid wedge resonators to create inverted-plate ChG resonators was proposed to enable operation in the mid-infrared.

6. CONCLUSIONS

6.1 Summary

With long-wavelength transparency, high nonlinearity, and amorphous structure, chalcogenides are ideally suited for integrated nonlinear optical devices operating in the near- and mid-infrared regions. The chalcogenide glass Ge-Sb-Se was characterized in both bulk and waveguide forms, exploring the potential of a chalcogenide nonlinear photonic platform. From z-scan measurements at 1.03 μm using circularly polarized, ~ 200 fs pulses at 374 kHz, $\text{Ge}_{28}\text{Sb}_{12}\text{Se}_{60}$ exhibited a nonlinear refractive index ~ 130 x fused silica and a two-photon absorption coefficient of 3.5 cm/GW. Given the large two-photon absorption coefficient, $\text{Ge}_{28}\text{Sb}_{12}\text{Se}_{60}$ shows promise for optical limiting applications at 1 μm .

Single-mode, air-clad $\text{Ge}_{28}\text{Sb}_{12}\text{Se}_{60}$ strip waveguides, fabricated with thermal evaporation and lift-off, were also demonstrated at 1.03 μm . The nonlinear loss of these waveguides were shown to be similar to bulk samples, with differences attributed to small variations in composition of ~ 4 atomic % or less. In the waveguides, the linear loss, 11.9 dB/cm on average, was dominated by scattering loss. The nonlinear loss of the fabricated waveguides was 11.5 cm/GW, reasonable considering the enhanced two-photon absorption with the 37.4 MHz repetition rate, the overlap of the mode with the waveguide structure, and slight variations in composition.

At longer wavelengths of 1.53-1.55 μm , further from the bandedge, the linear and nonlinear loss of strip Ge-Sb-Se waveguides was significantly reduced. The average linear loss of waveguides, fabricated by photo- or e-beam lithography and liftoff, ranged from 4-6 dB/cm, and was still dominated by scattering loss at 1.53 μm . The nonlinear loss of the waveguides fabricated with e-beam lithography was 0.0055 ± 0.0004 cm/GW, in line with bulk values from literature. Using spectral broadening measurements, the nonlinear parameter of the waveguides was found to be 5.6 ± 1.7 $\text{W}^{-1}\text{m}^{-1}$, ~ 4500 x that of standard single-mode fiber. The corresponding nonlinear refractive index of the waveguides is significantly lower than what is expected from bulk, and annealing is being explored as a possible solution to improve the thin film optical properties. In spite of this, the measured nonlinear parameter and *FOM* indicates preliminary promise for nonlinear applications such as ultrafast switching at telecom wavelengths.

Ge-Sb-Se ring resonators were designed for maximum four-wave mixing efficiency at 1.55 microns. The waveguide cross sectional dimensions of the ring and bus waveguide couplers were adjusted to provide the desired dispersion and coupling strength, using a fully-vectorial mode solver and FDTD simulations. First-generation rings with 6- μm radius were found to have loaded Q s of $\sim 5 \times 10^3$ - 1×10^4 , with intrinsic Q s up to ~ 1 - 2×10^4 , corresponding to losses ~ 25 - 50 dB/cm. Considering the size-dependent intrinsic Q s, the higher measured loss in the small ring structures, is likely due to stronger electric field at the rough sidewalls for tightly bent waveguides.

High- Q hybrid chalcogenide-silica wedge resonators were also demonstrated. First generation devices with 46.5 μm diameter exhibited intrinsic Q s up to 1.6×10^5 , and smaller 13.5 μm diameter devices had intrinsic Q s up to 9.6×10^3 . The smaller devices are expected to have higher loss than the larger devices, given the stronger electric field at the surfaces of the device, causing more scattering loss. A second generation of wedge resonators is in progress, utilizing

optimized dry etch formulas for reduced roughness. Thermal characterization of the wedge resonators was also performed, revealing a resonant wavelength shift of 60.5 pm/C, primarily due to the thermo-optic coefficient of the Ge-Sb-Se and silica. In the future, athermal designs utilizing negative thermo-optic materials to mitigate this shift can be studied.

Finally, in the mid-infrared, new single-mode, air-clad Ge-Sb-Se-on-MgF₂ waveguides were designed for operation at 3.5 μm , focusing on dimensions with near-zero dispersion for improved spectral broadening, compared to designs with no dispersion-engineering. Corresponding ring resonators were designed for optimized four-wave mixing efficiency at 3.5 μm . To date, other demonstrations of chalcogenide microrings have focused solely on linear properties and have failed to take advantage of the materials' excellent nonlinear optical properties. With our Ge-Sb-Se chalcogenide resonator designs, we hope to demonstrate resonantly-enhanced nonlinear optics in a chalcogenide platform, providing a route to reduce thresholds through improved nonlinearity, and to extend nonlinear device operation further into the mid-infrared, where the chalcogenide platform maintains excellent transparency.

6.2 Future directions

This research has raised multiple questions to investigate in the future. Our initial z-scan experiments at 1 μm highlighted the fact that the photosensitivity of chalcogenide materials is not well understood. Gaining a better sense of the exact origin and mechanisms behind this effect, along with developing models for how it scales with intensity and wavelength would aid researchers developing chalcogenides for practical applications. One could use Raman spectroscopy or X-ray absorption spectroscopy to systematically explore changes in atomic structure in the materials, under a range of illumination conditions and wavelengths. Examining various chalcogenide samples with different compositions may help give further clues to the

origins of photosensitivity, particularly if certain compositions are found to be more photostable than others. Additionally, by exploring the time response of photosensitivity with a time-resolved technique, one may gain further insight into possible mechanisms that could act on the given time scale.

From our chalcogenide waveguide studies, we found that the nonlinear refractive index in thin film and bulk can vary quite drastically, indicating the importance of checking thin film properties when fabricating new devices. We found at conferences that this is a widespread problem. Our collaborators are just beginning to explore annealing as a potential solution. In the future, the group plans to measure the nonlinearity of multiple waveguide samples as a function of annealing temperature, to determine optimal processing conditions which yield nonlinearity closest to bulk.

The Q measured in our first-generation $6\ \mu\text{m}$ rings prohibited an initial four-wave mixing demonstration. To enable such a demonstration in the near future, one could utilize the higher $Q \sim 8 \times 10^4$ measured in the larger $20\ \mu\text{m}$ ring resonators, with an important revision of the chip layout. We suggest including add-drop, critically-coupled, $20\ \mu\text{m}$ ring resonators, with just a single ring per input bus waveguide. (The current layout utilized multiple rings per bus waveguide for loss measurements in the larger ring resonators. While this was a compact, efficient layout for loss measurements, it reduced the power coupled to the ring and prohibited low power four-wave mixing demonstrations in the larger ring resonators.)

To further improve four-wave mixing efficiency, one could also explore approaches to increase Q . Our waveguide and ring resonator work focused on single-mode strip waveguides, which offer substantial dispersion engineering through waveguide dimensions, along with good

confinement, enabling few μm -radii bends with negligible calculated radiation loss. However, strip waveguides tend to have strong field along the full sidewalls of the waveguides, increasing scattering loss to values typically on the order of a few dB/cm or more. Two waveguide geometries shown to reduce loss are rib and strip-loaded waveguides, with typical losses near or at the material loss limit, $\sim 0.05\text{-}0.8$ dB/cm [106,163]. Since the optical mode is not as strongly confined in these geometries, radiation loss from bending is more severe, requiring larger ring resonators to avoid bend loss. Additionally, dispersion is more difficult to control. However, through careful design, M. R. E. Lamont et al. has shown broadband dispersion engineering in rib waveguides [209]. To significantly reduce propagation losses and improve Q , further exploration of rib or strip-loaded waveguides may be a promising path. Although using larger rings increases the mode volume, the improvement in Q may easily compensate, improving the overall efficiency. To explore this, one could design the dispersion and coupling of rib-based ring resonators, and then characterize Q and the four-wave mixing efficiency.

While strip waveguide-based ring resonator dimensions were optimized for four-wave mixing in this research, one could imagine designing and optimizing resonators for other effects, such as stimulated Brillouin scattering, Raman scattering, rotation sensing, or switching. The majority of this thesis work has focused on the near-infrared to leverage existing equipment and more readily available optical components. However, we believe chalcogenides may be most useful in the mid- and long-wave infrared, where high quality optical materials are lacking. For example, at $\sim 10\text{-}12$ μm , many commonly used materials, including Si, MgF_2 , and CaF_2 are absorbing, while Ge-Sb-Se remains transparent. We have successfully tested devices out to wavelengths ~ 1630 nm, and in the future, one could envision extending this work to longer wavelengths. For example, sensing waveguides and resonators could be developed and tested to

more precisely detect various chemicals in the mid- and long-wave infrared, $\sim 3\text{-}12\ \mu\text{m}$. One could begin with Q measurements to quantify the loss in basic resonator structures. One could also design and test waveguides for sensing, considering surface-enhanced infrared absorption (SEIRA) as a potential method for boosting sensitivity. Alternatively, one could design ultrafast chalcogenide-based switches and modulators in the mid-infrared, where components are limited.

The results presented show Ge-Sb-Se to be a promising candidate for nonlinear integrated optics, featuring high nonlinearity and low nonlinear loss at telecom wavelengths. Future research at the University of Colorado Boulder will build on this work, exploring intricacies of thin-film devices and processing, and developing compact, low-threshold nonlinear optical devices in the near- to long-wave infrared.

REFERENCES

- [1] K. F. Rauscher, “ROGUCCI – The Report,” in *IEEE Proceedings of the Reliability of Global Undersea Cable Communications Infrastructure Study & Global Summit*, Issue 1, 2010.
- [2] F. Burkhart, “AIM Photonics workshop ponders 2025 strategies,” SPIE Optics.org, <http://optics.org/news/8/4/5>
- [3] J. Viegas, “The NOOR Lab: Nano-Optics and Optoelectronics Research,” Masdar Institute of Science and Technology, <http://nanophotonics.labs.masdar.ac.ae/research.htm>, 2012.
- [4] S.E. Miller, “Integrated Optics: An Introduction”, *The Bell System Technical Journal* **48**, 2059–2068 (1969).
- [5] R. W. Boyd, *Nonlinear Optics* (Academic Press, 2009).
- [6] S. M. Hendrickson, A. C. Foster, R. M. Camacho, and B. D. Clader, “Integrated nonlinear photonics: emerging applications and ongoing challenges,” *Journal of the Optical Society of America B* **31** (12), 3193-3203 (2014).
- [7] K. E. Stubkjaer, “Semiconductor optical amplifier-based all-optical gates for high-speed optical processing,” *IEEE Journal of Selected Topics in Quantum Electronics* **6** (14), 1428-1435 (2000).
- [8] G. Steinmeyer, D. H. Sutter, L. Gallmann, N. Matuschek, and U. Keller, “Frontiers in ultrashort pulse generation: Pushing the limits in linear and nonlinear optics,” *Science* **286** (5444), 1507-1512 (1999).
- [9] T. J. Kippenberg, R. Holzwarth, and S. A. Diddams, “Microresonator-based optical frequency combs,” *Science* **332** (6029), 555-559 (2011).
- [10] A. G. Griffith, R. K. W. Lau, J. Cardenas, Y. Okawachi, A. Mohanty, R. Fain, Y. H. D. Lee, M. Yu, C. T. Phare, C. B. Poitras, A. L. Gaeta, and M. Lipson, “Silicon-chip mid-infrared frequency comb generation,” *Nature Communications* **6**, 1-5 (2015).
- [11] M. Davano, J. R. Ong, A. B. Shehata, A. Tosi, I. Agha, S. Assefa, F. Xia, W. M. J. Green, S. Mookherjea, and K. Srinivasan, “Telecommunications-band heralded single photons from a silicon nanophotonic chip,” *Applied Physics Letters* **100**, 261104 (2012).
- [12] C. Reimer, L. Caspani, M. Clerici, M. Ferrera, M. Kues, M. Peccianti, A. Pasquazi, L. Razzari, B. E. Little, S. T. Chu, D. J. Moss, and R. Morandotti, “Integrated frequency comb source of heralded single photons,” *Optics Express* **22**, 6535–6546 (2014).
- [13] V. G. Ta’eed, M. Shokooh-Saremi, L. Fu, I. C. M. Littler, D. J. Moss, M. Rochette, B. J. Eggleton, Y. Ruan, and B. Luther-Davies, “Self-phase modulation-based integrated optical

- regeneration in chalcogenide waveguides,” *IEEE Journal of Selected Topics in Quantum Electronics* **12** (3) 360-370 (2006).
- [14] Y. Yu, X. Gai, T. Wang, P. Ma, R. Wang, Z. Yang, D. -Y. Choi, S. Madden, and B. Luther-Davies, “Mid-infrared supercontinuum generation in chalcogenides,” *Optical Materials Express* **3** (8), 1075-1086 (2013).
- [15] C. R. Petersen, U. Moller, I. Kubat, B. Zhou, S. Dupont, J. Ramsay, T. Benson, S. Sujecki, N. Abdel-Moneim, Z. Tang, D. Furniss, A. Seddon, and O. Bang, “Mid-infrared supercontinuum covering the 1.3-13.3 μm molecular fingerprint region using ultra-high NA chalcogenide step-index fibre,” *Nature Photonics* **8** 830-834 (2014).
- [16] M. Nisoli, S. De Sivistri, and O. Svelto, “Generation of high energy 10 fs pulses by a new pulse compression technique,” *Applied Physics Letters* **68**, 2793 (1996).
- [17] A. Chong, J. Buckley, W. Renninger, and F. Wise, “All-normal-dispersion femtosecond fiber laser,” *Optics Express* **14** (21), 10095-10100 (2006).
- [18] X. Liu, R. M. Osgood Jr., Y. A. Vlasov, and W. M. J. Green, “Mid-infrared optical parametric amplifier using silicon nanophotonic waveguides,” *Nature Photonics* **4**, 557-560 (2010).
- [19] F. C. Cruz, D. L. Maser, T. Johnson, G. Ycas, A. Klose, F. R. Giorgetta, I. Coddington, and S. A. Diddams, “Mid-infrared optical frequency combs based on difference frequency generation for molecular spectroscopy,” *Optics Express*. **23** (20), 26814-26824 (2015)
- [20] A. Schliesser, N. Picque, and T. W. Hänsch, “Mid-infrared frequency combs,” *Nature Photonics* **6**, 440-449 (2012).
- [21] U. Willer et al., “Near- and mid-infrared laser monitoring of industrial processes, environment and security applications,” *Optics and Lasers in Engineering* **44**, 699 (2006).
- [22] C. Lecaplain, C. Javerzac-Galy, M. L. Gorodetsky, and T. J. Kippenberg, “Mid-infrared ultra-high-Q resonators based on fluoride crystalline materials,” *Nature Communications* **7**, 13383 (2016).
- [23] B. H. Stuart, *Infrared Spectroscopy: Fundamentals and Applications* (Wiley, 2004).
- [24] Frank K. Tittel, “Environmental trace gas detection using laser spectroscopy,” *Applied Physics B*. **67**, 273 (1998).
- [25] I. M. Craig, M. S. Taubman, A. S. Lea, M. C. Phillips, E. E. Josberger, and M. B. Raschke, “Infrared near-field spectroscopy of trace explosives using an external cavity quantum cascade laser,” *Optics Express* **21**, 30401 (2013).

- [26] M. R. Robinson, R. P. Eaton, D. M. Haaland, G. W. Koepp, E. V. Thomas, B. R. Stallard, and P. L. Robinson, "Noninvasive glucose monitoring in diabetic patients: a preliminary evaluation," *Clinical Chemistry* **38**, 1618 (1992).
- [27] N. S. Daghestani, R. Brownsword, and D. Weidmann, "Analysis and demonstration of atmospheric methane monitoring by mid-infrared open-path chirped laser dispersion spectroscopy," *Optics Express* **22** (S7), A1731-A1743 (2014).
- [28] U. Willer, M. Saraji, A. Khorsandi, P. Geiser, and W. Schade, "Near- and mid-infrared laser monitoring of industrial processes, environment and security applications," *Optics and Lasers in Engineering* **44**, 699 (2006).
- [29] D. Z. Garbuzov, H. Lee, V. Khalfin, R. Martinelli, J. C. Connolly, and G. L. Belenky, "2.3–2.7 μm room temperature CW operation of InGaAsSb–AlGaAsSb broad waveguide SCH-QW diode lasers," *IEEE Photonics Technology Letters* **11**, 794–796 (1999).
- [30] J. Faist, F. Capasso, D. L. Sivco, C. Sirtori, A. L. Hutchinson, and A. Y. Cho, "Quantum cascade laser," *Science* **264** (5158), 553-556 (1994).
- [31] S. D. Jackson, "Towards high-power mid-infrared emission from a fibre laser," *Nature Photonics* **6**, 423 (2012).
- [32] C. Erny, K. Moutzouris, J. Biegert, D. Kuhlke, F. Adler, A. Leitenstorfer, and U. Keller, "Mid-infrared difference-frequency generation of ultrashort pulses tunable between 3.2 and 4.8 μm from a compact fiber source," *Optics Letters* **32**, 1138-1140 (2007).
- [33] J. Peng, "Developments of mid-infrared optical parametric oscillators for spectroscopic sensing: a review," *Optical Engineering* **53** (6), 061613 (2013).
- [34] H. K. Choi, *Long-Wavelength Infrared Semiconductor Lasers*, (John Wiley & Sons, Inc., 2004), Chap. 3.
- [35] F. Capasso, "High-performance midinfrared quantum cascade lasers," *Optical Engineering* **49** (11), 111102 (2010).
- [36] V. Fortin, F. Maes, M. Bernier, S. T. Bah, M. D'Auteuil, and R. Vallee, "Watt-level erbium-doped all-fiber laser at 3.44 μm ," *Optics Letters* **41** (3) 559-562 (2016).
- [37] F. Träger, *Springer Handbook of Lasers and Optics*, (Springer-Verlag, 2012), pp. 708-709.
- [38] A. Krier, *Mid-Infrared Semiconductor Optoelectronics*, 2nd ed. (Springer-Verlag, 2006), pp. 248.
- [39] Y. Liu, Y. Xuan, X. Xue, P.-H. Wang, S. Chen, A. J. Metcalf, J. Wang, D. E. Leaird, M. Qi, and A. M. Weiner, "Investigation of mode coupling in normal-dispersion silicon nitride microresonators for Kerr frequency comb generation," *Optica* **1**, 3 (2014).

- [40] L. Chang, X. Jiang, S. Hua, C. Yang, J. Wen, L. Jiang, G. Li, G. Wang, and M. Xiao, "Parity-time symmetry and variable optical isolation in active-passive-coupled microresonators," *Nature Photonics* **8**, 524-529 (2014).
- [41] D. K. Armani, T. J. Kippenberg, S. M. Spilane, and K. J. Vahala, "Ultra-high-Q toroid microcavity on a chip," *Nature* **421**, 905-908 (2003).
- [42] H. Lee, T. Chen, J. Li, K. Y. Yang, S. Jeon, O. Painter, and K. J. Vahala, "Chemically etched ultrahigh-Q wedge-resonator on a silicon chip," *Nature Photonics* **6**, 369-373 (2012).
- [43] V. B. Braginsky, M. L. Gorodetsky, and V. S. Ilchenko, "Quality-factor and nonlinear properties of optical whispering-gallery modes," *Physics Letters A* **137**, 393-397 (1989).
- [44] M. L. Gorodetsky, A. A. Savchenkov, and V. S. Ilchenko, "Ultimate Q of optical microsphere resonators," *Optics Letters* **21**, 453-455 (1996).
- [45] M. Soltani, S. Yegnanarayanan, and A. Adibi, "Ultra-high Q planar silicon microdisk resonators for chip-scale silicon photonics," *Optics Express* **15** (8) 4694-4704 (2007).
- [46] A. Gondarenko, J. S. Levy, and M. Lipson, "High confinement micron-scale silicon nitride high Q ring resonator," *Optics Express* **17** (14) 11366-11370 (2009).
- [47] J. Hofer, A. Schliesser, and T. J. Kippenberg, "Cavity optomechanics with ultrahigh-Q crystalline microresonators," *Physical Review A* **82**, 031804(R) (2010).
- [48] L. Maleki, "Sources: The optoelectronic oscillator," *Nature Photonics* **5**, 728-730 (2011).
- [49] D. T. Spencer, J. F. Bauters, M. J. R. Heck, and J. E. Bowers, "Integrated waveguide coupled Si₃N₄ resonators in the ultrahigh-Q regime," *Optica* **1** (3) 153-157 (2014).
- [50] A. Gondarenko, J. S. Levy, and M. Lipson, "High confinement micron-scale silicon nitride high Q ring resonator," *Optics Express* **17** (14) 11366-11370 (2009).
- [51] Q. Li, A. A. Eftekhari, M. Sodagar, Z. Xia, A. H. Atabaki, and A. Adibi, "Vertical integration of high-Q silicon nitride microresonators into silicon-on-insulator platform," *Optics Express* **21** (15) 18236-18248 (2013).
- [52] T. M. Benson, S. V. Boriskina, P. Sewell, A. Vukovic, S. C. Greedy, and A. I. Nosich, "Micro-optical resonators for microlasers and integrated optoelectronics" in S. Janz et al. (eds), *Frontiers in Planar Lightwave Circuit Technology*, 29-70. Springer 2006.
- [53] S. M. Grist et al., "Silicon photonic micro-disk resonators for label-free biosensing," *Optics Express* **21**, 7994-8006 (2013).

- [54] X. Jiang *et al.*, “On-Chip Optical Nonreciprocity Using an Active Microcavity,” *Scientific Reports* **6**, 38972 (2016).
- [55] P. Del Hays, T. Herr, E. Gavartin, M. L. Gordetsky, R. Holzwarth, and T. J. Kippenberg, “Octave spanning tunable frequency comb from a microresonator,” *Physical Review Letters* **107**, 063901 (2011).
- [56] M. R. Krogstad, S. Ahn, W. Park, and J. T. Gopinath, “Nonlinear characterization of Ge₂₈Sb₁₂Se₆₀ bulk and waveguide devices,” *Optics Express*, **23** (6), 7870-7878 (2015).
- [57] L. Razzari, D. Duchesne, M. Ferrera, R. Morandotti, S. Chu, B. E. Little, and D. J. Moss, “CMOS-compatible integrated optical hyper-parametric oscillator,” *Nature Photonics* **4**, 41-45 (2010).
- [58] J. S. Levy, A. Gondarenko, M. A. Foster, A. C. Turner-Foster, A. L. Gaeta, and M. Lipson, “CMOS-compatible multiple-wavelength oscillator for on-chip optical interconnects,” *Nature Photonics* **4**, 37-40 (2010).
- [59] A. A. Savchenkov, A. B. Matsko, V. S. Ilchenko, I. Solomatine, D. Seidel, and L. Maleki, “Tunable optical frequency comb with a crystalline whispering gallery mode resonator,” *Physical Review Letters* **101**, 093902 (2008).
- [60] C. Y. Wang, T. Herr, P. Del’Hays, A. Schliesser, J. Hofer, R. Holzwarth, T. W. Haensch, N. Picque, and T. J. Kippenberg, “Mid-infrared optical frequency combs at 2.5 μm based on crystalline microresonators,” *Nature Communications* **4** (1345), 2335 (2013).
- [61] B. J. Eggleton, B. Luther-Davies, and K. Richardson, “Chalcogenide photonics,” *Nature Photonics* **5** (3), 141-148 (2011).
- [62] G. P. Agrawal, *Nonlinear Fiber Optics*, 5th ed. (Academic Press, 2013), Chap. 11.
- [63] C. J. Kruckel, A. Fulop, T. Klintberg, J. Bengtsson, P. A. Andrekson, and V. Torres-Company, “Linear and nonlinear characterization of low-stress high-confinement silicon-rich nitride waveguides,” *Optics Express* **23** (20) 25827-25837 (2015).
- [64] W. Liang, A. B. Matsko, A. A. Savchenkov, V. S. Ilchenko, D. Seidel, and L. Maleki, “Generation of Kerr combs in MgF₂ and CaF₂ microresonators,” in *Joint Conference of the IEEE International Frequency Control and the European Frequency and Time Forum (FCS) Proceedings* (IEEE, 2011), pp. 1–6.
- [65] G. Lenz, J. Zimmermann, T. Katsufuji, M. E. Lines, H. Y Hwang, S. Spaelter, R. E. Slusher, S.-W. Cheong, J. S. Sanghera, and I. D. Aggarwal, “Large Kerr effect in bulk Se-based chalcogenide glasses,” *Optics Letters* **25** (4), 254-256 (2000).
- [66] <http://infraredtraininginstitute.com/thermography-information/infrared-transparent-materials/>

- [67] Schott Infrared Chalcogenide Glasses Datasheet, IRG22,
http://www.us.schott.com/d/advanced_optics/8240cca9-245b-41ec-8049-fd4c39279756/1.0/schott-infrared-chalcog-glasses-irg22-january-2016-us.pdf
- [68] Schott Infrared Chalcogenide Glasses Datasheet, IRG25,
http://www.us.schott.com/d/advanced_optics/d91edc7a-ce5a-4d0a-a772-02278ec382c0/1.0/schott-infrared-chalcog-glasses-irg25-january-2016-us.pdf
- [69] Schott Infrared Chalcogenide Glasses Datasheet, IRG26,
http://www.us.schott.com/d/advanced_optics/866702a2-39e9-41a5-ac2b-c28e10f0fbff/1.0/schott-infrared-chalcog-glasses-irg26-january-2016-us.pdf
- [70] P. T. Lin, V. Singh, H. -Y. G. Lin, T. Tiwald, L. C. Kimerling, and A. M. Agarwal, "Low-stress silicon nitride platform for mid-infrared broadband and monolithically integrated microphotonics," *Advanced Optical Materials* **1** (10) 732-739 (2013).
- [71] B. Maniscalco, P. M. Kaminski, J. M. Walls, "Thin film thickness measurements using scanning white light interferometry," *Thin Solid Films* **550**, 10-16 (2014).
- [72] J. S. Sanghera, C. M. Florea, L. B. Shaw, P. Pureza, V. Q. Nguyen, M. Bashkansky, Z. Dutton, and I. D. Aggarwal, "Non-linear properties of chalcogenide glasses and fibers," *Journal of Non-Crystalline Solids* **354** (2-9), 462-467 (2008).
- [73] A. Zakery and S. R. Elliot, "Optical properties and applications of chalcogenide glasses: a review," *Journal of Non-Crystalline Solids* **330** (1-3), 1-12 (2003).
- [74] G. K. Ahluwalia, *Applications of Chalcogenides: S, Se, and Te* (Springer, 2016).
- [75] J. Ihm, "Urbach tails and the structure of chalcogenide glasses," *Solid State Communications* **53** (3), 293-296 (1985).
- [76] M. M. Wakkad, E. Kh Shokr, and S. H. Mohamed, "Optical and calorimetric studies of Ge-Sb-Se glasses," *Journal of Non-Crystalline Solids* **265**, 157-166 (2000).
- [77] K. J. Rao, *Structural Chemistry of Glasses*, (Elsevier Science Ltd., 2002), pp. 26.
- [78] http://www.wikiwand.com/en/Structure_of_liquids_and_glasses
- [79] M. F. Thorpe, D. J. Jacobs, and B. R. Djordjevic, "The structure and rigidity of network glasses," in *Insulating and Semiconducting glasses*, P. Boolchand, ed. (World Scientific, 2000), pp. 94-145.
- [80] K. Tanaka, "Structural phase transitions in chalcogenide glasses," *Physical Review B* **39**, 1270-1279 (1989).

- [81] W. -H. Wei, R. -P. Wang, X. Shen, L. Fang, and B. Luther-Davies, "Correlation between structural and physical properties in Ge-Sb-Se glasses," *Journal of Physical Chemistry* **117**, 16571-16576 (2013).
- [82] M. Shpotyuk, M. Hyla, O. Shpotyuk, and V. Gurin, "Radiation-induced bond switching in chalcogenide semiconductor glasses from first-principles quantum-chemical calculations: On the role of dipole-type charged coordination defects," *Computational Materials Science* **113**, 112-116 (2016).
- [83] J. D. Musgraves, K. Richardson, and H. Jain, "Laser-induced structural modification, its mechanisms, and applications in glassy optical materials," *Optical Materials Express* **1** 921-935 (2011).
- [84] J.-F. Viens, C. Meneghini, A. Villeneuve, T. V. Galstian, E. J. Knystautas, M. A. Duguay, K. A. Richardson, and T. Cardinal, "Fabrication and characterization of integrated optical waveguides in sulfide chalcogenide glasses," *Journal of Lightwave Technology* **17** (7) 1184-1191 (1999).
- [85] M. A. Hughes, W. Yang, and D. W. Hewak, "Spectral broadening in femtosecond laser written waveguides in chalcogenide glass," *Journal of the Optical Society of America B* **26** (7) 1370-1378 (2009).
- [86] A. Canciamilla, S. Grillanda, F. Morichetti, C. Ferrari, J. Hu, D. Musgraves, K. Richardson, A. Agarwal, L. C. Kimerling, and A. Melloni, "Photo-induced trimming of coupled ring-resonator filters and delay lines in As₂S₃ chalcogenide glass," *Optics Letters* **36** (20), 4002-4004 (2011).
- [87] K. Shimakawa, A. Kolobov, and S. R. Elliott, "Photoinduced effects and metastability in amorphous semiconductors and insulators," *Advances in Physics* **44**, 475-588 (1995).
- [88] J. Hu, V. Tarasov, N. Carlie, N.-N. Feng, L. Petit, A. Agarwal, K. Richardson, and L. Kimerling, "Si-CMOS-compatible lift-off fabrication of low-loss planar chalcogenide waveguides," *Optics Express* **15** (19), 11798-11807 (2007).
- [89] A. Herzog, B. Hadad, V. Lyubin, M. Klebanov, A. Reiner, A. Shamir, and A. A. Ishaaya, "Chalcogenide waveguides on a sapphire substrate for mid-IR applications," *Optics Letters* **39** (8) 2522-2525 (2014).
- [90] B. Luther-Davies, P. Ma, S. Madden, D.-Y. Choi, Z. Yang, and R. Wang, "Chalcogenide glass waveguides for the mid-infrared," in *CLEO: 2013*, OSA Technical Digest (online) (Optical Society of America, 2013), paper CTh4F.6.
- [91] J. M. Harbold, F. O. Ilday, F. W. Wise, and B. G. Aiken, "Highly nonlinear Ge-As-Se and Ge-As-S-Se glasses for all-optical switching," *Photonics Technology Letters* **14** (6), 822-824 (2002).

- [92] F. Smektala, C. Quemard, V. Couderc, and A. Barthelemy, "Non-linear optical properties of chalcogenide glasses measured by z-scan," *Journal of Non-Crystalline Solids* **274** (1-3), 232-237 (2000).
- [93] T. Wang, X. Gai, W. Wei, R. Wang, Z. Yang, X. Shen, S. Madden, and B. Luther-Davies, "Systematic z-scan measurements of the third order nonlinearity of chalcogenide glasses," *Optical Materials Express* **4** (5), 1011-1022 (2014).
- [94] M. Olivier, J.C. Tchahame, P. Němec, M. Chauvet, V. Besse, C. Cassagne, G. Boudebs, G. Renversez, R. Boidin, E. Baudet, and V. Nazabal, "Structure, nonlinear properties, and photosensitivity of $(\text{GeSe}_2)_{100-x}(\text{Sb}_2\text{Se}_3)_x$," *Optical Materials Express* **4** (3), 525-540 (2014).
- [95] S. Dai, F. Chen, Y. Xu, Z. Xu, X. Shen, T. Xu, R. Wang, and W. Ji, "Mid-infrared optical nonlinearities of chalcogenide glasses in Ge-Sb-Se ternary system," *Optics Express* **23** (2), 1300-1307 (2015).
- [96] F. Theberge, P. Mathieu, N. Thire, J.-F. Daigle, B. E. Schmidt, J. Fortin, R. Vallee, Y. Messaddeq, and F. Legare, "Mid-infrared nonlinear absorption in As_2S_3 chalcogenide glass," *Optics Express* **24** (21) 24600-24610 (2016).
- [97] Y. Huang, F. Chen, R. Lin, X. Zhang, S. Dai, Q. Nie, and X. Zhang, "Glass formation and mid-infrared optical nonlinearities of chalcogenide glasses in germanium-tin-sulfur ternary system," *Optical Materials Express* **6** (10), 3053-3062 (2016).
- [98] P. A. Thielen, L. B. Shaw, P. C. Pureza, V. Q. Nguyen, J. S. Sanghera, and I. D. Aggarwal, "Small-core As-Se fiber for Raman amplification," *Optics Letters* **28** (16), 1406-1408 (2003).
- [99] S. Shabahang, G. Tao, M. P. Marquez, H. Hu, T. R. Ensley, P. J. Delfyett, and A. F. Abouraddy, "Nonlinear characterization of robust multimaterial chalcogenide nanotapers for infrared supercontinuum generation," *Journal of the Optical Society of America B* **31** (3), 450-457 (2014).
- [100] S. Spälter, H. Y. Hwang, J. Zimmermann, G. Lenz, T. Katsufuji, S.-W. Cheong, and R. E. Slusher, "Strong self-phase modulation in planar chalcogenide glass waveguides," *Optics Letters* **27** (5), 363-365 (2002).
- [101] P. Ma, D.-Y. Choi, Y. Yu, X. Gai, Z. Yang, S. Debbarma, S. Madden, and B. Luther-Davies, "Low-loss chalcogenide waveguides for chemical sensing in the mid-infrared," *Optics Express* **21** (24), 29927-29937 (2013).
- [102] C. Tsay, F. Toor, C. F. Gmachl, and C. B Arnold, "Chalcogenide glass waveguides integrated with quantum cascade lasers for on-chip mid-IR photonic circuits," *Optics Letters* **35** (20), 3324-3326 (2010).

- [103] J. Hu, N. Carlie, N. N. Feng, L. Petit, A. Agarwal, K. Richardson, L. Kimerling, “Planar waveguide-coupled high-index-contrast, high-Q resonators in chalcogenide glass for sensing,” *Optics Letters* **33** (21), 2500-2502 (2008).
- [104] L. Li, H. Lin, S. Qiao, Y. Zou, S. Danto, K. Richardson, J. D. Musgraves, N. Lu, and J. Hu, “Integrated flexible chalcogenide glass photonic devices,” *Nature Photonics* **8**, 643-649 (2014).
- [105] O. Aktas, E. Ozgur, O. Tobail, M. Kanik, E. Huseyinoglu, and M. Bayindir, “A new route for fabricating on-chip chalcogenide microcavity resonator arrays,” *Advanced Optical Materials* **2** (7), 618-625 (2014).
- [106] J. Chiles, M. Malinowski, A. Rao, S. Novak, K. Richardson, and S. Fathpour, “Low-loss, submicron chalcogenide integrated photonics with chlorine plasma etching,” *Applied Physics Letters* **106** (11), 111110 (2015).
- [107] T. D. Vo, M. D. Pelusi, J. Schröder, F. Luan, S. J. Madden, D.-Y. Choi, D. A. P. Bulla, B. Luther-Davies, and B. J. Eggleton, “Photonic mulit-impairment monitoring of 640 Gb/s signals using photonic chip based RF spectrum analyzer,” *Optics Express* **18** (4), 3938-3945 (2010).
- [108] P. Klocek and L. Columbo, “Index of refraction, dispersion, bandgap, and light scattering in GeSe and GeSbSe glasses,” *Journal of Non-Crystalline Solids* **93** (1), 1-16 (1987).
- [109] P. Klocek, *Handbook of Infrared Optical Materials* (Marcel Dekker, Inc., 1991).
- [110] R. de Nalda, R. del Coso, J. Requejo-Isidro, J. Olivares, A. Suarez-Garcia, J. Solis, and C. N. Afonso, “Limits to the determination of the nonlinear refractive index by the z-scan method,” *Jouranl of the Optical Society of America B* **19** (2) 289 (2002).
- [111] P. W. Smith, W. J. Tomlinson, D. J. Eilenberger, and P. J. Maloney, “Measurement of electronic optical Kerr coefficients,” *Optics Letters* **6** (12) 581-583 (1981).
- [112] S. R. Friberg and P. W. Smith, “Nonlinear optical glasses for ultrafast optical switches,” *IEEE Journal of Quantum Electronics* **23** (12) 2089 (1987).
- [113] M. Sheik-Bahae, A. A. Said, T. H. Wei, D. J. Hagan, and E. W. Van Stryland, “Sensitive measurement of optical nonlinearities using a single beam,” *IEEE Journal of Quantum Electron.* **26** (4), 760-769 (1990).
- [114] M. Dinu, F. Quochi, and H. Garcia, “Third-order nonlinearities in silicon at telecom wavelengths,” *Applied Physics Letters* **82** (18), 2954-2956 (2003).
- [115] B. K. Rhee, J. S. Byun, E. W. Van Stryland, “Z scan using circularly symmetric beams,” *Journal of the Optical Society of America B*, **13** (12) 2720-2723 (1996).

- [116] B. Gu, W. Ji, and X.-Q. Huang, “Analytical expression for femtosecond-pulsed z scans on instantaneous nonlinearity,” *Applied Optics* **47** (9), 1187-1192 (2008).
- [117] M. Falconieri, “Thermo-optical effects in Z-scan measurements using high-repetition-rate lasers,” *Journal of Optics A: Pure and Applied Optics* **1** (6), 662-667 (1999).
- [118] M. Sheik-Bahae, D. Crichton Hutchings, D. J. Hagan, and E. W. Van Stryland, “Dispersion of bound electronic nonlinear refraction in solids,” *IEEE Journal of Quantum Electronics* **27** (6), 1296-1309 (1991).
- [119] M. Dinu, “Dispersion of phonon-assisted nonresonant third-order nonlinearities,” *IEEE Journal of Quantum Electron.* **39**(11), 1498–1503 (2003).
- [120] F. Ö. Ilday, J. R. Buckley, H. Lim, F. W. Wise, and W. G. Clark, “Generation of 50-fs, 5nJ pulses at 1.03 μm from a wave-breaking-free fiber laser,” *Optics Letters* **28** (15), 1365-1367 (2003).
- [121] M. Hass, J. W. Davisson, H. B. Rosenstock, and J. Babiskin, “Measurement of very low absorption coefficients by laser calorimetry,” *Applied Optics* **14** (5), 1128-1130 (1975).
- [122] Vitron IG-5 Datasheet, <http://www.vitron.de/datasheets/VITRON%20IG-5%20Datenblatt%20Jan%202015.pdf>.
- [123] Schott Infrared Chalcogenide Glasses Datasheet, http://www.schott.com/advanced_optics/english/download/schott-infrared-chalcog-glasses-family-sheet-october-2013-eng.pdf.
- [124] K. Shinkawa and K. Ogusu, “Pulse-width dependence of optical nonlinearities in As_2Se_3 chalcogenide glass in the picosecond-to-nanosecond region,” *Optics Express* **16** (22), 18230-18240 (2008).
- [125] A. Ganjoo, H. Jain, C. Yu, J. Irudayaraj, and C. G. Pantano, “Detection and fingerprinting of pathogens: Mid-IR biosensor using amorphous chalcogenide films,” *Journal of Non-Crystalline Solids* **354** (19-25), 2757-2762 (2008).
- [126] K. Tanaka and H. Hisakuni, “Photoinduced phenomena in As_2S_3 glass under sub-bandgap excitation,” *Journal of Non-Crystalline Solids* **198-200** (1) 714-718 (1996).
- [127] T. M. Monro and H. Ebendorff-Heidepriem, “Progress in microstructured optical fibers,” *Annual Review of Materials Research* **36**, 467-495 (2006).
- [128] H. Guo, C. Hou, F. Gao, A. Lin, P. Want, Z. Zhou, M. Lu, W. Wei, and B. Peng, “Third-order nonlinear optical properties of $\text{GeS}_2\text{-Sb}_2\text{S}_3\text{-CdS}$ chalcogenide glasses,” *Optics Express* **19** (22), 23275-23284 (2010).

- [129] R. C. Miller, "Optical second harmonic generation in piezoelectric crystals," *Applied Physics Letters* **5** (1), 17-19 (1964).
- [130] Q. Zhang, W. Liu, L. Liu, L. Xu, Y. Xu, and G. Chen, "Large and opposite changes of the third-order optical nonlinearities of chalcogenide glasses by femtosecond and continuous-wave laser irradiation," *Applied Physics Letters* **91** (18), 1-3 (2007).
- [131] W. Liu, Q. Zhang, L. Liu, L. Xu, Y. Xu, G. Chen, "Enhancement of second-order optical nonlinearity in photo-darkened Ge₂₅Sb₁₀S₆₅ chalcogenide glass by femtosecond laser light," *Optics Communications* **282** (10), 2081-2084 (2009).
- [132] K. Shimakawa, A. Kolobov, and S. R. Elliott, "Photoinduced effects and metastability in amorphous semiconductors and insulators," *Advances in Physics* **44** (6), 475-588 (1995).
- [133] A. V. Kolobov, H. Oyanagi, K. Tanaka, and K. Tanaka, "Structural study of amorphous selenium by in situ EXAFS: Observation of photoinduced bond alternation," *Physical Review B* **55** (2), 726-734 (1997).
- [134] A. V. Kolobov, H. Oyanagi, A. Roy, and K. Tanaka, "A nanometer scale mechanism for the reversible photostructural change in amorphous chalcogenides," *Journal of Non-Crystalline Solids* **232-234** (1), 80-85 (1998).
- [135] K. Ogusu, K. Suzuki, and H. Nishio, "Simple and accurate measurement of the absorption coefficient of an absorbing plate by use of the Brewster angle," *Optics Letters* **31** (7), 909-911 (2006).
- [136] J. Troles, F. Smektala, G. Boudebs, A. Monteil, B. Bureau, and J. Lucas, "Optical limiting behavior of infrared chalcogenide glasses," *Journal of Optoelectronics and Advanced Materials* **4** (3), 729-735 (2002).
- [137] A. Prasad, C. J. Zha, R. P. Wang, S. Madden, and B. Luther-Davies, "Properties of Ge_xAs_ySe_{1-x-y} glasses for all-optical signal processing," *Optics Express*, **16** (4), 2804-2815 (2008).
- [138] L. Petit, N. Carlie, H. Chen, S. Gaylord, J. Massera, G. Boudebs, J. Hu, A. Agarwal, L. Kimerling, and K. Richardson, "Compositional dependence of the nonlinear refractive index of new germanium-based chalcogenide glasses," *Journal of Solid State Chemistry* **182** (10), 2756-2761 (2009).
- [139] V. Mizrahi, K. W. DeLong, and G. I. Stegeman, M. A. Saifi, and M. J. Andrejco, "Two-photon absorption as a limitation to all-optical switching," *Optics Letters* **14** (20) 1140-1142 (1989).

- [140] M. R. Krogstad, S. Ahn, W. Park, and J. T. Gopinath, "Optical characterization of chalcogenide Ge–Sb–Se waveguides at telecom wavelengths," *IEEE Photonics Technology Letters* **28**, 2720–2723 (2016).
- [141] M. Popovic, "Complex-frequency leaky mode computations using PML boundary layers for dielectric resonant structures," in *Integrated Photonics Research*, Vol. 91 of OSA Trends in Optics and Photonics (Optical Society of America, 2003), paper ITuD4.
- [142] T. M. Murphy, "SSPROP," Available: [http://www.photonics.umd.edu /software/ssprop/](http://www.photonics.umd.edu/software/ssprop/) [23 November 2015].
- [143] J. W. Nicholson and W. Rudolph, "Noise sensitivity and accuracy of femtosecond pulse retrieval by phase and intensity from correlation and spectrum only (PICASO)," *Journal of the Optical Society of America B*, **19** (2), 330-339, (2002).
- [144] F. P. Payne and J. P. R. Lacey, "A theoretical analysis of scattering loss from planar optical waveguides," *Optical and Quantum Electronics* **26** (10), 977-986 (1994).
- [145] A.W. Snyder and J. D. Love, *Optical Waveguide Theory* (Chapman & Hall, 1983).
- [146] F. Grillot, L. Vivien, S. Laval, and E. Cassan, "Propagation loss in single-mode ultrasmall square silicon-on-insulator optical waveguides," *Journal of Lightwave Technology* **24** (2), 891-896 (2006).
- [147] P. K. Tien, "Light waves in thin films and integrated optics," *Applied Optics* **10**, 2395-2413 (1971).
- [148] C. Ciminelli, V. M. N. Passaro, F. Dell'Olio, and M. N. Armenise, "three-dimensional modelling of scattering loss in InGaAsP/InP and silica-on-silicon bent waveguides," *Journal European Optical Society-Rapid Publications* **4**, 09015 (2009).
- [149] G. T. Reed and A. P. Knights, *Silicon Photonics*, (John Wiley & Sons, Ltd., 2004).
- [150] E. A. J. Marcatili and S. E. Miller: *Bell Syst. Tech. J.* **48**, 2191 (1969).
- [151] R. G. Hunsperger, *Integrated Optics Theory and Technology*, 6th ed. (Springer, 2009), Chap. 6.
- [152] M. Fox, *Optical Properties of Solids*, 2nd ed. (Oxford University Press, 2007), Chap. 2.
- [153] Schott IRG25 datasheet: http://www.schott.com/d/advanced_optics/a8acc8e2-8855-4be6-8b2a-e4b2ada72a15/1.0/schott-infrared-chalcog-glasses-irg25-january-2016-eng.pdf

- [154] S. Afshar V. and T. M. Monro, "A full vectorial model for pulse propagation in emerging waveguides with subwavelength structures part I: Kerr nonlinearity," *Optics Express* **17**, (4), 2298-2318 (2009).
- [155] G. Tittelbach, B. Richter, and W. Karthe, "Comparison of three transmission methods for integrated optical waveguide propagation loss measurement," *Pure Applied Optics* **2**, 683-706 (1993).
- [156] A. Harke, M. Krause, and J. Mueller, "Low-loss singlemode amorphous silicon waveguides," *Electronics Letters*, **41** (25), 1377-1379 (2005).
- [157] J. D. B. Bradley, C. C. Evans, J. T. Choy, O. Reshef, P. B. Deotare, F. Parsy, K. C. Phillips, M. Loncar, and E. Mazur, "Submicrometer-wide amorphous and polycrystalline anatase TiO₂ waveguides for microphotonic devices," *Optics Express* **20**, (21) 23821-23831 (2012).
- [158] H. K. Tsang, R. V. Pentyl, I. H. White, R. S. Grant, W. Sibbett, J. B. D. Soole, H. P. LeBlanc, N. C. Andreadakis, R. Bhat, and M. A. Koza, "Two-photon absorption and self-phase modulation in InGaAsP/InP multi-quantum-well waveguides," *Journal of Applied Physics* **70**, 3992 (1991).
- [159] T.-K. Liang, H.-K. Tsang, "Nonlinear absorption and raman scattering in silicon-on-insulator optical waveguides," *IEEE Journal of Selected Topics in Quantum Electronics* **10** (5), 1149-1153 (2004).
- [160] F. Smektala, C. Quemard, V. Couderc, A. Barthélémy, "Non-linear optical properties of chalcogenide glasses measured by Z-scan," *Journal of Non-Crystalline Solids* **274** (1-3), 232-237 (2000).
- [161] B. Gu, Y.-X. Fan, J. Chen, H.-T. Wang, J. He, and W. Ji, "Z-scan theory of two-photon absorption saturation and experimental evidence," *Journal of Applied Physics* **102**, 083101 (2007).
- [162] J. -F. Lami, P. Gilliot, and C. Hirlimann, "Observation of interband two-photon absorption saturation in CdS," *Physical Review Letters* **77** (8), 1632-1635 (1996).
- [163] S. J. Madden, D.-Y. Choi, D. A. Bulla, A. V. Rode, B. Luther-Davies, V. G. Ta'eed, M. D. Pelusi, and B. J. Eggleton, "Long, low loss etched As₂S₃ chalcogenide waveguides for all-optical signal regeneration," *Optics Express* **15** (22), 14414-14421 (2007).
- [164] M. Asobe, K. Suzuki, T. Kanamori, and K. Kubodera, "Nonlinear refractive index measurement in chalcogenide-glass fibers by self-phase modulation," *Applied Physics Letters* **80** (10) 1153-1154 (1992).
- [165] C.-Y. Tai, J. S. Wilkinson, N. M. B. Perney, M. C. Netti, F. Cattaneo, C. E. Finlayson, and J. J. Baumberg, "Determination of nonlinear refractive index in a Ta₂O₅ rib waveguide using self-phase modulation," *Optics Express* **12** (21) 5110-5116 (2004).

- [166] Y. Ruan, B. Luther-Davies, W. Li, A. Rode, V. Kolev, and S. Madden, "Large phase shifts in As₂S₃ waveguides for all-optical processing devices," *Optics Letters* **30** (19) 2605-2607 (2005).
- [167] N. Singh, D. D. Hudson, Y. Yu, C. Grillet, S. D. Jackson, A. Casas-Bedoya, A. Read, P. Atanackovic, S. G. Duvall, S. Palomba, B. Luther-Davies, S. Madden, D. J. Moss, and B. J. Eggleton, "Midinfrared supercontinuum generation from 2 to 6 μm in a silicon nanowire," *Optica* **2** (9) 797-802 (2015).
- [168] G. P. Agrawal, "Effect of two-photon absorption on the amplification of ultrashort optical pulses," *Physical Review E* **48** (3) 48-50 (1993).
- [169] R. M. Almeida, L. F. Santos, A. Simens, A. Ganjoo, and H. Jain, "Structural heterogeneity in chalcogenide glass films prepared by thermal evaporation," *Journal of Non-Crystalline Solids* **353** (18-21), 2066-2068 (2007).
- [170] A. Ureña, A. Piarristeguy, M. Fontana, C. Vigreux-Bercovici, A. Pradel, and B. Arcondo, "Characterisation of thin films obtained by laser ablation of Ge₂₈Se₆₀Sb₁₂ glasses," *Journal of Physics and Chemistry of Solids* **68** (5-6), 993-997 (2007).
- [171] V. Balan, C. Vigreux, and A. Pradel, "Chalcogenide thin films deposited by radio-frequency sputtering," *Journal of Optoelectronics and Advanced Materials* **6** (3), 875-882 (2004).
- [172] M. Frumar, B. Frumarova, P. Nematic, T. Wagner, J. Jedelsky, and M. Hrdlicka, "Thin chalcogenide films prepared by pulsed laser deposition – new amorphous materials applicable in optoelectronics and chemical sensors," *Journal of Non-Crystalline Solids* **352**, 544-561 (2006).
- [173] E. Baudet, C. Cardinaud, A. Girard, E. Rinnert, K. Michel, B. Bureau, and V. Nazabal, "Structural analysis of RF sputtered Ge-Sb-Se thin films by Raman and X-ray photoelectron spectroscopies," *Journal of Non-Crystalline Solids* **444**, 64-72 (2016).
- [174] R. G. DeCorby, N. Ponnampalam, M. M. Pai, H. T. Nguyen, P. K. Dwivedi, T. J. Clement, C. J. Haugen, J. N. McMullin and S. O. Kasap, "High index contrast waveguides in chalcogenide glass and polymer," *IEEE Journal of Selected Topics in Quantum Electron.* **11** (2), 539-546 (2005).
- [175] J. J. Wathen, P. Apiratikul, C. J. K. Richardson, G. A. Porkolab, G. M. Carter, and T. E. Murphy, "Efficient continuous-wave four-wave mixing in bandgap-engineered AlGaAs waveguides," *Optics Letters* **39** (11) 3161-6164 (2014).
- [176] P. Apiratikul, "Semiconductor waveguides for nonlinear optical signal processing," PhD Dissertation, Department of Electrical and Computer Engineering, University of Maryland (2009).

- [177] J. Li, F. Chen, X. Shen, S-X. Dai, R-F. Xu, and Q-H. Nie, “Sub-micrometer-thick and low-loss $\text{Ge}_{20}\text{Sb}_{15}\text{Se}_{65}$ rib waveguides for nonlinear optical devices,” *Optoelectronics Letters* **11** (3), 203-206 (2015).
- [178] W. Zhang, S. Dai, X. Shen, Y. Chen, S. Zhao, C. Lin, L. Zhang, and J. Bai, “Rib and strip chalcogenide waveguides based on Ge-Sb-Se radio-frequency sputtered films,” *Materials Letters* **98**, 42 (2013).
- [179] R. E. Howard, E. L. Hu, and L. D. Jackel, “Multilevel resist for lithography below 100 nm,” *IEEE Transactions on Electron Devices* **28** (11), 1378-1381 (1981).
- [180] A. A. Tseng, K. Chen, C. D. Chen, and K. J. Ma, “Electron beam lithography in nanoscale fabrication: recent development,” *IEEE Transactions on Electronic Packaging Manufacturing* **26** (2), 141-149 (2003).
- [181] J. Tauc, *Amorphous and Liquid Semiconductors*. (Plenum, 1974).
- [182] N. F. Nott and E. A. Davis, *Electronic Processes in Noncrystalline Materials*, (Oxford University Press, 1979).
- [183] H. Liu, Z. Liu, E. S. Lamb, and F. Wise, “Self-similar erbium-doped fiber laser with large normal dispersion,” *Optics Letters*, **30** (2014).
- [184] B. Oktem, C. Ulgudur, and F. Omer Ilday, “Soliton-similariton fibre laser,” *Nature Photonics* **4** (2010).
- [185] J. Hu, M. Torregiani, F. Morichetti, N. Carlie, A. Agarwal, K. Richardson, L. C. Kimerling, and S. Melloni, “Resonant cavity-enhanced photosensitivity in As_2S_3 chalcogenide glass at 1550 nm telecommunication wavelength,” *Optics Letters* **35** (6), 874-876 (2010).
- [186] J. E. McCarthy, H. T. Bookey, N. D. Psaila, R. R. Thomson, and A. K. Kar, “Mid-infrared spectral broadening in an ultrafast laser inscribed gallium lanthanum sulphide waveguide,” *Optics Express* **20** (2) 1545-1551 (2012).
- [187] X. Gai, S. Madden, D-Y. Choi, D. Bulla, and B. Luther-Davies, “Dispersion engineered $\text{Ge}_{11.5}\text{As}_{24}\text{Se}_{64.5}$ nanowires with a nonlinear parameter of $136\text{W}^{-1}\text{m}^{-1}$ at 1550nm,” *Optics Express* **18** (18) 18866–18874 (2010).
- [188] D-Y. Choi, S. Madden, D. Bulla, R. Wang, A. Rode, and B. Luther-Davies, “Thermal annealing of arsenic tri-sulphide thin films and its influence on device performance,” *Journal of Applied Physics* **107**, 053106 (2010).
- [189] Präzision Glas & Optik GmbH, Mendes, Germany.
- [190] Y. Chen, X. Shen, R. Wang, G. Wang, S. Dai, T. Xu, Q. Nie, “Optical and structural properties of Ge–Sb–Se thin films fabricated by sputtering and thermal evaporation,”

Journal of Alloys and Compounds **548**, 155-160 (2013).

- [191] D-Y. Choi, A. Wade, S. Madden, R. Wang, D. Bulla, and B. Luther-Davies, "Photo-induced and thermal annealing of chalcogenide films for waveguide fabrication," *Physics Procedia* **48**, 195-205 (2013).
- [192] Q. Xu, S. Manipatruni, B. Schmidt, J. Shakya, and M. Lipson, "12.5 Gbit/s carrier-injection-based silicon micro-ring silicon modulators," *Optics Express* **15** (2) 430-436 (2007).
- [193] T. Barwicz, M.A. Popović, P.T. Rakich, M.R. Watts, H.A. Haus, E.P. Ippen and H.I. Smith, "Microring-resonator-based add-drop filters in SiN: fabrication and analysis," *Optics Express* **12**, 1437-1442 (2004).
- [194] C. Sun, M.T. Wade, Y. Lee, J.S. Orcutt, L. Alloatti, M.S. Georgas, A.S. Waterman, J.M. Shainline, R.R. Avizienis, S. Lin, B.R. Moss, R. Kumar, F. Pavanello, A.H. Atabaki, H.M. Cook, A.J. Ou, J.C. Leu, Y.-H. Chen, K. Asanović, R.J. Ram, M.A. Popović, and V.M. Stojanović, "Single-chip microprocessor that communicates directly using light," *Nature* **528**, 534-538 (2015).
- [195] A. Ksendzov and Y. Lin, "Integrated optics ring-resonator sensors for protein detection," *Optics Letters* **30**, 3344-3346 (2005).
- [196] I. M. White, H. Zhu, J. D. Suter, N. M. Hanumegowda, H. Oveys, M. Zourob, and X. Fan, "Refractometric sensors for lab-on-a-chip based on optical ring resonators," *IEEE Sensors Journal* **7** (1) 2009.
- [197] C.M. Gentry, J.M. Shainline, M.T. Wade, M.J. Stevens, S.D. Dyer, X. Zeng, F. Pavanello, T. Gerrits, S.W. Nam, R.P. Mirin, and M.A. Popović, "Quantum-correlated photon pairs generated in a commercial 45 nm complementary metal-oxide semiconductor microelectronics chip," *Optica* **2**, 1065-1071 (2015).
- [198] S. M. Spillane, T. J. Kippenberg, and K. J. Vahala, "Ultralow-threshold Raman laser using a spherical dielectric microcavity," *Nature* **415** 621-623 (2002).
- [199] J. Li, H. Lee, and K. Vahala, "Low-noise Brillouin laser on a chip at 1064 nm," *Optics Letters* **39** (2) 287-290 (2014).
- [200] L.-W. Luo, G. S. Wiederhecker, J. Cardenas, C. Poitras, and M. Lipson, "High quality factor etchless silicon photonic ring resonators," *Optics Express* **19** (7) 6284-6289 (2011).
- [201] M. Ferrera, D. Duchesne, L. Razzari, M. Peccianti, R. Morandotti, P. Cheben, S. Janz, D.-X. Xu, B. E. Little, S. Chu, and D. J. Moss, "Low power four wave mixing in an integrated, micro-ring resonator with $Q = 1.2$ million," *Optics Express* **17**, 14098-14103 (2009).

- [202] P. P. Absil, J. V. Hryniewicz, B. E. Little, P. S. Cho, R. A. Wilson, L. G. Joneckis, and P.-T. Ho, "Wavelength conversion in GaAs micro-ring resonators," *Optics Letters* **25** (8), 554-556, (2000).
- [203] Pan Ma, Duk-Yong Choi, Yi Yu, Zhiyong Yang, Khu Vu, Thach Nguyen, Arnan Mitchell, Barry Luther-Davies, and Steve Madden, "High Q factor chalcogenide ring resonators for cavity-enhanced MIR spectroscopic sensing," *Optics Express* **23**, 19969-19979 (2015).
- [204] Antonio Canciamilla, Stefano Grillanda, Francesco Morichetti, Carlo Ferrari, Juejun Hu, J. David Musgraves, Kathleen Richardson, Anu Agarwal, Lionel C. Kimerling, and Andrea Melloni, "Photo-induced trimming of coupled ring-resonator filters and delay lines in As₂S₃ chalcogenide glass," *Optics Letters* **36**, 4002-4004 (2011)
- [205] W. Bogaerts, P. De Heyn, T. Van Vaerenbergh, K. De Vos, S. K. Selvaraja, T. Claes, P. Dumon, P. Bienstman, D. Van Thourhout, and R. Baets, "Silicon microring resonators," *Laser & Photonics Reviews* **6** (1), 47-73 (2012).
- [206] A. Melloni, F. Morichetti, and M. Martinelli, "Four-wave mixing and wavelength conversion in coupled-resonator optical waveguides," *Journal of the Optical Society of America B* **25** (12) C87-C97 (2008).
- [207] A. Trita, C. Lacava, P. Minzioni, J. -P. Colonna, P. Gautier, J. -M. Fedeli, and I. Cristiani, "Ultra-high four-wave mixing efficiency in slot waveguides with silicon nanocrystals," *Applied Physics Letters* **99**, 191105 (2011).
- [208] John Heebner, Rohit Grover, and Tarek A. Ibrahim, *Optical Microresonators: Theory, Fabrication and Applications* (Springer 2008).
- [209] M. E. Lamont, C. Martijn de Sterke, and B. J. Eggleton, "Dispersion engineering of highly nonlinear As₂S₂ waveguides for parametric gain and wavelength conversion," *Optics Express* **15** (15) 9458 (2007).
- [210] L. Vivien and L. Pavesi, *Handbook of Silicon Photonics*, (Taylor & Francis, 2013) Chap. 4.
- [211] Milos Popovic, "Theory and design of high-index-contrast microphotonic circuits," *Ph.D. Thesis, MIT*, pp. 308-313 and 117-128, 2008.
- [212] G. Kang, M. R. Krogstad, M. Grayson, D. Kim, H. Lee, J. T. Gopinath, and W. Park, "High-Q chalcogenide-silica hybrid wedge resonators," *Submitted to Optics Express* (2017).
- [213] K. Y. Yang, K. Beha, D. C. Cole, X. Yi, P. Del-Haye, H. Lee, J. Li, D. Y. Oh, S. A. Diddams, S. B. Papp, and K. J. Vahala, "Broadband dispersion-engineered microresonator on a chip," *Nature Photonics* **10**, 316-320 (2016).

- [214] R. Ramiro-Manzano, N. Prtljaga, L. Pavesi, G. Pucker, and M. Ghulinyan, “A fully integrated high-Q whispering-gallery wedge resonator,” *Optics Express* **20** (20) 22934-22942 (2012).
- [215] G. Kang, M. R. Krogstad, M. Grayson, S. Cho, J. T. Gopinath, and W. Park, “Design and fabrication of high-Q chalcogenide glass micro-disk resonators,” presented at *SPIE Photonics West*, (2017).
- [216] B. E. Little, J. –P. Laine, and H. A. Haus, “Analytic theory of coupling from tapered fibers and half-blocks into microsphere resonators,” *Journal of Lightwave Technology* **17** (4) 704 (1999).
- [217] O. Aktas and M. Bayindir, “Tapered nanoscale chalcogenide fibers directly drawn from bulk glasses as optical couplers for high-index resonators,” *Applied Optics* **56** (3) 385 (2017).
- [218] T. J. Kippenberg, J. Kalkman, A. Polman, and K. J. Vahala, “Demonstration of an erbium-doped microdisk laser on a silicon chip,” *Physical Review A* **74** (5), 051802 (2006).
- [219] J. Komma, C. Schwarz, G. Hofmann, D. Heinert, and R. Nawrodt, “Thermo-optic coefficient of silicon at 1550 nm and cryogenic temperatures,” *Applied Physics Letters* **101**, 041905 (2012).
- [220] L. He, Y. –F. Xiao, C. Dong, J. Zhu, V. Gaddam, and L. Yang, “Compensation of thermal refraction effect in high-Q toroidal microresonator by polydimethylsiloxane coating,” *Applied Physics Letters* **93**, 201102 (2008).
- [221] H. S. Choi, S. Ismail, and A. M. Armani, “Studying polymer thin films with hybrid optical microcavities,” *Optics Letters* **36**, 2152–2154 (2011).
- [222] P. Alipour, A. H. Atabaki, A. A. Eftekhar, and A. Adibi, “Athermal performance in titania-clad microresonators,” On SOI. *Frontiers in Optics 2010/Laser Science XXVI (2010)*, paper FThQ6 (2010).
- [223] B. A. Rose, A. J. Maker, and A. M. Armani, “Characterization of thermo-optic coefficient and material loss of high refractive index silica sol-gel films in the visible and near-IR” *Optics Materials Express* **2** (5), 671-681 (2012).
- [224] C. Delezoide, “Polymer microring resonators for optofluidic evanescent field sensors,” *Ph.D. Thesis, Ecole normale sup'erieure de Cachan*, pp. 120-125, (2012).
- [225] A. C. Turner, M. A. Foster, A. L. Gaeta, and M. Lipson, “Ultra-lower power parametric frequency conversion in a silicon microring resonator,” *Optics Express* **16** (7) 4881-4887, (2008).

- [226] C. C. Li, H. K. Kim, and M. Migliuolo, "Er-doped glass ridge-waveguide amplifiers fabricated with a collimated sputter deposition technique," *IEEE Photonics Technology Letters* **9** (9) 1223-1225, (1997).
- [227] B. Argence, B. Chanteau, O. Lopez, D. Nicolodi, M. Abgrall, C. Chardonnet, C. Daussy, B. Darquie, Y. Le Coq, and A. Amy-Klein, "Quantum cascade laser frequency stabilization at the sub-Hz level," *Nature Photonics* **9**, 456-461 (2015).
- [228] K. L. Vodopyanov, O. Levi, P. S. Kuo, T. J. Pinguet, J. S. Harris, M. M. Fejer, B. Gerard, L. Becouarn, and E. Lallier, "Optical parametric oscillation in quasi-phase-matched GaAs," *Optics Letters* **29** (16) 1912-1914 (2004).
- [229] S. Afshar V., W. Q. Zhang, H. Ebendorff-Heidepriem, and T. M. Monro, "Small core optical waveguides are more nonlinear than expected: experimental confirmation," *Optics Letters* **34** (22) 3577-3579 (2009).
- [230] V. R. Almeida, R. R. Panepucci, and M. Lipson, "Nanotaper for compact mode conversion," *Optics Letters* **28** (15) 1302-1304 (2003).
- [231] M. R. Krogstad, S. Ahn, W. Park, and J. T. Gopinath, "Corrections to 'Optical characterization of chalcogenide Ge-Sb-Se waveguides at telecom wavelengths'," *to be submitted to Photonics Technology Letters* (2017).
- [232] G. W. Scherer, "Stress-induced index profile distortion in optical waveguides," *Applied Optics* **19** (12) 2000-2006 (1980).
- [233] S. Khasminskaya, F. Pyatkov, K. Slowik, S. Ferrari, O. Kahl, V. Kovalyuk, P. Rath, A. Vetter, F. Hennrich, M. M. Kappes, G. Gol'tsman, A. Korneev, C. Rockstuhl, R. Krumpke, and W. H. P. Pernice, "Fully integrated quantum photonic circuit with an electrically driven light source," *Nature Photonics* **10**, 727-733 (2016).
- [234] L. L. Boyer, J. A. Harrington, M. Hass, and H. B. Rosenstock, "Multiphonon absorption in ionic crystals," *Physical Review B* **11** (4) 1665-1680 (1975).
- [235] F. Vanier, M. Rochette, N. Godbout, and Y. A. Peter, "Raman lasing in As₂S₃ high-Q whispering gallery mode resonators," *Optics Letters* **38** (23), 4966-4969 (2013).
- [236] Q. Du, Y. Huang, J. Li, D. Kita, J. Michon, H. Lin, L. Li, S. Novak, K. Richardson, W. Zhang, and H. Hu, "Low-loss photonic device in Ge-Sb-S chalcogenide glass," *Optics Letters* **41** (13), 3090-3093 (2016).
- [237] X. Gai, B. Luther-Davies, T. P. White, "Photonic crystal nanocavities fabricated from chalcogenide glass fully embedded in an index-matched cladding with a high Q-factor (> 750,000)," *Optics Express* **20** (14), 15503-15515 (2012).

- [238] H. Lin, L. Li, Y. Zou, S. Danto, J. D. Musgraves, K. Richardson, S. Kozacik, M. Murakowski, D. Prather, P. T. Lin, and V. Singh, "Demonstration of high-Q mid-infrared chalcogenide glass-on-silicon resonators," *Optics Letters*, **38** (9) 1470-1472 (2013).
- [239] M.W. Lee, C. Grillet, C. Monat, E. Mägi, S. Tomljenovic-Hanic, X. Gai, S. Madden, D. Y. Choi, D. Bulla, B. Luther-Davies, and B. J. Eggleton, "Photosensitive and thermal nonlinear effects in chalcogenide photonic crystal cavities," *Optics Express* **18** (25), 26695-26703 (2010).
- [240] A. Villeneuve, C. C. Yang, G. I. Stegeman, C.-H. Lin, and H.-H. Lin, "Nonlinear refractive-index and two photon-absorption near half the band gap in AlGaAs," *Applied Physics Letters* **62**, 2465-2467 (1993).
- [241] W. C. Hurlbut, Y.-S. Lee, K. L. Vodopyanov, P. S. Kuo, and M. M. Fejer, "Multiphoton absorption and nonlinear refraction of GaAs in the mid-infrared," *Optics Letters* **32** (6), 668-670 (2007).

Appendix A

Circuit schematic for pulse-picking

Shown in Figure A.1 is the schematic for the circuit used for reduced repetition rate z-scans (described in Chapter 2). This circuit converts a photodiode signal to a TTL (0-5V) trigger signal for the AOM pulse picker driver, at reduced repetition rate 100 times lower than input repetition rate. An input signal from a photodiode, at the repetition rate of the laser, is provided to a high speed comparator (Maxim Integrated, MAX9010, designed for circuits up to 200 MHz) and compared with a reference voltage level, to provide a clean, TTL-compatible signal at the repetition rate of the laser. This is sent to a counter (NXP USA Inc., 74HCT4059N), which is wired to divide down the repetition rate by a factor of 100. Protection circuitry is included to prevent the RF driver from always being on, by monitoring the average of the counter output with a low pass filter, and passing a second comparator output to an AND gate (NXP USA Inc., 74HCT08N). (Note that if the AOM received constant RF power, it would be irreparably damaged.) If the average power is at or below an acceptable level, then the circuit will output a series of high speed, low duty cycle pulses synchronized to the laser. If the average power exceeds an acceptable level, then the circuit will output 0V, still safe for the RF driver. Note that the programmable counter can be re-wired to divide by other fixed values.

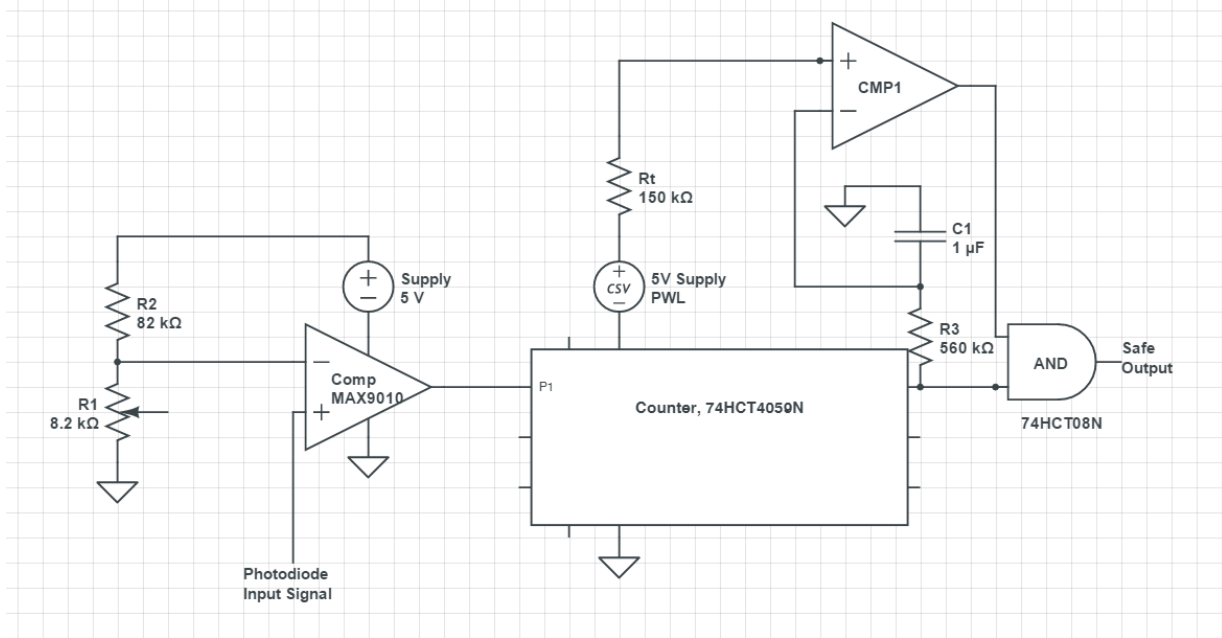


Figure A.1. Circuit schematic for driving pulse picker. Illustrates circuit used to generate low duty-cycle trigger signal necessary to drive acousto-optic modulator to pick pulses.

Appendix B

Z-scan fitting procedure

Open aperture z-scan traces were fit numerically to the following fit equation using Origin [113]:

$$T_{open} \approx 1 - \frac{q_0(z)}{2^{3/2}} + \frac{q_0(z)^2}{3^{3/2}} - \frac{q_0(z)^3}{4^{3/2}} + \frac{q_0(z)^4}{5^{3/2}} - \frac{q_0(z)^5}{6^{3/2}} + \frac{q_0(z)^6}{7^{3/2}} - \frac{q_0(z)^7}{8^{3/2}} + \frac{q_0(z)^8}{9^{3/2}}, \quad (\text{B.1})$$

Here, z is the sample's distance from focus, and $q_0(z)$ is given by

$$q_0(z) = \frac{\beta I_0 L_{eff}}{\left[1 + \left(\frac{z\lambda}{\pi w^2} \right)^2 \right]}, \quad (\text{B.2})$$

where I_0 is the peak on-axis intensity, w is the beam waist, λ is the wavelength, and the effective sample length, $L_{eff} = (1 - \exp[-\alpha L]) / \alpha$, where L is the physical sample length and α is the linear absorption coefficient. For the values of q_0 studied, all ≤ 0.59 , using 9 terms in the sum provided accuracy within 0.05%. For the fits, both β and w were used as fit parameters.

Closed aperture z-scan traces were fit numerically to the expression provided by Gu et al. shown below, assuming a Gaussian temporal profile [116]:

$$T_{closed}(x, s) = \sum_{m,m'=0}^M g_m(x, \Delta\phi_0, Q_0) g_{m'}^*(x, \Delta\phi_0, Q_0) A_{mm'} S_{mm'}(x, s) \quad (\text{B.3})$$

$$g_m(x, \Delta\phi_0, Q_0) = \frac{i^m \Delta\phi_0 (x+i)}{m!(x^2+1)^m [x+i(2m+1)]} \prod_{n=1}^m \left[1 + i \left(n - \frac{1}{2} \right) \frac{Q_0}{\Delta\phi_0} \right] \quad (\text{B.4})$$

$$S_{mm'}(x, s) = \frac{1 - \exp[B_{mm'}(x) \ln(1-s)]}{B_{mm'}(x)s} \quad (\text{B.5})$$

$$B_{mm'}(x) = \frac{(m+m'+1)(1+x^2)}{[x+i(2m+1)][x-i(2m'+1)]} \quad (\text{B.6})$$

$$A_{mm'} = \frac{1}{\sqrt{m+m'+1}} \quad (\text{B.7})$$

$$Q_0 = \beta I_0 L_{eff} \quad (\text{B.8})$$

$$\Delta\phi_0 = \frac{2\pi n_2 I_0 L_{eff}}{\lambda} \quad (\text{B.9})$$

and

$$I_0 = \frac{2P_{avg}}{\pi w_0^2 R_{rep} t_{fwhm}} \quad (\text{B.10})$$

where $x = z/z_0$ is the normalized sample position, $z_0 = \pi w_0^2 / \lambda$ is the confocal parameter, S is the linear transmittance of the circular aperture, P_{avg} is the average incident power (taking into account front sample surface reflection), R_{rep} is the repetition rate, and t_{fwhm} is the full-width at half maximum pulse duration.

Mathematica's NonlinearModelFit was used to fit data, summing terms up to $M = 13$, satisfying Gu's optimum upper sum limit to ensure a high level of accuracy [116]. For fits, the values of β and w determined earlier from open aperture scans were left fixed, and the phase shift $\Delta\phi_0$ (directly proportional to n_2) was left as a free parameter. An example Mathematica notebook file for fitting closed aperture z-scan data is provided below:

```
(*Mathematica Code for fitting closed aperture z-scan*)
(*Note: First copy and paste data from Excel spreadsheet in
between "" in the line below to import data:*)
data=ImportString["", "TSV"];
```

```

ClearAll[M, s, lambda, R, t, Trans, w, P, DD, S, A, gm, gn, T,
nlm, B, n2, Intensity, phi, q, SumCheck];

(*Sets up constants from experiment in SI units, and how many
terms to sum up to (M)*)
M=13;
s=0.376; (*aperture transmission*)
R=37.5*^6; (*laser rep rate in Hz*)
t=218*^-15; (*laser FWHM pulse width in seconds*)
Trans=0.786; (*front fresnel reflection→this is fraction of
light that's actually incident on sample*)
Leff=0.0019; (*effective sample length*)

(*Constants, some from open ap fits, that change from trace to
trace w/i experiment, in SI units*)
P=6.0*^-3; (*Power in Watts, before taking into account fres
reflection*)
w=32.15*^-6; (*beam waist in meters from 9 term open ap fit*)
B=30.8*^-11; (*TPA coefficient in m/W from 9 term open ap fit*)

(*Derived constants*)
Intensity=2*P*Trans/(Pi*w^2*R*t)
q=B*Intensity*Leff

(*Intermediate calculations*)
DD=(m+n+1)*(1+x^2)/(x+I*(2*m+1))/(x-I*(2*n+1));
S=(1-Exp[DD*Log[1-s]])/(DD*s);
A=(m+n+1)^(-(1/2));
gm=I^m*phi^m*(x+I)/(m!*(x^2+1)^m*(x+I*(2*m+1)))*Product[1+I*(u-
0.5)*q/phi,{u,1,m}];
gn=Conjugate[I^n*phi^n*(x+I)/(n!*(x^2+1)^n*(x+I*(2*n+1)))*Produc
t[1+I*(v-0.5)*q/phi,{v,1,n}]];

T=Sum[Sum[gm*gn*A*S,{n,0,M}],{m,0,M}];

nlm=NonlinearModelFit[data,{Sum[Sum[I^m*phi^m*(x+I)/(m!*(x^2+1)^
m*(x+I*(2*m+1)))*Product[1+I*(u-
0.5)*q/phi,{u,1,m}]*Conjugate[I^n*phi^n*(x+I)/(n!*(x^2+1)^n*(x+I
*(2*n+1)))*Product[1+I*(v-0.5)*q/phi,{v,1,n}]]*(m+n+1)^(-
(1/2))*(1-Exp[DD*Log[1-s]])/(DD*s),{n,0,M}],{m,0,M}],phi<Pi,
phi>0},{phi},x];
nlm["ParameterConfidenceIntervalTable"]

(*Show[ListPlot[data],Plot[nlm[x],{x,-10,10},PlotRange→All],
Frame→True,

```

```

PlotLabel→"Closed Aperture Z-scan for IG5, 218 fs, 1.03 microns,
P=6.00mW",
PlotRange→{{-10,10},{0.86,1.06}},
FrameLabel→{"z/z0","Normalized Transmittance"},
LabelStyle→{FontFamily->"Arial",
FontSize→14},GridLines→Automatic]*)

Show[Plot[nlm[x],{x,-
10,10},PlotRange→All,PerformanceGoal→"Quality"],ListPlot[data],
Frame→True,
LabelStyle→{FontFamily->"Arial",FontSize→16},
PlotLabel→"Closed Aperture Z-scan for IG5, 218 fs, 1.030
microns, P=6.00mW",
PlotRange→{{-10,10},{0.86,1.06}},
FrameLabel→{"z/z0","Normalized Transmittance"},
GridLines→Automatic]

nlm["BestFitParameters"]

```

Appendix C

Waveguide design code

C.1 Number of modes

The following code shows how to calculate the number of modes over a range of waveguide cross sectional dimensions, using a mode solver developed by Dr. Milos Popovic [141]. To do this, a rectangular waveguide cross section is input with corresponding refractive indices and dimensions, and the effective index n_{eff} of the first three modes is calculated at a chosen wavelength. Modes will be guided if $n_{sub} < n_{eff} < n_{core}$, where n_{core} is the refractive index of the core, and n_{sub} is the highest refractive index of the cladding (the substrate in the below example). Note that for our applications, we were interested in waveguides supporting one or two modes at most, so only the first three modes were calculated. However, the code can easily be modified to calculate more modes.

“Strip_1550nm_SiO2sub_SU8clad_nmodes.m”

```
%Waveguide Top File
%Commands to run Milos' 2d finite difference vectorial mode solver
clear all
clc
%Parameters (lengths are in microns!)
wavelength=1.55;

%start clock to keep track of how long calculation takes
tic

%Define refractive index of materials at 1550 nm
nChal=2.659633;
```

```

nSiO2=1.444;
nSU8=1.575;

%Assign specific materials for core, substrate, and cladding
nSub=nSiO2;
nCore=nChal;
nClad=nSU8;

r=0;
c=0;
count=0;
w_array=zeros(1,8);
h_array=zeros(1,7);
n1_array=zeros(1,56);
a_matrix=zeros(8,7);
gamma_matrix=zeros(8,7);

%For range of cross-sectional dimensions, solve for first 3 modes
for w=0.500:0.1:1.2
    c=0;
    r=r+1;
    w_array(1,r)=w;
    for h=0.100:.1:0.700
        c=c+1;
        h_array(1,c)=h;

w
h

xres=0.01; %microns
yres=0.01; %microns
xpad=2; %microns
ypad=2; %microns
Nmodes=3; %# of modes to solve for,

%Run si solver 3d (mode solver) to solve for propagation constants
[N,F] = sisolver3d([nSub nSub nSub; nClad nCore nClad; nClad nClad nClad],
[xpad w xpad], [ypad h ypad], [xres yres], 2*pi/wavelength,
struct('NMODES_CALC',Nmodes,'mu_guess',nCore*2*pi/wavelength));

%View the modes
SZ.F = F; SZ.N = N; modeview(SZ)

%Calculate effective index of modes (scale the propagation constant)
neff=F.beta/(2*pi/wavelength)
count=count+1;
n1_matrix(r,c)=neff(1,1);
n2_matrix(r,c)=neff(2,1);
n3_matrix(r,c)=neff(3,1);
%n4_matrix(r,c)=neff(4,1);
mode_matrix(r,c)=(neff(1,1)>nClad)+(neff(2,1)>nClad)+(neff(3,1)>nClad)%+(neff
(4,1)>nSub)

```

```
%Note: As is, this code solves for the first 3 modes, so it can tell whether
there are no guided modes, 1 guided mode, 2 guided modes, or ≥3 guided modes.
In principle, if there is interest in multimode waveguides, one can adjust
this code to solve for more modes (4, 5, 6, etc.).
```

```
    end
end
toc

%Plot # of modes
figure(3), imagesc([0.100 0.700], [0.5 1.2], mode_matrix);
set(gca, 'ydir', 'normal');
```

C.2 Second-order dispersion

The following code shows how to calculate the second order dispersion over a range of waveguide cross sectional dimensions, using a mode solver developed by Dr. Milos Popovic [141]. For each given cross section size, the propagation constant of the first guided mode is calculated at three nearby frequencies. Note that at each frequency, the constituent materials' refractive indices are updated using their given material dispersion, to include the effect of material dispersion. A finite difference formula is used to calculate the second order derivative of the propagation constant with respect to frequency, which yields the second order dispersion, including both the effects of the waveguide geometry and material dispersion. Using for loops, the process is repeated for a range of cross sectional dimensions.

“Strip_1550nm_disp_fine_fixed_SU8clad.m”

```
%Waveguide Top File
%Commands to run Milos' 2d finite difference vectorial mode solver
clear all
clc
%Parameters (lengths are in microns!)
wavelength=1.550;

tic

%Case 2
```

```

nAir=1.0000;
nSU8=1.575;
nChal=@(x) sqrt(1+2.75840+3.09812*x^2/(x^2-0.399523^2)+1.64139*x^2/(x^2-
45.1071^2));%IRG25, ref index info/Schott;
nSiO2=@(x) sqrt(1+0.6961663*x^2/(x^2-0.0684043^2)+0.4079426*x^2/(x^2-
0.1162414^2)+0.8974794*x^2/(x^2-9.896161^2)); %ref index info, Malitson;
%Will set nCore, nSub later, and re-set each time I change the wavelength

nClad=nSU8; %ignoring dispersion of SU8 for now, since unknown/un-measured at
1550

r=0;
c=0;
count=0;
w_array=zeros(1,8);
h_array=zeros(1,6);
nl_array=zeros(1,48);

disp_matrix=zeros(8,6);
neff_matrix=zeros(8,6);
ngroup_matrix=zeros(8,6);

for w=0.500:0.100:1.200
    c=0;
    r=r+1;
    w_array(1,r)=w;
    for h=0.20:.10:0.70
        c=c+1;
        h_array(1,c)=h;

w
h

xres=0.01; %microns
yres=0.01; %microns
xpad=2; %microns
ypad=2; %microns
Nmodes=1; %# of modes to solve for,

%Run si solver 3d to calculate propagation constant
nCore=nChal(wavelength); %update index to account for IRG25 dispersion!
nSub=nSiO2(wavelength)
[N,F] = sisolver3d([nSub nSub nSub; nClad nCore nClad; nClad nClad nClad],
[xpad w xpad], [ypad h ypad], [xres yres], 2*pi/wavelength,
struct('NMODES_CALC',Nmodes,'mu_guess',nCore*2*pi/wavelength));
%View the modes
SZ.F = F; SZ.N = N; modeview(SZ)

%Calculate effective index of modes (scale the propagation constant)
neff=F.beta/(2*pi/wavelength)
count=count+1

```

```

%Calculate the 2nd order dispersion (and 4th order dispersion and group index
too now!)
w2=2*pi*3e14/wavelength;
dw=w2/1000;

w1=w2-dw;
w3=w2+dw;

w0=w2-(2*dw);
w4=w2+(2*dw);

wavelength1=2*pi*3e14/w1;
wavelength3=2*pi*3e14/w3;

wavelength0=2*pi*3e14/w0;
wavelength4=2*pi*3e14/w4;

nCore=nChal(wavelength3); %update index to account for IRG25 dispersion!
nSub=nSiO2(wavelength3);
[N3,F3] = sisolver3d([nSub nSub nSub; nClad nCore nClad; nClad nClad nClad],
[xpad w xpad], [ypad h ypad], [xres yres], 2*pi/wavelength3,
struct('NMODES_CALC',Nmodes,'mu_guess',nCore*2*pi/wavelength3));

nCore=nChal(wavelength1); %update index to account for IRG25 dispersion!
nSub=nSiO2(wavelength1);
[N1,F1] = sisolver3d([nSub nSub nSub; nClad nCore nClad; nClad nClad nClad],
[xpad w xpad], [ypad h ypad], [xres yres], 2*pi/wavelength1,
struct('NMODES_CALC',Nmodes,'mu_guess',nCore*2*pi/wavelength1));

%calculate up to 2nd order dispersion using finite difference (B2)
Dispersion_s_per_m2=(F3.beta-2*F.beta+F1.beta)/(dw^2)*(-
2*pi*3e14/(wavelength^2))*(10^12)
B0_per_m=F.beta*1e6;
B1_ps_per_m=(F3.beta-F.beta)/dw*1e6*(1e12)
B2_ps2_per_m=(F3.beta-2*F.beta+F1.beta)/(dw^2)*1e6*((1e12)^2)
% %Also calculate group index from 1st order dispersion
n_group=B1_ps_per_m*1e-12*3e8 %unitless
B2net_ps2_per_m=B2_ps2_per_m; %%Note that material dispersion is already
included!

disp_matrix(r,c)=B2_ps2_per_m;
neff_matrix(r,c)=neff;
ngroup_matrix(r,c)=n_group;

end
end
%

figure(1), imagesc([0.200 0.700], [0.500 1.200], neff_matrix);
set(gca,'ydir','normal');

figure(2), imagesc([0.200 0.700], [0.500 1.200], ngroup_matrix);
set(gca,'ydir','normal');

```

```
figure(3), imagesc([0.200 0.700], [0.500 1.200], disp_matrix);  
set(gca, 'ydir', 'normal');
```

```
toc
```

C.3 Effective area and nonlinear parameter

The following code shows an example calculation of the effective area and nonlinear parameter of a mode over a range of waveguide cross sectional dimensions. To do this, for a given waveguide cross section, the electric field, the H field, and propagation constant of the first guided mode of the waveguide is calculated using a mode solver developed by Dr. Milos Popovic [141]. The fields are then used to calculate the effective area and nonlinear parameter by numerically evaluating the corresponding integrals, using the definitions for the effective area and nonlinear parameter given in chapter 3, Section 3.2.3 of the thesis. Using for loops, the calculation is repeated for a range of cross sectional dimensions.

“Strip_1550nm_SiO2sub_SU8clad_aeff.m”

```
%Waveguide Top File  
%Commands to run Milos' 2d finite difference vectorial mode solver  
clear all  
close all  
clc  
%Parameters (lengths are in microns!)  
wavelength=1.550;  
  
tic  
  
%Set refractive indices for materials at 1550 nm  
nChal=2.659633;  
nSiO2=1.444;  
nSU8=1.575;  
  
%Choose which materials are the substrate, core, and cladding  
nSub=nSiO2;  
nCore=nChal;  
nClad=nSU8;
```

```

r=0;
c=0;
count=0;
w_array=zeros(1,8);
h_array=zeros(1,6);
n1_array=zeros(1,48);
a_matrix=zeros(8,6);
gamma_matrix=zeros(8,6);
n2vect_factor_matrix=zeros(8,6);

%For range of waveguide widths w and heights h, solve for 1st mode and
%calculate vectorial area and effective nonlinearity

for w=0.5:0.1:1.2
    c=0;
    r=r+1;
    w_array(1,r)=w;
    for h=0.2:0.1:0.7
        c=c+1;
        h_array(1,c)=h;

w
h

xres=0.01; %microns
yres=0.01; %microns
xpad=1; %microns
ypad=1; %microns
Nmodes=1; %# of modes to solve for,

%Run si solver 3d to solve for modes
[N,F] = sisolver3d([nSub nSub nSub; nClad nCore nClad; nClad nClad nClad],
[xpad w xpad], [ypad h ypad], [xres yres], 2*pi/wavelength,
struct('NMODES_CALC',Nmodes,'mu_guess',nCore*2*pi/wavelength));
%View the modes
SZ.F = F; SZ.N = N; modeview(SZ)

%Calculate effective index of modes (scale the propagation constant)
neff=F.beta/(2*pi/wavelength)
count=count+1
n1_matrix(r,c)=neff(1,1);

%%%%%%%%%%%%%%%%%%%%%%%%%%%%%%%%%%%%%%%%%%%%%%%%%%%%%%%%%%%%%%%%%%%%%%%%
%%%%%%%%%%%%%%%%%%%%%%%%%%%%%%%%%%%%%%%%%%%%%%%%%%%%%%%%%%%%%%%%%%%%%%%%
% %Below: using fixed E4 vectorial A_eff definition, and vectorial n2 factor
Ex_modef=F.Ex(:, :, 1)';
Ey_modef=F.Ey(:, :, 1)';
Ez_modef=F.Ez(:, :, 1)';
Hx_modef=F.Hx(:, :, 1)';
Hy_modef=F.Hy(:, :, 1)';
Hz_modef=F.Hz(:, :, 1)';

test=size(Ex_modef);

```

```

xmax1=test(1,1);
ymax1=test(1,2)-1;

%size to same dimensions (up to 10 nm error (1 pixel) expected; should be
small, given wg dimensions relative to this)
Ex_mode=Ex_modef(1:xmax1,1:ymax1);
Ey_mode=Ey_modef(1:xmax1,1:ymax1);
Hx_mode=Hx_modef(1:xmax1,1:ymax1);
Hy_mode=Hy_modef(1:xmax1,1:ymax1);
Ez_mode=Ez_modef(1:xmax1,1:ymax1);

e_cross_h_dot_z=Ex_mode.*conj(Hy_mode)-Ey_mode.*conj(Hx_mode);
Aeff_vectorial=sum(sum(e_cross_h_dot_z))^2/(sum(sum(e_cross_h_dot_z.*conj(e_c
ross_h_dot_z))))*xres*yres %in square microns!

Ymax=round((h+2*yypad)/yres)-1;
Xmax=round((w+2*xypad)/xres-1);

B=zeros(Ymax,Xmax);

%assigning core values
for rr=round(yypad/yres+1):round((ypad+h)/yres)
    for cc=round(xypad/xres):round(xypad/xres+w/xres)
        B(rr,cc)=1;
    end
end

%assigning substrate values
for rr=1:round(yypad/yres)
    for cc=1:Xmax
        B(rr,cc)=0;
    end
end

length_sq=Ex_mode.*conj(Ex_mode)+Ey_mode.*conj(Ey_mode)+Ez_mode.*conj(Ez_mode
);

EdotE=Ex_mode.*(Ex_mode)+Ey_mode.*(Ey_mode)+Ez_mode.*(Ez_mode);
n2_vectorial_factor_fixed=8.85e-12/(4*pi*1e-
7)/3*nCore^2*sum(sum((2*length_sq.*length_sq+EdotE.*conj(EdotE)).*B))/sum(sum
(e_cross_h_dot_z.*conj(e_cross_h_dot_z)))

gamma_eff=2*pi()*936e-20*n2_vectorial_factor_fixed/(wavelength*1e-
6*Aeff_vectorial*1e-12)

a_matrix(r,c)=Aeff_vectorial; %in square microns!!
n2vect_factor_matrix(r,c)=n2_vectorial_factor_fixed; %in SI
gamma_matrix(r,c)=gamma_eff; %in SI
%%%%%%%%%%%%%%%%%%%%%%%%%%%%%%%%%%%%%%%%%%%%%%%%%%%%%%%%%%%%%%%%%%%%%%%%
%pause
    end
end

```

```
toc
```

```
figure(1), imagesc([0.200 0.700], [0.50 1.200], a_matrix);  
set(gca, 'ydir', 'normal');  
figure(2), imagesc([0.200 0.700], [0.50 1.200], gamma_matrix);  
set(gca, 'ydir', 'normal');  
figure(3), imagesc([0.200 0.700], [0.50 1.200], n2vect_factor_matrix);  
set(gca, 'ydir', 'normal');
```

C.4 Bend loss for curved waveguides

The following code shows how to calculate the bend loss as a function of bend radius for a given waveguide cross section. A mode solver developed by Dr. Milos Popovic [141] is used to calculate the propagation constant of a waveguide bent in a circle. As described in Chapter 3, Section 3.2.1 of the thesis, the imaginary part of the propagation constant is then used to calculate the radiative loss due to bending the waveguide.

“ChG_ring_bendloss_1550nm_fixed_clean.m”

```
%Waveguide Top File  
%Commands to run Milos' 2d finite difference vectorial mode solver  
clear all  
clc  
%Parameters (lengths are in microns!)  
wavelength=1.55;  
  
%Case 2  
nAir=1.0000;  
nChal=2.659633;  
nSiO2=1.444;  
%nMgF2=1.37;  
  
nSub=nSiO2  
nCore=nChal  
nClad=nAir  
  
r=0;  
count=0;  
  
%Set waveguide core width w and height h, in microns.  
w=0.800;  
h=0.330;  
  
%Guess effective index as starting point  
%(for faster run time, choose starting effective index near neff of a  
straight waveguide first)  
n_guess=2.3;
```

```

R_array=zeros(1,10);

%a is the variable radius
for a=1:0.5:5.5
    R_eff=a
    r=r+1;
    R_array(1,r)=R_eff;

%Run si solver 3d
[N,F] = sisolver3d([nSub nSub nSub; nClad nCore nClad; nClad nClad nClad], [2
w 2], [2 h 2], [.01 .010], 2*pi/wavelength, struct('radius',R_eff-w/2-
2, 'mu_guess',R_eff*n_guess*2*pi/wavelength, 'PMLwidth',[0 1. 0
0], 'PMLsigma',[0.2 0.2]));

%View the modes
modeview( struct('N',N, 'F',F) );

%Calculate effective index of modes (scale the propagation constant)
%fixed 2.25.14
gamma=F.beta;
beta_actual=F.beta/R_eff;
n_eff_bend=beta_actual*wavelength/(2*pi)

count=count+1;
trans90=exp(-1*imag(gamma)*pi); %added in 3/2/17
trans90_array(1,count)=trans90; %added in 3/2/17
alpha_per_cm_array(1,count)=log(trans90)/(-1*R_eff*1e-4*pi/2)

end

%Plot the output bend loss as a function of radius
figure(3), scatter(R_array,alpha_per_cm_array)
xlabel('Effective Radius (microns)')
ylabel('alpha (1/cm)')
title('Bending Alpha vs Radius for 800 nm x 330 nm air-clad Chalcogenide
Waveguide')

R_array'
alpha_per_cm_array'

```

C.5 Higher-order dispersion (up to 5th order)

The following code shows how to calculate higher order dispersion (up to 5th order) over a range of waveguide cross sectional dimensions. For each given cross section size, the propagation constant of the first guided mode is calculated at a number of nearby frequencies. Note that at

each frequency, the constituent materials' refractive indices are updated using their given material dispersion, to include the effect of material dispersion. Finite difference formulas are used to calculate the first, second, third, fourth, and fifth order derivative of the propagation constant with respect to frequency, which yields the first- through fifth-order dispersion, including both the effects of the waveguide geometry and material dispersion. Using for loops, the process is repeated for a range of cross sectional dimensions. Dispersion is discussed in Chapter 3, Section 3.2.2.

“Strip_1550nm_disp_fine_fixed_90nmby2000nm_HODexample.m”

```
%Waveguide Top File
%Commands to run Milos' 2d finite difference vectorial mode solver
clear all
clc
%Parameters (lengths are in microns!)
wavelength=1.550;

tic

%Set up material refractive indices, including dispersion formulas
nAir=1.0000;
nChal=@(x) sqrt(1+2.75840+3.09812*x^2/(x^2-0.399523^2)+1.64139*x^2/(x^2-
45.1071^2));%IRG25, ref index info/Schott;
nSiO2=@(x) sqrt(1+0.6961663*x^2/(x^2-0.0684043^2)+0.4079426*x^2/(x^2-
0.1162414^2)+0.8974794*x^2/(x^2-9.896161^2)); %ref index info, Malitson;
%Will set nCore, nSub later, and re-set each time I change the wavelength

nClad=nAir;

r=0;
c=0;
count=0;
w_array=zeros(1,9); %7
h_array=zeros(1,7); %5
n1_array=zeros(1,63); %35
a_matrix=zeros(9,7); %7,5
gamma_matrix=zeros(9,7);%7,5

%Right now, just set to calculate for a 2 um (W) x 90 nm (H) waveguide, but
%could adjust to calculate over a range of widths and heights
for w=2.0:0.070:2.0
    c=0;
    r=r+1;
    w_array(1,r)=w;
    for h=0.090:.010:0.090
        c=c+1;
```

```

    h_array(1,c)=h;

w
h

xres=0.01;    %microns
yres=0.005;  %microns
xpad=1;      %microns
ypad=2;      %microns
Nmodes=1;    %# of modes to solve for,

%Run si solver 3d to solve for mode
nCore=nChal(wavelength); %update index to account for IRG25 dispersion!
nSub=nSiO2(wavelength)
[N,F] = sisolver3d([nSub nSub nSub; nClad nCore nClad; nClad nClad nClad],
[xpad w xpad], [ypad h ypad], [xres yres], 2*pi/wavelength,
struct('NMODES_CALC',Nmodes,'mu_guess',nCore*2*pi/wavelength));
%View the modes
SZ.F = F; SZ.N = N; modeview(SZ)

%Calculate effective index of modes (scale the propagation constant)
neff=F.beta/(2*pi/wavelength)
count=count+1

%%%%%%%%%%higher order dispersion%%%%%%%%%%
%Calculate the dispersion (up to 5th order dispersion and group index too!)
w2=2*pi*3e14/wavelength;
dw=w2/1000;

w1=w2-dw;
w3=w2+dw;

w0=w2-(2*dw);
w4=w2+(2*dw);

wavelength1=2*pi*3e14/w1;
wavelength3=2*pi*3e14/w3;

wavelength0=2*pi*3e14/w0;
wavelength4=2*pi*3e14/w4;

%additional test wavelength for odd-ordered higher order dispersion terms
(added 11/17/15)
wp32=w2+(3/2*dw);
wavep32=2*pi*3e14/wp32;
wp12=w2+(1/2*dw);
wavep12=2*pi*3e14/wp12;
wm32=w2-(3/2*dw);
wavem32=2*pi*3e14/wm32;
wm12=w2-(1/2*dw);
wavem12=2*pi*3e14/wm12;
wp52=w2+(5/2*dw);
wavep52=2*pi*3e14/wp52;
wm52=w2-(5/2*dw);
wavem52=2*pi*3e14/wm52;

```

```

nCore=nChal(wavelength3); %update index to account for IRG25 dispersion!
nSub=nSiO2(wavelength3);
[N3,F3] = sisolver3d([nSub nSub nSub; nClad nCore nClad; nClad nClad nClad],
[xpad w xpad], [ypad h ypad], [xres yres], 2*pi/wavelength3,
struct('NMODES_CALC',Nmodes,'mu_guess',nCore*2*pi/wavelength3));

nCore=nChal(wavelength1); %update index to account for IRG25 dispersion!
nSub=nSiO2(wavelength1);
[N1,F1] = sisolver3d([nSub nSub nSub; nClad nCore nClad; nClad nClad nClad],
[xpad w xpad], [ypad h ypad], [xres yres], 2*pi/wavelength1,
struct('NMODES_CALC',Nmodes,'mu_guess',nCore*2*pi/wavelength1));

nCore=nChal(wavelength4); %update index to account for IRG25 dispersion!
nSub=nSiO2(wavelength4);
[N4,F4] = sisolver3d([nSub nSub nSub; nClad nCore nClad; nClad nClad nClad],
[xpad w xpad], [ypad h ypad], [xres yres], 2*pi/wavelength4,
struct('NMODES_CALC',Nmodes,'mu_guess',nCore*2*pi/wavelength4));

nCore=nChal(wavelength0); %update index to account for IRG25 dispersion!
nSub=nSiO2(wavelength0);
[N0,F0] = sisolver3d([nSub nSub nSub; nClad nCore nClad; nClad nClad nClad],
[xpad w xpad], [ypad h ypad], [xres yres], 2*pi/wavelength0,
struct('NMODES_CALC',Nmodes,'mu_guess',nCore*2*pi/wavelength0));

nCore=nChal(wavep12); %update index to account for IRG25 dispersion!
nSub=nSiO2(wavep12);
[Np12,Fp12] = sisolver3d([nSub nSub nSub; nClad nCore nClad; nClad nClad
nClad], [xpad w xpad], [ypad h ypad], [xres yres], 2*pi/wavep12,
struct('NMODES_CALC',Nmodes,'mu_guess',nCore*2*pi/wavep12));

nCore=nChal(wavep32); %update index to account for IRG25 dispersion!
nSub=nSiO2(wavep32);
[Np32,Fp32] = sisolver3d([nSub nSub nSub; nClad nCore nClad; nClad nClad
nClad], [xpad w xpad], [ypad h ypad], [xres yres], 2*pi/wavep32,
struct('NMODES_CALC',Nmodes,'mu_guess',nCore*2*pi/wavep32));

nCore=nChal(wavep52); %update index to account for IRG25 dispersion!
nSub=nSiO2(wavep52);
[Np52,Fp52] = sisolver3d([nSub nSub nSub; nClad nCore nClad; nClad nClad
nClad], [xpad w xpad], [ypad h ypad], [xres yres], 2*pi/wavep52,
struct('NMODES_CALC',Nmodes,'mu_guess',nCore*2*pi/wavep52));

nCore=nChal(wavem12); %update index to account for IRG25 dispersion!
nSub=nSiO2(wavem12);
[Nm12,Fm12] = sisolver3d([nSub nSub nSub; nClad nCore nClad; nClad nClad
nClad], [xpad w xpad], [ypad h ypad], [xres yres], 2*pi/wavem12,
struct('NMODES_CALC',Nmodes,'mu_guess',nCore*2*pi/wavem12));

nCore=nChal(wavem32); %update index to account for IRG25 dispersion!
nSub=nSiO2(wavem32);
[Nm32,Fm32] = sisolver3d([nSub nSub nSub; nClad nCore nClad; nClad nClad
nClad], [xpad w xpad], [ypad h ypad], [xres yres], 2*pi/wavem32,
struct('NMODES_CALC',Nmodes,'mu_guess',nCore*2*pi/wavem32));

```

```

nCore=nChal(wavem52); %update index to account for IRG25 dispersion!
nSub=nSiO2(wavem52);
[Nm52,Fm52] = sisolver3d([nSub nSub nSub; nClad nCore nClad; nClad nClad
nClad], [xpad w xpad], [ypad h ypad], [xres yres], 2*pi/wavem52,
struct('NMODES_CALC',Nmodes,'mu_guess',nCore*2*pi/wavem52));

%calculate up to 2nd order dispersion (B2)
Dispersion_s_per_m2=(F3.beta-2*F.beta+F1.beta)/(dw^2)*(-
2*pi*3e14/(wavelength^2))*(10^12)
B0_per_m=F.beta*1e6
B1_ps_per_m=(F3.beta-F.beta)/dw*1e6*(1e12)
B2_ps2_per_m=(F3.beta-2*F.beta+F1.beta)/(dw^2)*1e6*((1e12)^2)

%Also calculate 3rd - 5th order dispersion
B3_ps3_per_m_check=(Fp32.beta-3*Fp12.beta+3*Fm12.beta-
Fm32.beta)/(dw^3)*1e6*((1e12)^3) %added 11/17/2015
B4_ps4_per_m=(F4.beta-4*F3.beta+6*F.beta-
4*F1.beta+F0.beta)/(dw^4)*1e6*((1e12)^4)
B5_ps5_per_m=(Fp52.beta-5*Fp32.beta+10*Fp12.beta-10*Fm12.beta+5*Fm32.beta-
Fm52.beta)/(dw^5)*1e6*((1e12)^5) %added 11/17/2015

%Also calculate group index from 1st order dispersion
n_group=B1_ps_per_m*1e-12*3e8 %unitless
%%%%%%%%%%%%%%%%%%%%%%%%%%%%%%%%%%%%%%%%%%%%%%%%%%%%%%%%%%%%%%%%%%%%%%%%

end
end

%%Commented out plot of dispersion below
%%(useful if calculating dispersion over a range of waveguide dimensions)
%%figure(3), imagesc([0.320 0.380], [0.620 0.780], disp_matrix);%figure(3),
imagesc([0.520 0.600], [1.34 1.46], disp_matrix);
%set(gca,'ydir','normal');

toc

```

Appendix D

Split Step Code

D.1 Split-step base code with two-photon absorption

Below is split-step code, with our modifications to include the effects of two-photon absorption, for the case of no Raman. Base split-step code was provided from T. M. Murphy's group at <http://www.photonics.umd.edu/software/ssprop/> [142]. The general concept behind split-step code is discussed in Chapter 3, under Section 3.2.7.

“sspropc_tpa_mk.c”

```
/* File:          sspropc.c
 * Author:       Thomas E. Murphy (tem@umd.edu)
 * Created:     1/17/2001
 * Modified:    2/5/2006
 * Version:     3.0
 * Description:  This file solves the nonlinear Schrodinger
 *              equation for propagation in an optical fiber
 *              using the split-step Fourier method described
 *              in "Nonlinear Fiber Optics" (G. Agrawal, 2nd
 *              ed, Academic Press, 1995, Chapter 2). The
 *              routine is compiled as a Matlab MEX program,
 *              which can be invoked directly from Matlab.
 *              The code makes extensive use of the fftw
 *              routines, which can be downloaded from
 *              http://www.fftw.org/, for computing fast
 *              Fourier transforms. The corresponding m-file
 *              (sspropc.m) provides information on how to
 *              call this routine from Matlab.
 */
```

```
/******
```

Copyright 2006, Thomas E. Murphy

This file is part of SSPROP.

SSPROP is free software; you can redistribute it and/or modify it under the terms of the GNU General Public License as published by the Free Software Foundation; either version 2 of the License, or (at your option) any later version.

SSPROP is distributed in the hope that it will be useful, but WITHOUT ANY WARRANTY; without even the implied warranty of MERCHANTABILITY or FITNESS FOR A PARTICULAR PURPOSE. See the GNU General Public License for more details.

You should have received a copy of the GNU General Public License along with SSPROP; if not, write to the Free Software Foundation, Inc., 59 Temple Place, Suite 330, Boston, MA 02111-1307 USA

*****/

```
#include <stdlib.h>
#include <string.h>
#include <math.h>
#include "fftw3.h"
#include "mex.h"

#ifdef SINGLEPREC

#define REAL float
#define COMPLEX fftwf_complex
#define PLAN fftwf_plan
#define MAKE_PLAN fftwf_plan_dft_1d
#define DESTROY_PLAN fftwf_destroy_plan
#define EXECUTE fftwf_execute
#define IMPORT_WISDOM fftwf_import_wisdom_from_file
#define EXPORT_WISDOM fftwf_export_wisdom_to_file
#define FORGET_WISDOM fftwf_forget_wisdom
#define WISFILENAME "fftwf-wisdom.dat"

#else

#define REAL double
#define COMPLEX fftw_complex
#define PLAN fftw_plan
#define MAKE_PLAN fftw_plan_dft_1d
#define DESTROY_PLAN fftw_destroy_plan
#define EXECUTE fftw_execute
#define IMPORT_WISDOM fftw_import_wisdom_from_file
#define EXPORT_WISDOM fftw_export_wisdom_to_file
#define FORGET_WISDOM fftw_forget_wisdom
#define WISFILENAME "fftw-wisdom.dat"

#endif
```

```

#define abs2(x) ((*x)[0] * (*x)[0] + (*x)[1] * (*x)[1])
#define prodr(x,y) ((*x)[0] * (*y)[0] + (*x)[1] * (*y)[1])
#define prodi(x,y) ((*x)[0] * (*y)[1] - (*x)[1] * (*y)[0])
#define round(x) ((int)(x+0.5))
#define pi 3.1415926535897932384626433832795028841972

int nt = 0; /* number of fft points */
static int firstcall = 1; /* =1 when sspropc first invoked */
int allocated = 0; /* =1 when memory is allocated */
static int method = FFTW_PATIENT; /* planner method */
PLAN p1,p2,ip1,ip2; /* plans for fft and ifft */
COMPLEX *u0, /* these vectors are */
*ufft, *uhalf, *uv, *u1, /* workspace vectors used in */
*halfstep; /* performing the calculations */

void sspropc_destroy_data(void);
void sspropc_save_wisdom(void);
void sspropc_initialize_data(int);
void cmult(COMPLEX*, COMPLEX*, COMPLEX*);
void cscale(COMPLEX*, COMPLEX*, REAL);
int ssconverged(COMPLEX*, COMPLEX*, REAL);
void mexFunction(int, mxArray* [], int, const mxArray* []);

void sspropc_destroy_data(void)
{
    if (allocated) {
        DESTROY_PLAN(p1);
        DESTROY_PLAN(p2);
        DESTROY_PLAN(ip1);
        DESTROY_PLAN(ip2);
        mxFree(u0);
        mxFree(ufft);
        mxFree(uhalf);
        mxFree(uv);
        mxFree(u1);
        mxFree(halfstep);
        nt = 0;
        allocated = 0;
    }
}

void sspropc_save_wisdom(void)
{
    FILE *wisfile;

    wisfile = fopen(WISFILENAME, "w");
    if (wisfile) {
        mexPrintf("Exporting FFTW wisdom (file = %s).\n", WISFILENAME);
        EXPORT_WISDOM(wisfile);
        fclose(wisfile);
    }
}

void sspropc_load_wisdom(void)
{
    FILE *wisfile;

```

```

wisfile = fopen(WISFILENAME, "r");
if (wisfile) {
    mexPrintf("Importing FFTW wisdom (file = %s).\n", WISFILENAME);
    IMPORT_WISDOM(wisfile);
    fclose(wisfile);
}
}

void sspropc_initialize_data(int n)
{
    FILE* wisfile;          /* wisdom file */

    nt = n;

    if (firstcall) {
        sspropc_load_wisdom();
        firstcall = 0;
    }

    u0 = (COMPLEX*) mxMalloc(sizeof(COMPLEX)*nt);
    ufft = (COMPLEX*) mxMalloc(sizeof(COMPLEX)*nt);
    uhalf = (COMPLEX*) mxMalloc(sizeof(COMPLEX)*nt);
    uv = (COMPLEX*) mxMalloc(sizeof(COMPLEX)*nt);
    u1 = (COMPLEX*) mxMalloc(sizeof(COMPLEX)*nt);
    halfstep = (COMPLEX*) mxMalloc(sizeof(COMPLEX)*nt);

    mexPrintf("Creating FFTW plans (length = %d) ... ", nt);

    p1 = MAKE_PLAN(nt, u0, ufft, FFTW_FORWARD, method);
    p2 = MAKE_PLAN(nt, uv, uv, FFTW_FORWARD, method);
    ip1 = MAKE_PLAN(nt, uhalf, uhalf, FFTW_BACKWARD, method);
    ip2 = MAKE_PLAN(nt, ufft, uv, FFTW_BACKWARD, method);
    mexPrintf("done.\n");

    allocated = 1;
}

/* computes a = b.*c for complex length-nt vectors a,b,c */
void cmult(COMPLEX* a, COMPLEX* b, COMPLEX* c)
{
    int jj;

    for (jj = 0; jj < nt; jj++) {
        a[jj][0] = b[jj][0] * c[jj][0] - b[jj][1] * c[jj][1];
        a[jj][1] = b[jj][0] * c[jj][1] + b[jj][1] * c[jj][0];
    }
}

/* assigns a = factor*b for complex length-nt vectors a,b */
void cscale(COMPLEX* a, COMPLEX* b, REAL factor)
{
    int jj;

```

```

    for (jj = 0; jj < nt; jj++) {
        a[jj][0] = factor*b[jj][0];
        a[jj][1] = factor*b[jj][1];
    }
}

int ssconverged(COMPLEX* a, COMPLEX* b, REAL t)
{
    int jj;
    REAL num, denom;

    for (jj = 0, num = 0, denom = 0; jj < nt; jj++) {
        denom += b[jj][0] * b[jj][0] + b[jj][1] * b[jj][1];
        num += (b[jj][0] - a[jj][0]/nt)*(b[jj][0] - a[jj][0]/nt) +
            (b[jj][1] - a[jj][1]/nt)*(b[jj][1] - a[jj][1]/nt);
    }
    return (num/denom < t);
}

void mexFunction(int nlhs, mxArray *plhs[],
                 int nrhs, const mxArray *prhs[])
{
    REAL scale;           /* scale factor */
    REAL dt;              /* time step */
    REAL dz;              /* propagation stepsize */
    int nz;                /* number of z steps to take */
    int nalpha;           /* number of beta coeffs */
    double* alphap;       /* alpha(w) array, if applicable */
    int nbeta;             /* number of beta coeffs */
    double* beta;         /* dispersion polynomial coeffs */
    REAL gamma;           /* nonlinearity coefficient */
    REAL TPA_eff_real;    /*TPA coefficient defined as TPA/2Aeff, no i in
definition!!*/
    REAL traman = 0;     /* Raman response time */
    REAL toptical = 0;   /* Optical cycle time = lambda/c */
    int maxiter = 4;     /* max number of iterations */
    REAL tol = 1e-5;     /* convergence tolerance */

    REAL* w;              /* vector of angular frequencies */

    int iz,ii,jj;        /* loop counters */
    REAL phase, TPA_phas, alpha,
        wii, fii, TPA;    /* temporary variables */
    COMPLEX
        nlp,              /* nonlinear phase */
        *ua, *ub, *uc;    /* samples of u at three adjacent times */
    char argstr[100];    /* string argument */

    if (nrhs == 1) {
        if (mexGetString(prhs[0],argstr,100))
            mexErrMsgTxt("Unrecognized option.");

        if (!strcmp(argstr,"-savewisdom")) {
            sspropc_save_wisdom();
        }
    }
}

```

```

else if (!strcmp(argstr, "-forgetwisdom")) {
    FORGET_WISDOM();
}
else if (!strcmp(argstr, "-loadwisdom")) {
    sspropc_load_wisdom();
}
else if (!strcmp(argstr, "-patient")) {
    method = FFTW_PATIENT;
}
else if (!strcmp(argstr, "-exhaustive")) {
    method = FFTW_EXHAUSTIVE;
}
else if (!strcmp(argstr, "-measure")) {
    method = FFTW_MEASURE;
}
else if (!strcmp(argstr, "-estimate")) {
    method = FFTW_ESTIMATE;
}
else
    mexErrMsgTxt("Unrecognized option.");
return;
}

if (nrhs < 7)
    mexErrMsgTxt("Not enough input arguments provided.");
if (nlhs > 1)
    mexErrMsgTxt("Too many output arguments.");

sspropc_initialize_data(mxGetNumberOfElements(prhs[0]));

/* parse input arguments */
dt = (REAL) mxGetScalar(prhs[1]);
dz = (REAL) mxGetScalar(prhs[2]);
nz = round(mxGetScalar(prhs[3]));
nalpna = mxGetNumberOfElements(prhs[4]);
alphap = mxGetPr(prhs[4]);
beta = mxGetPr(prhs[5]);
nbeta = mxGetNumberOfElements(prhs[5]);
gamma = (REAL) mxGetScalar(prhs[6]);
TPA_eff_real = (REAL) mxGetScalar(prhs[7]); /*modify this and following
lines for TPA*/
if (nrhs > 8)
    traman = (mxIsEmpty(prhs[8])) ? 0 : (REAL) mxGetScalar(prhs[8]);
if (nrhs > 9)
    toptical = (mxIsEmpty(prhs[9])) ? 0 : (REAL) mxGetScalar(prhs[9]);
if (nrhs > 10)
    maxiter = (mxIsEmpty(prhs[10])) ? 4 : round(mxGetScalar(prhs[10]));
if (nrhs > 11)
    tol = (mxIsEmpty(prhs[11])) ? 1e-5 : (REAL) mxGetScalar(prhs[11]);
/*end mods for TPA */

if ((nalpna != 1) && (nalpna != nt))
    mexErrMsgTxt("Invalid vector length (alpha).");

/* compute vector of angular frequency components */
/* MATLAB equivalent: w = wspace(tv); */

```

```

w = (REAL*)mxMalloc(sizeof(REAL)*nt);
for (ii = 0; ii <= (nt-1)/2; ii++) {
    w[ii] = 2*pi*ii/(dt*nt);
}
for (; ii < nt; ii++) {
    w[ii] = 2*pi*ii/(dt*nt) - 2*pi/dt;
}

/* compute halfstep and initialize u0 and u1 */

for (jj = 0; jj < nt; jj++) {
    if (nbeta != nt)
        for (ii = 0, phase = 0, fii = 1, wii = 1;
            ii < nbeta;
            ii++, fii*=ii, wii*=w[jj])
            phase += wii*((REAL)beta[ii])/fii;
    else
        phase = (REAL)beta[jj];
    alpha = (nalpha == nt) ? (REAL)alphap[jj] : (REAL)alphap[0];
    halfstep[jj][0] = +exp(-alpha*dz/4)*cos(phase*dz/2);
    halfstep[jj][1] = -exp(-alpha*dz/4)*sin(phase*dz/2);
    u0[jj][0] = (REAL) mxGetPr(prhs[0])[jj];
    u0[jj][1] = mxIsComplex(prhs[0]) ? (REAL)(mxGetPi(prhs[0])[jj]) : 0.0;
    u1[jj][0] = u0[jj][0];
    u1[jj][1] = u0[jj][1];
}

mxFree(w); /* free w vector */

mexPrintf("Performing split-step iterations ... ");

EXECUTE(p1); /* ufft = fft(u0) */
for (iz = 0; iz < nz; iz++) {
    cmult(uhalf, halfstep, ufft); /* uhalf = halfstep.*ufft */
    EXECUTE(ip1); /* uhalf = nt*ifft(uhalf) */
    for (ii = 0; ii < maxiter; ii++) {
/*only modify first case for TPA since there is no Raman!!*/
        if ((traman == 0.0) && (toptical == 0)) {

            for (jj = 0; jj < nt; jj++) {
                phase = gamma*(u0[jj][0]*u0[jj][0] +
                    u0[jj][1]*u0[jj][1] +
                    u1[jj][0]*u1[jj][0] +
                    u1[jj][1]*u1[jj][1])*dz/2;

                TPA_phas = TPA_eff_real*(u0[jj][0]*u0[jj][0] +
                    u0[jj][1]*u0[jj][1] +
                    u1[jj][0]*u1[jj][0] +
                    u1[jj][1]*u1[jj][1])*dz/2;

                uv[jj][0] = (uhalf[jj][0]*cos(phase) +
                    uhalf[jj][1]*sin(phase))/nt;

```

```

        uv[jj][1] = (-uhalf[jj][0]*sin(phase) +
                    uhalf[jj][1]*cos(phase))/nt;

        uv[jj][0] = uv[jj][0]*exp(TPA_phas); /*including effects of TPA on
field envelope*/
        uv[jj][1] = uv[jj][1]*exp(TPA_phas); /*including effects of TPA on field
envelope*/

    }

} else { /*please note that this case is not modified for TPA!!!*/

    jj = 0;
    ua = &u0[nt-1]; ub = &u0[jj]; uc = &u0[jj+1];
    nlp[1] = -toptical*(abs2(uc) - abs2(ua) +
                prodr(ub,uc) - prodr(ub,ua))/(4*pi*dt);
    nlp[0] = abs2(ub) - traman*(abs2(uc) - abs2(ua))/(2*dt)
        + toptical*(prodi(ub,uc) - prodi(ub,ua))/(4*pi*dt);

    ua = &u1[nt-1]; ub = &u1[jj]; uc = &u1[jj+1];
    nlp[1] += -toptical*(abs2(uc) - abs2(ua) +
                prodr(ub,uc) - prodr(ub,ua))/(4*pi*dt);
    nlp[0] += abs2(ub) - traman*(abs2(uc) - abs2(ua))/(2*dt)
        + toptical*(prodi(ub,uc) - prodi(ub,ua))/(4*pi*dt);

    nlp[0] *= gamma*dz/2;
    nlp[1] *= gamma*dz/2;

    uv[jj][0] = (uhalf[jj][0]*cos(nlp[0])*exp(+nlp[1]) +
                uhalf[jj][1]*sin(nlp[0])*exp(+nlp[1]))/nt;
    uv[jj][1] = (-uhalf[jj][0]*sin(nlp[0])*exp(+nlp[1]) +
                uhalf[jj][1]*cos(nlp[0])*exp(+nlp[1]))/nt;

    for (jj = 1; jj < nt-1; jj++) {
        ua = &u0[jj-1]; ub = &u0[jj]; uc = &u0[jj+1];
        nlp[1] = -toptical*(abs2(uc) - abs2(ua) +
                    prodr(ub,uc) - prodr(ub,ua))/(4*pi*dt);
        nlp[0] = abs2(ub) - traman*(abs2(uc) - abs2(ua))/(2*dt)
            + toptical*(prodi(ub,uc) - prodi(ub,ua))/(4*pi*dt);

        ua = &u1[jj-1]; ub = &u1[jj]; uc = &u1[jj+1];
        nlp[1] += -toptical*(abs2(uc) - abs2(ua) +
                    prodr(ub,uc) - prodr(ub,ua))/(4*pi*dt);
        nlp[0] += abs2(ub) - traman*(abs2(uc) - abs2(ua))/(2*dt)
            + toptical*(prodi(ub,uc) - prodi(ub,ua))/(4*pi*dt);

        nlp[0] *= gamma*dz/2;
        nlp[1] *= gamma*dz/2;

        uv[jj][0] = (uhalf[jj][0]*cos(nlp[0])*exp(+nlp[1]) +
                    uhalf[jj][1]*sin(nlp[0])*exp(+nlp[1]))/nt;
        uv[jj][1] = (-uhalf[jj][0]*sin(nlp[0])*exp(+nlp[1]) +
                    uhalf[jj][1]*cos(nlp[0])*exp(+nlp[1]))/nt;
    }
}

```

```

    /* we now handle the endpoint where jj = nt-1 */
    /*this part is also modified for TPA */
    ua = &u0[jj-1]; ub = &u0[jj]; uc = &u0[0];
    nlp[1] = -toptical*(abs2(uc) - abs2(ua) +
                    prodr(ub,uc) - prodr(ub,ua))/(4*pi*dt);
    nlp[0] = abs2(ub) - traman*(abs2(uc) - abs2(ua))/(2*dt)
            + toptical*(prodi(ub,uc) - prodi(ub,ua))/(4*pi*dt);

    ua = &u1[jj-1]; ub = &u1[jj]; uc = &u1[0];
    nlp[1] += -toptical*(abs2(uc) - abs2(ua) +
                    prodr(ub,uc) - prodr(ub,ua))/(4*pi*dt);
    nlp[0] += abs2(ub) - traman*(abs2(uc) - abs2(ua))/(2*dt)
            + toptical*(prodi(ub,uc) - prodi(ub,ua))/(4*pi*dt);

    nlp[0] *= gamma*dz/2;
    nlp[1] *= gamma*dz/2;

    uv[jjj][0] = (uhalf[jjj][0]*cos(nlp[0])*exp(+nlp[1]) +
                  uhalf[jjj][1]*sin(nlp[0])*exp(+nlp[1]))/nt;
    uv[jjj][1] = (-uhalf[jjj][0]*sin(nlp[0])*exp(+nlp[1]) +
                  uhalf[jjj][1]*cos(nlp[0])*exp(+nlp[1]))/nt;

    /*again, commented out 2 lines, as these are still in the 2nd case
    which we won't run into*/
    /* uv[jjj][0] = uv[jjj][0]*exp(-1*TPA); */ /*including effects of TPA
    on field envelope*/
    /* uv[jjj][1] = uv[jjj][1]*exp(-1*TPA); */ /*including effects of TPA on
    field envelope*/
}

EXECUTE(p2); /* uv = fft(uv) */
cmult(ufft,uv,halfstep); /* ufft = uv.*halfstep */
EXECUTE(ip2); /* uv = nt*ifft(ufft) */
if (ssconverged(uv,u1,tol)) { /* test for convergence */
    cscale(u1,uv,1.0/nt); /* u1 = uv/nt; */
    break; /* exit from ii loop */
} else {
    cscale(u1,uv,1.0/nt); /* u1 = uv/nt; */
}
}
if (ii == maxiter)
    mexWarnMsgTxt("Failed to converge.");
cscale(u0,u1,1); /* u0 = u1 */
}
mexPrintf("done.\n");

/* allocate space for returned vector */
plhs[0] = mxCreateDoubleMatrix(nt,1,mxCOMPLEX);
for (jj = 0; jj < nt; jj++) {
    mxGetPr(plhs[0])[jj] = (double) u1[jjj][0]; /* fill return vector */
    mxGetPi(plhs[0])[jj] = (double) u1[jjj][1]; /* with u1 */
}

sspropc_destroy_data();

```

```
}
```

D.2 Example using split-step code to calculate spectral broadening

Example code for simulating the spectral broadening in a waveguide is shown below. Note that this code calls the split-step solver in Appendix D.1.

“splitstep_mex_1550nm_700by340_stripTM_picasofit.m”

```
% This file solves the nonlinear Schrodinger equation for
% pulse propagation in an optical fiber using the split-step
% Fourier method described in:
%
% Agrawal, Govind. Nonlinear Fiber Optics, 2nd ed. Academic
% Press, 1995, Chapter 2
%
% The following effects are included in the model: up to 5th order
% dispersion, loss, and self-phase modulation (n2). The core
% routine for implementing the split-step propagation is
% called sspropc_tpa_mk.m (modified to include 2-photon absorption)

close all
clc

%%%%%%%%%%%%%%%%%%%%%%%%%%%%%%%%%%%%%%%%%%%%%%%%%%%%%%%%%%%%%%%%%%%%%%%%
%Start with A=[,], where 1st column is time in fs, and 2nd column is
%magnitude of Electric field E, and 3rd column is phase of E
x = A(:,1)/1000; %convert time values to ps
yamp = A(:,2);
yphase=A(:,3);
maxy=max(yamp);
yamp=yamp/maxy; %normalize by letting max value be 1
%%%%%%%%%%%%%%%%%%%%%%%%%%%%%%%%%%%%%%%%%%%%%%%%%%%%%%%%%%%%%%%%%%%%%%%%

% CONSTANTS

c = 299792458; % speed of light (m/s)

% NUMERICAL PARAMETERS
Lwg=10; %length of waveguide in millimeters (mm)
dt = 0.001; % time step (ps)
nt = 2^14; % number of points in FFT
dz = 1e-6; % distance stepsize (m)
nz = Lwg*1e-3/dz; % number of z-steps
maxiter = 500; % max # of iterations
tol = 1e-5; % error tolerance

% OPTICAL PARAMETERS for strip airclad IG5 on SiO2 waveguide, TM 700x340 nm
at 1550nm!!
lambda = 1546.96; % wavelength (nm)
alpha = 4.12/4.34*100; % linear loss, alpha (1/m)
```

```

TPA=-0.014e-11; two-photon absorption coefficient measured in wg first (m/W)
beta2 = 6.2025*1000; % beta2 (ps^2/km)
beta3 = -4.34e-2*1000; % GVD slope (ps^3/km)
beta4=1.05e-4*1000; %(ps^4/km)
beta5=2.82e-6*1000; %(ps^5/km)
ng = 3.0919; % group index of waveguide
n2 = 4.8e-19; % nonlinear index (m^2/W)
Aeff = 0.3156; % effective area (um^2)
Trans=0.9305; %0.9565*.96; %transmission coefficient for waveguide, using eff
index and index for fiber/air

```

```

% CALCULATED QUANTITIES

```

```

T = nt*dt; % FFT window size (ps)
gamma = 2e21*pi*n2/(lambda*Aeff); % nonlinearity coef (m^-1.W^-1)
TPA_eff_real=TPA/2/(Aeff*1e-12); %real effective TPA coef (m^-1.W^-1)
t = ((1:nt)'+(nt+1)/2)*dt; % vector of t values (ps)
w = 2*pi*((0:nt/2-1),(-nt/2:-1))'/T; % vector of w values (rad/ps)
v = 1000*((0:nt/2-1),(-nt/2:-1))'/T; % vector of v values (GHz)
vs = fftshift(v); % swap halves for plotting
betap = [0 0 beta2/1000 beta3/1000 beta4/1000 beta5/1000]'; % polynomial beta
coeffs.. converted from ps^2/km to ps^2/m, etc.

```

```

% STARTING FIELD

```

```

%Er Fiber laser (using picaso results)
tfwhm= 0.169153;
tp0 = tfwhm; % actual pulse width FWHM (ps) (rough!!)
Rep=17.8e6; %rep rate (Hz)
Pavg=1.596e-3; %average power in watts

```

```

CEin=0.177; %input coupling efficiency est and pol-dep loss
P0=Pavg/(tp0*1e-12*Rep)*Trans*CEin; % peak power (W)
Tp = tfwhm/sqrt(2); %pulse width at 1/e point
Ln1 = 1/(P0*gamma), % nonlinear length (m)
Ld = 1000*Tp^2/abs(beta2), % dispersion length (m)

```

```

yamp_inter = interp1(x,yamp,t,'spline',0);
yphase_inter = interp1(x,yphase,t,'spline',0);
y=yamp_inter.*exp(-1*1i.*yphase_inter); %complex electric field
u0 = sqrt(P0)*y; %starting field (W^.5) includes chirp

```

```

%%%%%%%%%%%%%%%%%%%%%%%%%%%%%%%%%%%%%%%%%%%%%%%%%%%%%%%%%%%%%%%%%%%%%%%%

```

```

sspropc_tpa_mk -estimate

```

```

% PROPAGATE

```

```

tic %added to start MATLAB timer

```

```

u = sspropc_tpa_mk(u0,dt,dz,nz,alpha,betap,gamma,TPA_eff_real);

```

```

% PLOT OUTPUT

```

```

figure(1);
t00 = 50*tp0;
it = find(abs(t)<t00);
a0 = abs(u0).^2/P0;
a0 = a0./max(a0);    %normalizing from juliet
a1 = abs(u).^2/P0;
a1 = a1./max(a1);    % normalizing from juliet

plot (t(it),a0(it),t(it),a1(it));    %plot all normalized from juliet
grid on;
xlabel ('t (ps)');
ylabel ('|u(z,t)|^2 (W)');
legend('initial','final') %added 4/29/14
title ('Initial and Final Pulse Shapes');

figure(2);
iv = find(abs(vs)<80000);    %iv = find(abs(vs)<40000);
S0 = fftshift(abs(dt*fft(u0)/sqrt(2*pi)).^2);
S = fftshift(abs(dt*fft(u)/sqrt(2*pi)).^2);

max_initial_a0=max(a0);
max_final_a1=max(a1);

%normalizing
S0 = S0./max(S0); %from juliet
S = S./max(S);    %from juliet

plot (vs(iv),S0(iv)/P0,vs(iv),S(iv)/P0);
grid on;
xlabel ('\nu (GHz)');
ylabel ('|U(z,\nu)|^2');
legend('initial','final') %added 4/29/14
title ('Initial and Final Pulse Spectra');

%now, plot phase of output, from juliet
S0phi = angle((dt*fft(u0)/sqrt(2*pi)).^2);
Sphi = angle((dt*fft(u)/sqrt(2*pi)).^2);

%unwrapping output phase.. it is very impnt to fftshift before
%unwrapping or there will be big discontinuities in data!
S0phi = unwrap(fftshift((S0phi)));
Sphi = unwrap(fftshift((Sphi)));

%convert this to vs. lambda
lambda0= lambda*1e-9;    %optical carrier frequency
vs0 = 3e8/lambda0;    %conversion from 0 frequency to optical carrier
frequency
vs = vs0+(vs*1e9);

lambda = 3e8./(vs(iv));
Sphilambda = Sphi(iv).*(lambda.^2)./3e8;
S0philambda = S0phi(iv).*(lambda.^2)./3e8;

```

```

Slambda = S(iv).*(lambda.^2)./3e8;
S0lambda = S0(iv).*(lambda.^2)./3e8;
Slambda = Slambda./max(Slambda);
S0lambda = S0lambda./max(S0lambda);

figure(3)
plot(lambda*1e9, S0lambda, 'g', lambda*1e9, (Slambda), 'b')
grid on;
ylabel ('|U(z,\nu)|^2');
title ('Initial and Final Pulse Spectra');
xlabel('lambda (nm)');
legend('initial','final') %added 4/29/14

figure(4);
plot(vs, (S0phi), 'g', vs, (Sphi), 'b')
grid on;
xlabel('lambda (nm)');
ylabel('phase (rad)');
title('Initial and final Pulse Spectral Phase');
legend('initial','final') %added 4/29/14

%saves data to file
jjj = (t00*1e12/((dt^2)*nt)) + (3e8/lambda0);
jjjh = (-t00*1e12/((dt^2)*nt)) + (3e8/lambda0);
uvt = find(jjjh<vs & vs<=jjj);
size(vs(uvt))
size(t(it))

%saving time, initial intensity, final intensity, frequency(GHz), initial
spectral
% intensity, final spectral intensity, intial spectral phase, final spectral
phase
AA =
[t(it)';a0(it)';a1(it)';vs(uvt)';S0(uvt)'/P0;S(uvt)'/P0;S0phi(uvt)';Sphi(uvt)
'];
fid = fopen('splitstep.out','w');
fprintf(fid,'%12.9f\t %12.9f\t %12.9f\t %12.9f\t %12.9f\t %12.9f\t %12.9f\t
%12.9f\n',AA);
fclose(fid)

nz*dz/Ld
gamma
toc %added to check elapsed time

```

Appendix E

Ring design code

E.1 Ring code for four-wave mixing

The code below iteratively solves for the resonances nearest a target design wavelength. For four-wave mixing applications, assuming both pump and signal on resonance, the code uses dispersion to calculate the phase mismatch between the idler and resonance, for calculations of four-wave mixing efficiency. The general ring resonator design process is described more in Chapter 4, in Section 4.3.1.

“ChG_ring_1550nm_iterative_quadratic_fixedReff_example.m”

```
%%Also kept dw for ALL dispersion calcs to 1/1000 for now...
%3/17/2016 Update:  switch to iterative quadratic process for resonances (see
code below)

%1/8/2016 Update:  Fixed to include material dispersion in wg sim/neff calc,
and
%correspondingly fixed disp calc & recorded variables

%1/5/2016 edited to calc dispersion and resonances near 1550 nm for fixed
%wg dimension, varying only ring radius

%Waveguide Top File
%Commands to run Milos' 2d finite difference vectorial mode solver
clear all
close all
clc

tic
```

```

%Set waveguide materials below: (upper cladding, air, is dispersionless)
nAir=1.0000;
nChal=@(x) sqrt(1+2.75840+3.09812*x^2/(x^2-0.399523^2)+1.64139*x^2/(x^2-
45.1071^2));%IRG25, ref index info/Schott;
nSiO2=@(x) sqrt(1+0.6961663*x^2/(x^2-0.0684043^2)+0.4079426*x^2/(x^2-
0.1162414^2)+0.8974794*x^2/(x^2-9.896161^2)); %ref index info, Malitson;
%Will set nCore, nSub later, and re-set each time I change the wavelength
nClad=nAir;

%Initialize arrays to keep track of useful parameters
size1=10; %#of different test radiuses R_eff
R_array=zeros(1,size1);
m_p_array=zeros(1,size1);
lambda_p_array=zeros(1,size1);
lambda_s_array=zeros(1,size1);
lambda_i_array=zeros(1,size1); %where resonance is!!
lambda_c_array=zeros(1,size1); %where converted idler actually is
dlam_array=zeros(1,size1);
n_eff_pump_array=zeros(1,size1);
n_eff_signal_array=zeros(1,size1);
B2_ps2_per_m_array=zeros(1,size1);
n_group_array=zeros(1,size1);
dk_array=zeros(1,size1);
n_eff_c_array=zeros(1,size1);
L_array=zeros(1,size1);

count=0;
c=0;
for R_eff=3:1:12 %[3,4,5,6,7,8,9,10,11,12,13,14,15] %vary ring radius from 3
to 12 microns
    c=c+1;
    R_array(1,c)=R_eff;
    count=count+1

%Set waveguide core width w and height h, in microns.
filename = '1550nm_ChGring_sim_w800_h330_iterquad_fixedReff_example.xlsx';
w=0.800;
h=0.330;
%Guess effective index as starting point.
n_guess=2.04; %2.0337+0.3;

%Initialize arrays for finding resonance nearest 1550 nm (in inner for loop)
r=0;
size2=10; % # of different test wavelengths for finding the nearest
resonances
wave_array=zeros(1,size2);
w_array=zeros(1,size2);
m_array=zeros(1,size2);

%%%%%%%%%%%%%%%%%%%%%%%%%%%%%%%%%%%%%%%%%%%%%%%%%%%%%%%%%%%%%%%%%%%%%%%%
fprintf('First finding pump resonance... \n');
%First run through neff, dispersion at 1550
wavelength=1.55;

```

```

w2=2*pi*3e14/wavelength;
dw=w2/1000;
w1=w2-dw;
w3=w2+dw;
wavelength1=2*pi*3e14/w1;
wavelength3=2*pi*3e14/w3;
nCore=nChal(wavelength); %update index to account for IRG25 dispersion!
nSub=nSiO2(wavelength);
[N,F] = sisolver3d([nSub nSub nSub; nClad nCore nClad; nClad nClad nClad],
[1.5 w 1.5], [1 h 1], [.01 .010], 2*pi/wavelength, struct('radius',R_eff-w/2-
1.5,'mu_guess',R_eff*n_guess*2*pi/wavelength,'PMLwidth',[0 1. 0
0],'PMLsigma',[0.2 0.2]));
%View the modes
modeview( struct('N',N,'F',F) );

nCore=nChal(wavelength3); %update index to account for IRG25 dispersion!
nSub=nSiO2(wavelength3);
[N3,F3] = sisolver3d([nSub nSub nSub; nClad nCore nClad; nClad nClad nClad],
[1.5 w 1.5], [1 h 1], [.01 .010], 2*pi/wavelength3, struct('radius',R_eff-
w/2-1.5,'mu_guess',R_eff*n_guess*2*pi/wavelength3,'PMLwidth',[0 1. 0
0],'PMLsigma',[0.2 0.2]));

nCore=nChal(wavelength1); %update index to account for IRG25 dispersion!
nSub=nSiO2(wavelength1);
[N1,F1] = sisolver3d([nSub nSub nSub; nClad nCore nClad; nClad nClad nClad],
[1.5 w 1.5], [1 h 1], [.01 .010], 2*pi/wavelength1, struct('radius',R_eff-
w/2-1.5,'mu_guess',R_eff*n_guess*2*pi/wavelength1,'PMLwidth',[0 1. 0
0],'PMLsigma',[0.2 0.2]));

%Calculate effective index of modes (scale the propagation constant)
beta_actual=F.beta/R_eff;
n_eff_bend=real(beta_actual)*wavelength/(2*pi)

%calculate up to 2nd order dispersion, (in ps^n/m)
B0=F.beta/R_eff*1e6; %(units of 1/m)
B1=(F3.beta/R_eff-F.beta/R_eff)/dw*1e6*(1e12); %(units of ps/m)
B2=(F3.beta/R_eff-2*F.beta/R_eff+F1.beta/R_eff)/(dw^2)*1e6*((1e12)^2);
%%(units of ps^2/m) material and wg included implicitly
n_group=B1*1e-12*3e8; %unitless

%Calculate 'm' value, and find closest integer m to 1550 nm:
m_res=2*pi*R_eff/wavelength*n_eff_bend;
m_p=round(m_res);
fprintf('Target pump resonance is m_p=%.4f. \n',m_p);
m_p_array(1,c)=m_p;
m_s=m_p+1;
m_i=m_p-1;
m_guess_p=m_res;
fprintf('First guess pump resonance is m_p=%.5f. \n',m_guess_p);
toler=1e-8; %tolerance for m (i.e. how well we need to get resonance)

AA=real(R_eff*1e-6*B2/1e24/2);
BB=real(R_eff*1e-6*B1/1e12);
CC=real(R_eff*1e-6*B0-m_p);
dw_soln=(-BB+sqrt(BB^2-(4*AA*CC)))/(2*AA);

```

```

w_new_guess=dw_soln+2*pi*3e14/wavelength; %in SI, in Hz
new_wavelength=2*pi*3e8/w_new_guess/1e-6; %in microns!
fprintf('First guess pump wavelength is %.5f nm.
\n',new_wavelength*1000);
err_p=(new_wavelength-wavelength)/wavelength;
fprintf('Relative error in pump wavelength guess is %.3e. \n',err_p);
%pause
%Run through while loop to find actual resonance for pump closest to 1550nm
but still on resonance:
%%%%%%%%%%%%%%%%%%%%%%%%%%%%%%%%%%%%%%%%%%%%%%%%%%%%%%%%%%%%%%%%%%%%%%%%
while (abs(err_p)>toler)
    wavelength=new_wavelength;
    w2=2*pi*3e14/wavelength;
    dw=w2/1000;
    w1=w2-dw;
    w3=w2+dw;
    wavelength1=2*pi*3e14/w1;
    wavelength3=2*pi*3e14/w3;
    nCore=nChal(wavelength); %update index to account for IRG25 dispersion!
    nSub=nSiO2(wavelength);
    [N,F] = sisolver3d([nSub nSub nSub; nClad nCore nClad; nClad nClad
nClad], [1.5 w 1.5], [1 h 1], [.01 .010], 2*pi/wavelength,
struct('radius',R_eff-w/2-
1.5,'mu_guess',R_eff*n_guess*2*pi/wavelength,'PMLwidth',[0 1. 0
0],'PMLsigma',[0.2 0.2]));
    %View the modes
    modeview( struct('N',N,'F',F) );

    nCore=nChal(wavelength3); %update index to account for IRG25 dispersion!
    nSub=nSiO2(wavelength3);
    [N3,F3] = sisolver3d([nSub nSub nSub; nClad nCore nClad; nClad nClad
nClad], [1.5 w 1.5], [1 h 1], [.01 .010], 2*pi/wavelength3,
struct('radius',R_eff-w/2-
1.5,'mu_guess',R_eff*n_guess*2*pi/wavelength3,'PMLwidth',[0 1. 0
0],'PMLsigma',[0.2 0.2]));

    nCore=nChal(wavelength1); %update index to account for IRG25 dispersion!
    nSub=nSiO2(wavelength1);
    [N1,F1] = sisolver3d([nSub nSub nSub; nClad nCore nClad; nClad nClad
nClad], [1.5 w 1.5], [1 h 1], [.01 .010], 2*pi/wavelength1,
struct('radius',R_eff-w/2-
1.5,'mu_guess',R_eff*n_guess*2*pi/wavelength1,'PMLwidth',[0 1. 0
0],'PMLsigma',[0.2 0.2]));

    %Calculate effective index of modes (scale the propagation constant)
    beta_actual=F.beta/R_eff;
    n_eff_bend=real(beta_actual)*wavelength/(2*pi);

    %calculate up to 2nd order dispersion, (in ps^n/m)
    B0=F.beta/R_eff*1e6; %(units of 1/m)
    B1=(F3.beta/R_eff-F.beta/R_eff)/dw*1e6*(1e12); %(units of ps/m)
    B2=(F3.beta/R_eff-2*F.beta/R_eff+F1.beta/R_eff)/(dw^2)*1e6*((1e12)^2);
%%(units of ps^2/m) material and wg included implicitly
    n_group=B1*1e-12*3e8; %unitless

```

```

%Calculate 'm' value, and find closest integer m to 1550 nm:
m_res=2*pi*R_eff/wavelength*n_eff_bend;
m_guess_p=m_res;
fprintf('Next guess pump resonance is mp= %.5f. \n',m_guess_p);

AA=real(R_eff*1e-6*B2/1e24/2);
BB=real(R_eff*1e-6*B1/1e12);
CC=real(R_eff*1e-6*B0-m_p); %fixed, using target m_p
dw_soln=(-BB+sqrt(BB^2-(4*AA*CC)))/(2*AA);
w_new_guess=dw_soln+2*pi*3e14/wavelength; %in SI, in Hz
new_wavelength=2*pi*3e8/w_new_guess/1e-6; %in microns!
fprintf('Next guess pump wavelength is %.5f nm.
\n',new_wavelength*1000);
err_p=(new_wavelength-wavelength)/wavelength;
fprintf('Relative error in next guess pump wavelength is %.3e.
\n',err_p);
%pause
end
%Once tolerance met for pump, record the pump neff, dispersion, etc.
lambda_p=wavelength;
lambda_p_array(1,c)=lambda_p;
B2_ps2_per_m_array(1,c)=B2;
n_group_array(1,c)=n_group;
n_eff_p=n_eff_bend;
n_eff_pump_array(1,c)=n_eff_p;
fprintf('Final pump resonance is m_p=%.6f. \n',m_res);
%%%%%%%%%%%%%%%%%%%%%%%%%%%%%%%%%%%%%%%%%%%%%%%%%%%%%%%%%%%%%%%%%%%%%%%%
%note idler wavelength guess
idler_wavelength_guess=2*pi*R_eff*n_eff_bend/m_i;

%Set new wavelength to guess of where signal resonance will be:
fprintf('Now finding signal resonance. \n');
new_wavelength=2*pi*R_eff*n_eff_bend/m_s;
fprintf('First guess signal wavelength is %.5f nm. \n',new_wavelength*1000);
err_s=(new_wavelength-wavelength)/wavelength;
fprintf('Relative error in signal wavelength is %.3e. \n',err_s);

%Run through similar procedure to make sure signal wavelength on resonance
(within specified tolerance)
while(abs(err_s)>toler)
    wavelength=new_wavelength;
    w2=2*pi*3e14/wavelength;
    dw=w2/1000; %w2*1e-6; %w2/1000;
    w1=w2-dw;
    w3=w2+dw;
    wavelength1=2*pi*3e14/w1;
    wavelength3=2*pi*3e14/w3;
    nCore=nChal(wavelength); %update index to account for IRG25 dispersion!
    nSub=nSiO2(wavelength);
    [N,F] = sisolver3d([nSub nSub nSub; nClad nCore nClad; nClad nClad
nClad], [1.5 w 1.5], [1 h 1], [.01 .010], 2*pi/wavelength,
struct('radius',R_eff-w/2-
1.5,'mu_guess',R_eff*n_guess*2*pi/wavelength,'PMLwidth',[0 1. 0
0], 'PMLsigma',[0.2 0.2]));
    %View the modes
    modeview( struct('N',N,'F',F) );

```

```

nCore=nChal(wavelength3); %update index to account for IRG25 dispersion!
nSub=nSiO2(wavelength3);
[N3,F3] = sisolver3d([nSub nSub nSub; nClad nCore nClad; nClad nClad
nClad], [1.5 w 1.5], [1 h 1], [.01 .010], 2*pi/wavelength3,
struct('radius',R_eff-w/2-
1.5,'mu_guess',R_eff*n_guess*2*pi/wavelength3,'PMLwidth',[0 1. 0
0],'PMLsigma',[0.2 0.2]));

nCore=nChal(wavelength1); %update index to account for IRG25 dispersion!
nSub=nSiO2(wavelength1);
[N1,F1] = sisolver3d([nSub nSub nSub; nClad nCore nClad; nClad nClad
nClad], [1.5 w 1.5], [1 h 1], [.01 .010], 2*pi/wavelength1,
struct('radius',R_eff-w/2-
1.5,'mu_guess',R_eff*n_guess*2*pi/wavelength1,'PMLwidth',[0 1. 0
0],'PMLsigma',[0.2 0.2]));

%Calculate effective index of modes (scale the propagation constant)
beta_actual=F.beta/R_eff;
n_eff_bend=real(beta_actual)*wavelength/(2*pi);

%calculate up to 2nd order dispersion, (in ps^n/m)
B0=F.beta/R_eff*1e6; %(units of 1/m)
B1=(F3.beta/R_eff-F.beta/R_eff)/dw*1e6*(1e12); %(units of ps/m)
B2=(F3.beta/R_eff-2*F.beta/R_eff+F1.beta/R_eff)/(dw^2)*1e6*((1e12)^2);
%%(units of ps^2/m) material and wg included implicitly
n_group=B1*1e-12*3e8; %unitless

%Calculate new signal 'm' value, given effective index:
m_res=2*pi*R_eff/wavelength*n_eff_bend;
fprintf('Next guess signal resonance is ms=%.5f. \n',m_res);
m_guess_s=m_res;

AA=real(R_eff*1e-6*B2/1e24/2);
BB=real(R_eff*1e-6*B1/1e12);
CC=real(R_eff*1e-6*B0-m_s); %fixed, using target m_signal
dw_soln=(-BB+sqrt(BB^2-(4*AA*CC)))/(2*AA);
w_new_guess=dw_soln+2*pi*3e14/wavelength; %in SI, in Hz
new_wavelength=2*pi*3e8/w_new_guess/1e-6; %in microns!
fprintf('Next guess signal wavelength is %.5f nm. \n',new_wavelength);
err_s=(new_wavelength-wavelength)/wavelength;
fprintf('Relative error in guess signal wavelength is %.3e. \n',err_s);
end
%Once tolerance met for signal, record the signal wavelength, etc.
fprintf('Final signal resonance is m_s=%.6f. \n',m_res);
lambda_s=wavelength;
lambda_s_array(1,c)=lambda_s;
dlam=lambda_s-lambda_p; %spacing btwn pump and signal resonances
dlam_array(1,c)=dlam;
n_eff_signal_array(1,c)=n_eff_bend;
%%%%%%%%%%%%%%%%%%%%%%%%%%%%%%%%%%%%%%%%%%%%%%%%%%%%%%%%%%%%%%%%%%%%%%%%

%Set new wavelength to guess of where idler resonance will be:
%Note that this 3rd while loop to find idler not actually necessary....
fprintf('Now finding idler resonance. \n');

```

```

new_wavelength=idler_wavelength_guess;
fprintf('First guess idler wavelength is %.5f nm. \n',new_wavelength*1000);
err_i=(new_wavelength-wavelength)/wavelength;
fprintf('Relative error in first guess idler wavelength is %.5f. \n',err_i);

while(abs(err_i)>toler)
    wavelength=new_wavelength;
    w2=2*pi*3e14/wavelength;
    dw=w2/1000; %w2*1e-6; %w2/1000;
    w1=w2-dw;
    w3=w2+dw;
    wavelength1=2*pi*3e14/w1;
    wavelength3=2*pi*3e14/w3;
    nCore=nChal(wavelength); %update index to account for IRG25 dispersion!
    nSub=nSiO2(wavelength);
    [N,F] = sisolver3d([nSub nSub nSub; nClad nCore nClad; nClad nClad
nClad], [1.5 w 1.5], [1 h 1], [.01 .010], 2*pi/wavelength,
struct('radius',R_eff-w/2-
1.5,'mu_guess',R_eff*n_guess*2*pi/wavelength,'PMLwidth',[0 1. 0
0],'PMLsigma',[0.2 0.2]));
    %View the modes
    modeview( struct('N',N,'F',F) );

    nCore=nChal(wavelength3); %update index to account for IRG25 dispersion!
    nSub=nSiO2(wavelength3);
    [N3,F3] = sisolver3d([nSub nSub nSub; nClad nCore nClad; nClad nClad
nClad], [1.5 w 1.5], [1 h 1], [.01 .010], 2*pi/wavelength3,
struct('radius',R_eff-w/2-
1.5,'mu_guess',R_eff*n_guess*2*pi/wavelength3,'PMLwidth',[0 1. 0
0],'PMLsigma',[0.2 0.2]));

    nCore=nChal(wavelength1); %update index to account for IRG25 dispersion!
    nSub=nSiO2(wavelength1);
    [N1,F1] = sisolver3d([nSub nSub nSub; nClad nCore nClad; nClad nClad
nClad], [1.5 w 1.5], [1 h 1], [.01 .010], 2*pi/wavelength1,
struct('radius',R_eff-w/2-
1.5,'mu_guess',R_eff*n_guess*2*pi/wavelength1,'PMLwidth',[0 1. 0
0],'PMLsigma',[0.2 0.2]));

    %Calculate effective index of modes (scale the propagation constant)
    beta_actual=F.beta/R_eff;
    n_eff_bend=real(beta_actual)*wavelength/(2*pi);

    %calculate up to 2nd order dispersion, (in ps^n/m)
    B0=F.beta/R_eff*1e6; %(units of 1/m)
    B1=(F3.beta/R_eff-F.beta/R_eff)/dw*1e6*(1e12); %(units of ps/m)
    B2=(F3.beta/R_eff-2*F.beta/R_eff+F1.beta/R_eff)/(dw^2)*1e6*((1e12)^2);
    %% (units of ps^2/m) material and wg included implicitly
    n_group=B1*1e-12*3e8; %unitless

    %Calculate new idler 'm' value, given effective index:
    m_res=2*pi*R_eff/wavelength*n_eff_bend;
    fprintf('Next guess idler resonance is mi=%.5f. \n',m_res);
    m_guess_i=m_res;

```

```

AA=real(R_eff*1e-6*B2/1e24/2);
BB=real(R_eff*1e-6*B1/1e12);
CC=real(R_eff*1e-6*B0-m_i); %fixed, using target m_idler (trying to find
mp-1 wavelength)
dw_soln=(-BB+sqrt(BB^2-(4*AA*CC)))/(2*AA);
w_new_guess=dw_soln+2*pi*3e14/wavelength; %in SI, in Hz
new_wavelength=2*pi*3e8/w_new_guess/1e-6; %in microns!
fprintf('Next guess idler wavelength is %.5f nm.
\n',new_wavelength*1000);
err_i=(new_wavelength-wavelength)/wavelength;
fprintf('Relative error in idler guess is %.3e. \n',err_i);
end
%Once tolerance met for idler, record the idler wavelength, etc.
fprintf('Final idler resonance is m_i=%.6f. \n',m_res);
lambda_i=wavelength;
fprintf('Final idler wavelength is %.6f nm. \n',lambda_i*1000);
lambda_i_array(1,c)=lambda_i; %%%%%%%%%%%
%%%%%%%%%%

%Finally, also calculate neff for actual converted idler (non-resonant)
wavelength:
wavelength=1/(2/lambda_p-1/lambda_s);
fprintf('Converted wavelength from energy conservation is %.6f nm.
\n',wavelength*1000);

%Run si solver 3d
nCore=nChal(wavelength); %update index to account for IRG25 dispersion!
nSub=nSiO2(wavelength);
[N,F] = sisolver3d([nSub nSub nSub; nClad nCore nClad; nClad nClad nClad],
[1.5 w 1.5], [1 h 1], [.01 .010], 2*pi/wavelength, struct('radius',R_eff-w/2-
1.5,'mu_guess',R_eff*n_guess*2*pi/wavelength,'PMLwidth',[0 1. 0
0], 'PMLsigma',[0.2 0.2]));

%View the modes
modeview( struct('N',N,'F',F) );
%Calculate effective index
beta_actual=F.beta/R_eff;
lambda_c=wavelength; %in microns--this is the converted idler wavelength
(from E conservation)!
n_eff_c=beta_actual*wavelength/(2*pi);

lambda_c_array(1,c)=lambda_c;
n_eff_c_array(1,c)=n_eff_c;
L_array(1,c)=2*pi*R_eff; %in microns

dk=(m_p-1)/R_eff-(2*pi*n_eff_c/lambda_c) %in 1/micron
dk_array(1,c)=dk;
end

%Store data and write to file
data_matrix1=real([R_array; m_p_array;
lambda_p_array;
lambda_s_array;

```

```

lambda_i_array; %where resonance is!!
lambda_c_array; %where converted idler actually is
n_eff_signal_array;
n_eff_pump_array;
B2_ps2_per_m_array;
n_group_array;
n_eff_c_array;
R_array;
dk_array;
L_array]');

%write simulation data to file:
data_cells=num2cell(data_matrix1);          %Convert data to cell array
col_header={'R_eff_fixed (um)', 'm_p', 'lambda_p (um)', 'lambda_s (um)',
'lambda_i (um)', 'lambda_c (um)', 'neff_s', 'neff_p', 'B2_p (ps2/m)',
'ngroup_p', 'neff_c', 'R_eff_fixed (um)', 'dk (1/um)', 'L (um)'};          %Row
cell_array (for column labels)
output_matrix=[col_header; data_cells];          %Join cell arrays
xlswrite(filename,output_matrix);          %Write data and both headers

toc

```

E.2 Phase matching code for concentric (pulley) couplers

The code below calculates the propagation constants for a ring and concentric (pulley) coupler, for a fixed gap distance and varying coupler waveguide width. This can be used to find the phase-matched width desired for coupling from a curved waveguide to a ring resonator, as described in Chapter 4, in Section 4.2.4.

“ChG_ring_Concentric_Coupling_1550nm_Example.m”

```

%Waveguide Top File
%Commands to run Milos' 2d finite difference vectorial mode solver
clear all
clc
%Parameters (lengths are in microns!)
filename = '1550nm_ChG_coupling_example.xlsx';
wavelength=1.55;

%Case 2
nAir=1.0000;
nChal=2.659633;
nSiO2=1.444;
%nMgF2=1.37;

nSub=nSiO2

```

```

nCore=nChal
nClad=nAir

r=0;
count=0;
% w_array=zeros(1,6);
% h_array=zeros(1,6);
% n1_array=zeros(1,36);
% n2_array=zeros(1,36);

%Set waveguide core width w and height h, in microns.
w=0.800;
h=0.330;

%Guess effective index as starting point.
n_guess=2.65; %2.0335;

beta_array1=zeros(1,11);
beta_array2=zeros(1,11);
w2_array=zeros(1,11);

%a is the variable radius (currently ranges from 40 to 120 microns, in
%intervals of 10 microns
for w2=0.4:.02:0.7 %40 to 120 in 20's
    R_eff=6;
    xgap=0.100;

    r=r+1;
    w2_array(1,r)=w2;

%Run si solver 3d
[N,F] = sisolver3d([nSub nSub nSub nSub nSub; nClad nCore nClad nCore nClad;
nClad nClad nClad nClad nClad], [1 w xgap w2 1], [1 h 1], [.01 .010],
2*pi/wavelength, struct('NMODES_CALC',2,'radius',R_eff-w/2-
1,'mu_guess',R_eff*n_guess*2*pi/wavelength,'PMLwidth',[0 1. 0
0],'PMLsigma',[0.2 0.2]));

%View the modes
modeview( struct('N',N,'F',F) );

%Calculate effective index of modes (scale the propagation constant)
%fixed 2.25.14
gamma=F.beta;
beta_actual=F.beta/R_eff;
n_eff_bend=beta_actual*wavelength/(2*pi)

count=count+1;
beta_array1(1,count)=real(beta_actual(1,1));
beta_array2(1,count)=real(beta_actual(2,1));

end

```

```

figure(2), scatter(w2_array,beta_array1)
hold on
scatter(w2_array,beta_array2)
xlabel('2nd wg width (microns)')
ylabel('beta actual [1/um]')
title('beta vs. 2nd wg width for 800 nm by 330 nm ChG wgs, Rcent=6mic,
1550nm, xgap=100 nm')

%Store data and write to file
data_matrix1=real([w2_array; beta_array1;
beta_array2;]);

%write simulation data to file:
data_cells=num2cell(data_matrix1);      %Convert data to cell array
col_header={'width w2 (um)', 'beta_actual 1 (1/um)', 'beta_actual 2 (1/um)'};
%Row cell array (for column labels)
output_matrix=[col_header; data_cells]; %Join cell arrays
xlswrite(filename,output_matrix);      %Write data and both headers

```

Appendix F

Derivation of thermal resonant wavelength shift in wedge resonator

In this section, we calculate the shift in resonant wavelength for a microresonator, and show how to relate this to the thermo-optic coefficient of the resonator for the hybrid chalcogenide-silica wedge resonator geometry used in Chapter 5. In a microresonator, the resonant wavelength, λ_{res} is given by

$$\lambda_{res} = \frac{2\pi R n_{eff}}{m}, \quad (\text{F.1})$$

where R is the radius, n_{eff} is the effective index, and m is an integer. One can differentiate to find dependence on temperature, T :

$$\frac{d\lambda_{res}}{dT} = \frac{\partial}{\partial T} \left(\frac{2\pi R n_{eff}}{m} \right). \quad (\text{F.2})$$

Separating into contributions from thermal expansion and the thermo-optic coefficient, one finds

$$\frac{d\lambda_{res}}{dT} = \frac{2\pi}{m} \left(R \frac{\partial n_{eff}}{\partial T} + n_{eff} \frac{\partial R}{\partial T} \right). \quad (\text{F.3})$$

Note that the coefficient of thermal expansion α_L is given by

$$\alpha_L = \frac{1}{L} \frac{dL}{dT}, \quad (\text{F.4})$$

where L is the length. The wedge resonator geometry used in this work is composed primarily of silica (with α_{L,SiO_2}), but also includes a thin, 125-nm layer of chalcogenide (with $\alpha_{L,ChG}$), as illustrated in Figure F.1.

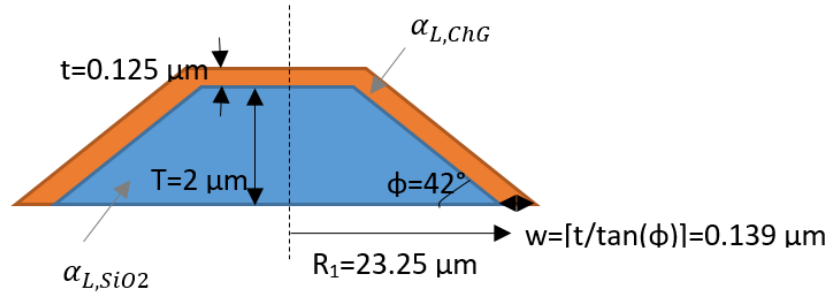


Figure F.1. Schematic of hybrid wedge resonator cross section. Resonator consists of 2000-nm thick layer SiO₂ wedge with 23.25 μm radius, 42 degree wedge angle, and 125-nm thick ChG (Ge-Sb-Se) layer.

Letting $R = L$, one finds

$$\frac{\partial R}{\partial T} \approx \frac{\Delta R}{\Delta T} = \alpha_{L,SiO_2} R_1 + \alpha_{L,ChG} w. \quad (\text{F.5})$$

where R_1 is the silica resonator radius and w is the lateral ChG thickness, as illustrated in Figure

F.1. Plugging Equation F.5 into Equation F.3, one gets

$$\frac{d\lambda_{res}}{dT} = \frac{2\pi}{m} \left(R \frac{\partial n_{eff}}{\partial T} \right) + \frac{2\pi}{m} \left(n_{eff} \alpha_{L,SiO_2} R_1 + n_{eff} \alpha_{L,ChG} w \right). \quad (\text{F.6})$$

Note that the first term contains the contribution from the thermo-optic coefficient, and the second term contains contributions from thermal expansion of SiO₂ and ChG. It is useful to note magnitudes of thermo-optic coefficient and thermal expansion for our materials, which are provided in Table F.1.

Table F.1. Thermo-optic and thermal expansion coefficients.

Material	dn/dT (K ⁻¹)	α _L (K ⁻¹)	Reference	Calculated Contribution of thermal expansion to dλ/dT (pm/°C)
IRG25 (ChG)	7.44x10 ⁻⁵	1.4x10 ⁻⁵	[62]	0.13
SiO ₂	~1x10 ⁻⁵	0.57x10 ⁻⁶	[108,109]	0.88
Combined				1.01

We measured dλ/dT~60.5 pm/°C, so the total calculated contribution from thermal expansion of ~1 pm/°C, calculated from the values in Table F.1 and Equation F.6, is negligible.

Neglecting the thermal expansion contribution, one finds

$$\frac{d\lambda_{res}}{dT} \approx \frac{2\pi}{m} \left(R \frac{\partial n_{eff}}{\partial T} \right). \quad (F.7)$$

Substituting Equation F.1 to eliminate m, this can be re-written as

$$\frac{d\lambda_{res}}{dT} \approx \left(\frac{\lambda_{res}}{n_{eff}} \frac{\partial n_{eff}}{\partial T} \right). \quad (F.7)$$

Re-arranging, one can calculate the thermo-optic coefficient of the resonator to be

$$\frac{\partial n_{eff}}{\partial T} \approx \left(\frac{n_{eff}}{\lambda_{res}} \frac{d\lambda_{res}}{dT} \right). \quad (F.8)$$

A summary of the measured $\frac{d\lambda_{res}}{dT}$ and corresponding calculated $\frac{dn_{eff}}{dT}$ are provided in Table

F.2. From this data, the average $\frac{d\lambda_{res}}{dT}$ =59 pm/C, with average $\frac{dn_{eff}}{dT}$ =5.5x10⁻⁵ K⁻¹.

Table F.2. Summary of measured thermal resonant shift and thermo-optic coefficient.

Date	$\frac{d\lambda_{res}}{dT}$ (pm/C)	λ_{res} (nm)	n_{eff}	Calculated $\frac{dn_{eff}}{dT}$ (K ⁻¹)
11.23.16	60.5	1584.7	1.4755	5.6×10^{-5}
11.29.16	60.9	1566.1	1.4795	5.8×10^{-5}
11.29.16	55.6	1566.1	1.4795	5.3×10^{-5}
Average	59.0			5.5×10^{-5}

Appendix G

Microscope Components

A list of parts used in the optical microscope for device characterization is listed in Table G.1.

Table G.1. Parts list for microscope

Vendor	Part Number	Description
Edmund Optics	59-671	Manual upper zoom module for 12.5x zoom
Edmund Optics	59-756	Coaxial lower zoom module for 12.5x zoom
Edmund Optics	56-626	2.0x TV tube
Edmund Optics	59-683	Mounting clamp for 12.5x zoom lens
Edmund Optics	54-794	Rack and pinion coarse/fine movement
Edmund Optics	39-353	$\frac{3}{4}$ -inch diameter stainless post, 18-inch height
Edmund Optics	46-144	10X Mitutoyo plan apo infinity corrected objective, long working distance of 33.5 mm, 0.28 NA, M26x36 TPI threads
Edmund Optics	59-675	Adapter for Mitutoyo objective
Edmund Optics	54-262	Breadboard adapter for $\frac{3}{4}$ -inch diameter post